Solar radiation transport in the cloudy atmosphere: a 3D perspective on observations and climate impacts

Solar radiation transport in the cloudy atmosphere: a 3D perspective on observations and climate impacts

Anthony B Davis[1,3] **and Alexander Marshak**[2]

[1] Los Alamos National Laboratory, Space and Remote Sensing Group, Los Alamos, NM 87545, USA
[2] NASA—Goddard Space Flight Center, Climate and Radiation Branch, Greenbelt, MD 20771, USA

E-mail: Anthony.B.Davis@jpl.nasa.gov and Alexander.Marshak@nasa.gov

Abstract

The interplay of sunlight with clouds is a ubiquitous and often pleasant visual experience, but it conjures up major challenges for weather, climate, environmental science and beyond. Those engaged in the characterization of clouds (and the clear air nearby) by remote sensing methods are even more confronted. The problem comes, on the one hand, from the spatial complexity of *real* clouds and, on the other hand, from the dominance of multiple scattering in the radiation transport. The former ingredient contrasts sharply with the still popular *representation* of clouds as homogeneous plane-parallel slabs for the purposes of radiative transfer computations. In typical cloud scenes the opposite asymptotic transport regimes of diffusion and ballistic propagation coexist. We survey the three-dimensional (3D) atmospheric radiative transfer literature over the past 50 years and identify three concurrent and intertwining thrusts: first, how to assess the damage (bias) caused by 3D effects in the operational 1D radiative transfer models? Second, how to mitigate this damage? Finally, can we exploit 3D radiative transfer phenomena to innovate observation methods and technologies? We quickly realize that the smallest scale resolved computationally or observationally may be artificial but is nonetheless a key quantity that separates the 3D radiative transfer solutions into two broad and complementary classes: stochastic and deterministic. Both approaches draw on classic and contemporary statistical, mathematical and computational physics.

(Some figures in this article are in colour only in the electronic version)

Contents

List of abbreviations/acronyms

nD	n-dimensional ($n = 1, 2, 3$)
n+1D	n-plus-one-dimensional (i.e. space–time)
ACE	Aerosol, Clouds and ocean Ecosystem (upcoming NASA mission)
AERONET	AEROsol observation NETwork
ARM	Atmospheric Radiation Measurement (DOE program)
AOT	aerosol optical thickness
ASTER	Advanced Space-borne Thermal Emission and Reflection Radiometer (on Terra)
ATBD	Algorithm Theory-Based Document
BC	boundary condition
BRDF	bi-directional reflectance distribution function
CCN	cloud condensation nuclei
CKD	correlated-k distribution (method for spectral integration)
CERES	Clouds and the Earth's Radiant Energy System
CRM	cloud resolving model
Ci	cirrus
Cu	cumulus
CWC	condensed/cloud water content
CWP	condensed/cloud water path
DISORT	DIScrete Ordinate RT (DISORT), a popular 1D RT code
DOAS	differential optical absorption spectroscopy
DOE	US Department of Energy
EarthCARE	Earth, Clouds, Aerosols and Radiation Experiment (ESA-JAXA mission)
EM	electromagnetic
ERBE	Earth Radiation Budget Experiment
ETA	effective thickness approximation
ESA	European Space Agency
FIRE'87	1987 First ISCCP Regional Experiment
FOV	field-of-view
GCM	global climate model
GHG	greenhouse gas
GLAS	Geoscience Laser Altimeter System
GSFC	Goddard Space Flight Center (NASA center)
GWTSA	Gamma-weighted two-stream approximation
H–G	Henyey–Greenstein, a phase function model
ICA	Independent Column Approximation
ICESat	Ice, Cloud and land Elevation Satellite
IPA	Independent Pixel Approximation
IR	infra-red
ISCCP	International Satellite Cloud Climatology Project
IWC	ice water content
IWP	ice water path
JAXA	Japan Aerospace eXploration Agency
LANL	Los Alamos National Laboratory (part of DOE complex)
LEO	low-Earth orbit
LES	Large-Eddy Simulation
LIDAR	LIght raDAR
LITE	Lidar-In-space Technology Experiment
LWC	liquid water content
LWP	liquid water path
MC	Monte Carlo
McICA	Monte Carlo ICA
MFP	mean-free-path
MISR	Multi-angle Imaging Spectro-Radiometer (on Terra)
MMCR	millimeter-wave cloud radar
MMF	multi-scale modeling framework
MODIS	Moderate Resolution Imaging Spectro-radiometer (on Terra and Aqua)
MPL	Micro-Pulse Lidar
MTI	Multispectral Thermal Imager
MuSCL	Multiple-Scattering Cloud Lidar
MWR	microwave radiometer
NASA	National Aeronautics and Space Administration

NCAR	National Center for Atmospheric Research
NDCI	Normalized Difference Cloud Index
NDVI	Normalized Difference Vegetation Index
NFOV	narrow FOV
NIPA	Nonlocal IPA
NIR	near IR (spectrum)
NOAA	National Oceanic and Atmospheric Administration
OCO	Orbiting Carbon Observatory
ODE	ordinary differential equation
PDE	partial differential equation
PDF	probability density function
RADAR	RAdio-frequency Detection And Ranging
RMS	root-mean-square
RT	radiative transfer
RTE	RT equation
RULLI	Remote Ultra-Low Light Imaging (a special LANL sensor)
SNR	signal-to-noise ratio
SORCE	SOlar Radiation and Climate Experiment
Sc	stratocumulus
SF	(2nd-order) structure function
SHDOM	Spherical Harmonics Discrete Ordinates Method
St	stratus
SWIR	shortwave IR (spectrum)
SZA	solar zenith angle
THOR	THickness from Off-beam Returns (an airborne MuSCL system)
TIR	thermal IR
TM	Thematic Mapper
TOA	top of atmosphere
UAV	unmanned aerial vehicle
UV	ultra-violet (spectrum)
Var	Variance
VIS	visible (spectrum)
VNIR	visible to near IR (spectrum)
VZA	viewing zenith angle
WAIL	Wide-Angle Imaging Lidar
WRF	Weather Research and Forecasting (NCAR community) model

1. Context, motivation and outline

1.1. Overview of the historical record

Clouds have forever been objects of fascination by artists and scientists alike. The earliest recorded observations and explanations of clouds certainly go back to antiquity, when in most circumstances philosophy, mythology and natural science were not yet distinguishable. Da Vinci, Renaissance man *par excellence*, experimented with smoke and light. Newton famously explained the rainbow based on geometric optics, dispersion and the hypothesis of microscopic spherically shaped cloud/rain particles. The emergence of cloud physics and dynamics can be traced to Luke Howard (1772–1864) and, more specifically, his 1802 lecture 'On the Modifications of Clouds (...)' delivered to the London Askesian Society.

Therein, he introduced a classification of clouds (stratus, cumulus, cirrus, nimbus) that is still in use [1]; it was entirely based on visual appearance. Atmospheric visibility was studied empirically by Bouguer, Lambert and Beer in that order from the early 1700s to mid-1800s. The law of exponential transmission encapsulates their research. Lambert also uncovered his famous 'cosine' law of radiometry: a collimated beam deposits energy on a surface in proportion to its projection onto a plane perpendicular to the beam.

Just over a century ago, Gustav Mie published his famous paper [2] on the scattering and absorption of electromagnetic (EM) waves by spheres in 1908. Peter Debye [3] was working independently on the same problem at the same time, and published his own paper in 1909. They were, however, both preceded by Ludvig Lorenz who investigated the problem earlier, publishing his work in 1890 ... in Danish. The origin of multiple-scattering theory follows a similar pattern. Arthur Schuster's 1905 paper [4] is often cited as the first use of what would become known as two-stream theory in radiative transfer, but previous and apparently independent studies had been published by Lommel [5] in 1887 and by Chowlson [6] in 1889. At any rate, the foundations of radiative transfer theory *per se* were laid by Karl Schwarzschild and E Arthur Milne for the angularly resolved case and by Arthur Eddington for the coarser (flux-based) diffusion approximation. After that, radiative transfer became entangled with particle transport. For the decades leading up to the end of WWII, transport theory was driven by early nuclear engineering projects: designing and building both steady-state and super-critical devices. Of course, both reactors and weapons have their nature-made counterparts in nuclear astrophysics. Astrophysics, both theoretical and observational, has always been a driver for advances in radiative transfer *per se*.

The definitive reference for one-dimensional (1D) radiative transfer (RT) in horizontally uniform plane-parallel atmospheres is Chandrasekhar's 1950 monograph [7]. The earliest study we are aware of in three-dimensional (3D) RT in the usual sense of horizontally non-uniform plane-parallel atmospheres is in Giovanelli's 1959 paper [8], 50 years ago at the time of this writing; he used 3D diffusion theory. However, shortly before that, in 1956, Richards [9] had investigated isotropic point sources embedded in dense uniform clouds, again, where the diffusion regime prevails. In 1958, Chandrasekhar published a rigorous RT-based study [10] of a narrow collimated beam ('pencil-beam') penetrating a uniform semi-infinite isotropically scattering medium. For reasons that will become clear as we proceed, we are highly interested in these non-uniform source problems, which are 3D in their own right, even with solar RT in mind (think Green functions). We will cover further developments in atmospheric 3D RT in the main body of the paper, especially in the later sections (sections 6–8).

At present, we can identify two equally important application areas for atmospheric RT in general, and 3D in particular: broadband radiative energy budget estimation and wavelength-specific optical remote sensing signal modeling. Figure 1 illustrates the magnitude of the challenge posed by the spatial complexity of cloudiness.
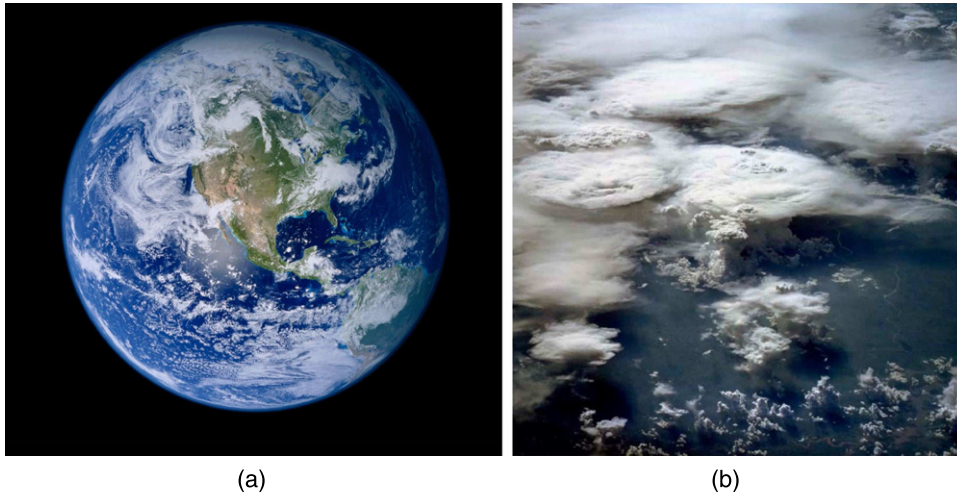
(a) (b)

Figure 1. *Clouds.* Left (*a*): the famous 'blue marble' full-face portrait of the Earth snapped by Apollo 17 astronauts on their way to the Moon. Right (*b*): a complex cloud scene viewed from the Space Shuttle.

1.2. Solar radiation energetics in the presence of clouds: climate modeling requirements on RT

Clouds are a naturally occurring component of the climate system: they are the planet's first line of defense for regulating its intake of solar energy, obviously a key quantity in climate balance. The global albedo of the Earth is ≈ 0.3, largely due to the powerful reflection by the most opaque clouds (cf figure 1(*a*)). They are also essential to the hydrological cycle, all scales considered from the droplet ($\sim 10^{-5}$m) to the raindrop ($\sim 10^{-3}$m) to the cloud system ($\sim 10^{+4}$m) to the grid scales ($\sim 10^{+5}$m) of global climate models (GCMs). Yet clouds are taken for granted by the majority of the climate modeling community. They are not mentioned at all in the 22 pages of the most recent 'Climate Change 2007: Synthesis Report— Summary for Policymakers' by the Intergovernmental Panel for Climate Change (http://www.ipcc.ch/) while aerosols are mentioned six times. We find some solace in the 18 pages of 'The Report of Working Group I (Physical Science Basis) of the IPCC—Summary for Policymakers' [11] where clouds are mentioned four times (and aerosols 11), including the ominous statement that *'Cloud feedbacks remain the largest source of uncertainty.'*

This under-appreciation of clouds is unfortunate because our skill in predicting their effect on the radiative and overall energy budgets at the 50–200 km scales of interest in GCMs (cf figure 1(*b*)) is not so good. This is in large part because the clouds themselves are not well predicted. However, the required RT is also overly simplified by assuming that in each layer clouds occupy a fraction, A_c, between 0 and 1, and that within the cloudy and cloud-free portions horizontal uniformity is assumed. This makes the spatial aspect of the GCM RT problem amenable to a weighted average of 1D computations. How to combine the various layers, accounting for their radiative interactions is more tricky. This usually amounts to assuming either maximum or random overlap geometry of the cloudy portions depending on whether or not A_c goes to zero in between cloudy layers [12]. The treatment of the spatial transport problem is expedited with a two-stream

or diffusion-type model while the real computational effort on radiation in GCMs is expended in the spectral domain. That is to be expected since the goal here is to compute by integration over the entire solar spectrum how much radiation is reflected back to space and how much solar heating occurs across the atmospheric layers and at the surface.

Cloud particles are not strong absorbers. Gases are, and clouds bounce the solar radiation through the gases very efficiently. Now the spectral variations of gaseous absorption are complex and shift with temperature and pressure. The spectral domain thus gets the lion's share of the CPU cycles in GCM solar RT 'parametrizations,' a.k.a. shortwave radiation 'schemes;' this is even more the case in the thermal IR (a.k.a. long-wave) spectrum where the RT is dominated by ubiquitous emission and absorption processes rather than incoming radiation and multiple scattering.

If we want to inject more realism into the spatial part of the solar RT problem in GCMs, it has to be via a very efficient computation. We briefly discuss such solutions, with particular emphasis on the recent trend toward use of 'multi-scale modeling frameworks' (MMFs) in climate modeling [13, 14, and references therein]. MMFs embed cloud resolving models (CRMs) with kilometer-scale resolutions in each GCM grid-cell, thus removing the need to predict A_c and effective optical properties for the uniform cloud. Consequently, a whole new 3D RT problem arises to get the energetics accurate enough, by some dynamics-based criterion, at every point in the CRM.

1.3. Active and passive optical diagnostics of clouds: remote sensing requirements on RT

In solar heating rate estimation, we perform at a minimum full-range angular and spectral integrals. Moreover, some level of spatial integration is usually in order: approximately kilometer scales for CRMs, hundreds of kilometers for GCMs, up to the planetary scale for elementary '0D' energy balance models. Remote sensing requirements for RT sharply contrast to this picture: pixel scales range from meters to tens of kilometers,

radiance propagation direction is at best sparsely sampled (often fixed at a single value), and narrow spectral bands are used.

Although there is a new trend toward 'smart' detector systems that process data near the focal plane, satellite remote sensing data harvesting is currently band-width limited. How many radiance samples can we measure at a reasonable signal-to-noise ratio (SNR), store and forward to a ground station? Once received, the 'level 0' data in raw bytes and packets are used to generate calibrated and geo-registered 'level 1' radiance data, ready for extraction of geophysical information by a wide variety of retrieval techniques. This key operation produces 'level 2' data on a pixel-by-pixel or region-by-region basis in a given image. Once collected into a latitude–longitude grid it becomes 'level 3' data, conveniently stratified and formatted for the end-users.

In one form or another, remote sensing always leads to an inverse problem. Of particular interest to us are the so-called 'physics-based' retrieval techniques that invariably start with forward RT modeling of remote sensing signals. Sensitivity studies will reveal whether or not existing or planned observations, for known or assumed instrumental error, will support the retrieval of an inherent property of the target. If there is sensitivity, one can design a retrieval algorithm with the right level of complexity (e.g. 1D or 3D RT) and accuracy (e.g. account or not for polarization effects), and the right tradeoff between efficiency and flexibility (e.g. pre-computed look-up tables versus RT computations on the fly).

In principle, the goal of inverse RT is to infer *geometrical*, *structural* and *optical* properties of the medium that define the forward RT problem locally and globally; such optical properties would describe for instance reflection, scattering and absorption processes. In practice, end-users of remote sensing 'products' are generally more interested in the *physical* and *chemical* properties that determine the optical parameters of the airborne particles; this leads to another inverse problem to solve. There is therefore tacit pressure to combine these two non-trivial inverse problems even though they might be best treated separately. In our experience, this cannot be done without making further assumptions about the medium, e.g. the particles are spherical and their radii are log–normally distributed. Once such serial assumptions become buried in Algorithm Theoretical Basis Documents (ATBDs), it becomes harder to trace the source of remote sensing uncertainties.

Geometrical and structural properties of interest in cloud remote sensing are cloud height, thickness and shape (e.g. through its outer aspect ratio, where a slab has an infinite aspect ratio). Deliverable optical properties of clouds (defined formally below) will characterize scattering and/or absorption through transport coefficients—or derived properties such as the mean-free-path—at the observation wavelength. Valid but more difficult questions about physico-chemical (a.k.a. microphysical) properties of cloud particles include their phase (liquid, ice or a macroscale mix of both), their size (e.g. via moments of the size distribution) and their density. This last quantity is highly valued since it may, for instance, give a hint at the effect of pollution on clouds. Particulate emission can indeed increase the number of cloud condensation nuclei

(CCN), and thus affect the cloud radiative properties that matter for the climate [15–17].

To provide answers to all of the above questions about clouds, multiple wavelengths, multiple viewing angles and more and more multiple polarization channels must be brought to bear. That is indeed the comprehensive suite of optical characteristics the next generation of space-based instrument will combine [18, 19]. However, such a broad grasp in radiometric detail will always require sampling tradeoffs; typically, they will involve spectral and spatial resolution. It is therefore unlikely that a single optical sensor can answer all the questions we have about the continuum of airborne particulates ranging from aerosols to clouds. Multiple instruments looking at the same scene give us a better chance. More and more, data will be fused from multiple satellites flying in a close formation such as the current 'a train' constellation [20].

From the signal modeling as well as engineering perspectives, we distinguish 'passive' and 'active' instruments where the former use natural sources of radiation while the latter provide their own. Even considering the increased complexity, cost and power requirements of the latter technology, an active approach is often the best choice. The focus of this review is on the solar spectrum, with reflection and scattering of sunlight being at the origin of the signal. We will nonetheless consider pulsed lasers as an alternate source, and we will discuss LIDAR (LIght raDAR). We also remind the reader that longer wavelengths, from the thermal IR to the microwave region, have also been used to probe clouds, both passively and actively. Active radio-frequency instrumentation (RADAR) has long been used to monitor precipitation. However, for the last couple of decades millimeter-wavelength sources have become available that reveal the stuff that clouds are made of.

The authors' institutional bias is toward satellite remote sensing, but suborbital (airborne and ground-based) observations will also be considered in all of the above-mentioned modalities. There are, however, cloud-probing technologies that defy this classification. What would one call an airborne instrument [21, 22] that is flown into the thick of a cloud where it fires laser pulses and its time-resolved radiometry of the resulting multiply scattered light is used to determine the cloud's overall thickness and volume-averaged extinction coefficient (a local measure of opacity)? Where is the 'remote' in this sensing? We would argue that this '*in situ* cloud lidar' is indeed a remote sensing technology by virtue of the key role of RT in the signal prediction, hence data processing. Moreover, the goal is to use *li*ght for *d*etection-*a*nd-*r*anging of the cloud's upper and lower boundaries.

There are other observations that defy some of the conventional wisdom about what constitutes remote sensing. For instance, physical climate scientists really want to know globally the up-welling, top-of-atmosphere (TOA) flux across the solar spectrum (i.e. the local albedo when normalized to the incoming flux) as it varies in space and time. NASA has dedicated entire multi-platform instrumental missions to this measurement: the Earth Radiation Budget Experiment (ERBE) [23] and follow-on Clouds and the Earth's Radiant Energy System (CERES) [24]. The problem amounts to sampling

at best a small number of radiances emanating from a given locale and inferring a specific weighted integral over all the radiances. So an 'angular model,' the tell-tale RT ingredient in remote sensing, is required. *A priori*, determination of this cloud scene attribute is not going after any of its geometrical, physical and chemical properties. *A posteriori*, the angular model selection has a lot to do with the cloud scene properties, even if we are not motivated here to retrieve them with specified accuracy.

Insolation of the surface across the solar spectrum is another important quantity strongly affected by clouds in all of their 3D glory. Can it be determined by remote sensing? Currently, the answer is yes, but with difficulty and depending on the time-scale of interest. Given only TOA radiances, this quantity is even more dependent on assumptions in the required RT- and composition-modeling than the TOA solar flux. It is nonetheless a high-value target for climate science, weather forecasting and many kinds of biogeophysical investigation.

In summary, it is useful to separate the applications of RT in the cloudy atmosphere into energetics and diagnostics because, in many respects, the solution techniques will have a very different flavor. However, the threads of observational radiometry and computational transport intertwine in ways we do not need to unravel completely. Rather we should follow both strands and see the knots as opportunities for further research.

1.4. Outline

In the following section, we describe the fundamental physical processes of atmospheric radiation transport at the microscopic, mesoscopic and macroscopic levels. Armed with a complete description of the local balance of the radiant energy budget, we introduce outer cloud geometry in section 3 and solve in representative cases the radiation transport problem; several applications illustrate these solutions. In section 4, we introduce RT Green functions for dense scattering and at-most-weakly absorbing media in space and in time; because of the remote sensing applications, particular attention is given to the description of transport from boundary sources to boundary/external observers. In section 5, we partition the 3D radiation transport problem space into two sectors: resolved and unresolved spatial variability, leading to different phenomenologies and contrasting flavors of solution techniques.

Sections 6 and 7 are devoted, respectively, to the assessment and mitigation of the 'damage' that 3D radiation transport phenomena cause in operational applications that have adopted 1D RT models. Both energy budget estimation and cloud remote sensing are covered with several examples for each of these two tasks. Tables are turned in section 8 where we describe, with examples, how 3D radiation transport phenomena can be used to design new algorithms and new instruments for cloud remote sensing. We offer some concluding remarks in section 9.

We will assume the reader has a basic background in statistical, mathematical and computational physics, but no more than curiosity about cloud physics, optics, observation and radiation energetics. Atmospheric scientists in general, and scientists from the National Aeronautics and Space Administration (NASA) in particular, are prone to acute 'acronymitis' (13 abbreviations defined so far, 97 in all). They are defined on the fly, but a comprehensive list of acronyms and abbreviations is also provided at the end of the paper. References will help the reader delve further into the topic of realistic-yet-practical modeling of solar radiation transport in the Earth's cloudy atmosphere, and possibly in other natural media.

2. Radiative transfer in the cloudy atmosphere: optics with statistical and quantum physics

2.1. Emission, propagation, absorption and scattering

The Sun is a distant source of thermal radiation that impinges on the Earth as an essentially unidirectional spatially uniform flux $F_{0\lambda}$ measured conventionally in W m^{-2} broadband and spectrally nm^{-1}. This flux indeed has a rich spectral structure that departs from black-body radiance at the effective 5775 K temperature of the Sun's photosphere; it is tabulated in great detail by Kurucz [25]. The solar spectrum extends in wavelength from $\lambda \approx 0.2\,\mu$m to ∞, with everything beyond $4\,\mu$m considered to be the *thermal* infra-red (TIR). It is divided into the ultra-violet (UV), largely absorbed by stratospheric ozone, the visible (VIS) and the *near*-IR (NIR) regions with partitions at 0.4 and $0.7\,\mu$m; the IR region of interest is also referred to as the *solar* IR or *reflected* IR to distinguish it from the TIR that peaks at 10–12 μm and is dominated by terrestrial radiation sources.

The integral of $F_{0\lambda}$ across all wavelengths is $\approx$1365 W m^{-2}, a number that matters of course tremendously for the Earth's climate, including 12 W m^{-2} beyond $4\,\mu$m in the TIR. It varies slightly and is monitored as continuously and accurately as possible from space by missions such as SOlar Radiation and Climate Experiment (SORCE) [26] and soon Glory [18]. The goal of solar radiation transport is to track the fate of this influx of radiant energy from the somewhat elusive TOA [27]. It can be either reflected back to space (and clouds play a critical role in this mechanism that regulates the global climate), transmitted to the surface (where it is either absorbed or reflected) or absorbed by one of many possible atmospheric constituents (that can be either in gaseous, liquid or solid phase). In this process of energy-driven computation, one can also branch off to the prediction of signals for all matter of sensors. This is the basis of physics-based atmospheric remote sensing in the solar spectrum. It is advantageous to use the Sun's abundant light in passive modalities. There are also good reasons to turn to pulsed lasers in active ones. By far the most popular laser technology used in this part of the spectrum is solid-state Nd : YAG which transmits at 1064 nm, often frequency-doubled to 532 nm (as in green-colored laser pointers), where molecules scatter 16× more and aerosols somewhat more as well. Also, silicon-based photon detection is at its most efficient in this spectral region.

Constituents of the molecular atmosphere of primary interest in solar spectrum are N_2, O_2, O_3, NO_2, H_2O, NH_4,

CO, CO_2 and CH_4. The first two, by far the most abundant species, are responsible for the Rayleigh scattering that gives us the familiar blue hue of ultra-clear skies (no clouds or pollution). Spatially and spectrally selective absorption is how the atmosphere gains heat at the expense of the solar radiation budget. Nitrogen has negligible absorption in the solar spectrum. Oxygen, the other symmetric diatomic molecule in the mix, absorbs some sunlight but not enough to contribute energetically meaningful heating. This is of course for basic quantum mechanical reasons that put their transitional, vibrational and rotational energies in other parts of the electromagnetic (EM) spectrum. However, O_2 has a few narrow forbidden transitions between 0.63 and 0.78 μm known as the γ-, B- and A-bands. Figure 2 shows the details of the O_2 A-band, which we will develop a strong interest in further on. The main role of ozone is to block the solar UV from reaching altitudes below $\sim$35 km, fortunately for most life-forms. Ozone also has a weak spectrally smooth feature across the VIS regions known as the Chappuis band. For all practical purposes, the stratospheric O_3 layer defines the TOA for solar radiation; at $\approx$6 pressure scale heights ($\approx$8 km each), scattering is still negligible (although detectable by sensitive lidar techniques). All of the other molecules listed contribute absorption bands in the NIR. Methane is an under-appreciated absorber, more effective in the solar spectrum than carbon dioxide [28].

In applications where spectral integrals must be estimated, scanning the solar spectrum one-wavelength-at-a-time is not an efficient way of performing the computation. Among the practical ways of capturing gaseous absorption (at a given pressure and temperature), the most popular is currently the so-called 'correlated-k distribution' (CKD) method [29, 30]. In CKD modeling, the gaseous absorption coefficient is re-ordered by strength and weighted by its occurrence within a spectral region small enough that other optical properties vary little. In essence, a Lebesgue integration [31] is used in a case where variability is too unwieldy for a Riemann approach. For a detailed account of molecular absorption and associated modeling techniques, we refer the interested reader to the classic monograph by Goody and Yung [32].

In this review, we focus on scattering alone or in combination with absorption. Beyond molecular/Rayleigh scattering, atmospheric optics at any given wavelength are determined by the properties of aerosols (typically sub-micrometer size airborne particulates) and cloud particles that range from $\sim$1 to many tens of micrometers in size. The latter can be either liquid or solid depending on environmental conditions. At larger sizes, the Stokes flow results in net fall speeds, so we are dealing with drizzle, rain and other forms of precipitation. Aerosols and clouds interact radiatively (cf section 6.5) and microphysically. Aerosols are indeed necessary to trigger cloud formation by 'activation' of tiny CCN. To a first approximation there is one cloud particle per CCN, so increasing the small aerosol population by polluting the air affects cloud properties: more particles compete for the same amount of condensed water, and end up smaller on average. We will see that this 'indirect' aerosol effect (in climate parlance) makes clouds more reflective [16], as is
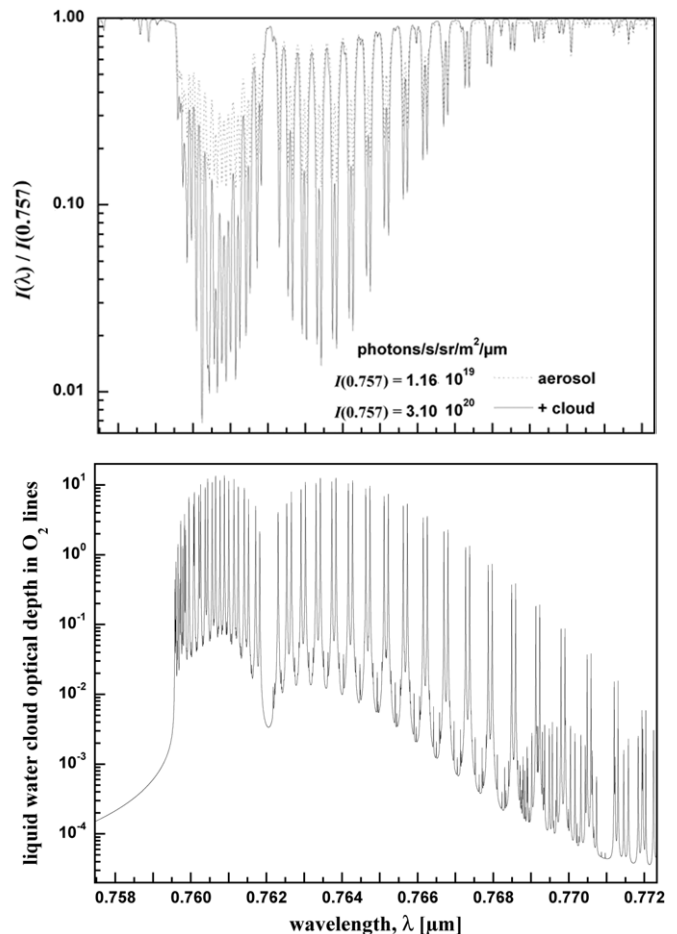
Figure 2. *Simulated O_2 A-band spectra in reflection.* Bottom: fine structure of the A-band displayed using, as a relevant example, the O_2 optical thickness across a layer from 860 to 911 hPa (altitudes 0.85 to 1.3 km), where one could find a typical low-level cloud. Top: the reference spectrum (dashed) is for a background aerosol atmosphere above an ocean surface in a typical state (Cox–Munk [33] model for 5 m s^{-1} wind speed). The other (solid) is for the same situation plus a liquid water cloud at 911–860 hPa with an optical depth of 64. Line-by-line computations were coarsened to the 0.0146 nm resolution of the Orbiting Carbon Observatory (OCO) spectrometer. Both spectra were normalized to maximum radiance (given, for reference, in the inset). Computations were kindly provided by Dr Hartmut Bösch (University of Leicester, Department of Physics and Astronomy, Earth Observation Science, Space Research Centre).

dramatically illustrated by ship tracks in satellite imagery [34]. There are further ramifications of this impact of pollution on the life-cycle of clouds, all the way to the systematic suppression of precipitation [15]. Apart from changing planetary albedo by making clouds more persistent, this effect can lead to changes for hydrology and climate in the affected regions.

Beyond particle-size range, the distinction between cloud and aerosol is much more about constitution than density. Apart from trace chemicals in solution, as well as small internally mixed particulates, cloud particles are made of condensed water. Aerosols by contrast have an extremely diverse chemical make-up, with more or less propensity for 'wetting' within the prevailing water vapor. In spite of some preconceptions, this distinction should not be seen as a question

of altitude: there are indeed clouds at ground level (e.g. fogs and blowing snow) and there are aerosols in the stratosphere (e.g. from large volcanic eruptions). Nor is it about the local density: there are highly opaque aerosol plumes (e.g. from wild fires) and there are 'sub-visible' cirrus clouds. From the radiation transport perspective, however, there are two extreme regimes that nature mixes in interesting and challenging ways: optically thin (a.k.a. clear-sky) regions and optically thick regimes.

This brings us to the fundamental issue of radiation propagation, which is at the core of transport theory *per se*. Physicists will anticipate here a categorization based on the Knudsen number, the ratio of the mean-free-path (MFP) to the characteristic outer scale of the flow. We will soon spell out some serious physical drawbacks to the conceptualization of radiation transport as a flow of 'photons' through a participating medium. Nonetheless, one can envision a kinetic theory framework and think about optically thin regions of the atmosphere as dominated by (fast) ballistic motion, while the optically thick ones are dominated by (slow) diffusive motion. In the following three subsections we will present in more technical detail radiation transport theory and position it with respect to classic physical optics.

2.2. Microscopic transport model: wave equation

What does Maxwell's electromagnetic (EM) wave theory of light as a vector wave field bring to the table? Theoretically, it should be the starting point. Yet, until quite recently, its role was limited to the computation of the optical properties of atmospheric particles, one at a time. How much does it absorb? How much does it scatter and how is that portion distributed according to scattering angle?

The reader will not be surprised to hear that the standard assumption about particle shape is a sphere. The answers to the above questions then depend only on the non-dimensional size parameter $2\pi r/\lambda$, where r is the radius of the sphere, and the complex index of refraction of the material, with the imaginary part controlling absorption. As mentioned in Section 1, Lorenz–Mie theory for scattering and absorption of EM waves by spheres was established over a century ago. The topic is still revealing some finer but fascinating details in the area of resonances [35]. For in-depth surveys, we refer the reader to the monographs by Bohren and Huffman [36] and Mishchenko *et al* [37]. As one might also suspect, the spherical assumption is often a very coarse approximation, but for an important class of airborne particles of interest here it is in fact a very good one: liquid cloud droplets, ranging between ≈ 2 and $\approx 30\,\mu$m in radius. These droplets form the vast majority of low-level clouds such as stratus (St), cumulus (Cu) and stratocumulus (Sc) where mean or modal radii vary between 5 and $15\,\mu$m from cloud to cloud and from base to top (generally increasing). In turn, these cloud types dominate the radiation energy budget, especially via reflectivity (i.e. their significant contribution to the Earth's global albedo of ≈ 0.3). Figure 3 shows the outcome of a Lorenz–Mie computation of the differential scattering cross-section (in a normalization explained further on) averaged over a population of randomly positioned droplets with a so-called
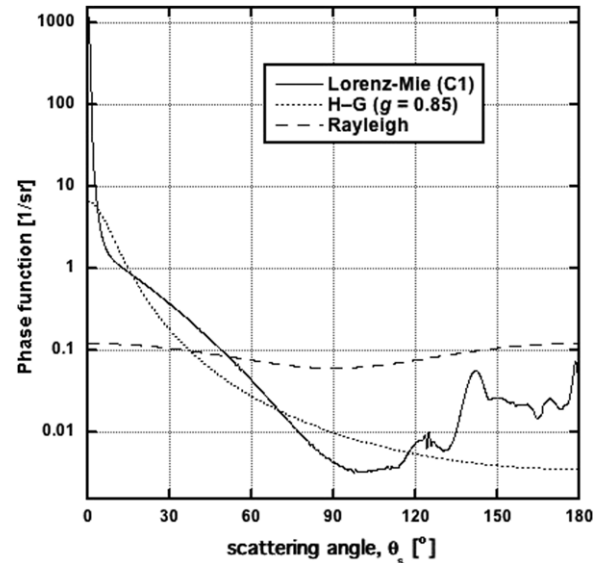

Figure 3. *Scattering phase functions.* The cloud 'C1' phase function is plotted versus θ_s for $\lambda = 0.532\,\mu$m; the ($g = 0.85$) Henyey–Greenstein model in (33) and the Rayleigh scattering phase function, $P(\theta_s) = (3/16\pi)(1 + \cos^2\theta_s)$, are also plotted.

'Deirmendjian C1' size distribution [38]. Even in semi-log axes, we note the strong forward peak as well as the well-known rainbow feature at $\approx 138°$. The former property is traceable to diffraction while the latter is attributable, to first order, to geometric optics, a reasonable approximation in the limit of large size parameters ($r \gg \lambda$). For reference, the Rayleigh scattering case is plotted as well; it applies to the opposite limit of small size parameters ($r \ll \lambda$).

Many important atmospheric particulates are, however, very far from spherical, not the least being ice crystals in elevated clouds that come in very diverse shapes ('habits'). 'Equivalent sphere' models have of course been used and abused to represent parametrically non-spherical particle populations in cloud and aerosol optics [39, 40]. In the case of cold clouds, typical ice crystal sizes are fortunately significantly larger than those of droplets, tens to hundreds of micrometers. Ray-tracing computations— assuming geometrical optics—therefore deliver reasonably accurate results in many cases, from regular hexagonal shapes [41] to convoluted fractal morphologies [42]. However, present computational resources open the road to practical high-accuracy methods that can capture the optical properties of non-spherical particles, from the first principles of EM wave theory [43–45, among others]. For a detailed survey of the topic, we refer the interested reader to the monographs on this topic authored and edited by Mishchenko *et al* [37, 46].

At any rate, most angular details in the single-particle differential scattering cross-section are smoothed by averaging over the distribution of particle sizes, $N(r)$, which is typically quite broad. The persistent diffraction peak survives averaging as does the rainbow, which is, to a good approximation, a geometrical optics (hence size-independent) feature.

Along the spectral dimension, macroscopic objects such as aerosol and cloud particles have of course much smoother

variations than molecules, particularly for absorption. Cross-sections in Lorenz–Mie theory are represented as follows:

$$\xi_{\lambda x}(r) = \pi r^2 \times Q_x(2\pi r/\lambda), \tag{1}$$

where Q_x is the efficiency ratio partitioned into scattering (x = s) and absorption (x = a) for a given size parameter. No sub-index is used for the extinction cross-section, the sum of scattering and absorption. In the limit of (liquid or ice) water spheres much larger than λ, we have $Q \approx Q_s \approx 2$; in the opposite (Rayleigh scattering) limit of very small particles, we have $Q \approx Q_s \propto (r/\lambda)^4$, hence

$$\xi_{\lambda s}^{\text{(Rayleigh)}}(r) \sim r^6/\lambda^4. \tag{2}$$

The overall cross-section for scattering[4] $\overline{\xi_{\lambda s}}$ averaged over a size distribution $N(r)$ dominated by the population with $r \gg \lambda$ is thus expected to scale as $\overline{r^2}$, the mean square of the particle size since that is the surface exposed to the incoming beam. Moreover, the geometrical shape factor Q will be exactly 2 for spheres by Babinet's principle [47]. Absorption is more of a volume than surface process, so the corresponding cross-section $\overline{\xi_{\lambda a}}$ will tend to scale as $\overline{r^3}$. It is also much smaller than $\overline{\xi_{\lambda s}}$ because the imaginary part of the complex index of refraction is generally much smaller than the real part. Figure 4 shows the extinction cross-section (times droplet density, 'σ' curve), and the ratio of the scattering to extinction cross-section ('ϖ_0' curve). We note that droplet absorption starts in earnest beyond 1.6 μm but, at the same time, there is less solar energy to absorb. We will see further on that multiple scattering makes bulk absorption a very strong function of $\overline{\xi_{\lambda a}} \propto 1 - \varpi_0$.

Wavelengths where particles absorb the most are at a premium in remote sensing since they will give access to the effective particle radius [48]

$$r_e = \overline{r^3}/\overline{r^2}. \tag{3}$$

As for the extinction cross-section $\overline{\xi_\lambda} = \overline{\xi_{\lambda s}} + \overline{\xi_{\lambda a}}$, it is empirically represented as a power law:

$$\overline{\xi_\lambda} \sim \lambda^{-\alpha}, \tag{4}$$

where α is known as the Ångström exponent. Gamma distribution functions are a popular 2-parameter representation of $N(r)$, namely,

$$N(r) \sim r^{b-1} \exp\left[-(b-1)r/r_m\right], \tag{5}$$

where r_m is the mode (requiring $b > 1$) and b defines the shape of the distribution. For instance, the above-mentioned C1 distribution is obtained for $r_m = 4\,\mu$m and $b = 7$ (leading to $r_e = 6\,\mu$m). We note that (4) is exact for this assumption in regimes where $\xi(r)$ is a power law in the size parameter $2\pi r/\lambda$.

In the limit of particles very small with respect to λ, the Rayleigh scattering cross-section in (2) is retrieved and $\alpha \approx 4$, which is the basis of the classic explanation of

---

[4] We use an $\overline{\text{overscore}}$ to denote averages over disorder in the particle population, both spatial and with respect to size.

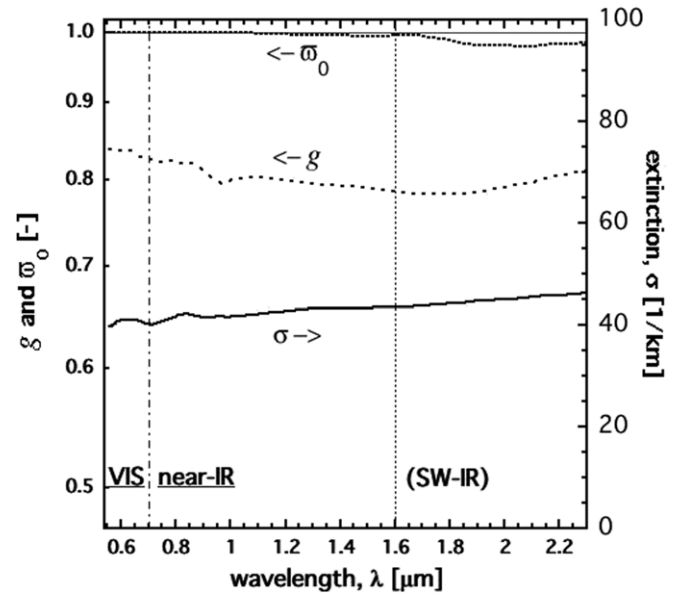**Figure 4.** *Spectral dependence of cloud optical properties in the solar spectrum.* Single-scattering albedo $\varpi_0 = \overline{\xi_s}/\overline{\xi}$ (short dashes) in (18), asymmetry factor g (long dashes) from (20) and extinction $\sigma = \overline{\xi} \times$ droplet density (solid line, right-hand axis) are plotted versus wavelength λ for the 'C1' cloud droplet-size distribution. The VIS/NIR dividing line at 0.7 μm is highlighted, as well as where silicon-based sensors become too inefficient and other materials must be sought for light detection in the 'shortwave' IR (or SWIR) where the available solar radiation is dwindling anyway.

the blue color of clear skies. In the limit of particles very large with respect to λ, geometric optics become ever more accurate and we have $\xi_\lambda(r) \sim r^2$ irrespective of λ, and α is very small. Figure 4 shows the spectral dependence of scattering and extinction cross-sections for cloud droplets based on Lorenz–Mie theory and the C1 distribution. This small value of α contributes to the characteristic whiteness of clouds, but so does multiple scattering (as demonstrated further on). Aerosol particle distributions have α somewhere in between the Rayleigh and geometric-optics limits, and its value from observations clearly informs us about the particle-size distribution.

All of the above contributions of EM wave theory are about transport coefficients encapsulated in particle cross-sections for interaction with radiation. In particular, nothing has been said about propagation through the cloudy atmosphere viewed as an optical medium, nor about multiple scattering. In the next subsection we introduce the highly successful—but purely phenomenological—theory of radiative transfer, with or without polarization. It is noteworthy that rigorous derivation of the polarized (a.k.a. 'vector') radiative transfer equation was obtained only quite recently by Mishchenko [49] from microphysical predicates, i.e. Maxwell's EM wave equations and statistical optics. The key assumption is, as can be expected intuitively, that the medium is 'dilute': inter-particle distances are large with respect to λ. Each particle is therefore in the far field of all the others. Mishchenko's derivation is for steady sources and spatially uniform particulate media. He generalized his derivation to spatially variable media, but only when the 'clumps' are small with respect to the MFP [50].

Much of the work we present further on is for media that are spatially variable over a wide range of scales that typically include the MFP, and we also have a strong interest in transient sources (namely, pulsed lasers).

2.3. Mesoscopic transport model: radiative transfer equation

Liouville's theorem states that Hamiltonian particle dynamics under a constant external force field $\boldsymbol{F}(\boldsymbol{x})$ preserves volume in the particle's phase space, hence phase-space density $f(t, \boldsymbol{x}, \boldsymbol{v})$ for non-interacting particles, where $\boldsymbol{v}$ is velocity. From there, Boltzmann's equation expresses that any change in $f(t, \boldsymbol{x}, \boldsymbol{v})$ for an ensemble of particles is due to collisions, thus providing a basis for kinetic theory. The linear Boltzmann/transport equation follows from the clear distinction between 'material' particles, which are assumed very massive (hence essentially stationary), and 'transported' particles, which move relatively fast and can be scattered or absorbed by the material. We can also drop the $(\boldsymbol{F}/\text{mass}) \cdot \nabla_v f$ term that would normally appear in the Lagrangian derivative $\mathrm{d}f/\mathrm{d}t$ since we can generally neglect the effects of external force fields on massless particles. We are left with a simple Eulerian relation for detailed balance in a small phase-space volume:

$$\frac{\mathrm{d}f}{\mathrm{d}t} = \frac{\partial f}{\partial t} + \boldsymbol{v} \cdot \nabla f = \text{gains} - \text{losses}. \qquad (6)$$

Now suppose that we are dealing with monokinetic particles, the so-called '1-group' transport: $\boldsymbol{v} \equiv c\boldsymbol{\Omega}$ and $f \mapsto f_1 \delta(v-c)/c^2$, f_1 is the particle density in the phase space made of $\mathbb{R}^3$ for $\boldsymbol{x}$ (or a subset thereof) and the associated two-dimensional space of directions for $\boldsymbol{\Omega}$. It is tempting to view RT as a flow of light particles (photons), which it is not since Mishchenko's [51] microphysical derivation of the RT equation (RTE) is purely classical. Radiant energy is nonetheless redistributed dynamically in space and time, and we need to know how. Also, we prefer to work with radiance (a.k.a. specific intensity)

$$I_\lambda(t, \boldsymbol{x}, \boldsymbol{\Omega}) = c E_\lambda f_{1\lambda}(t, \boldsymbol{x}, \boldsymbol{\Omega}), \qquad \text{with } E_\lambda = h\nu_\lambda = ch/\lambda, \qquad (7)$$

where h is Planck's constant. Radiance has units of $\mathrm{W\,m^{-2}\,sr^{-1}\,nm^{-1}}$. One often sees spectral radiance $I_\nu = I_\lambda |\mathrm{d}\lambda/\mathrm{d}\nu|$ using wavenumber ν measured in the conventional spectroscopy units of $\mathrm{cm^{-1}}$: $\nu = 10^7/\lambda$, when λ is in nm. In view of (6), this seven-dimensional field is constrained locally by the monochromatic integro-differential 3D RTE

$$\left[\frac{1}{c}\left(\frac{\partial}{\partial t} \right) + \boldsymbol{\Omega} \cdot \nabla + \sigma_\lambda(\boldsymbol{x}) \right] I_\lambda$$

$$= \sigma_{\lambda s}(\boldsymbol{x}) \int_{4\pi} P_\lambda(\boldsymbol{x}, \boldsymbol{\Omega}' \cdot \boldsymbol{\Omega}) I_\lambda(t, \boldsymbol{x}, \boldsymbol{\Omega}') \, \mathrm{d}\boldsymbol{\Omega}'$$

$$+ Q_\lambda(t, \boldsymbol{x}, \boldsymbol{\Omega}). \qquad (8)$$

Here, we use

$$\sigma_\lambda(\boldsymbol{x}) = n(\boldsymbol{x}) \times \xi_\lambda(\boldsymbol{x}) \qquad (9)$$

to denote the extinction coefficient in $\mathrm{m^{-1}}$, where material particle density n is the integral of $N(r)$, cf (5), over all values

of r. Like the advection term in (6), this is a net loss for the radiant energy budget in a small volume around the light beam defined geometrically by the pair $(\boldsymbol{x}, \boldsymbol{\Omega})$, so these two terms are grouped on the left-hand side. On the other side of the equation, we have the gains. First, we have in-scattering where $\sigma_{\lambda s} = n\xi_s$ denotes the scattering coefficient while the 'phase function' P_λ (cf figure 3) derives from the differential cross-section for scattering, namely,

$$\sigma_{\lambda s} P_\lambda = n(\boldsymbol{x}) \times \frac{\mathrm{d}\xi_{s\lambda}}{\mathrm{d}\boldsymbol{\Omega}}. \qquad (10)$$

Note that we normalize the phase function so that $\int_{4\pi} P_\lambda(\boldsymbol{\Omega}' \to \boldsymbol{\Omega}) \, \mathrm{d}\boldsymbol{\Omega}' = 1, \forall \boldsymbol{\Omega}$. Second, we have Q_λ, denoting a (volume) source term.

Mathematically, there is no difference between the above time-dependent RTE and the linear Boltzmann equation used in particle transport theory, primarily used for neutrons. Physically, they are fundamentally different since, as sketched above, the linear Boltzmann equation follows from coarse-grained particle dynamics [52] while the RTE follows from Maxwell's equations using statistical optics methods [51]. At present, however, the rigorous derivation requires steady sources and essentially uniform optical media. The general (3D time-dependent) RTE in (8) remains a phenomenology.

We have so far neglected polarization. To account for the transport of polarized light, we need to redefine I as a formal four-dimensional vector, and P_λ as a 4×4 scattering matrix that can mix different polarization states. In his classic monograph [7], Chandrasekhar gives the complete phenomenological elaboration of polarized/vector RT while Mishchenko's microphysical derivation [51] captures polarization by definition, being grounded in EM wave theory. We have also assumed axially symmetric scattering, meaning either spherical or randomly oriented material particles.

Using (8), RT computations can be performed one frequency at a time, and then integrated as necessary over λ. Because of this simplification of the radiation transport physics, we will drop λ (or ν) subscripts from most of the remainder. Finally, one might be surprised that we retain the possibility of time-dependence in a paper on clouds and sunlight, a very steady source indeed over time-of-flight durations. The reason for this is that we will develop further on a strong interest in sources that are Dirac δ's in time, both for heuristics and for exploratory observations using pulsed laser sources.

The important local scale in transport is the MFP ℓ, which is the sole parameter of the basic transmission law in *homogeneous* media of infinite extent. Indeed, ignoring momentarily time-dependence, scattering, internal sources and the spatial variability of σ, (8) reduces to $\boldsymbol{\Omega} \cdot \nabla I = -\sigma I$. For a given beam, distance from an arbitrary point $\boldsymbol{x}$ along $\boldsymbol{\Omega}$ is denoted s; we then have a simple ordinary differential equation (ODE) to solve, $\mathrm{d}I/\mathrm{d}s = -\sigma I$, hence $I(s) = I_0 \exp(-\sigma s)$ (Beer's law). We can interpret physically $I(s)/I_0$ from this *direct* transmission law as the probability that the transported particle will cover a distance s, or more, before suffering a collision of any type. The probability density function (PDF)

of the random variable s is therefore $\sigma \exp(-\sigma s)$. The qth-order moment of this PDF is $\langle s^q \rangle = \Gamma(q+1)\langle s \rangle^q$ $(q > -1)$, where $\Gamma(x)$ is Euler's gamma function and, for $q = 1$,[5]

$$\langle s \rangle = \ell = 1/\sigma \tag{11}$$

is the MFP, from the given extinction of the infinite uniform medium.

What if the optical medium is spatially heterogeneous? Then the transmission law becomes specific to the point x and direction Ω of departure:

$$T(x, \Omega; s) = \exp\left(-\int_0^s \sigma(x + \Omega s')\,ds'\right). \tag{12}$$

So will the MFP, and all other moments of s. The spatial-directional and/or ensemble-average transmission law can be denoted $\overline{T}(s) = \overline{T(x, \Omega; s)}$. What are its properties?

This fundamental question has been investigated recently by Kostinski [53], who proceeds from a refreshing discrete-point statistical perspective on particle transport theory in general, as well as by the present authors [54], who use the conventional (continuum-based) RTE. Either way, the prediction for $\overline{T}(s)$ is that it is sub-exponential in the following sense: for the associated step PDF, $|d\overline{T}/ds|$, moments obey $\langle s^q \rangle > \Gamma(q+1)\langle s \rangle^q$ for $q > 1$. This implies that the large-s decay of $\overline{T}(s)$ is slower than the exponential law dictated by the *actual* MFP derived from the ensemble-average transmission law. Moreover, this ensemble-average MFP $\langle s \rangle$ is greater than $1/\overline{\sigma(x)}$, the naive prediction using (11). For a large class of media with long-range spatial correlations, ensemble-average MFP is indeed given by $\overline{1/\sigma(x)}$ [54]. We can think of $\overline{\sigma(x)}$ as the extinction associated with the mean particle density, i.e. $\overline{n(x)\xi}$, noting that this assumption is equivalent to the reasonable requirement of total mass or material particle number conservation.

The general '1+3+2 dimensional' monochromatic RT problem on (t, x, Ω) for a given medium becomes completely determined only after stating initial and boundary conditions, which we will defer until we discuss specific cloud geometries. At present, we only need to note (*i*) that the optical medium $M \subseteq \mathbb{R}^3$ can be considered convex with no loss of generality (just set coefficients to 0 as necessary) and (*ii*) that conditions on the boundary ∂M can be 'absorbing' (i.e. no incoming radiation) or express primary sources (e.g. solar illumination) or secondary sources (i.e. partial or total reflection, with or without bi-directional redistribution).

2.4. Macroscopic transport model: diffusion equation

In the case of clouds, we can go one step further away from the microphysical model introduced in in section 2.2, leading to the RT equivalent of the hydrodynamic limit in kinetic theory. This involves averages of (8) over direction space. To this effect, we introduce here the standard (z-axis) polar angles (θ, ϕ) to describe Ω, thus $\Omega_z = \mu = \cos\theta$, $\Omega_{x(y)} = \sqrt{1 - \mu^2}\cos(\sin)\phi$ and $d\Omega = d\mu\,d\phi$.

[5] We use ⟨angular brackets⟩ to denote ensemble averages of quantities dependent on random processes implicit in transport theory.

2.4.1. Definitions and derivation.
Following the original derivation by Eddington in 1916 [55], we define the moments

$$J(t, x) = \int_{4\pi} I(t, x, \Omega)\,d\Omega, \tag{13}$$

$$F(t, x) = \int_{4\pi} \Omega I(t, x, \Omega)\,d\Omega, \tag{14}$$

$$\mathsf{K}(t, x) = \int_{4\pi} \Omega\Omega I(t, x, \Omega)\,d\Omega, \tag{15}$$

known in RT as the scalar (a.k.a. actinic) flux, vector flux and tensor flux, respectively. These quantities all have well-known counterparts in kinetic theory: $U = J/c$ is the energy density of the radiation field, F its current density and $\mathsf{P} = \mathsf{K}/c$ its pressure tensor.

We then have the following expressions for the conservation of energy and momentum:

$$c^{-1}\frac{\partial J}{\partial t} + \nabla \cdot F = -\sigma_a(x)J + q_J(t, x), \tag{16}$$

$$c^{-1}\frac{\partial F}{\partial t} + \nabla \cdot \mathsf{K} = -\sigma_t(x)F + q_F(t, x), \tag{17}$$

where the new source terms follow from $q(t, x, \Omega)$ in (8) using the definitions in (13)–(14). Two new coefficients have also appeared. First, we have the absorption coefficient, $\sigma_a = \sigma - \sigma_s = (1 - \varpi_0)\sigma$, where we introduce the very useful 'single scattering albedo' parameter:

$$\varpi_0 = \sigma_s/\sigma. \tag{18}$$

Second, we have the *transport* extinction,

$$\sigma_t = (1 - g)\sigma_s + \sigma_a = (1 - \varpi_0 g)\sigma, \tag{19}$$

where, letting $\mu_s = \Omega' \cdot \Omega$

$$g = 2\pi \int_{-1}^{+1} \mu_s P(\mu_s)\,d\mu_s \tag{20}$$

is known as the 'asymmetry factor' of the phase function, the mean cosine of the scattering angle. It is notable that droplet-size distributions observed in boundary-layer clouds yield $g \approx 0.85$ in the solar spectrum (cf figure 4) with remarkably small cloud-to-cloud variability [56]. Higher-level ice clouds (and most aerosol) tend to have somewhat smaller values, $g \approx 0.8$ [57] or even less [58]. Particles much smaller than the wavelength are essentially Rayleigh scatterers, and their g is close to 0.

Can we close the system of equations in (16)–(17)? A simple closure follows if we brutally truncate the expansion of $I(t, x, \Omega)$ in spherical harmonics at first order (a 'P$_1$' approximation in transport terminology):

$$I(t, x, \Omega) \approx [J(t, x) + 3\Omega \cdot F(t, x)]/4\pi \tag{21}$$

and, accordingly,

$$P(x, \Omega' \cdot \Omega) \approx [1 + 3g(x)\Omega' \cdot \Omega]/4\pi \tag{22}$$

for the phase function. This immediately tells us that the radiation pressure tensor K/c from (15) is isotropic, i.e. off-diagonal components vanish and on-diagonal components are equipartitioned (each one equal to 1/3 of the radiant energy density J/c). By substitution into (17), we obtain

$$\partial_t \boldsymbol{F} + \nabla J/3 = -\sigma_t(\boldsymbol{x})\boldsymbol{F} + \boldsymbol{q}_F(t, \boldsymbol{x}), \qquad (23)$$

which complements the exact conservation law in (16).

The PDE system in (16) and (23) is known as the telegrapher's problem. It is causal in the sense that bulk velocities do not exceed c. However, the preferred diffusion model uses one more approximation: to neglect the time derivative in (23), hence

$$\boldsymbol{F} = -\nabla J/3\sigma_t(\boldsymbol{x}) + \boldsymbol{q}_F(t, \boldsymbol{x})/\sigma_t(\boldsymbol{x}). \qquad (24)$$

This is the desired constitutive law, a closed expression for the vector flux that can be explicitly combined with (16). It is the radiative counterpart of Fick's law of diffusivity,

$$\boldsymbol{F} = -(D/c)\nabla J, \qquad (25)$$

where

$$D(\boldsymbol{x}) = c/3\sigma_t(\boldsymbol{x}) = c\ell_t(\boldsymbol{x})/3, \qquad (26)$$

plus a local correction for source anisotropy, namely, $\ell_t(\boldsymbol{x})\boldsymbol{q}_F(t, \boldsymbol{x})$. Equations (16) and (24) thus define the radiation diffusion model, as an approximation to full time-dependent 3D RT theory. We can expect violations of causality in this approximation, but they are limited for the most part to early times in the important case of 'δ-in-time' sources. We experimented with the more accurate telegrapher's transport problem in (16) and (23) for space–time Green function estimation [59], but the resulting expressions are complex, and it may be possible, in practice, to avoid those regions of space–time where diffusion breaks down.

Finally, we note that there are other derivations of the macroscopic transport model encapsulated in diffusion theory, with the most insightful coming from asymptotic analysis of the general RTE; the interested reader is referred to the original papers by Larsen [60] and Pomraning [61].

2.4.2. Reconsideration of directional details. In view of (25)–(26), we recognize that the *transport* MFP

$$\ell_t = 1/\sigma_t \qquad (27)$$

is a locally defined length scale that matters a lot in diffusion theory; in the absence of absorption, there is no other to work with. It is easy to see that ℓ_t is larger than ℓ in (11) by a factor

$$\frac{1}{1 - \varpi_0 g} = \sum_{n=0}^{\infty} (\varpi_0 g)^n. \qquad (28)$$

It can be shown [62, 63] that the nth term in this sum is the contribution from the order n in an infinite sequence of forward-biased scattering events, as quantified by g in (20). We can thus think of the transport MFP as the distance covered on average by a collimated beam of light incident on a forward-scattering medium before it has all but lost the memory of its original direction.

Underlying this spatial ramification of a directional memory effect, there is a diffusion process in direction space. If a light beam starts, for simplicity, with a vertical direction cosine $\mu_0 = 1$, hence $\theta_0 = 0$, its first scatter will send it off in a random azimuthal direction ϕ_1 and a random polar angle θ_1, according to the scattering phase function. This is nothing more than a first step in a discrete-time random walk on the unit sphere: $(\theta_n, \phi_n), n \in \mathbb{N}$. Since that space is finite, we estimate that $n^\star \approx 1/(1 - \varpi_0 g)$ is the characteristic number of steps required to 'dilute' the original collimated beam over the whole sphere. Now, each step into this directional memory loss process leaves a trace in propagation space. The first step $\boldsymbol{s}_1$ moves, on average, the transported particle a distance $\langle s \rangle = \ell$ along the positive z-axis; the next step moves it $\langle \mu_1 s \rangle = g\ell$ further along the same axis and ϖ_0 times that to factor in the possibility of suffering an absorption. That is the physical interpretation of the first two terms of the expansion in (28), and a recursion argument [62] shows that subsequent steps contribute all the others.

Reconsidering figure 3, it is intuitively clear that this directional diffusion may be better described as a 2-level process: first move around within the forward diffraction peak, based on another (smaller) value of the elementary step variance, then populate the rest of the sphere using an effective g that is smaller than 0.85. The first part captures the spirit of 'small-angle' approximation in RT. It plays an important role in the transmitted radiation field of hazes and cirrus clouds, and it is responsible for the silver lining of optically thick 3D clouds (often a visually stunning phenomenon). However, it is not important for the reflected radiation. Neither is it important for the *truly* diffuse transmission at any optical depth, since it is a perturbation around the direct beam. In contrast, diffuse transmission as well as reflection will be dominated by the second angular diffusion process controlled by an effective $g' < g$. We define g' formally in the next subsection.

2.4.3. Extension of the range of validity. Under what conditions do we expect the diffusion/P_1 theory to be a reasonable approximation to atmospheric radiation transport? It is in essence an asymptotic limit of transport [60, 61] where the small parameter is the ratio of the transport MFP to the outer scale of the system. In other words, we recognize here the small Knudsen numbers that we have already mapped to the *opaque* cloudy regions of the atmosphere. Another condition that favors diffusion (thinking of long random walks) is weak absorption. In the limit of no absorption (no volume sinks) whatsoever and no volume sources, the diffusion equations in (16) and (24) can be combined into the familiar heat/diffusion equation:

$$\left[c^{-1}\frac{\partial}{\partial t} - \nabla \cdot (D\nabla) \right] J = 0. \qquad (29)$$

If furthermore the boundary sources are steady and extinction (hence diffusivity) is uniform, we obtain the Laplace equation, $-\nabla^2 J = 0$, for which many analytical and numerical solution methods exist.

What are diffusion/P_1 theory's main vulnerabilities? Even in regimes where physical intuition tells us that radiation transport should be diffusive, we can maybe improve its performance. Indeed, we suspect that the 2-term spherical-harmonic expansions of $I(t, \boldsymbol{x}, \boldsymbol{\Omega})$ in (21) and certainly of $P(\boldsymbol{x}, \mu_s)$ in (22) can be very unrealistic in clouds. In the case of radiance, (21) fails near collimated sources such as solar or laser illumination. In the case of the phase function, we recall that cloud particles have very forward-peaked scattering. To wit, (22) yields unphysical negative values in backscattering directions if $g(\boldsymbol{x}) > 1/3$, which includes the values of interest for clouds (0.75–0.85).

The fix is the same for both problems: the radiance field is broken naturally into its un-collided and diffuse components, and the phase function is recast as the sum of a Dirac δ in the forward direction—physically, just a boost in ballistic propagation—and a residual 2-term expansion. So we think of (21) as only the diffuse radiance, and replace the 1-parameter model phase function in (22) with the 2-parameter model in

$$
\begin{aligned}
P(\boldsymbol{x}, \mu_s) \approx \frac{1}{4\pi}[&f(\boldsymbol{x})2\delta(1 - \mu_s) \\
&+ (1 - f(\boldsymbol{x}))(1 + 3g'(\boldsymbol{x})\mu_s)].
\end{aligned}
\tag{30}
$$

This leads to the following rescaling of the local optical properties:

$$
\sigma' = (1 - \varpi_0 f)\sigma,
$$

$$
1 - \varpi_0' = \frac{1}{1 - \varpi_0 f}(1 - \varpi_0),
\tag{31}
$$

$$
1 - \varpi_0' g' = \frac{1}{1 - \varpi_0 f}(1 - \varpi_0 g),
$$

where f is the fraction of 'δ-scattering.' The smaller extinction reflects the boost in ballistic propagation while the effective absorption is increased. Finally, physically meaningful values of

$$
g' = \frac{g - f}{1 - f}
\tag{32}
$$

can now go up to $1/3(1 - f)$ in (30) and (31); so it is better if we can rationalize $f \geqslant 2/3$.

Following Joseph *et al* [64], we can take $f = g^2$, hence $g' = g/(1 + g)$, because it fits the two first spherical-harmonic moments of the popular Henyey–Greenstein (H–G) model phase function [65] illustrated in figure 3. It is given by

$$
P(\mu_s) = \left(\frac{1}{4\pi}\right)\frac{1 - g^2}{(1 + g^2 - 2g\mu_s)^{3/2}},
\tag{33}
$$

and has g^l as its lth spherical-harmonic moment. For liquid water clouds, where $g \approx 0.85$, we obtain $f \approx 0.72$ (exceeding 2/3), hence $\sigma' \approx 0.28\sigma$ and $g' \approx 0.46$ when $\varpi_0' = \varpi_0 = 1$. Alternatively, the whole diffraction peak—half of the scattered energy for particles with very large size parameters (by Babinet's principle)—can be recast as prolonged propagation in the original direction: hence $f = 0.5$ (not exceeding 2/3), thus $\sigma' \approx 0.5\sigma$ and $g' \approx 0.7$ when $\varpi_0' = \varpi_0 = 1$.

3. Cloud geometry models, solutions of the corresponding RT problems, and applications

Several things that happen to the radiant energy after leaving its source have already been mentioned—propagation, scattering and absorption—but there is one more possibility. Radiation can propagate to a boundary point and then escape the medium altogether. When integrated over direction and space, escaping radiation matters hugely for the radiant energy balance of the medium.

This leads us to the natural mathematical completion of the RT problem statement by setting the boundary conditions (BCs). In a nutshell, we need to quantify the radiant energy entering or re-entering, via reflection, the medium through ∂M, the boundary of a convex set $M \subseteq \mathbb{R}^3$ where we wish to solve the RTE.

3.1. The plane-parallel slab

3.1.1. Boundary conditions and escaping radiation. The simplest possible cloud geometry is a plane-parallel slab $M_{pp}(H) = \{\boldsymbol{x} \in \mathbb{R}^3; 0 < z < H\}$ and the simplest BCs are the 'absorbing' type, expressing that no radiation enters $M_{pp}(H)$:

$$
I(t, x, y, 0, \boldsymbol{\Omega}) = 0, \qquad \Omega_z = \mu > 0,
\tag{34}
$$

$$
I(t, x, y, H, \boldsymbol{\Omega}) = 0, \qquad \Omega_z = \mu < 0,
\tag{35}
$$

for $t \geqslant 0$ (the usual time domain) and $(x, y)^T \in \mathbb{R}^2$. Of course, in the above case of absorbing BCs, the source term $Q(t, \boldsymbol{x}, \boldsymbol{\Omega})$ in (8) will not vanish everywhere, and it can in fact be used to specify solar irradiation of $M_{pp}(H)$. We model this internal source as a steady spatially uniform mono-directional beam aligned with $\boldsymbol{\Omega}_0 = \boldsymbol{\Omega}(\theta_0, \phi_0)$ that is directly transmitted from the $z = 0$ plane, and then once scattered:

$$
\begin{aligned}
Q(\boldsymbol{x}, \boldsymbol{\Omega}) = &F_0\sigma_s(\boldsymbol{x})\,P(\boldsymbol{x}, \boldsymbol{\Omega}_0 \to \boldsymbol{\Omega}) \\
&\times \exp\left[-\int_0^z \sigma\left(x - \Omega_{0x}\frac{z - z'}{\Omega_{0z}}, y - \Omega_{0y}\frac{z - z'}{\Omega_{0z}}, z'\right)\frac{\mathrm{d}z'}{\Omega_{0z}}\right],
\end{aligned}
\tag{36}
$$

where F_0 is the (spectral) solar flux in W m^{-2}(nm^{-1} of wavelength, as needed). Note that we have encoded here a beam entering the slab at $z = 0$, which we will always view as the illuminated upper boundary (z increases downward here). Alternatively, we can set $Q(\boldsymbol{x}, \boldsymbol{\Omega}) \equiv 0$ and use a straightforward variation of (34) to do the same job:

$$
I(x, y, 0, \boldsymbol{\Omega}) = F_0\delta(\boldsymbol{\Omega} - \boldsymbol{\Omega}_0), \qquad \mu, \mu_0 > 0,
\tag{37}
$$

where $\mu_0 = \Omega_{0z}$. In this case, the estimated radiance field will contain the un-collided (directly transmitted) light as well as the diffuse light. For an isotropic source, the right-hand side of (37) would be simply F_0/π. We note that we can assume $F_0 = 1$ without loss of generality since the linearity of the RTE can be invoked to sum over wavelengths, as weighted by $F_{0\lambda}$, after the fact.

If the cloudy medium $M_{pp}(H)$ is above a partially reflective surface at $z = H$, then there is re-entering radiation to account for. In this case, (35) is modified, becoming

$$
I(x, y, H, \mathbf{\Omega})
$$
$$
= \alpha(x, y) \int_{\mu' > 0} P_s(x, y, \mathbf{\Omega}' \to \mathbf{\Omega}) I(x, y, H, \mathbf{\Omega}') d\mathbf{\Omega}',
$$
$$
\mu < 0, \tag{38}
$$

which is designed to look like the in-scattering term in (8). Here, α is the local surface albedo, defined as the ratio of up-welling to down-welling hemispherical fluxes,

$$
F_{\pm}(\mathbf{x}) = \int_{-\pi}^{+\pi} d\phi \int_0^{\pm 1} I(\mathbf{x}, \mathbf{\Omega}) \mu \, d\mu, \tag{39}
$$

at $z = H$:

$$
\alpha(x, y) = F_-(x, y, H)/F_+(x, y, H). \tag{40}
$$

The *surface* phase function, denoted here by P_s, is normalized to $\int_{\mu' > 0} P_s(\mathbf{\Omega}' \to \mathbf{\Omega}) d\mathbf{\Omega}' = 1, \forall \mu < 0$; it is used here as a representation of the bi-directional reflectance distribution function (BRDF) [66, 67]. Two contrasting examples of surface scattering/reflection are the isotropic (a.k.a. Lambertian) case, $P_s(\mathbf{\Omega}' \to \mathbf{\Omega}) = \mu'/\pi$ and the specular (a.k.a. Fresnel) case, $P_s(\mathbf{\Omega}' \to \mathbf{\Omega}) = \delta(\mu' + \mu)\delta(\phi' - \phi)$.

Of particular interest in cloud remote sensing are the radiance fields that describe steady solar radiation escaping the plane-parallel medium at its upper and lower boundaries: $I(x, y, 0, \mathbf{\Omega})$, $\mu < 0$ and $I(x, y, H, \mathbf{\Omega})$, $\mu > 0$, respectively, for observers above and below the cloud layer. It is convenient to normalize the reflected radiance such that it reads as the effective albedo the cloud would have if the (sampled) radiance field was uniform in direction:

$$
R(x, y, \mathbf{\Omega}) = \pi I(x, y, 0, \mathbf{\Omega})/\mu_0 F_0, \qquad \mu < 0; \tag{41}
$$

$$
T(x, y, \mathbf{\Omega}) = \pi I(x, y, H, \mathbf{\Omega})/\mu_0 F_0, \qquad \mu > 0, \tag{42}
$$

where we have similarly recast the transmittance field. These functions describe how the cloud layer redistributes the spatially uniform and unidirectional solar beam both horizontally and directionally. In space-based observation, one is often looking straight down ($\mathbf{\Omega} = -\hat{z}$) at the nadir radiance field while the detector overflies the scene. In ground-based observation, a static detector often looks straight up ($\mathbf{\Omega} = +\hat{z}$) and captures zenith radiance as the clouds are advected by (Taylor's 'frozen turbulence hypothesis' is often invoked to interpret a time series of zenith radiance as an approximation of the horizontal spatial variations).

In the simpler diffusion theory for RT in the denser clouds, the BCs need to be stated as well. Physically, one needs to constrain the fluxes of radiant energy crossing the upper and lower boundaries. In plane-parallel geometry, we first need to evaluate hemispherical fluxes in (39) that cross an arbitrary constant-z plane in the $\pm$ directions, for given J and $\mathbf{F}$:

$$
F_{\pm} = \frac{J/2 \pm F_z}{2}, \tag{43}
$$

from (13)–(14) and (21). Restoring time-dependence, the absorbing BCs in (34)–(35) thus become

$$
4F_+(t, \vec{\rho}, 0) = J(t, \vec{\rho}, 0) + 3\chi F_z(t, \vec{\rho}, 0) = 0, \tag{44}
$$

$$
4F_-(t, \vec{\rho}, H) = J(t, \vec{\rho}, H) - 3\chi F_z(t, \vec{\rho}, H) = 0, \tag{45}
$$

for all $\vec{\rho} = (x, y)^{\mathrm{T}} \in \mathbb{R}^2$ and $t > 0$ and where, until further notice, we take $\chi = 2/3$. In the above case of absorbing boundaries, we need at least one non-vanishing volume source term. For the steady solar beam, (36) yields

$$
q_J(\mathbf{x}) = F_0 \sigma_s(x, y, z)
$$
$$
\times \exp\left[-\int_0^z \sigma\left(x - \Omega_{0x} \frac{z - z'}{\Omega_{0z}}, y - \Omega_{0y} \frac{z - z'}{\Omega_{0z}}, z' \right) \frac{dz'}{\Omega_{0z}} \right], \tag{46}
$$

$$
\mathbf{q}_F(\mathbf{x}) = q_J(\mathbf{x}) g(\mathbf{x}) \mathbf{\Omega}_0. \tag{47}
$$

When the surface at the lower boundary is partially reflective, as in (38), we mandate the time-dependent version of (40) and, accordingly, the left-hand side of (45) becomes

$$
[1 - \alpha(\vec{\rho})] J(t, \vec{\rho}, H) - 3\chi [1 + \alpha(\vec{\rho})] F_z(t, \vec{\rho}, H) = 0. \tag{48}
$$

Solar radiation escaping a plane-parallel cloud, *a priori* with internal 3D structure, is characterized in diffusion theory by the local hemispheric fluxes

$$
R(\vec{\rho}) = F_-(\vec{\rho}, 0)/\mu_0 F_0 = J(\vec{\rho}, 0)/2\mu_0 F_0, \tag{49}
$$

$$
T(\vec{\rho}) = F_+(\vec{\rho}, H)/\mu_0 F_0 = J(\vec{\rho}, H)/2\mu_0 F_0, \tag{50}
$$

when (44)–(45) have been used, recalling that this assumes the internal source model in (46)–(47). Consequently, the transmittance field here is only for the diffuse component; if *total* transmittance is required, one must add the local directly transmitted flux (normalized to the incident flux):

$$
T_{\mathrm{dir}}(x, y) =
$$
$$
\exp\left[-\int_0^H \sigma\left(x - \Omega_{0x} \frac{H - z}{\Omega_{0z}}, y - \Omega_{0y} \frac{H - z}{\Omega_{0z}}, z \right) \frac{dz}{\Omega_{0z}} \right].
$$

For an isotropic boundary source, we have F_0/π on the right-hand side side of (37); its diffusion counterpart in (44) is then

$$
4F_+(t, \vec{\rho}, 0) = J(t, \vec{\rho}, 0) + 3\chi F_z(t, \vec{\rho}, 0) = 4F_0. \tag{51}
$$

Notably, the same happens to the collimated source model at the upper boundary in (37) since the diffusion framework cannot distinguish directional and isotropic *boundary* sources. In this case, it is conventional to treat χ, which multiplies $F_z(t, \vec{\rho}, 0)$ and $F_z(t, \vec{\rho}, H)$ in boundary conditions (44)–(45), as an adjustable parameter that can differ—although typically not much—from 2/3. This numerical parameter is known as the 'extrapolation length' (reckoned in units of ℓ_t) and it enables diffusion results to follow more closely transport-theoretical predictions. Physically, χ is used to compensate for the fully expected weakness of diffusion theory in the radiative boundary layer, i.e. up to 1–2 times ℓ_t in vertically measured distance from either boundary. There is no violation of energy conservation here as long as the same substitution is made in

(49)–(50) for the hemispherical fluxes in the opposite direction (i.e. for *escaping* radiation). Specifically, we now have

$$R(\vec{\rho}) = J(\vec{\rho}, 0)/2F_0 - 1, \qquad (52)$$

$$T(\vec{\rho}) = J(\vec{\rho}, H)/2F_0, \qquad (53)$$

where it is understood that (i) the reflected flux must now be derived from an estimate of $J(\vec{\rho}, 0)$ that includes the incoming radiation and (ii) the transmitted flux is now diffuse + direct.

3.1.2. Mainstream one-dimensional radiative transfer. So far, we have made no assumptions about the internal structure of the plane-parallel medium, nor about the spatial variations of the optional lower surface BRDF. A widespread assumption that eases computations is exact translational symmetry in the horizontal ($\vec{\rho}$) plane. This leads to the so-called 1D RT theory[6] where optical properties and at least the radiance field can still vary in the vertical (z) direction. This is of course a gross approximation of real clouds that should always be— but still too rarely is—questioned before use. Depending on the specifics of the application (cloud type, tolerance to error, etc), it is not necessarily a bad approximation, but often is (cf section 6).

For a comprehensive survey of computational techniques for solving the 1D RTE, we refer the interested reader to the monograph edited by Lenoble [68]. The most popular are identified by their approach to Ω-space: spherical harmonics ('P$_N$' methods) and discrete ordinates ('S$_N$' methods); both approaches benefit from Fourier mode decoupling in the azimuthal variable that follows directly from the invariance of the slab medium and solar source under horizontal translation. The adopted solutions in z-space are quite diverse: coupled ODEs, eigenvalue methods, Gauss–Seidel iteration, successive orders of scattering, invariant embedding, 'adding/doubling' (illustrated below in 1D, equivalently, S$_2$ theory) or any other technique.

One class of 1D RT models is fully tractable, and therefore extensively used in atmospheric radiation science: *uniform* slabs in the diffusion/P$_1$ approximation derived above and/or for two-stream/S$_2$ models, i.e. when the angular quadrature is reduced to two beams [69, 70]. The P$_3$ model was also worked out in closed form (as a special case of the S$_4$ model with Gaussian quadrature points and weights) [71]. It naturally outperformed the standard P$_1$ model [72, 73] and will likely replace it over time in GCM shortwave schemes.

These simplified angular representations are expected to become more accurate as the cloudy medium becomes more opaque, i.e. optical thickness

$$\tau = \sigma H = H/\ell \qquad (54)$$

increases with H for a given extinction σ, equivalently, the MFP $\ell = 1/\sigma$ decreases for a given geometrical thickness H. Very few other cloud geometries are amenable to completely analytical treatment, one exception being uniform spheres within the diffusion approximation (cf section 3.3 and

---

[6] In the atmospheric RT community, only spatial dimensions are counted up front.

references therein). Although far more relevant to aerosols than clouds, the opposite asymptotic limit of transport theory, τ vanishingly small, is amenable to the single-scattering approximation. This computation, including flux estimation via angular integration, can be performed analytically for a number of geometries including slabs [74] and spheres [75].

In the two-stream model, diffusion-type equations arise for the sum and difference of the up- and down-welling fluxes and conversely, using the correspondence in (43). Intuitively, this plane-parallel cloud geometry may be a reasonable approximation to solar RT in the real world for single-layered unbroken stratiform clouds, and possibly better still if spatial and/or angular integrals are targeted, as in radiation energy budget modeling, for instance, in GCMs.

3.1.3. 1D 'adding/doubling' and diffusion theory for $\varpi_0 = 1$. In the procedure outlined above to derive boundary-leaving radiances and fluxes, one necessarily solves the transport or diffusion equations for all the points in the medium. This may not be optimal when one is only interested in the overall radiation budget, let alone remote sensing applications, where *only* radiances and fluxes at the boundaries matter. The adding/doubling method can be used to obtain directly R and T as functions of ϖ_0 in [0, 1], g in [−1, +1] and $\tau \geqslant 0$. To illustrate this computational technique as well as the essential transport physics of uniform slab clouds, we will invoke 'literal' 1D RT, i.e. where the entire steady-state radiance field is reduced to $\{I_+, I_-\}$ expressed in watts, with no steradians or even m^2 to worry about. In one spatial dimension, the phase function reduces to the discrete probabilities of scattering forward, $p_{\mathrm{f}} = (1 + g)/2$, or backward, $p_{\mathrm{b}} = 1 - p_{\mathrm{f}} = (1 - g)/2$.

Suppose we know the reflectivity/albedo $R = I_-(0)/F_0$ and transmittance $T = I_+(H)/F_0$ of a 1D 'slab' (i.e. the interval [0, H]), for given optical properties $\{\sigma, \varpi_0, g\}$. If these local properties are all uniform between $z = 0$ and $z = H$, then only the non-dimensional product in (54) matters; we can take either H or ℓ (hence σ) as unity without loss of generality. Knowing $\{R, T\}(\tau)$, can we compute it for $\tau + \delta\tau$, where $\delta\tau \ll 1$? If we denote $\{r, t\} = \{R, T\}(\delta\tau)$, then it is not hard to show that

$$R + \delta R = r + Rt^2/(1 - Rr) \qquad (55)$$

and

$$T + \delta T = tT/(1 - Rr), \qquad (56)$$

where the $1/(1 - Rr)$ factor accounts for any number of reflections between the two layers: $t \times [\sum_{n=0}^{\infty}(Rr)^n] \times T$ in transmission and without the last T but with $R \times t$ instead for reflection. Since the additional layer is infinitesimally thin, we have $\{r, t\} \approx \{0^+, 1^-\}$, hence $\{R + \delta R, T + \delta T\} \approx \{r + Rt^2(1 + Rr), tT(1 + Rr)\}$. More specifically, we have

$$r = \varpi_0(1 - g)\delta\tau/2 \qquad (57)$$

and

$$t = 1 - \delta\tau + \varpi_0(1 + g)\delta\tau/2 \qquad (58)$$

if we invoke the single-scattering approximation. By substitution, elimination and keeping only 1st-order terms, we end up with the following coupled nonlinear ODEs to solve:

$$R' = -2[1 - \varpi_0(1+g)/2] R + [\varpi_0(1-g)/2] (1 + R^2),$$
$$(59)$$

$$T' = -[1 - \varpi_0(1+g)/2] T + [\varpi_0(1-g)/2] R T, \qquad (60)$$

where derivatives are with respect to τ, with initial conditions $\{R, T\}(0) = \{0, 1\}$. The ODE in (59) is in the classic Ricatti form.

Starting with the simpler case of conservative scattering ($\varpi_0 = 1$), where we know that $R + T = 1$; the solutions of (59)–(60) are then

$$R(\tau) = (1-g)\tau/(2\chi + (1-g)\tau), \qquad (61)$$

$$T(\tau) = 1 - R(\tau) = 1/(1 + (1-g)\tau/2\chi), \qquad (62)$$

with $\chi = 1$. Solution of the corresponding 1D diffusion model (i.e. for slab geometry in three spatial dimensions) for an isotropic boundary source leads to the same expressions but with χ determined by the precise boundary conditions, recalling that $\chi \approx 2/3$. The product $(1-g)\tau$ in (61)–(62) is the 'scaled' optical depth of the cloud. We see from (27) that it is simply the distance ratio

$$\tau_t = H/\ell_t = \sigma_t H = (1-g)\tau \qquad (63)$$

in the present $\varpi_0 = 1$ case, clearly a key quantity in diffusive transport theory. We note that the δ-rescaling transformation in (31) leaves τ_t invariant.

When expanding (62) for $\tau \ll 1$, we obtain $T(\tau) \approx 1 - (1-g)\tau/2\chi$, where we do not recognize the direct transmission that should dominate: $T_{dir}(\tau) = \exp(-\tau) \approx 1 - \tau$ for normally incident collimated illumination; nor do we see $T_{iso}(\tau) = 2\int_0^1 \exp(-\tau/\mu_0)\mu_0\,d\mu_0 \approx 1 - 2\tau$ for the actual isotropic illumination. This reminds us that, for spatial dimension $\geqslant 2$, the diffusion model targets only the optically thick regime. The accuracy of the diffusion transport model can, however, be improved for solar radiation by using the internal anisotropic source terms in (46)–(47); see [70] for details. This of course introduces a dependence on the cosine of the solar zenith angle μ_0, and opens up the possibility that the δ-rescaling transformation in (31) will have a positive impact on the diffusion model's performance (with respect to the full multi-stream transport model).

3.1.4. Three elementary applications. As a first application, we return to the question of the intense whiteness of clouds viewed in reflection geometry. We have already established that clouds are very weakly absorbing in the visible spectrum and their scattering properties are spectrally flat (cf figure 4). Multiple scattering will always whiten clouds since any dependence of τ on λ is significantly flattened after being passed through the cloud albedo expression in (61), and more so as the asymptotic diffusion regime ($\tau_t = (1-g)\tau \gg 2\chi$) is approached. By the same token, the expression for diffuse cloud transmittance in (61) also flattens the spectral slope but simultaneously lowers the light levels, hence the uniformly

gray appearance of the base of thick stratus clouds or of the non-illuminated side of cumulus-type clouds. So we would very much like to know: how optically thick are clouds across the visible spectrum?

Bohren *et al* [76] established empirically that a human observer cannot distinguish the direction of the Sun through a cloud of forward-scattering particles ($g \approx 0.85$) when τ exceeds 8–10; this is of course when the diffuse light overwhelms not only the direct but also the forward-scattered light. Based on (61), we are interested in comparing numerically τ and $2\chi/(1-g)$. When equal, we have $R(\tau) \approx T(\tau) \approx 1/2$; therefore, as τ approaches and increases beyond $2\chi/(1-g)$, clouds become powerful diffusers of light. Values in the literature for χ range from $1/\sqrt{3} \approx 0.577$ to a transcendental number ≈ 0.7104, and we recall that liquid water clouds have $g \approx 0.85$ while their ice water counterparts are closer to 0.75. So the range for $2\chi/(1-g)$ is 7–9 for liquid clouds (very close to Bohren *et al*'s empirical range) and 5–6 for ice clouds. Interestingly, this is at the low end of the climatology for low/warm clouds, which can thus be deemed by and large diffusive, and at the high end for high/cold cirrus (Ci) clouds, which indeed will rarely block the Sun completely (and frequently display halos, Sun-dogs and other such single-scattering phenomena [77]).

Clouds matter for the radiation part of the energy cycle in the climate system, largely because they are optically thick, and they also play a key role in the atmospheric part of the hydrological cycle. So, as a second application, we ask: how much water is there in a typical cloud?

This amount is given by its liquid/ice water *path* (LWP/IWP) in $\mathrm{kg\,m^{-2}}$ defined as the vertical integral of mass density of water in the cloud droplets or crystals, a.k.a. liquid/ice water *content* (LWC/IWC) in $\mathrm{kg\,m^{-3}}$:

$$CWC(z) = n(z) \times \rho_w \times \frac{4\pi}{3}\overline{r^3}(z), \qquad (64)$$

where condensed water content (CWC), given by $LWC + IWC$ and ρ_w is the density of condensed water, $\approx 10^3\,\mathrm{kg\,m^{-3}}$, hence

$$CWP = LWP + IWP = \int_0^H CWC(z)\,dz. \qquad (65)$$

CWP, LWP or IWP can also be measured as the thickness (say, in mm) of the layer of all the water of interest in clouds aloft, were it all precipitated, which is the same as in (65) above but without ρ_w in (64) and reducing all the length dimensions to, say, mm. We now compare CWP and cloud optical depth

$$\tau = \int_0^H \sigma(z)\,dz, \qquad (66)$$

where

$$\sigma(z) = n(z) \times 2 \times \pi\overline{r^2}(z) \approx \frac{3}{2}\frac{CWC(z)/\rho_w}{r_e} \qquad (67)$$

in the limit of large size parameters ($Q \approx 2$ in Lorenz–Mie scattering theory). If the 2nd and 3rd droplet-radius moments

have the same vertical profile, i.e. r_e in (3) is invariant with altitude, then [78]

$$\tau = \frac{3}{2} \frac{CWP/\rho_w}{r_e}. \tag{68}$$

Equivalently, τ is $1.5\times$ the ratio of CWP and r_e when expressed in the same units. As an example, we can take $\tau = 15$, which yields the reasonable cloud albedo value of $R = 0.63$ for the canonical $g = 0.85$ and $\chi = 2/3$ in (61); we also take $r_e = 10\,\mu$m, another often-used value (although far less justifiably than $g = 0.85$). We then find that CWP is only 0.1 mm. This illustrates how so little water, if dispersed into many small particles in the atmosphere, can provide powerful reflectivity for the planet. Adding water vapor to the mix raises the 'precipitable' water thickness to several millimeters in most locales. So clouds use only a small fraction of all the water in the atmosphere.

Finally, we note that solving (68) for CWP makes clear why both τ and r_e are highly desirable retrieval products in cloud remote sensing.

As a third and final application, we turn to the above-mentioned indirect effect of aerosols on climate via cloud albedo, a.k.a. the Twomey effect [16]. For clouds forming in clean air, we can count on $n \approx 100\,\text{CCN cm}^{-3}$; in polluted air, this number can be $10\times$ more. Consequently, $\overline{r^3}$ (hence r_e) will have to go down and, for a fixed cloud water budget given by CWP in (65) and (68), τ will necessarily go up. In view of (61), this means more reflective clouds. In the absence of further feedbacks, this will cool the climate. If, due to the larger population of smaller droplets, precipitation is also delayed or even suppressed, the longer life-cycle of clouds goes in the same direction. The tough question about dynamical and microphysical feedbacks then becomes critically important, and is being actively investigated.

3.1.5. 1D 'adding/doubling' and diffusion theory for $\varpi_0 < 1$.
The case of non-vanishing absorption ($\varpi_0 < 1$) is more involved. For the diffusion or S_2 models, we find

$$R(\tau) = \frac{1 - X^2}{1 + X^2 + 2X \coth Y} \tag{69}$$

and

$$T(\tau) = \frac{2X \cosh Y}{1 + X^2 + 2X \coth Y}, \tag{70}$$

where

$$X = \chi \sqrt{d(1 - \varpi_0)/(1 - \varpi_0 g)} = \chi \ell_t/L_d \tag{71}$$

and

$$Y = \sqrt{d(1 - \varpi_0)(1 - \varpi_0 g)}\, \tau = H/L_d \tag{72}$$

with $d = 1, 2, 3$ being the number of spatial dimensions. It is readily shown that all the factors of 3 in (21)–(26) and (44)–(45) ultimately come from the three spatial dimensions considered therein. In particular, the $d = 1$ case (with $\chi = 1$) in (69)–(72) is the general solution of the Riccati ODE system in (59)–(60). The $d = 3$ case has naturally attracted considerable attention in the atmospheric RT literature [70, 79, 80, among many others].

A new length scale appears:

$$L_d = \ell_t \bigg/ \sqrt{\frac{3(1 - \varpi_0)}{1 - \varpi_0 g}} = 1/\sqrt{3(1 - \varpi_0)(1 - \varpi_0 g)}\,\sigma \tag{73}$$

in $d = 3$; quantities X and Y are ratios of L_d with the extrapolation length and the slab thickness, respectively. It is commonly known as the 'diffusion length' of the medium. When $L_d \to \infty$ ($\varpi_0 \to 1$), the expressions in (69)–(70) revert to (61)–(62) for any choice of d. The key (local) scale ratio here,

$$\ell_t/L_d = X/\chi = \sqrt{\frac{3(1 - \varpi_0)}{1 - \varpi_0 g}}, \tag{74}$$

is known as the 'similarity' factor. We note that the δ-rescaling transformation in (31) leaves both X and Y, hence ℓ_t and L_d, invariant. So no performance improvement can be expected here; again, that calls for diffuse/direct separation and better solar source representation using anisotropic internal source terms.

We therefore expect absorption to matter when $L_d \lesssim H$ ($Y \gtrsim 1$), equivalently, $\sqrt{(1 - \varpi_0 g)/3(1 - \varpi_0)} \lesssim \tau_t = \sigma_t H$, which in diffusion theory should itself be $\gtrsim$ unity. In this non-conservative case, the finite rate of radiant energy absorption in the slab is $A(\tau) = 1 - [R(\tau) + T(\tau)]$ in units of F_0. Like $R(\tau)$, $A(\tau)$ rises from 0 to an asymptotic value. For the isotropic source model leading to (69)–(70) in three spatial dimensions, we have

$$A(\infty) = 1 - R(\infty) = \frac{2X}{1 + X} \approx 2\chi \sqrt{\frac{3(1 - \varpi_0)}{1 - \varpi_0 g}}, \tag{75}$$

where we recognize the ratio in (74). This is a strong function of $(1 - \varpi_0)$ that results physically from the effectiveness of absorption when the transport is dominated by multiple scattering. To assess the power of multiple scattering as a catalyst of absorption, we focus on clouds where $A(\infty) \approx R(\infty) \approx 1/2$. This occurs when $1 - \varpi_0 \approx (1 - g)/48\chi^2$, which is in the range 0.006–0.01 (depending on the choice of χ) when $g = 0.85$: less than 1% of the collisions result in absorption. Furthermore, returning to finitely thick clouds, the approach to this asymptotic regime is exponentially fast, going as $T(\tau) \propto \exp[-\tau_t \sqrt{3(1 - \varpi_0)/(1 - \varpi_0 g)}]$. This high sensitivity of cloud reflectivity to $(1 - \varpi_0)$ is excellent news for remote sensing determination of r_e. Recall from section 2.2 that $\sigma_a = n\,\overline{\xi_a}$ scales roughly as $\overline{r^3}$, so $(1 - \varpi_0)$ will go as r_e. Fortunately there are several NIR wavelengths where condensed water has absorption bands. We can thus link clouds not only to the energy cycle (via $\overline{r^2}$) but also to the water cycle (via $\overline{r^3}$).

Absorption by cloud particles has important consequences for the solar radiation energy budget estimation as well as for satellite and ground-based remote sensing, particularly of cloud droplet size since, as previously noted, $1 - \varpi_0 = \sigma_a/\sigma$ scales as r_e. On a related note, the rapidly flat asymptotic behavior of $R(\tau)$ as $\tau \to \infty$ explains why opaque aerosol plumes composed of smoke from wild fires or volcanic ash are

a barely bluish shade of gray, and sometimes almost white, in spite of the tiny size of the particles. They may be Rayleigh-type scatterers, but they are also strongly absorbing; therefore, as in the case of clouds, multiple scattering quickly flattens the spectral behavior as opacity increases.

Since diffusion naturally delivers boundary fluxes and absorption rates, it is ideally suited for computation of the solar radiation budget. Beyond the version presented here explicitly, one can include the important dependence on solar zenith angle (SZA) cosine μ_0, which by definition varies over the globe, if the more sophisticated (direct/diffuse separated) version of the model is used. It is in fact the one used routinely in this task for GCM modeling, where it is known as the δ-Eddington model [70]. Unresolved spatial variability, however, remains a challenge in this application, to be discussed further on.

For remote sensing applications, one needs to go a step further and access the dependence on the viewing geometry. This geometry is captured by μ and $\phi - \phi_0$, the difference in azimuth between the (the so-called 'principal') plane, which contains the normal to the slab and the Sun and the observer's plane. In view of the sheer volume of remote sensing data, we would like to do this without reverting to numerical solutions of the full (multi-stream) 1D RTE. That is precisely the goal of 'asymptotic' RT theory. For a comprehensive survey of this modeling framework and numerous applications, we refer the interested reader to Kokhanovsky's recent review paper [81].

3.2. A new application for 1d RT: exploitation of the solar background in lidar

One person's noise is another person's signal. In this section, we will show two examples of how noise can be treated as a signal; the 'new' signal can be then used for reaping a new harvest of information on clouds. We target ground- and space-based lidars.

3.2.1. Ground-based micro-pulse lidar (MPL). MPL, developed in 1992 [86], is now widely used to retrieve heights of cloud layers and vertical distributions of aerosol [87]. Conventional lidar observation is predicated on 1D time-dependent RT in the single-scattering limit in the special case of scattering through 180°. A periodic train of laser pulses is transmitted into the vertical direction and the collocated receiver points in the same direction, with a FOV just big enough to contain, within tolerance, the slightly diverging transmitted beam. The MPL's time-dependent returned signal is proportional to the amount of light backscattered by atmospheric molecules, aerosols and clouds. Measured photon counts are converted into attenuated backscatter profiles. In this process, noise sources need to be accounted for [88, 89]. A significant source of noise present at all times is solar background light measured by the MPL detector in addition to backscattered laser light.

When lidars point straight up, the background noise is the diffusely transmitted sunlight in zenith radiance, which has been extensively used to retrieve cloud optical properties [90, 91]. However, the solar background signal is given in units
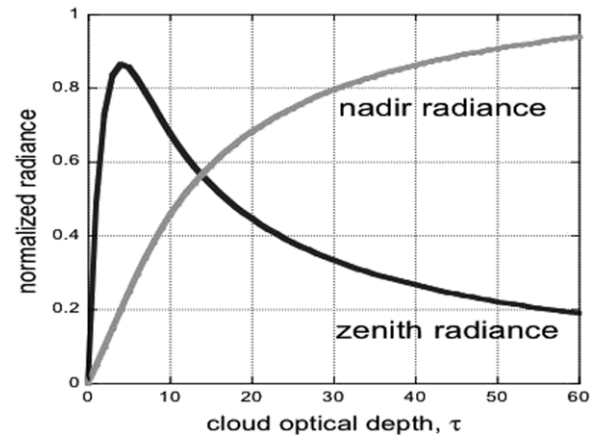

Figure 5. *Normalized zenith and nadir radiances versus cloud optical depth.* Calculations from the 1D DIScrete Ordinate RT (DISORT) code [82] for SZA = 60°. Surface is black and the C1 phase function, as specified by Garcia and Siewert [83], was used.

of photon counts and, for retrieval purposes, photon counts must be first converted to actual radiance. This can be done in a laboratory or using collocated measurements of zenith radiance. For MPL solar background calibration, we used a collocated multi-spectral photometer that tracks the Sun if not hidden by clouds in a narrow field-of-view (FOV). This is precisely what a standard Cimel instrument does for the AERONET (AErosol RObotic NETwork) [92]; it also provides zenith radiance either as part of its routine observations in the principal plane or in its 'cloud mode' [90].

After solar background calibration, we can translate measured zenith radiance to cloud optical depth τ. In contrast to nadir radiance, zenith radiance is not a one-to-one function of cloud optical depth; see figure 5. Two cloud optical depths give the same zenith radiance: one for thinner clouds, the other for thicker clouds. Thus, it is impossible to unambiguously retrieve cloud optical depth from solar background signal of a one-channel MPL. To remove this ambiguity, a rule is needed to distinguish thick from thin clouds. Chiu *et al* [84] proposed a reasonable criterion assuming that, if a lidar beam is completely attenuated, the detected clouds have the larger optical depth.

Figure 6 illustrates two hours of observations of the MPL at NASA's Goddard Space Flight Center (GSFC), Greenbelt, MD, on 29 October 2005. Calibrations of MPL solar background signals were conducted against one year of principal plane observations of the collocated AERONET Cimel. As we can see from the time series of vertical backscatter profile of MPL (panel 6(*a*)), there was a somewhat broken cloud field. To separate thin from thick clouds, it was assumed that clouds were thin if the returned signal was not completely attenuated. Figure 6(*b*) shows the time series of retrieved cloud optical depth. The retrieved values were validated against an AERONET Cimel operated in cloud mode [90, 93]. The mean cloud optical depths from MPL and Cimel are 41 and 44, respectively, and their correlation is around 0.86. Except for a few outliers, errors of retrievals from MPL are around 10–15% compared with those retrieved from Cimel.
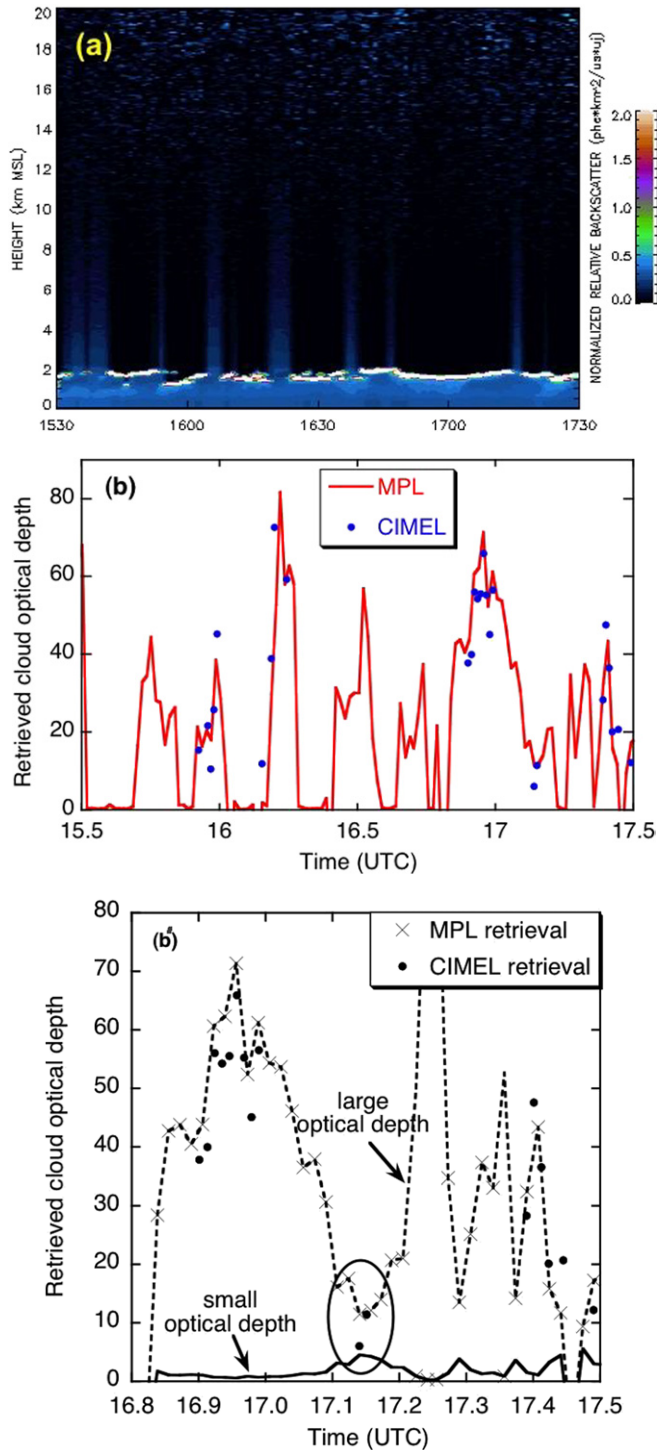
For certain radiance values, these two optical depths are substantially different and it is easy to remove any ambiguity using a 'returned' or 'not-returned' signal. For instance, when lidar pulses are completely attenuated (not-returned), the larger cloud optical depth is the obvious choice (e.g. 16.8–17.1 UTC). Conversely, when lidar pulses are not completely attenuated, the smaller optical depth is the clear solution (e.g. 17.25 UTC). The problem arises when both of these optical depths result in completely attenuated lidar pulses. In these cases, the margin of difference is too small to confidently determine which optical depth is the correct solution (cf circled data in figure 6(b')). As a result, τ values ranging approximately from 3 to 15 are hard to resolve. Retrieval of these intermediate optical depths may require further information, such as another lidar wavelength or additional sensors.

3.2.2. Space-based geoscience laser altimeter system (GLAS). As for the MPL, laser pulses transmitted from GLAS on board ICESat (Ice, Cloud and land Elevation Satellite) and other space-borne lidars can only penetrate clouds to a depth of a few MFPs. As a result, only optical depths of thinner clouds (less than ≈3 for GLAS) are retrieved reliably from the reflected lidar signal. We illustrate here possible retrievals of optical depth of thick clouds using solar background light by treating the GLAS receiver as a solar radiometer. As in the case with ground-based lidars, we first need to calibrate the reflected solar radiation received by the photon-counting detectors. The solar background radiation is regarded as a noise to be subtracted in the retrieval process of the lidar products.

Yang *et al* [85] recently used three calibration methods that agreed well with each other: (1) calibration with coincident airborne and GLAS observations; (2) calibration with coincident Geostationary Operational Environmental Satellite (GOES) and GLAS observations of deep convective clouds; (3) first-principles calibration, using the optical depths of thin water clouds over ocean readily retrieved by GLAS's active remote sensing. Cloud optical depth was also retrieved from the calibrated solar background signal using a one-to-one relationship similar to the one shown in figure 5, but for the known SZA.

To illustrate how passive remote sensing with GLAS complements its original active remote sensing, we use a thick marine Sc cloud observation. The Sc scene (figure 7(a)) was recorded by GLAS on 1 November 2003. The cloud deck is optically thick and the standard GLAS active remote sensing was unable to retrieve its optical depth. However, this information can be obtained using solar background signal. Figure 7(b) shows the retrieved cloud optical depth field. The signal physics are the same here as for the MPL. The problem of ambiguity in τ does not arise here, but the reflected radiance signal levels off for large τ and, moreover, the receiver can saturate. Although we do not in this case have independent validation data, we are confident the same retrieval accuracy can be achieved as for the MPL, at least for moderately opaque clouds.

Figure 6. *Ground-based MPL observations at NASA–GSFC.* (*a*) Time series of range-corrected vertical backscatter profiles. (*b*) Corresponding time series of cloud optical depths retrieved from MPL and Cimel (cloud mode). (*b′*) Same as the last third of panel (*b*), but co-plotted with the two possible optical depths that correspond to the same zenith radiance. Adapted from Chiu *et al* [84].

However, it is not always possible to separate thinner from thicker cloud. In figure 6(b') we have plotted together the two possible optical depths; the solid line corresponds to smaller optical depths and the dashed one to larger optical depths.
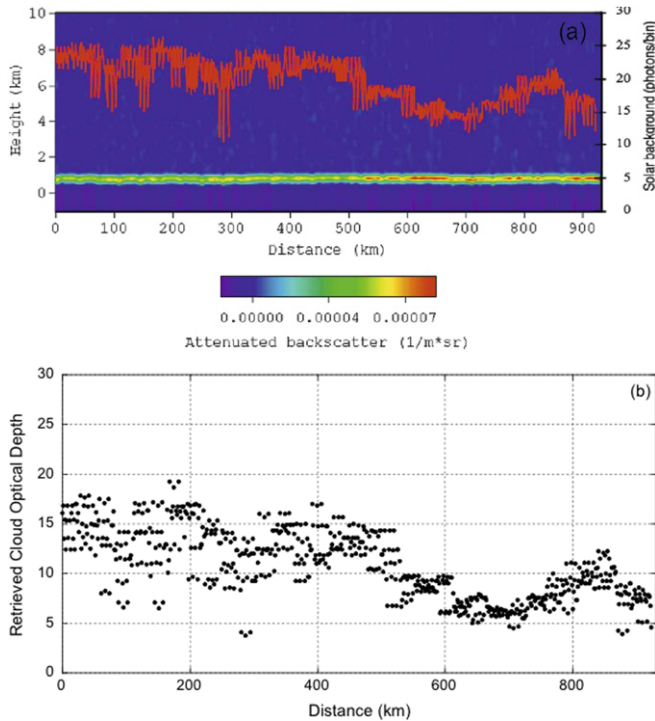
Figure 7. *GLAS observation of a thick marine stratocumulus deck over the southern Pacific Ocean*: the 1 November 2003, transect goes from 35.13°–43.29° S and 84.30°–85.80° W. (*a*) 0.532 μm backscattering image and the corresponding solar background photon counts in units of photons/bin; (*b*) cloud optical depth retrieved from the 0.532 μm solar background at 0.2 s resolution (1.4 km). Adapted from Yang *et al* [85].

3.3. The spherical cloud: a tractable problem in 3D radiation transport

So far, we have only used 1D RT taken either literally (in $d = 1$ space) or in the framework of slab geometry (in $d = 3$) when translational invariance prevails, i.e. the cloud is horizontally, if not completely, uniform. At the very least, this crude cloud model has brought us some physical insights. The resulting 1D RT may even be justifiably applied to the analysis of real-world clouds as long as they are in a single unbroken opaque layer, the essence of stratiform (St) cloud decks. However, we are compelled to address—hopefully by way of analytical computation—clouds that are at the opposite end of the gamut in outer geometry: clouds that, like cumulus (Cu), are finite in all three dimensions. For this class, we propose to use a spheroid as an archetype.

Other finite shapes have been investigated using both transport and diffusion theories: parallelepipeds-diffusion [94], parallelepipeds-transport [95, 96], truncated cylinders with vertical axis of rotation with diffusion [97], and probably others. However, in the diffusion framework, such shapes with sharp edges invariably lead to non-trivial problems where different eigenfunction expansions must be matched. Strangely overlooked in the literature, spheroids do not have this complication.

Davis [98] worked out the problem of diffusive radiation transport in optically thick non-absorbing spherical clouds under solar illumination properly distributed over one

hemisphere. Although the incoming solar flux is correctly modulated by the cosine of the angle between the local outgoing normal and the given direction of the Sun, this spatially varying flux is converted at the boundary into an isotropic source. This is in step with the boundary-source model used in a previous section for the plane-parallel slab. Although not very realistic for less than asymptotically large optical depths (thus reducing the thickness of the radiative boundary layer), it does allow the model to be solved in closed form. In the following, we outline the problem and compare its solution in the diffusion approximation with the golden standard of Monte Carlo (MC) implementation of the corresponding linear transport problem.

For a general optical medium defined by an open and convex set $M \subset \mathbb{R}^3$, with the closed boundary set ∂M, the slab-based BC in (37) expressing illumination by a collimated beam becomes

$$I(\boldsymbol{x}, \boldsymbol{\Omega}) = \begin{cases} F_0 \delta(\boldsymbol{\Omega} - \boldsymbol{\Omega}_0), & \boldsymbol{x} \in \partial M_R, \\ 0, & \boldsymbol{x} \in \partial M_T, \end{cases} \tag{76}$$

for all $\boldsymbol{x} \in \partial M$. This set has been partitioned as follows:

$$\begin{cases} \partial M_R = \{\boldsymbol{x} \in \partial M; \boldsymbol{\Omega}_0 \cdot \boldsymbol{n}(\boldsymbol{x}) \leqslant 0\}, \\ \partial M_T = \{\boldsymbol{x} \in \partial M; \boldsymbol{\Omega}_0 \cdot \boldsymbol{n}(\boldsymbol{x}) > 0\}, \end{cases} \tag{77}$$

where $\boldsymbol{n}(\boldsymbol{x})$ is the out-going normal to ∂M at $\boldsymbol{x}$. For an *isotropic* boundary source distributed over ∂M_R with the same overall solar flux intercepted by M, the right-hand side of the top line in (76) becomes $F_0 |\boldsymbol{\Omega}_0 \cdot \boldsymbol{n}(\boldsymbol{x})|/\pi$.

For convex media, ∂M_F ($F = R, T$) are two simply-connected sets. The choice of subscripts adopted here hints at the fact that radiation *escaping* M through ∂M_F contributes to reflection if $F = R$ and transmission if $F = T$. Note that this partition between reflection and transmission is based on *where* the radiation escapes, rather than *in what direction* it is heading. This distinction does not arise in slab geometry. In the present finite 3D geometry, this choice of definition has the advantage of separating topologically the cloud boundary into its 'sunny' and 'shady' sides. In the case of a spherical cloud, $M(r_c) = \{\boldsymbol{x} \in \mathbb{R}^3; \|x\| < r_c\}$, with $\boldsymbol{\Omega}_0 = +\hat{\boldsymbol{z}}$, we have

$$\begin{cases} \partial M_R(r_c) = \{\boldsymbol{x} \in \mathbb{R}^3; \|\boldsymbol{x}\| = r_c, z \leqslant 0\}, \\ \partial M_T(r_c) = \{\boldsymbol{x} \in \mathbb{R}^3; \|\boldsymbol{x}\| = r_c, z > 0\}. \end{cases}$$

The natural choice of coordinate system here is[7]

$$\boldsymbol{x} = (r \cos \vartheta, r \sin \vartheta \cos \varphi, r \sin \vartheta \sin \varphi)^{\mathrm{T}}.$$

For the simple diffusion model in a uniform sphere, with no volume sources or sinks (conservative scattering), the transport equation is simply $-\nabla^2 J = 0$, where $\nabla = (\partial_r, r\partial_\vartheta, 0)^{\mathrm{T}}$ in this axi-symmetric situation. The applicable Robin BCs for $J(r, \vartheta)$ on $\partial M(r_c) = \{\boldsymbol{x} \in \mathbb{R}^3; \|\boldsymbol{x}\| = r_c\}$ are

$$F_{\text{in}}(\vartheta) = \tfrac{1}{4}(1 + \chi \ell_t \partial_r) J|_{r=r_c}$$

$$= \begin{cases} F_0 |\cos \vartheta|, & \pi/2 \leqslant \vartheta \leqslant \pi, \\ 0, & 0 \leqslant \vartheta < \pi/2. \end{cases}$$

---

[7] Note the curly fonts used here to distinguish spatial from directional spherical coordinates.

The original paper [98] gives the derivation of the 0th and 1st coefficients in the natural expansion in (spatial) spherical harmonics:

$$J(r, \vartheta) = \sum_{l \geqslant 0} r^l P_l(\vartheta).$$

Those two are the only ones that matter for the out-going boundary fluxes

$$F_{\text{out}}(\vartheta) = \tfrac{1}{4}(1 - \chi \ell_t \partial_r) J|_{r=r_c} = J(r_c, \vartheta)/2,$$

if integrated over the sunny and shady hemispheres. Indeed, we are interested here in the transmission

$$T = \frac{1}{\pi r_c^2 F_0} \int_0^{\pi/2} F_{\text{out}}(\vartheta)\, dS(\vartheta), \tag{78}$$

where $dS(\vartheta) = 2\pi r_c^2 \sin(\vartheta)\, d\vartheta$ and, by conservation, cloud albedo $R = 1 - T$. This integral is easily done with spherical harmonics and leads to the simple result that

$$\frac{R}{T} = \frac{r_c}{\chi \ell_t} = \frac{(2r_c)/\ell_t}{2\chi}, \tag{79}$$

where the numerator can be interpreted as the scaled optical *diameter* of the sphere. Since we have $R + T = 1$ in this pure scattering case, we can solve for R and T as needed.

Figure 8 shows validation data for the above diffusion model obtained by implementing a MC solution of the corresponding problem in linear transport theory. More specifically, we solved the steady-state version of (8) in $M(r_c)$ with $\varpi_0 = 1$ and the H–G phase function in (33) for $g = 0$ and 0.85 using BCs in (76) for a collimated solar beam as well as the isotropic boundary source with the same flux (i.e. modulated by the *local* cosine of the SZA). We see that the two types of illumination converge to the same answer for spheres of large optical thickness. The diffusion-theoretical prediction for the ordinate, $(R/T)/(2r_c/\ell_t)$, is $1/2\chi$. This gives 3/4 for $\chi = 2/3$ but, due to our stated flexibility about χ, can fall in the range 0.70–0.86. The MC data support this prediction, particularly toward the low end (high χ).

The result in (79) is quite remarkable because, going back to (61)–(62) for the non-absorbing slab model, we find

$$\frac{R}{T} = \frac{(1-g)\tau}{2\chi} = \frac{H/\ell_t}{2\chi}, \tag{80}$$

which has precisely the same interpretation (since H is the 'diameter' of the slab).

This leads us to some minor speculation. Let us broaden the scope to non-absorbing ellipsoidal clouds $M(a, b, c) = \{x \in \mathbb{R}^3; (x/a)^2 + (y/b)^2 + (z/c)^2 < 1\}$ illuminated along the positive z-axis, but restrict ourselves to oblate cases, i.e. vertical aspect ratio $\min\{a, b\}/c \geqslant 1$. We already know that the cases $a = b = c = r_c$ and $c = H/2$ with $a = b = \infty$ lead to the same expression for R/T, namely, $c/\chi\ell_t$. Could it be the same answer for arbitrary a and b? (This is most easily verified in the case of infinite horizontal cylinders, where $b = \infty$ and $a = c = r_c$.) In other words, for isolated horizontally (as well as vertically) finite clouds, R/T depends linearly on
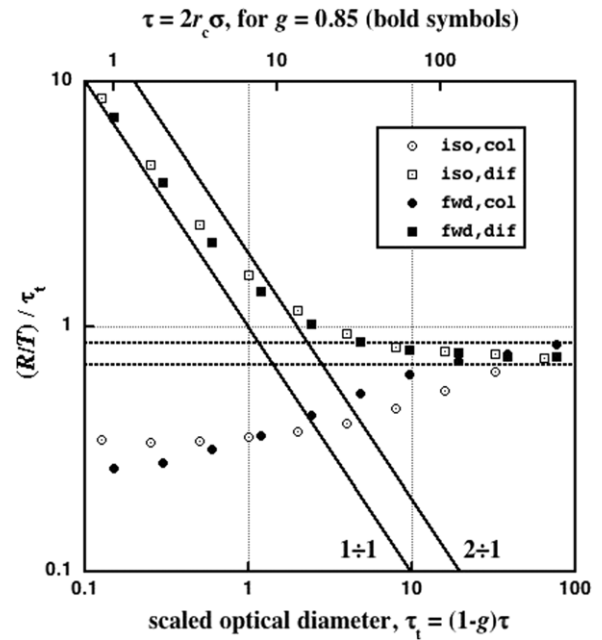

Figure 8. *Overall reflection/transmission ratio for conservatively scattering spherical clouds of varying optical thickness.* MC simulation results for the ratio R/T divided by the scaled optical diameter of the sphere, $\tau_t = 2(1 - g)\sigma r_c$, are plotted versus τ_t. The analytical diffusion model described in the main text predicts a constant value of $1/2\chi$. The possible range for this number is indicated (horizontal dashed lines) and it is validated by the MC-based computational linear transport, the usual standard of accuracy, for large τ_t, as expected. Both collimated and diffuse (but latitude-dependent) illumination was used and both isotropic (empty symbols) and H–G ($g = 0.85$, full symbols) phase functions were considered. The line for clouds with $R = T$ (1–1) and $R = 2T$ (2–1) is indicated by the (solid) diagonal lines, and the former gives the small-τ_t limit for diffuse illumination scenario. For the small τ_t with collimated illumination, a constant ratio is expected; for more detail; see Dickinson *et al* [75] recent study in single scattering.

the optical thickness of M but does not seem to depend on its aspect ratio. If so, we can exploit this result for a new (*inherently* 3D) concept in cloud remote sensing, as described further on (cf section 8.2.1).

4. Spatial and temporal Green functions

We are primarily interested in the relatively small subset of Green functions for boundary sources and boundary observers. Recalling that $\vec{\rho} = (x, y)^T$, we therefore take the unidirectional boundary-source function $I(t, \vec{\rho}, 0, \Omega)$, $\mu > 0$, for the RT problem to be as in (37) but with $F_0 = 1$ and concentrated in space and time with factors $\delta(t)$ and $\delta(\vec{\rho})$. For a normally incident pulsed laser beam, we furthermore take $\Omega_0 = \hat{z}$ ($\mu_0 = 1$). The spatial Green function for plane-parallel media, often described as the 'pencil-beam' problem, has attracted a lot of attention in RT, starting with Chandrasekhar [10] up to the present, as well as in neutron transport [99]. It is particularly challenging when $\mu_0 < 1$ [100], when scattering is anisotropic, and when $H < \infty$ [101]. Closed-form expressions for such transport-theoretical Green functions have been proposed as benchmarks for numerical 3D transport codes at large.

For a unitary isotropic point-source at the cloud boundary, also of interest here, we replace the $\delta(\mathbf{\Omega} - \mathbf{\Omega}_0)$ factor by $1/\pi$.

4.1. The diffusion PDE-based approach to space–time Green functions

When the space–time Green function of a uniform slab cloud is targeted, the simplest possible diffusion model—that based on an isotropic boundary source—is obtained by replacing $4F_0$ on the right-hand side side of (51) with $4\delta(t)\delta(\vec{\rho})$. We note that, even when the cloud is homogeneous, the Green function problem is inherently 3D because the source is concentrated at a single point.

We now take 2D Fourier-in-$\vec{\rho}$-space and Laplace-in-time transforms of the key diffusion-theoretical quantity $J(t, \boldsymbol{x})$, yielding

$$\tilde{J}(s, \vec{k}; z) = \int_0^\infty \mathrm{d}t \iint_{\mathbb{R}^2} \exp(-st + \mathrm{i}\vec{k} \cdot \vec{\rho})\, J(t, \vec{\rho}, z)\, \mathrm{d}\vec{\rho}(x, y) \tag{81}$$

and similarly for $\tilde{\boldsymbol{F}}(s, \vec{k}; z)$ from $\boldsymbol{F}(t, \boldsymbol{x})$. Note that we can now consider the Laplace and Fourier conjugates of time and position in the horizontal plane (s and $\vec{k}$, respectively) as parameters rather than independent variables, hence the position of the ';' separator.

The classic diffusion PDE in (29), where there are no absorption losses, then morphs into a Helmoltz-type ODE in the remaining spatial variable, z. Equivalently, combination of Fourier–Laplace transformed versions of (16) and (24) yields

$$-\frac{\mathrm{d}^2 \tilde{J}}{\mathrm{d}z^2} + 3\sigma_{\mathrm{t}}[\sigma_{\mathrm{a}} + \sigma_{\mathrm{a}}^{(\mathrm{e})}]\tilde{J} = 0. \tag{82}$$

This ODE is subject to boundary conditions

$$\left(1 - \frac{\chi}{\sigma_{\mathrm{t}}}\frac{\mathrm{d}}{\mathrm{d}z}\right)\tilde{J}\bigg|_{z=0} = 4, \qquad \left(1 + \frac{\chi}{\sigma_{\mathrm{t}}}\frac{\mathrm{d}}{\mathrm{d}z}\right)\tilde{J}\bigg|_{z=H} = 0, \tag{83}$$

from (44)–(45), after incorporating (24) with $\boldsymbol{q}_F(t, \boldsymbol{x}) \equiv 0$. We have defined here

$$\sigma_{\mathrm{a}}^{(\mathrm{e})}(s, k) = k^2/3\sigma_{\mathrm{t}} + s/c \tag{84}$$

as an *effective* absorption coefficient that combines, as needed, with the true absorption coefficient in (82). Variation in time as well as horizontal fluxes indeed act like an absorption process in the transport of radiation along the vertical axis. So much so that the expressions in (69)–(70), respectively, for reflectivity and transitivity can be used here for $\tilde{R}(s, k)$ and $\tilde{T}(s, k)$. We must, however, redefine $(1 - \varpi_0)$ as $[\sigma_{\mathrm{a}} + \sigma_{\mathrm{a}}^{(\mathrm{e})}(s, k)]/\sigma$, and retain σ_{t} as $(1 - g)\sigma + \sigma_{\mathrm{a}}$, with no impact from the pseudo-absorption; in particular, if $\sigma_{\mathrm{a}} = 0$, we take ϖ_0 as unity whenever it multiplies g.

Can the resulting expressions for $\tilde{R}(s, k)$ and $\tilde{T}(s, k)$ be *inverse* Fourier–Laplace transformed explicitly? We have not succeeded ... unless, following Zege *et al* [102], we enlarge the domain and modify the Robin BCs in (83) to look like Dirichlet BCs:

$$\tilde{J}(-\chi/\sigma_{\mathrm{t}}) = 4, \qquad \tilde{J}(H + \chi/\sigma_{\mathrm{t}}) = 0, \tag{85}$$

which gives real meaning to the expression 'extrapolation length' for χ/σ_{t}. This approximate radiation diffusion theory leads to boundary-flux Green function expressions that can be Taylor-expanded into series of exponential functions with constant coefficients. An immediate benefit is that these can be Fourier–Laplace inverse-transformed term-by-term. The resulting space–time expressions as infinite sums are, however, slow to converge at large (ct, ρ). Fortunately, this situation can be reversed by using the Poisson sum-rule [59, 103, and references therein].

In the end, the space–time Green function is a spatial Gaussian at any fixed time, and time-dependence is a sum of exponential terms. Having explicit formulae for the Green functions enables the determination of far-field behavior for the marginal (space *or* time) Green functions, which turns out to be exponential on both accounts. The spatial Green function is thus $\sim \exp(-\rho/\rho^\star)$ as $\rho \to \infty$ and the characteristic horizontal transport distance is

$$\rho^\star = H/\pi R(\tau_{\mathrm{t}}), \tag{86}$$

where $\tau_{\mathrm{t}} = (1 - g)\tau$ and $R(\tau_{\mathrm{t}})$ is the two-stream estimate of cloud albedo in (61). The time-domain Green function is $\sim \exp(-ct/ct^\star)$ as $ct \to \infty$, where the e-folding path length is

$$ct^\star = \frac{3}{\pi^2} \times H \times \frac{\tau_{\mathrm{t}}}{R(\tau_{\mathrm{t}})^2}. \tag{87}$$

Coming from a model with strict similarity, i.e. solutions depending only on the combination of cloud properties in $(1 - g)\tau$, we can verify that $(\rho^\star)^2/ct^\star = H/3\tau_{\mathrm{t}} = D/c$ from (26).

Returning to the more accurate Robin BCs in (83), the lack of closed-form inverse transforms is not an impediment; quite the contrary, if the goal is to obtain expressions for the spatial or temporal moments of the Green function. The formal definition of the spatial moment of prime interest is

$$\langle \rho^2 \rangle_F = \frac{1}{F}\int_0^\infty \mathrm{d}t \iint_{\mathbb{R}^2} \rho^2 F(t, \vec{\rho})\, \mathrm{d}\vec{\rho}(x, y), \tag{88}$$

for $F = R, T$, where

$$F = \int_0^\infty \mathrm{d}t \iint_{\mathbb{R}^2} F(t, \vec{\rho})\, \mathrm{d}\vec{\rho}(x, y). \tag{89}$$

Temporal moments are defined similarly as

$$\langle t^q \rangle_F = \frac{1}{F}\int_0^\infty t^q \mathrm{d}t \iint_{\mathbb{R}^2} F(t, \vec{\rho})\, \mathrm{d}\vec{\rho}(x, y) \tag{90}$$

with $q = 1, 2$ or more, again for $F = R, T$.

Characteristic function theory from probability (see, e.g. Feller's treatise [104]) tells us how to obtain spatial or temporal moments from the successive derivatives of $\tilde{R}(s, k)$ or $\tilde{T}(s, k)$ with respect to s or k at the origin:

$$\langle \rho^2 \rangle_F = \frac{-2}{F}\frac{\partial^2 \tilde{F}}{\partial k^2}\bigg|_{s=0, k=0} \tag{91}$$

22

for the horizontal transport away from the point-source, and

$$\langle t^q \rangle_F = \frac{1}{F} \left(-\frac{\partial}{\partial s} \right)^q \tilde{F} \Big|_{s=0, k=0} \qquad (92)$$

for time. These last quantities describe how the incoming short pulse is stretched in the responses of the scattering medium; in particular, we can determine how the variance of the transit time, $\langle t^2 \rangle_F - \langle t \rangle_F^2$, varies with cloud parameters.

We can apply the above recipes for estimating spatial and temporal moments to the fluxes obtained in the diffusion limit, namely, (69)–(70). In the absence of true absorption, we only need to use

$$L_d^{(e)}(s,k) = 1/\sqrt{3\sigma_t \sigma_a^{(e)}(s,k)} \qquad (93)$$

when it appears in X and Y, in ratio with the extrapolation length ℓ_t and the slab thickness H, respectively, in the ancillary definitions (71)–(72).

Following Davis *et al* [105], we start with (69). This basic diffusion model predicts the following dependences of reflected Green function moments on the properties of conservatively scattering clouds:

$$\langle \rho^2 \rangle_R = \frac{8\chi}{3} \frac{1}{\tau_t} \times H^2 \times [1 + C_{R,\rho}^{(2)}(\tau_t/2\chi)], \qquad (94)$$

$$\langle ct \rangle_R = 2\chi \times H \times [1 + C_{R,ct}^{(1)}(\tau_t/2\chi)], \qquad (95)$$

$$\langle (ct)^2 \rangle_R = \frac{4\chi}{5} \tau_t \times H^2 \times [1 + C_{R,ct}^{(2)}(\tau_t/2\chi)], \qquad (96)$$

where we have highlighted the asymptotic (large τ_t) trends. The pre-asymptotic correction terms are given by

$$C_{R,\rho}^{(2)}(Z) = C_{R,ct}^{(1)}(Z) = \frac{Z + 3/2}{2Z(Z+1)},$$

$$C_{R,ct}^{(2)}(Z) = \frac{8Z^3 + 41Z^2/2 + 75Z/4 + 1/8}{2Z^2(Z+1)^2},$$

where, as in (79), we define

$$Z = R/T = \tau_t/2\chi. \qquad (97)$$

Time is recast here as the effective path length ct that the light has accumulated by random scattering in the medium, from emission to escape.

Similarly, following Davis and Marshak [106], we apply (91) and (92) to (70) with all ancillary definitions, and obtain

$$\langle \rho^2 \rangle_T = \frac{2}{3} \times H^2 \times [1 + C_{T,\rho}^{(2)}(\tau_t/2\chi)], \qquad (98)$$

$$\langle ct \rangle_T = \frac{1}{2} \tau_t \times H \times [1 + C_{T,ct}^{(1)}(\tau_t/2\chi)], \qquad (99)$$

$$\langle (ct)^2 \rangle_T = \frac{7}{20} \tau_t^2 \times H^2 \times [1 + C_{T,ct}^{(2)}(\tau_t/2\chi)], \qquad (100)$$

where

$$C_{T,\rho}^{(2)}(Z) = C_{T,ct}^{(1)}(Z) = \frac{4Z + 3}{2Z(Z+1)},$$

$$C_{T,ct}^{(2)}(Z) = \frac{56Z^3 + (166Z^2 + 15(10Z + 3))}{14Z^2(Z+1)^2}.$$

A striking difference between the above expressions for T-moments and their counterparts for R-moments in (94)–(96)
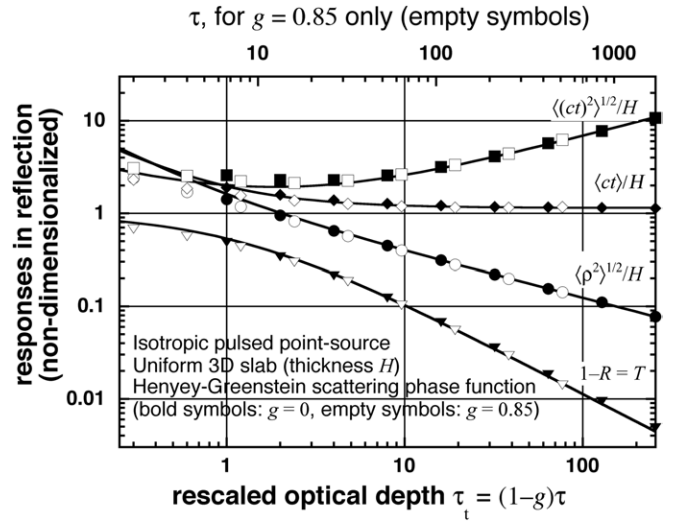

Figure 9. *Cloud responses to a pulsed isotropic point-source in reflection.* Diffusion predictions from (95)–(94), with correction terms, for moments and (61) for R, via $T = 1 - R$, are in solid lines; MC validation data are plotted with symbols. The best overall fit was obtained for $\chi = 1/\sqrt{3} \approx 0.58$. Adapted from [105].

is that the extrapolation length parameter χ has disappeared from the dominant terms. Recall that χ is a weak link in diffusion theory used to best capture radiative boundary-layer effects in the diffusion solution, by theoretical or numerical comparison with the full RT solution. There are obviously radiative boundary layers on both sides of the cloud where the transport regime goes from diffusing to streaming. However, the near-source/reflective side of an optically thick cloud is dominated by radiation that has suffered only a few scatterings (as little as a single one). So it is not surprising to see the signature parameter χ, used for boundary-layer control, play an important role in reflected light characteristics, but not in those of transmitted light.

Figures 9 and 10 illustrate the spatial and temporal moments of the reflected and transmitted Green functions respectively, for the simplest (isotropic boundary point-source) diffusion problem. Explicit expressions are in (94)–(96) for R-moments and (98)–(100) for T-moments; we also plot the normalized flux $T = 1 - R$ from (62). All the moments are normalized by cloud thickness H taken to the appropriate power; then the square-root of the second-order moments is computed, thus producing root-mean-square (RMS) statistics. These non-dimensionalized quantities are plotted against scaled optical depth $(1 - g)\tau$, which is characteristic of diffusion theory. Spatial and temporal moments estimated in the course of MC simulations of the corresponding RT problems, assuming both isotropic and $g = 0.85$ Henyey–Greenstein (33) phase functions, are also plotted. The MC runs provide validation data for the diffusion model since they result from a higher-level model.

The isotropic boundary point-source model is not very realistic for representing either localized laser beams (typically at normal incidence) or the uniform solar beam (typically at some oblique incidence). Nor is the assumption of a homogeneous cloud in view of the well-known tendency of
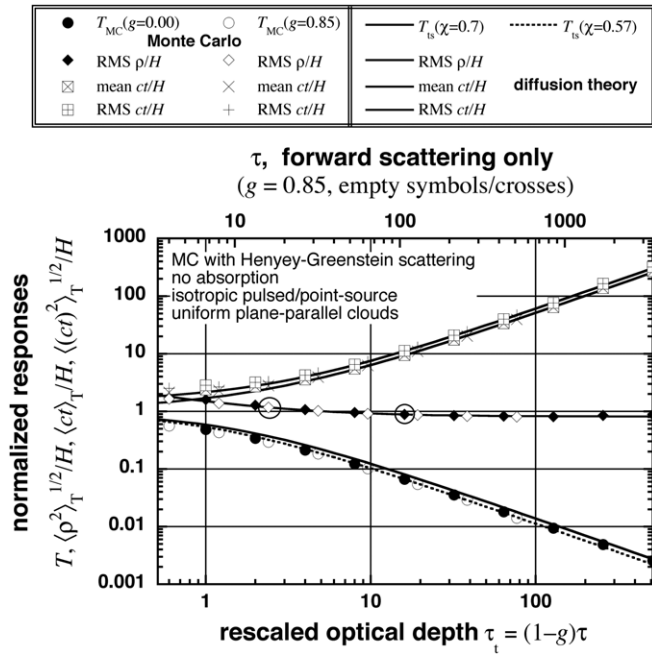
Figure 10. *Cloud responses to a pulsed isotropic point-source in transmission.* Diffusion predictions from (98)–(100), with correction terms, for moments and (62) for T are in solid lines; MC validation data are plotted with symbols (two values of χ used to reproduce the MC benchmarks). Adapted from [106].

stratiform clouds to develop robust internal gradients in LWC, hence in extinction σ from (67). Moreover, this cloud-scale stratification is overlaid in most clouds with significant random 3D fluctuations due to their inherent turbulence.

All of these limitations of the above transport model can be removed without leaving the framework of diffusion theory, and still leading to closed-form expressions at least for the spatial and temporal moments. We highlight one particularly simple approach for the small-scale random fluctuations in section 5.1.1. For further improvements, the interested reader is referred to the recent paper by Davis [107] for reflected light. The same enhancements are extended from reflected light to transmitted light by Davis *et al* [108]. Expressions therein are useful, but not simple.

4.2. New opportunities in cloud remote sensing

Apart from the high accuracy of the diffusion-based predictions for $\tau_t = (1-g)\tau \gtrsim 1$, the remarkable fact about figures 9 and 10 is that, in both cases, different space and time moments scale differently. This is very good news for cloud remote sensing using somehow observed Green functions, as discussed further on; indeed, given observed values for any two moments, one can estimate the two cloud properties H and τ, recalling that g hardly varies in nature (at least for liquid clouds [56]). The above-mentioned modeling refinements for laser-beam source representation as well as internal stratification and random fluctuations of extinction do not change these qualitative statements based on the asymptotic behavior of (94)–(100) visible in the associated figures 9–10.

There are many other ways of obtaining cloud optical depth τ that are already operational. For instance, in section 3.2

the level of solar background noise in lidar systems was exploited, just by treating the receiver as a basic narrow FOV radiometer. In essence, this technique consists in solving (61) for τ given R or (62) given T. We therefore extend the list of possible 'observables' by including the spatially and temporally integrated fluxes in (89), also plotted in the figures. In contrast, there are very few existing ways of obtaining physical cloud thickness H. The best is probably to use millimeter-wave cloud radar (MMCR), which is now available from many ground-based stations world-wide as well as from space (presently, only NASA's CloudSat mission, but more will come). This is the advanced active single-scattering technology for clouds that are too opaque in the visible/near-IR (VNIR) for thin-cloud/aerosol penetrating lidar; moreover, the backscattering follows Rayleigh's law since droplets are $\ll \lambda$. As powerful as MMCR has proven, it does not always work as originally planned; in particular, insects and even a light drizzle can saturate the dynamic range of an MMCR [109]. Even when it does work, it is not straightforward to translate the MMCR reflectivity, basically the droplet density $\times \overline{r^6}$ from (2), into VNIR-TIR cloud information that matters for the climate.

We also note that, for all the observational possibilities in (88)–(90), there are very different calibration requirements. Indeed, the normalization of F by F_0 in, e.g. (52)–(53), reminds us that these responses for steady and uniform illumination can be measured only if the radiometers have absolute calibration, which is notoriously difficult to establish and maintain with high precision. In contrast, the ratios in the moments *per se* (88) and (90) make their observation immune to unknown multiplicative constants in the fluxes, i.e. absolute calibration error.

An interesting difference between the plots for reflected light (figure 9) and its counterpart for transmitted light (figure 10) is that the mean and RMS values for path ct are closely related in T but diverge in R as $(1-g)\tau$ increases without bound. This is much better news for the observation of clouds in reflection than in transmission. It indeed turns out that $\sqrt{\langle t^2 \rangle_F}/\langle t \rangle_F$ is almost constant when $F = T$, but when $F = R$ it increases with τ. So, with access *only* to time-domain observations of *reflected* light, one can in principle infer both τ and H, still without any need for calibration.

A straightforward instrumental implementation of space–time RT Green function observation, potentially leading to Green function moment estimation, uses pulsed lasers [110, 111]. In this case, the receiver is very near the transmitter, at any rate, on the same side of the cloud; so the relevant moments are the $\langle \cdots \rangle_R$'s. Whether or not these moments are estimated explicitly with the field data, the above cloud information content analysis proves correct.

Reliance on the expensive technology of pulsed lasers is not strictly necessary to access time-domain observables such as $\langle t^q \rangle_F$. We will show in section 8 how in fact both spatial and temporal information can be determined even using a steady and uniform source such as the Sun. In this case, reflected quantities are obtained from airborne and space-based sensors, and transmitted ones from ground-based sensors.

4.3. The random-walk scaling approach to space–time Green functions

We have so far used a PDE-based theory of radiation diffusion to compute multiple-scattering Green functions, and we have systematically used MC simulation to validate numerically that RT approximation leading to convenient closed-form results. It is informative to go to the other extreme of this hierarchy in Green function models and perform a highly simplified version of MC simulation analytically, namely, estimate statistical properties of random (a.k.a. drunkard's) walks. This approach reveals the physical essence of the problem of transport in dense clouds. Specifically, one can derive the scaling exponents of $\tau_t = (1 - g)\tau$ in all the dominant terms of the Green function moments, cf (94)–(96) and figure 9 for reflected light, (98)–(100) and figure 10 for transmitted light. The same exponents appear in all other spatial or temporal moment estimations based on more sophisticated representations of the cloudy medium or the source term [107, 108]; in other words, the refinements affect only scaling prefactors and pre-asymptotic corrections.

We note first that the key cloud parameter in diffusion theory, τ_t, is the ratio of the only two scales that matter in random walks:

- H, the outer scale (size of the domain bounding the stochastic process);
- ℓ_t, the inner scale (MFP for effectively isotropic scattering).

The latter defines diffusivity, namely, $D = c\ell_t/d$ in d spatial dimensions.

4.3.1. Caveat about photons as 'particles' of light.
The term 'photon' was coined by Gilbert Lewis in 1926 to describe the quantum of the electromagnetic field, of which light is a prime example. Even if second quantification assigns energy $h\nu$, momentum h/λ and spin $\pm h$ to photons, it is fundamentally incorrect to think of them as either classic or quantic particles traveling through space–time at velocity c. For instance, by any definition, it is not the same photon (EM field excitation) that is incident and re-emitted by a scattering entity. Photons can populate energy levels in, e.g. thermal sources and laser cavities; they can also be detected using materials such as silicon endowed with photo-electronic responsivity. In between, it is light—not photons—that propagates in optical media according to the laws of RT theory, which is a non-trivial construct from *statistical* optics in a classic framework [49]. The radiance field predicted by the RTE, and associated boundary conditions, is only a probability of detecting a photon (per photon emitted at the source) with a roaming virtual instrument.

In MC computation, it is very tempting to talk about the 'photons' launched in a simulation. This should be avoided, proper terminology is 'histories' or 'trajectories' or 'realizations' or even 'Monte Carlo particles.' Recall that MC is only a random quadrature approach for estimating functionals, integrals over high-dimensional radiance fields. The random-walk theory presented here is basically a poor person's MC, with only some basic results from probability

theory to work with. So, although strongly reminiscent of wandering particles, we are dealing with light intensities, to be interpreted strictly as probability densities for detection events. Only at that point can one talk about photons and, more correctly, photo-electrons.

4.3.2. Elements of Brownian motion theory.
In boundary-free homogeneous 3D space, an isotropic source at $r = 0$ emits a diffusing 'wavefront' of particles propagating at a decreasing 'velocity' such that the mean distance from the origin, $\approx\sqrt{\langle r^2\rangle}$, grows only as $\sqrt{Dt}$. This is a classic reading of the famous law of diffusion

$$\langle r^2\rangle = 6Dt, \qquad (101)$$

in unbounded 3D space, which results directly from the well-known Green function for diffusion in three spatial dimensions: $n(t, r) = e^{-r^2/4Dt}/(4\pi Dt)^{3/2}$, itself the solution of $\partial_t n = \nabla^2 n$ for $t > 0$ when $n(0, r) = \delta(r)$.

In the statistical physics of Brownian motion, a lesser known but extremely useful result is the 'law of first returns' [112]. Focusing, for simplicity, on 1D random walks (where $D = c\ell_t$) along the z-axis, we seek the PDF of $t > 0$, the random epoch at which the coordinate of the Brownian particle (that left $z = 0$ at $t = 0$) first changes sign. It can be shown [113, 104] that

$$\Pr\{t, dt\} = \frac{c}{\sqrt{\pi}\ell_t}\left(\frac{\ell_t}{ct}\right)^{3/2} e^{-\ell_t/2ct} dt \sim \frac{dt}{t^{3/2}}, \qquad (102)$$

if we acknowledge, then ignore, the exponential cut-off at early times. This is an interesting PDF associated with the gambler's ruin problem: How long does it take a person who comes to the roulette table with \$1, and always bets 'red,' \$1 at a time, to walk away with nothing? There is actually no mean for this duration—it is divergent—and that may go a long way in explaining why gambling is addictive, and accordingly why casinos are open 24/7. Indeed, before losing everything in time with probability one (even the initial \$1) to this casino with an infinite bank, gains can be considerable—and last a correspondingly long time—for a significant number of players.

The corresponding RT problem is that of reflection from a semi-infinite ($H \to \infty$) non-absorbing medium, where $\langle ct\rangle_R$ is indeed infinite; this follows from (95) since the ratio $\langle ct\rangle_R/H$ becomes insensitive to scaled optical thickness τ_t. Alternatively, one can consider the ratio $\langle ct\rangle_R/\ell_t$ that will increase as $\tau_t = H/\ell_t$ when the transport MFP ℓ_t is held constant. Higher-order moments follow suite at even faster rates. Fractional-order moments of order $q < 1/2$ are, however, finite.

4.3.3. Transmitted light.
Now $r^2 = x^2 + y^2 + z^2$ and, by symmetry, all three components are equal in magnitude on average, at least in unbounded diffusion. Therefore, since $z = H$ whenever a transmission event occurs, $\rho^2 = x^2 + y^2 \approx (2/3)H^2$. This concurs with the expression in (98) for $\langle \rho^2\rangle_T$: it is asymptotically invariant with respect to τ_t, and the prefactor is correctly predicted.

Furthermore, when the bulk of the diffusing wavefront reaches the opposite boundary, we will be detecting the transmitted Green function at full strength. We can estimate this epoch by setting $\langle r^2 \rangle \approx (2/3)H^2$ in (101), hence $t \approx (2/3)H^2/6D = H^2/3c\ell_t = (H/c) \times \tau_t/3$. In other words, reinterpreting t as a random variable, we anticipate that $\langle ct \rangle_T/H \approx \tau_t/3$. This confirms the expectation in (99) based on 'exact' (PDE-based) diffusion theory, as illustrated in figure 10, for the scaling exponent if not the prefactor.

There is no simple argument for the scaling of the 2nd-order moment in time, also plotted in figure 10. The fact that it goes as $\langle ct \rangle_T^2$ tells us that the distribution of arrival times at the boundary opposite the source of diffusing particles is relatively narrow.

It is interesting that we can estimate at least the scaling of Green function moments in transmission without knowledge of the overall probability of transmission T. This is the theoretical equivalent of the above-stated instrumental fact that we do not need calibrated radiometry to derive moment-based observables of cloud Green functions. To derive the scaling of T with τ_t calls for the law of first returns in (102). Real clouds have finite physical and optical thicknesses, and real casinos have *finite* banks. We can approximate the probability of transmission—the 'always red' gambler breaks the casino's bank—by truncating the PDF in (102) at the characteristic transit time $\langle t \rangle_T \sim H^2/c\ell_t$ it takes for light from the pulse to be transmitted. This leads to

$$ T \approx \Pr\{t > \langle t \rangle_T\} = \int_{\langle t \rangle_T}^{\infty} \Pr\{t, \mathrm{d}t\} \sim \ell_t/H, \qquad (103) $$

i.e. the asymptotic behavior $T(\tau_t) \sim 1/\tau_t$ in (62), clearly visible in the corresponding curve in figure 10.

4.3.4. Reflected light. Temporal/path moments for reflected light can also be estimated for a finite diffusion domain, namely, $0 < z < H$, by defining a *truncated* (and, in principle, renormalized) version of the PDF in (102) for the first-return process. Allowing time for the particle to return to $z = 0$ after wandering deep into the medium (i.e. almost being transmitted at $z = H$), we compute specifically

$$ I_q = \int_0^{2\langle t \rangle_T} t^q \Pr\{t, \mathrm{d}t\}, \quad \text{hence} $$

$$ \langle t^q \rangle_R \approx \frac{I_q}{I_0} \sim \left(\frac{\ell_t}{c} \right)^{1/2} \left(\frac{H}{c\ell_t} \right)^{q-1/2}, \qquad (104) $$

where we have neglected the difference between I_0 and unity, namely, T in (103). Recalling once more that $H/\ell_t = \tau_t$, this leads to $\langle (ct)^q \rangle_R^{1/q} \sim H \times (\tau_t)^{1-1/q}$, as was found in the limit $\tau_t \to \infty$ in (95)–(96).

As previously noticed, it is remarkable that the moments $\langle (ct)^q \rangle_R$ all scale differently with τ_t whereas we fully expect that $\langle (ct)^q \rangle_T \sim \langle ct \rangle_T^q$, for $q \geqslant 2$. From the vantage of this random-walk approach to diffusion theory, we can trace this property to the mixture, made clear in (104), of short and long paths ct in reflected light. In RT language, this translates to reflected light being a relatively balanced mixture of light scattered both few and many times.

As we did for the spatial Green function in transmission, we can roughly estimate the RMS value of ρ for reflection from (101), with $D \sim c\ell_t$ and (104) for $q = 1$. We obtain $\langle \rho^2 \rangle_R \sim D\langle ct \rangle_R \sim H\ell_t$. In other words, the RMS ρ for reflected light goes as the harmonic mean of ℓ_t and H, the inner and outer scales of the diffusion problem at hand, which is just another reading of the dominant term in (94).

5. Realistic (3D) versus operational (1D) cloud RT

The atmospheric radiation communities engaged in both cloud remote sensing and energy cycling by clouds are, to this day, heavily invested in the plane-parallel slab representation of clouds, at least in operational settings where efficiency and/or simplicity are desirable in order to expedite frequent routine computations. This is irrespective of the pixel scale, which range from approximately tens of meters to approximately tens of kilometers, or of the grid scale of the dynamical model, which also range from approximately tens of meters in Large-Eddy Simulation (LES) models to ~100 km (and decreasing) in GCMs. So, in spite of decades of research into 3D RT effects, 1D RT models are still an unavoidable point of comparison.

Scale-by-scale variability analysis is key to 3D RT because it can be used to determine what processes need to be considered. So is the question of resolved versus unresolved spatial variability, be it in observations or in computations. Indeed the latter distinction, as artificial as it is, determines what kind of 3D RT solution should be explored. In the following, we examine both situations and, for each one, discuss illustrative methods that address the fundamental issues at hand.

5.1. Dealing with unresolved random fluctuations

If there are significant spatial fluctuations of optical properties at scales that are sub-pixel or sub-gridscale, then it is important to assess their effect on the RT. This assessment is necessarily probabilistic since, by definition, detailed structure is not given; a (usually small) number of statistical properties are of course given. Accordingly, only domain-average radiative properties are required of the RT model.

There are three broad classes of solution to this problem. On the one hand, one can figure out a way of modifying the given (typically, mean) optical properties in such a way that the new values can be used in a standard 1D RT model and yet deliver an accurate answer for the domain-average properties of interest. This is the 'effective medium' or 'homogenization' approach. On the other hand, one can maybe derive a mean-field theory for the RT at the scale of the domain and this may lead to new transport equations calling, in general, for new solution techniques. Between these two extremes, there is the so-called independent pixel/column approximation where multiple 1D RT computations are performed and their outcome is averaged over the variability of the input parameters; typically, cloud optical depth is varied.

We now illustrate each of these three approaches with two or three examples each, one more detailed than the other(s);

we also refer the interested reader to a more extensive survey by Barker and Davis [114].

5.1.1. Homogenization. Computationally speaking, the best way of accounting for 3D RT is to reduce it to a single 1D RT problem. That is the lofty goal of homogenization (a.k.a. effective medium) theory. As a first example of this ideal approach to the capture of unresolved spatial variability effects in a standard (typically, 1D) RT model, we mention Cahalan's [115] 'effective thickness approximation' (ETA). Therein a single 1D RT computation for cloud reflectivity can closely follow the prediction for the domain average of a detailed independent pixel approximation (see section 5.1.2 below) estimate for the bounded cascade model (see section 5.2.1 below); that stochastic model for horizontal cloud variability has a realistic lognormal-like PDF. The recipe is simple: replace the spatial mean optical depth $\overline{\tau}$ by $\eta\overline{\tau}$, where η is given by $\exp(\overline{\log \tau})/\overline{\tau}$, which is <1. This is a direct consequence of Jensen's inequality [116] in probability theory concerning averages of functions with definite convexity (in this case, the exponential). The η factor can be expressed approximately but conveniently with the parameters of the bounded cascade model. Thus recentered around the log-mode of the PDF, the variance has a minimal effect on the average over $R(\tau)$, which is highly nonlinear of the range of interest in the random variable τ. The ETA was soon adopted by some GCM modelers [117], and this helped them reconcile the prognostic cloud optical thickness from the hydrology cycle with what was needed to produce a realistic albedo in the stratocumulus regions.

As a second example, we describe the rescaling solution elaborated by Cairns *et al* in the years leading up to their 2000 paper [118]. Cairns' interesting effective medium theory draws on statistical physics and renormalization. It leads to

$$\sigma' = (1 - \epsilon)\overline{\sigma},$$

$$1 - \varpi_0' = \left[1 - \varpi_0\left(\frac{\epsilon}{1-\epsilon}\right)\right](1 - \varpi_0),$$

$$1 - \varpi_0'g' = \left[1 - \varpi_0\left(\frac{\epsilon}{1-\epsilon}\right)\right](1 - \varpi_0 g). \tag{105}$$

The new parameter for the unresolved variability is ϵ and $\overline{\sigma}$ is the average extinction over the presumably large region of interest. We see that $1/(1 + \varpi_0) \leqslant 1/2$ is a strict upper limit for ϵ; it is probably best to not approach this limit too closely in practice, especially not in diffusion modeling, because the rescaled g approaches unity (hence no actual scattering out of the incident beam). The δ-rescaling in (31), which improves the scattering phase function model in diffusion theory, leaves the product $(1 - \varpi_0 g)\sigma$ invariant; here it decreases both through σ and through $1 - \varpi_0 g$ as ϵ increases (since $g' > g$). For diffusion models with strict similarity, i.e. dependent only on $\sigma_t = (1 - \varpi_0 g)\sigma$, we have

$$\sigma_t' \approx (1 - 2\epsilon)\overline{\sigma}_t \tag{106}$$

when scattering is conservative or almost ($\varpi_0 \approx 1$). So the prediction is that the small-scale random internal variability

of clouds that Cairns and co-authors renormalized away have the net effect of reducing the (transport) extinction, hence the associated optical depth. This will in turn increase cloud transmittance and decrease reflectance.

We will see that *enhanced transmission and reduced reflection by clouds are robust predictions of all 3D RT models* under the assumption of a *fixed mean optical depth*. In this case, we have a fixed volume integral, hence mean value, of σ.

How does one obtain ϵ? Rossow *et al* [119] took an empirical approach using the database of the International Satellite Cloud Climatology Project (ISCCP, http://isccp.giss.nasa.gov) [120, and references therein] to examine the statistical relationships between inferred cloud optical depths at the small scale of satellite pixels and the radiances at larger scales typical of GCMs.

However, ϵ can also be computed from first principles. Recalling that overscores denote averages over the spatial variability, Cairns *et al* show specifically that the ensemble-average effects moderate-amplitude fluctuations on the 3D RTE are captured with

$$\epsilon = a - \sqrt{a^2 - v^2}, \tag{107}$$

where

$$v = \sqrt{\frac{\overline{\sigma^2}}{\overline{\sigma}^2} - 1} \qquad \text{and} \qquad a = \frac{1}{2}\left(1 + \frac{1}{\overline{\sigma} l_c}\right). \tag{108}$$

Parameter v is the standard-deviation-to-mean ratio, itself expressed with the RMS-to-mean ratio, for σ and we denote here the characteristic correlation scale of the spatial variability by l_c. We see that

- for small-scale fluctuations (i.e. when $l_c \ll$ transport MFP $\approx 1/\overline{\sigma}$), we anticipate little effect since $\epsilon \approx (v/a)^2/2 \lll 1$ (irrespective of v) as a becomes very large;
- for fluctuations at larger scales (i.e. when $\overline{\sigma} l_c \gtrsim 1$), we can have a strong impact ($\epsilon \lesssim 1/2$) although this scenario clearly stretches the validity of the model, in particular, amplitude is then limited to cases where $v^2 \lesssim a - 1/4$, hence $\overline{\sigma^2}/\overline{\sigma}^2 \lesssim 5/4 + 1/\overline{\sigma} l_c$;
- for fluctuations at the largest scales ($\overline{\sigma} l_c \gg 1$, hence $a \approx 1/2$ and $v \lesssim 1/2$), one should average over macroscale responses rather than try to find a single effective medium to account for micro-scale variability effects.

Figure 11 illustrates this analysis of ϵ. In the last ('slow') variability regime, the large-scale averaging of radiative responses can be computed locally using a strong uniformity assumption, which is the essence of the independent pixel/column approximation described next in a special (but representative) case.

The present authors come to the same scale-based classification of variability effects in RT from the standpoint of steady-state 3D diffusion theory [121]. They arrive at essentially the same scale-by-scale breakdown of spatial variability impacts using a the first-principles analysis of the propagation process [54], the only difference being that the
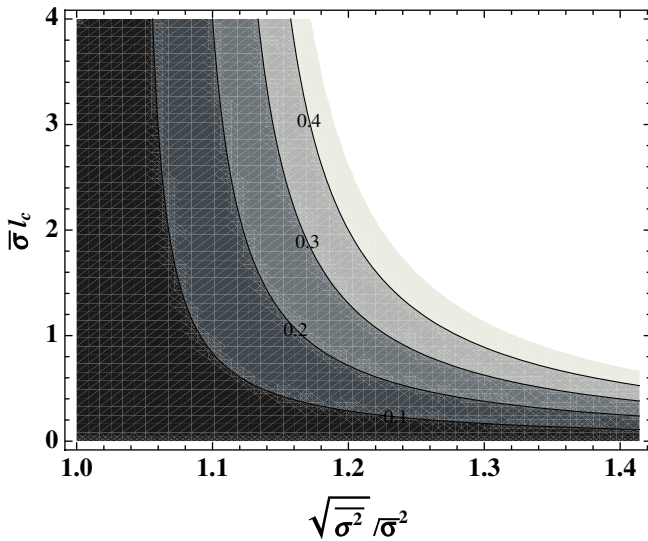
Figure 11. *Cairns' scaling factor ϵ used in* (106). Parameter ϵ is plotted as a function of $\overline{\sigma^2}^{1/2}/\overline{\sigma}$ and $\overline{\sigma}l_c$ using (107)–(108). Values up to ~1/3 can be used with some confidence; when $\varpi_0 = 1$, this upper limit leads to division of $1 - g$ at most by 2. Therefore, at most moderate 1-point variability ratio (RMS/mean for σ) can be considered. It can be only slightly more than unity, unless the correlations are very short range vis-à-vis the MFP defined here as $1/\overline{\sigma}$ (even though this is known to be an underestimation [54]).

transport MFP used in the above arguments is replaced by the usual MFP describing the mean distance between successive scatterings or, e.g. an emission or an absorption. In the same paper Davis and Marshak show, incidentally, that the *actual* MFP is $\overline{1/\sigma}$ in a broad class of variable media with long-range correlations, including clouds. Moreover, that estimate always exceeds $1/\overline{\sigma}$ (they are equal *only* when σ is uniform).

5.1.2. Independent pixel/column approximation (IPA/ICA). From the standpoint of computational expediency, the next best thing to homogenization, leading to a *single* 1D RT problem to solve, is the IPA/ICA where a *finite number* of such problems are solved. Alternatively, the closed-form solution of a 1D RT problem, such as obtained in section 3.1, may be averaged analytically over an explicitly assumed PDF for the variability of an optical property, typically, cloud optical depth. In this case, we do not leave the realm of closed-form expressions, with the obvious computational efficiency that ensues. We demonstrate with two IPA/ICA computations.

First, we invoke the simplest possible model for spatial variability of clouds, which is certainly the linear mixing model based on 'cloud fraction' A_c (between 0 and 1). We will see it again in sections 7.3 and 8.1.1. As easy as it is to conceptualize, defining and measuring A_c empirically is not straightforward, in particular, because it depends on what type of instrument is used and the resolution within a type [122]. At any rate, it is the first and still foremost application of the IPA/ICA concept, predating by far that terminology and the acronyms (introduced in the early 1990s [123, 124]). Take, for instance, scene albedo under a given solar illumination. The clouds are assumed plane-parallel and give $R(\mu_0; \tau_c)$ while the clear sky

gives $R(\mu_0; \tau_a)$ where the subscript 'a' pertains to the aerosol load. In combination, we get

$$\overline{R}(\mu_0; \tau_a, \tau_c, A_c) = A_c \times R(\mu_0; \tau_c) + (1 - A_c) \times R(\mu_0; \tau_a). \tag{109}$$

Simple enough! Since $R(\cdot)$ is a concave function ($\partial_\tau^2 R(\mu_0; \tau) < 0$), $\overline{R}$ will be smaller than $R(\mu_0; \overline{\tau})$, where $\overline{\tau} = A_c\tau_c + (1 - A_c)\tau_a$. This inequality is in fact the definition of a concave function, and the associated bias between $\overline{R(\tau)}$ and $R(\overline{\tau})$ did not go unnoticed by early developers of RT parametrizations for GCMs [125, 126].

Whether for the whole atmosphere or a single layer, we expect optical depth τ to vary continuously rather than in the above binary fashion. In the gamma-weighted IPA/ICA [127], one assumes that the 1-point statistics of τ follow

$$P_a(\tau) = \frac{1}{\Gamma(a)} \left(\frac{a}{\overline{\tau}}\right)^a \tau^{a-1} e^{-a\tau/\overline{\tau}}, \tag{110}$$

where

$$a = \frac{\overline{\tau}^2}{\text{Var}(\tau)} = \frac{1}{\overline{\tau^2}/\overline{\tau}^2 - 1} \tag{111}$$

is the new variability parameter. This particular choice of variability model follows naturally from the ease of integrating rational functions over arbitrary combinations of power laws and exponentials, resulting at most in exponential integral functions and/or incomplete gamma functions; possibly infinite series thereof that are easily summed numerically to a pre-specified accuracy. The above choice of PDF for τ is also justified on the basis of fine-scale satellite observations of many different kinds of cloud fields [128].

To illustrate, we plot

$$\overline{T}_a(\overline{\tau}_t) = \int_0^\infty \frac{1}{1 + \tau_t/2\chi} P_a(\tau_t) \, d\tau_t = \xi e^\xi E_a(\xi)|_{\xi = 2\chi a/\overline{\tau}_t} \tag{112}$$

in figure 12(*a*). Although in a different notations, Oreopoulos and Barker [129] did the same computation. Here, $E_a(\xi)$ is the exponential integral of any real order $a > 0$, and we note that $\xi = a/Z$ from (97). We note in figure 12(*a*) a systematic positive bias of $\overline{T}_a(\overline{\tau}_t)$ with respect to $\overline{T}_\infty(\overline{\tau}_t) = 1/(1 + \overline{\tau}_t/2\chi)$. We retrieve the well-known result in 3D RT: structured clouds transmit more (reflect less) than their homogeneous counterparts *with the same mean* τ. This is an immediate consequence of Jensen's inequality [116] for a convex function such as $T(\tau_t)$.

As another illustration, we plot

$$\overline{\langle ct \rangle_T}/H = \frac{\overline{T \times \langle ct \rangle_T}}{\overline{T}_a \times H}$$
$$= \frac{\chi}{2}[1 + a + \xi + (2 - \xi)/\overline{T}_a(\xi)]|_{\xi = 2\chi a/\overline{\tau}_t} \tag{113}$$

in figure 12(*b*). Note how we have properly weighted the path moment for transmitted light $\langle ct \rangle_T$ from (99), and then averaged over the gamma-PDF for τ in (110), and finally normalized the result by $\overline{T}_a$ in (112). As it turns out, the whole variation of flux-weighted mean path, $T \times \langle ct \rangle_T = \chi(\tau_t^2 + 6\chi\tau_t + 6\chi^2)/(\tau_t + 2\chi)^2$, is between $\chi \lesssim 1$ and $3\chi/2 \approx 1$.
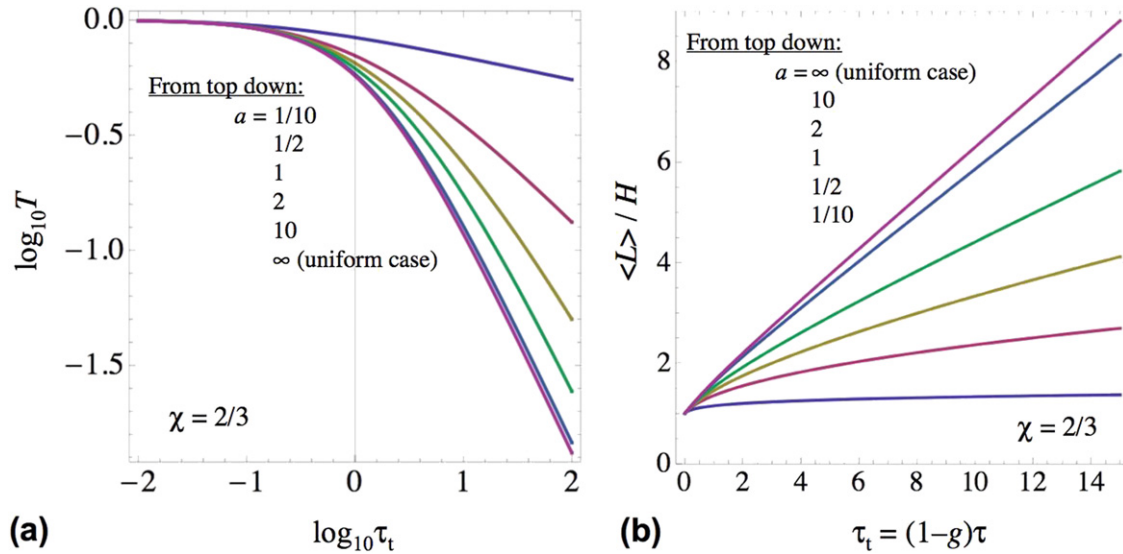
Figure 12. *Transmittance and associated mean path for a gamma-weighted diffusion model.* (*a*) The expression in (112) is plotted versus $\overline{\tau}_t$ for selected values of *a* in log-log axes; we note the increasing transmission as the unresolved variability increases (*a* decreases) at fixed $\overline{\tau}_t$. (*b*) Mean path length, in units of *H*, from (113) versus $\overline{\tau}_t$ for the same values of *a* as in panel (*a*); we note that paths decrease on average as variability increases (*a* decreases) at fixed $\overline{\tau}_t$. See text for more explanation.

So the systematic trend toward shorter paths due to spatial variability is traceable to the normalization by $\overline{T}_a$. Although one should also bring reflected light into the balance, shorter paths translate to systematically less absorption in variable clouds. In the limit of asymptotically large τ_t, (112) and (113) yield, respectively,

$$\overline{T}_a \propto \tau_t^{-\min\{a,1\}} \qquad \text{and} \qquad \overline{\langle ct \rangle_T}/H \propto \tau_t^{\min\{a,1\}}. \quad (114)$$

We resume our discussion of this simple variability model in section 7.1 where we find its prime application to GCM parametrization improvement.

5.1.3. Mean-field theory. Mean-field theory departs more radically from 1D RT than both homogenization, which attempts to reduce the 3D RT problem to a single 1D one, and the IPA, which attempts to reduce the 3D RT problem to a larger number of 1D ones. In this framework, which has a long and venerable history, we end up with new transport equations to solve. A classic example is the so-called 'stochastic' RT model, which was first introduced into atmospheric RT by Avaste and Vainikko in 1974 [130]. It recasts the highly 3D problem of solar RT in broken cloud layers as two *coupled* integro-differential equations, one for radiance in the clouds, the other for radiance in the clear regions. It predicts ensemble-average radiances and fluxes, which are generally used to represent instantaneous large-scale spatial averages. The coupling assumes a Poissonian spatial distribution of clouds in space (i.e. no correlations beyond the residual characteristic inter-cloud distance). Along beams cast through this randomly structured medium, clear-to-cloud transitions (and vice-versa) are Markovian. This leads to the mathematically simplest possible coupling between the two transport equations: linear crossing terms where the two new parameters are mean cloud fraction A_c and mean cloud aspect ratio $\gamma = L/H$ (where *L* is the mean horizontal cloud size).

The stochastic RT model continues to be refined [131, 132, among others], validated [133–135], and applied [136, 137, among others] to this day; see also section 7.3 below, especially figure 29. Interestingly, it was developed independently in the neutron transport community [138, 139] where, again, it remains very popular. Indeed, the question of small-scale spatial variability, unresolved in large-scale models for nuclear reactors, is taken very seriously for good reasons. Pomraning, one of its originators in neutronics, and coworkers later on re-introduced the stochastic RT model into climate science [140]. It has two well-known limits. When $\gamma \to \infty$, clouds are horizontally very extended and there is little radiative coupling with the clear regions, so the two-state IPA in (109) becomes accurate and, accordingly, the two RTEs decouple. In the opposite limit, $\gamma \to 0$, 'clouds' become so small that between two elementary events (e.g. scatterings) at finite distance the light samples many times both cloudy and clear air, so only the mean extinction (hence mean optical depth) matters, accordingly, the two RTEs degenerate to a single one. This latter case is known as the 'atomistic mix' limit. So, in a specific sense, the stochastic RT model goes continuously from the 1D RT case to the two-state IPA as γ increases from 0 to ∞.

Another interesting and under-appreciated contribution to the topic was by Stephens [141]. Targeting the spatial domain-average fluxes that matter in GCMs, he revisited the derivation of the two-stream 1D RT model. In this case, he had in hand a parametrized expression (based on numerical simulations in [142]) for the systematic directional effect of the radiative 'channeling' described further on (section 6.1). This process introduced a new optical coefficient (in the usual units of km^{-1}) that, like Cairns' ϵ, can be obtained in principle either from theory or from observations.

To illustrate mean-field theory within our own work, we revisit the time-dependent random-walk model used in
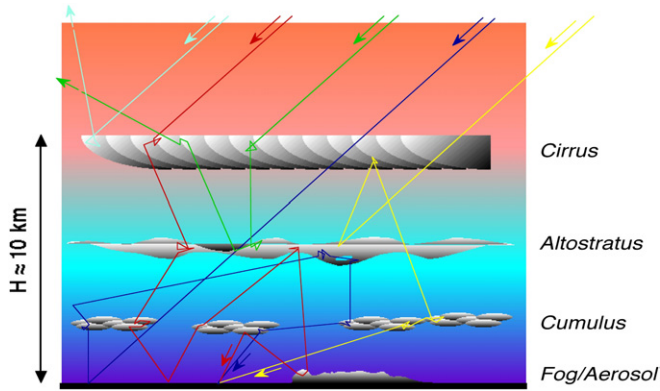
Figure 13. *Schematic of the anomalous diffusion and transport models for domain-average solar RT in columns with spatially complex cloudiness.* Sunlight gets trapped in clouds where the random steps in multiple-scattering trajectories are small. However, there are also relatively frequent large jumps between the clouds and/or the surface. Also note the large fraction of light bounced back to space. In the anomalous diffusion model [62], the random steps are implicitly drawn from symmetric Lévy-stable distributions [143] with indices $1 < \alpha \leqslant 2$ ($\alpha = 2$ reverts to the classic Gaussian case, and 'normal' diffusion ensues); computations are analytic. In the anomalous transport model [63], the random steps s are drawn from the gamma-weighted mean direct transmission law $\Pr\{s > S\} = (1 + \overline{\sigma} S/b)^{-b}$, where $1 < b \leqslant \infty$ ($b = \infty$ reverts to the classic exponential case, and 'normal' transport ensues); computations are numerical, using a modified 1D MC code. The asymptotic laws for the responses in reflection and transmission are as in the diffusion model, with $\alpha = \min\{2, b\}$, by Lévy's generalized central limit theorem [143, 144].

section 4.3. To this effect, we consider the present authors' theory of *anomalous* diffusion of solar radiation. In their original paper, Davis and Marshak [62] generalized the random-walk model to situations where steps are usually small (inside clouds) but not infrequently very large (between clouds). See schematic in figure 13.

Davis and Marshak [62] assumed PDFs for step size s with power-law tails, $\sim 1/s^{1+b}$, such that all moments of order $q > b$ are divergent. Yet it seems natural to require that the MFP (average value of s) be finite, hence we require $b > 1$. There are indeed theoretical reasons [54] stated in section 2.3 that the *mean* direct transmission law, hence free-path distribution, is sub-exponential. Moreover, there is empirical evidence [128] that the variability of extinction averaged over a range of scales is gamma-like; this in turn leads to power-law mean transmission [129].

Recall from section 2.4.2 that the transport MFP $\ell_t = \langle s \rangle/(1 - g)$ can be introduced using random-walk language, i.e. without reliance on (standard) diffusion theory, as the effective MFP for an isotropic (conservative) scattering. So we continue to use it here and address finite cloudy media with slab geometry (thickness H). We showed [62]

(i) that transmittance T_α scales as $\tau_t^{-\alpha/2}$ and
(ii) that the mean path for transmitted light $\langle ct \rangle_T$ goes as $H \times \tau_t^{\alpha - 1}$,

where $\alpha = \min\{b, 2\}$. These scaling laws revert to our findings in section 4.3 for any $b \geqslant 2$ (the upper limit for α), and we

note the difference with the gamma-weighted ICA predictions in (114).

For a more transport-like mean-field theory, yet closely related to the above anomalous *diffusion* model, we refer to Davis [63]. Therein, a new 1D *integral* RTE is obtained and solved numerically, and we refer to this model as anomalous *transport*. Large τ_t behavior is predicted correctly by anomalous diffusion as far as the scaling is concerned. However, the τ_t values at which the asymptotic regime is achieved are notably large. This casts doubts about the relevance of (analytic) anomalous diffusion to real cloudy atmospheres and argues for the more robust (computational) anomalous transport model.

5.2. Dealing with resolved spatial variability

Suppose now that all the spatial variations of the cloud optical properties are specified down to some 'small' scale. Furthermore, the radiation fields maybe required down to the same scale or maybe only to a courser one. Either way, 3D RT modelers must find ways to deliver answers for the *given* 3D cloud structure, and not any other. Fortunately, there are many ways of solving specific 3D RT problems, but implicit in this challenge is to deliver an answer at some pre-defined accuracy with an efficiency that may preclude many of the standard approaches.

So we need to discuss solutions of both the full 3D RT problem based on the linear Boltzmann equation as well as more practical approximations thereof. The former are very briefly described in section 5.2.3, primarily as accuracy benchmarks. The latter are exemplified by *computational* 3D diffusion modeling, a problem set up in section 2.4 and used *analytically* in section 6.1; for a relatively recent survey of numerical 3D RT approximation techniques, we refer the reader to Davis and Polonsky [145].

As an intermediate model that lies at the crossroads of standard 1D RT, full 3D RT and efficient approximations thereof, we have the *local IPA/ICA*, as defined in section 5.2.2. This is a straightforward answer to the resolved variability problem: we compute for each vertical column the 1D RT solution, but do not necessarily perform the spatial average used in section 5.1.2. At that point, we only had statistical knowledge of the variability, but here we know all the details.

First, however, we must touch on another issue. If we are pursuing more realistic modeling of RT in clouds, then it can only be as realistic as the 3D representation of the clouds themselves. In the applications, this preliminary question has to be addressed in order to gauge the computational effort in the RT. There are both stochastic and physics-based approaches to cloud modeling.

- It is hard to argue against using state-of-the-art cloud resolving models precisely because they are based on a full suite of physics: fluid dynamics, fine-scale turbulence closures, multi-phase thermodynamics, cloud microphysics, even radiation (at least from a 1D RT model). These models unfold either in 2D or (more and more) in 3D. The microphysics, i.e. droplet-scale processes can use just a few moments
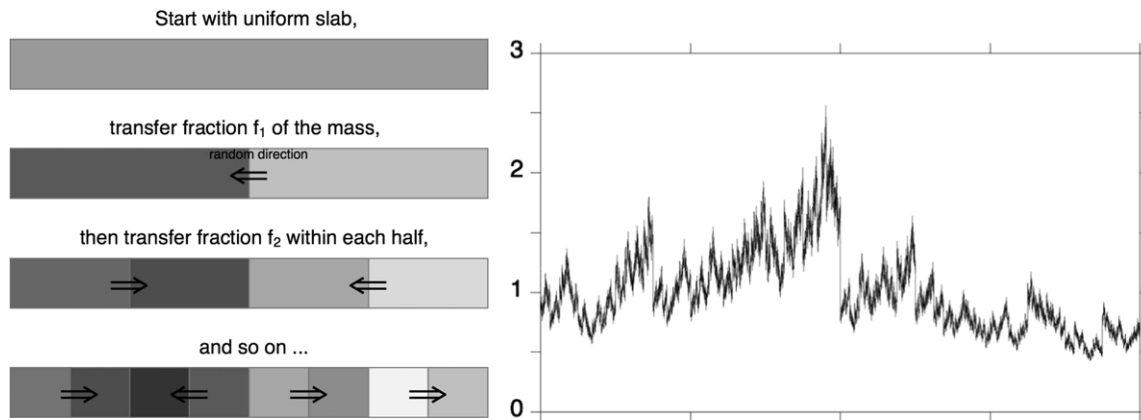
Figure 14. *A convenient stochastic cloud model for 3D RT studies.* Left: in the 1st step, a fraction f_1 of cloud 'mass' is transferred in a random horizontal direction from one half to the other. For every step after that, a fraction f_n is similarly transferred at scale $1/2^n$ such that $f_n/f_{n-1} = \cdots = f_2/f_1$. Right: the outcome for one realization at $n = 14$ when the parameters are $f_1 = 1/4$ and $f_1/f_2 = 2^{1/3}$. This so-called 'bounded cascade' model [115, 147] has been tuned to yield a 1-point standard deviation of 1/3 of the (unit) mean and 2-point correlations reflecting a Fourier spectrum in $1/k^{-5/3}$. These values are typical of the observed spatial variability of LWP [151] or LWC [148] for real marine Sc clouds.

or (more and more) the full particle-size distribution. However, hardware advances are now enabling 3D dynamics with the so-called 'bin' microphysics. Although they are as physically correct as possible, these models require the specification of very many atmospheric parameters and remain computationally expensive.

- Because they are not burdened with the memory requirement to capture complex multi-physics, specific realizations of stochastic models can have almost arbitrarily fine resolution. For the same reason, they are very efficient. Best of all, they can be tuned to reproduce the spatial statistics observed in real clouds. Stochastic cloud models are necessarily based on either ground-, aircraft- or satellite-based measurements of cloud structure; so they are constrained at most in 2D. Currently, there are no operational techniques to determine full 3D cloud structure, but on-going research may soon fill this gap [146].

5.2.1. Stochastic versus physics-based 3D cloud models. Taking a historical perspective, atmospheric 3D RT started logically with horizontally finite but otherwise homogeneous clouds (e.g. the spheres used in section 3.3). Then the 3D RT community moved to stochastic models that enabled much progress in 3D RT phenomenology during the 1990s. One of the more popular stochastic models was the bounded cascade introduced by Cahalan in 1994 [115]. Its simple generation algorithm is described in figure 14, and one realization is plotted. It is custom-designed to have a power-law horizontal wavenumber spectrum in $k^{-5/3}$, although other exponents between -2 (included) and -1 (excluded) can also be obtained. This mimics what has been observed again and again in nature. Moreover, the 1-point statistics of the bounded cascade are lognormal-like as is also observed in real clouds. Finally, the bounded cascade has interesting multifractal properties [147], again as seen in *in situ* data from real clouds, i.e. long records from aircraft sampling

the horizontal fluctuations of microphysical properties such as LWC [148, and references therein]. But there are other stochastic models that can do all that just as well [149, 150]. So which one to use? It can start as simple as a matter of taste. However, the robustness of the 3D RT results with respect to cloud model swap should ultimately be checked.

The bounded cascade, and other such scale-invariant constructs (cf [150, and references therein]), thus offered the community a simple way of producing geometrically plane-parallel clouds that had a rich statistically realistic texture in their horizontal structure. 2D generalizations were quickly developed for the bounded cascades and other fractal and multifractal stochastic models, and just as quickly put to use in MC simulation studies [152, 153]. Part of the power of stochastic cloud modeling is that only a small number of parameters need to be specified (say, $\lesssim 4$) as input to control the rules that draw on a pseudo-random number generator. Output is a cloud field with realistic 1- and 2-point statistics, possibly more. If necessary, any number of statistically indistinguishable realizations of the same stochastic model can be generated.

Eventually, non-parametric but *data-driven* stochastic models were developed [154–158, among others], which will generate realizations with the same specified statistics as (almost) any type of multivariate cloud data. In a sense, these models have very many parameters: the number of data points or, at least, the number of bins in the histograms, correlation functions etc., used to synthesize new realizations.

From there, it is a small step to go from such evolved stochastic models to physics-based dynamical cloud models, which over time were getting undeniably better (with more physics, hence more realism and more resolution). It is revealing that, in this review, the older work we cover is based on bounded cascades and kindred stochastic models (cf section 8.1.2) while the most recent work is based on cloud scenes generated with LES models and CRMs (cf section 8.2.2). It is also revealing that contemporary LES-based cloud models can use the fractal properties of their

output as validation that they are correctly capturing the highly nonlinear physics [159].

5.2.2. The local IPA/ICA. In section 5.1.2 we presented the IPA/ICA as a statistical technique based on available 1D RT theory to cope with *unresolved* spatial variability by averaging the 1D RT results over the 1-point cloud variability. However, in the present problem posed by *resolved* cloud structure, the idea of using 1D RT to predict not just a domain average but also the fluctuations of the radiation field itself is worthy of consideration.

Assume, for simplicity, that only the extinction coefficient $\sigma(x, y, z)$ varies spatially within a plane-parallel medium $M_{pp}(H)$ occupying the space between $z = 0$ and $z = H$; $M_{pp}(H)$ need not be the full support of the extinction field since there can be substantial regions of optical void inside $M_{pp}(H)$. With this option in mind, it is not much of a constraint to assume the outer cloud geometry is plane-parallel.

Formally, we can define without reference to any grid

$$\tau(x, y) = \int_0^H \sigma(x, y, z)\,\mathrm{d}z. \tag{115}$$

All other optical properties, single-scattering albedo ϖ_0 and phase function $P(\mathbf{\Omega}' \to \mathbf{\Omega})$, including asymmetry factor g in (20), are assumed uniform in $M_{pp}(H)$, but only for simplicity. The local IPA/ICA prediction for, say, reflected boundary flux is then $F_{1D}(x, y) = \mu_0 F_0 R(\tau(x, y), \varpi_0, g; \mu_0)$.

Let us put this idea into the broader context. The uniform plane-parallel slab model for clouds is much maligned by the 3D RT community, for scientifically sound reasons (cf section 6). However, that simple model is actually just one possible approximate solution to a difficult problem. Granted, one that has been abused. This abuse has established the plane-parallel model as an apparently immutable standard of reference, in atmospheric 3D RT research.

In the not too distant future, we hope to have this perspective reversed. At present, the plane-parallel model presented as the only one deemed *a priori* to be 'practical' enough for use in operational settings. We would rather see the plane-parallel model be humbly submitted as a possible approach, with advantages and flaws, to the challenging problem of radiation transport in the real 3D world. At that point, 3D RT becomes the standard of reference in the optics and energetics of the Earth's cloudy atmosphere. In the interim, we continue to use the plane-parallel slab model (where, by definition, all *net* horizontal fluxes are neglected) to predict even highly resolved radiation fields. Consideration of computational limitations should be secondary, partly because computational resources are improving tremendously from decade to decade (roughly the life-cycle of a major program or mission) and partly because of on-going efforts described in sections 7–8 to mitigate—even exploit—3D RT effects.

5.2.3. Computational 3D RT. There will always be a need for high accuracy and high precision benchmarks in 3D RT. In this subsection, we overview the two general numerical techniques: random and deterministic quadrature methods.

The interested reader is referred to a relatively recent survey by Evans and Marshak [160, and references therein] for more details. For a recent survey of the various 3D RT models in use and an illustration of their typical capability, we refer to Cahalan *et al*'s [161] overview of the Intercomparison of 3D Radiation Codes (I3RC). The I3RC is a grass-roots initiative that built up a challenging suite of cases designed to exercise the models with increasing scene complexity.

In short, there are discretization (deterministic) and probabilistic (Monte Carlo) methods for solving the integro-differential 3D RTE in (8), and there are potentially very powerful hybrid methods [162, 163].

Preliminaries. For easy reference, we rewrite the *steady-state* version of (8) succinctly as

$$\mathcal{L}I = \mathcal{S}I + q, \tag{116}$$

where $\mathcal{L}$ is the (differential) linear transport operator $\mathbf{\Omega} \cdot \nabla + \sigma$, $\mathcal{S}$ is the (integral) scattering operator $\sigma_s \int_{4\pi} P(\mathbf{\Omega}' \cdot \mathbf{\Omega})[\cdot]\,\mathrm{d}\mathbf{\Omega}'$ and q is the (optional) source term. This equation can be put in a purely integral form,

$$I = \mathcal{K}I + Q, \tag{117}$$

where

$$\mathcal{K} = \mathcal{L}^{-1}\mathcal{S} \tag{118}$$

is the full transport kernel and

$$Q = \mathcal{L}^{-1}q. \tag{119}$$

The physical interpretation (and numerical implementation) of the integral operator $\mathcal{L}^{-1}$ is an upwind 'sweep' through the 3D medium, in this case, collecting in Q all the light directly transmitted, using (12), from the primary sources in q to the generic point-and-direction of interest $(\boldsymbol{x}, \mathbf{\Omega})$. We will assume steady sources for the time being.

Formally, the solution of (117) can be written as a Neumann series

$$I = (1 - \mathcal{K})^{-1} Q = \sum_{n=0}^{\infty} \mathcal{K}^n Q. \tag{120}$$

Both deterministic and Monte Carlo methods capitalize on this expansion by successive iterations of $\mathcal{K}$. The physical interpretation of the series is radiance contributions from successive orders of scattering. The convergence rate of the Neumann series, and possibly its acceleration, is a central question in numerical transport methods. Theoretical analysis of this key issue is out of our present scope, but it should be known that it involves the eigen-value spectrum of the integral operator $\mathcal{K}$ in (118): numbers η that give non-trivial solutions to $\mathcal{K}\phi = \eta\phi$ where ϕ are eigen-functions. The radiative transfer equation has a unique positive eigenvalue that corresponds to a unique positive eigen-function. See Case and Zweifel [164] and Vladimirov [165] for more details.

To make this classic decomposition more transparent, suppose we know all the terms in (120) for some RT problem with everywhere conservative scattering ($\varpi_0 \equiv 1$), and we

call them $I_n^{(1)}$; the Neumann series then becomes $I(1) = \sum_{n=0}^{\infty} I_n^{(1)}$. Then suppose we want to know the solution of the same problem but with some uniform level of absorption (i.e. $0 \leqslant \varpi_0 < 1$). We can factor out ϖ_0 from each term in (120), leading to

$$I(\varpi_0) = \sum_{n=0}^{\infty} I_n^{(\varpi_0)} = \sum_{n=0}^{\infty} \varpi_0^n I_n^{(1)}, \qquad (121)$$

where the nth term of this Taylor series in ϖ_0 is the contribution to $I(\varpi_0)$ of radiation scattered n times. Although it is physically impossible to filter orders of scattering, some instruments are designed to select them as best possible. Sun-photometers use in principle only the 0th-order term $I_0^{(\varpi_0)}$, while standard lidars use in principle only the 1st-order term $I_1^{(\varpi_0)}$. In practice, both these types of observation need to be examined and possibly corrected for the presence of all the higher-order terms as soon as they collectively exceed the tolerance threshold for systematic overestimation.

Considering the expansion of the steady-state Green function into its order-of-scattering components in (121), it is interesting to note that both $G_0^{(\varpi_0)}(\boldsymbol{x}, \boldsymbol{\Omega})$ and $G_1^{(\varpi_0)}(\boldsymbol{x}, \boldsymbol{\Omega})$ are singular in the following sense. Given a distribution source terms $\delta(\boldsymbol{x} - \boldsymbol{x}_0)\delta(\boldsymbol{\Omega} - \boldsymbol{\Omega}_0)$, where either $\boldsymbol{x}_0$ or $\boldsymbol{\Omega}_0$ span less than their full supports, there is a measurable subset of points $(\boldsymbol{x}, \boldsymbol{\Omega})$ in the transport phase space where the resulting superposition $I_n^{(\varpi_0)}(\boldsymbol{x}, \boldsymbol{\Omega})$ ($n = 0, 1$) has discontinuities. An interesting corollary of this singularity property in *inverse* transport theory [166, and references therein] is that, with full and perfect knowledge of only these two terms, one can reconstruct exactly both $\sigma(\boldsymbol{x})$ from $I_0^{(\varpi_0)}$ and $\sigma_s(\boldsymbol{x})P(\boldsymbol{x}, \boldsymbol{\Omega}' \cdot \boldsymbol{\Omega})$ from both. Computed (x-ray) tomography works because $\varpi_0 \approx 0$ in (121); moreover, the robust features in x-ray images that enable the reconstruction technique to overcome the effects of noise and residual scattering result directly from those singularities. The corresponding instrument in atmospheric research is the sun-photometer, only interested in the non-scattered sunlight $I_0^{(\varpi_0)}$. Lidar and all forms of radar are only interested in $I_1^{(\varpi_0)}$ for a special value of $\boldsymbol{\Omega}' \cdot \boldsymbol{\Omega} = -1$, and they are indeed our main sources of tomographic information about the atmosphere.

All higher-order terms, $n \geqslant 2$, in (121) are smooth even for a single δ-source. Consequently they are an impediment to standard tomographic methods, lidar and radar in particular. Near the end of this review, we will describe a novel type of lidar (as well as a closely related passive solar technique) that performs a limited but useful form of cloud tomography using only the diffuse multiply scattered light field.

Finally, both deterministic and Monte Carlo (MC) methods can be generalized to account for time-dependence. This is, however, by far easier with MC methods than to have to discretize t deterministically. Even though this new dimension is not much extra burden on computer memory, one needs to carefully maintain congruence with the discretization of $\boldsymbol{x}$ in order to keep the numerical scheme stable. By contrast, in a MC scheme, it is as simple as adding path ct as a fourth independent variable to (x, y, z) when generating the random trajectories; ct is just the running sum of all the steps between scattering events, without the direction cosines that apply to

the propagation in spatial variables. Many time-dependent MC results were used to generate the figures in the previous section.

Deterministic methods. Both deterministic and Monte Carlo methods call for a grid, Cartesian or otherwise convenient, or an unstructured mesh, to define (in computer memory) the spatial variability of the optical medium as well as the source term q. It covers a finite subset M of $\mathbb{R}^3$. Deterministic methods also need the spatial grid to discretize the differential part of the 3D transport equation represented in (116) by $\mathcal{L}I$. Furthermore, these methods call for a discretization of direction space ('S_N' methods)—or a truncated expansion in spherical harmonics ('P_N' methods)—or both, to treat the scattering integral represented by $\mathcal{S}I$. The algorithm specified in (120) is technically known as 'source iteration,' and there are clever ways of accelerating its convergence, cf [167–169, among others].

The atmospheric 3D RT community is overwhelmingly dominated by Monte Carlo modelers, but there is one deterministic model called the spherical harmonics discrete ordinates method (SHDOM) by Evans [170] that evolved naturally from his spherical harmonics spatial grid model [171], adding the efficiency of spherical harmonics to the angular integrations and adaptive grid refinement in the spatial domain. SHDOM is freely available and quite widely used. Recent and welcome additions to this too short list of deterministic codes are the EVENT [172, 173] and RADUGA [174] models but, as far as we know, they are not openly distributed. Another interesting development is the application of wavelet transforms to the numerical solution of the 3D RTE [175, 176]. This recent effort was inspired by an early attempt at spatial representation of the 3D RTE by horizontal Fourier transforms [177], but leads to potentially far more efficient multi-scale methods with sparsely populated matrices to process.

Figure 15 shows an SHDOM computation. It is a detailed 3D rendering of the directionally averaged radiance field, $J(x, 0, z)/4\pi$ from (13), for the rotationally symmetric boundary-source Green function of a uniform cloud in the spatial domain. It is plotted both inside and outside the cloud using a logarithmic color-scale.

Monte Carlo methods. Where MC methods depart fundamentally from their deterministic counterparts is that they *only* need a grid or mesh to define the spatial distribution of optical properties and sources. After that, the elements of $\mathcal{K}$ in (118) are used as rules to generate a random realization of a Markov chain of propagation and scattering events. The integral source term Q is used to generate random starting points and the chain is stopped, in the absence of absorption, when it crosses the boundary of M. In the presence of absorption, there is a finite probability of terminating the chain inside the medium; alternatively, the 'weight' of the roaming Monte Carlo 'particle' can be reduced to track absorption. There are various ways of tallying Monte Carlo particles, with or without weights, to estimate precisely what is asked of the 3D RT model.
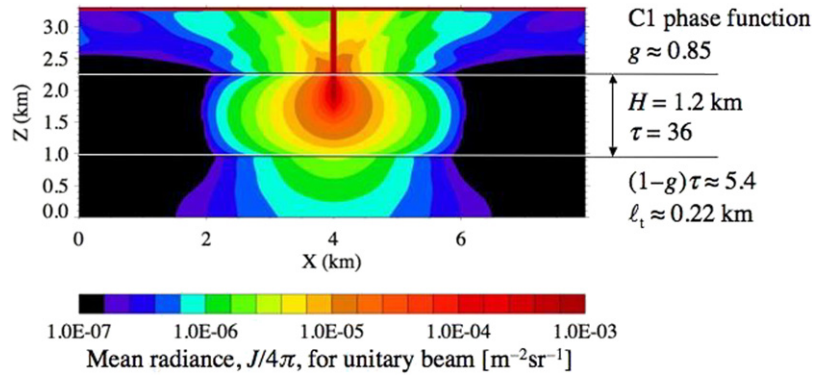
Figure 15. *A transect of mean radiance for the pencil-beam illumination problem inside a finite homogeneous slab, from SHDOM.* The optical medium is a uniform non-absorbing ($\varpi_0 = 1$) plane-parallel cloud of thickness $H = 1.2$ km and extinction $\sigma = 30$ km^{-1}, hence optical thickness $\tau = \sigma H = 36$. The phase function is for a 'C1' droplet-size distribution for $\lambda = 532$ nm. Mean radiance, $J/4\pi$ from (13), is plotted for a domain larger than the cloud itself. A close look at the *logarithmic* color-scale reveals that the light field in the cloud is decaying exponentially with distance from the source as dictated by $\rho^\star$ in (86). The 'rays' emanating from the source region near the top of the cloud are an artifact of the discrete ordinates scheme (in this case, $N_\mu = 12$ and $N_\phi = 24$). This result was graciously contributed by Dr Franklin Evans (University of Colorado).

Monte Carlo is at its best when tasked to compute spatial and/or angular integrals. Formally, we seek [179]

$$E = (f, I) = \int_{4\pi} \iiint_M f(\boldsymbol{x}, \boldsymbol{\Omega}) I(\boldsymbol{x}, \boldsymbol{\Omega}) \, d\boldsymbol{x} \, d\boldsymbol{\Omega}, \quad (122)$$

where $d\boldsymbol{x}$ denotes $dx \, dy \, dz$. Function f describes the response of a virtual detector inside or at the boundary of M. The bigger the support of f, the better the accuracy achieved for E, simply because all the more histories will contribute. We know the convergence rate is slow, in $1/\sqrt{N}$ (where N is the total number of histories generated); so the size of the support of f matters for the variance of the estimator, but its choice is dictated by the application. So, for a given application, in atmospheric RT in particular, there is always a tradeoff study to perform between deterministic and MC methods, as recently emphasized by Pincus and Evans [180].

Now, independently of f, there are many clever ways of reducing MC variance in general [181, 182, among others], and they find their way into atmospheric RT applications [183, 184, among others]. The most effective are to use an approximate deterministic solution to guide the Markov-chain sampling and determine the weight multiplier; these are the so-called 'hybrid' methods [163] and they remain an area of open research.

It is important to note that, in MC simulation, there is no need to forcibly truncate the Neumann series in (120). Indeed, if a MC particle wanders for too long (or into regions of less interest) by some criterion, it can be terminated at the flip of a digital coin ... or continued (temporarily) with twice the weight. This game of 'Russian Roulette' increases somewhat the variance, but ensures that there is no bias in the estimate of E.

It is also important to remember that, if f describes a domain-scale integration, as in the estimation of total (as opposed to local) reflectance or transmittance, MC can be not only more accurate but also faster than a deterministic estimate. In the deterministic model, radiance is computed everywhere whether or not it is required. When local values

of the boundary-leaving fluxes—and worse still radiance—are required, then deterministic methods have an edge.

As in figure 15 for SHDOM, figure 16 shows MC estimates of Green functions for a homogeneous plane-parallel cloud. In this case, we are looking at boundary-source/boundary-detector Green functions. The numerical noise is evident and increases as expected as the number of locally tallied histories decreases, i.e. as the distance from the source increases.

6. Assessment of 3D damage to 1D RT modeling

There has been a sustained interest in spatially variable sources in uniform media, this review included (cf figures 15–16). However, the vast majority of atmospheric 3D RT studies are based on spatially variable media and uniform sources. From the earliest theoretical studies [8] to the most recent data analyses [185], the latter use 1D RT as a reference. It may seem strange to use such a coarse representation of reality as a standard benchmark but we must bear in mind that, when it comes to the applications, RT is generally just a means to an end. So there is usually an expectation—and often a requirement—of expediency. Typically, the effects of 3D RT with respect to this benchmark are quantified under some reasonable assumption such as conservation of the total mass (i.e. number of material particles responsible for the scattering and absorption). We think of this activity as an assessment of the damage that 3D RT causes for the accepted *operational* 1D solution to the RT problem embedded in virtually all applications.

6.1. 3D RT phenomenology: how radiation flows around opaque regions and is channeled into the tenuous ones

One-dimensional atmospheric RT modeling is always aligned with the vertical (z) axis. Cloud shadows cast by the Sun under oblique incidence (as seen through an airplane window) are the most obvious cloud-related 3D RT effect. This may not be a big concern in the case of extensive stratiform clouds since
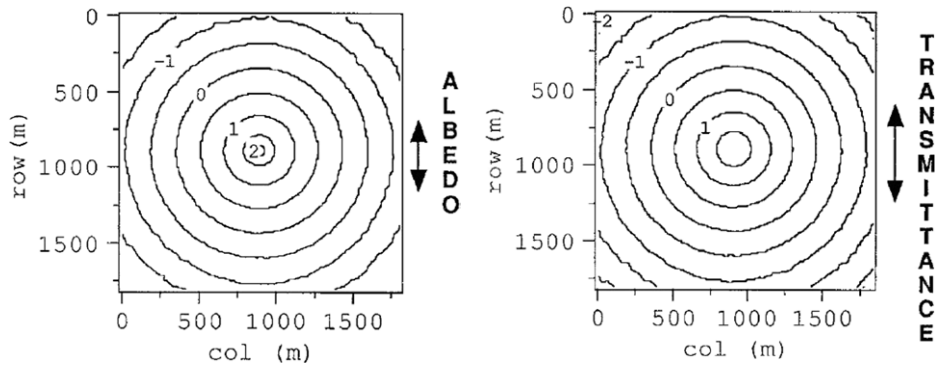
Figure 16. *Boundary fluxes for the pencil-beam illumination in a* $2 \times 2\,\mathrm{km}^2$ *domain for a finite homogeneous slab, from a MC scheme*. The optical medium is a uniform non-absorbing ($\varpi_0 = 1$) plane-parallel cloud of thickness $H = 0.3\,\mathrm{km}$ and optical thickness $\tau = 13$. The phase function is the H–G model in (33) with $g = 0.85$. Boundary fluxes are plotted for reflectance (left), $R(x, y) = F_-(x, y, 0)$, and transmission (right), $T(x, y) = F_+(x, y, H)$, on 128×128 grids. The isophotes are on a log-scale, so we recognize the exponential decay controlled by $\rho^\star$ in (86). Double-headed arrows on the side indicate the RMS values for ρ, i.e. $\langle x^2 + y^2 \rangle_F^{1/2}$ ($F = R, T$). The signature numerical noise of the MC method is visible at the lowest light levels. In this case, 10^8 histories were traced and this particular cloud has $R \approx T \approx 0.5$, leading to $\approx 0.5\%$ noise in the center and $\approx 5\%$ near the edge. Reproduced from [178].

they have, in the sense of fractal geometry, much more bulk than boundary both in 3D space and under vertical projection. However, we are curious about how this zeroth-order scattering statement generalizes to diffuse light and how it flows through 3D media such as cloudy skies.

As far as we know, not much can be proven analytically in full 3D RT in a scattering medium. Consequently, general statements about 3D RT phenomenology tend to be qualitative and substantiated largely by numerical experiments. The present authors have attempted to create at least one exception to this rule. There is a price, however, which is to use the asymptotic limit of 3D RT captured by diffusion theory and, moreover, to assume isotropic (rather than collimated) boundary sources. There is no doubt that many instances of solar RT in real clouds are in the diffusion regime, as compellingly demonstrated by King *et al* [186] using in-cloud radiometry. However, we already know that diffusion does not do so well in the radiative boundary layer, with a few MFPs from all boundaries. It appears that this is not a roadblock.

The details of the derivation are in the 2000 paper by Davis and Marshak [121]. Here we will only state, illustrate and discuss the 'theorem.' Let M be a 3D optical medium based on $M_0 = \{\boldsymbol{x} \in \mathbb{R}^3; 0 < x < L_x, 0 < y < L_y, 0 < z < H\}$: it is contained in a plane parallel slab of thickness H along the vertical and its spatial variability in M_0 is replicated cyclically in the horizontal plane with periods $L_{x,y}$ in the x, y directions, respectively. The medium is purely scattering ($\varpi_0 = 1$) and with horizontally averaged and scaled optical depth $(1 - g)\overline{\tau}$ sufficiently large for diffusion to be a reasonable model for the RT. Sources are uniformly distributed on cloud top ($z = 0$) but, as previously stated, modeled as isotropic, i.e. we neglect radiative boundary-layer effects in this solar case, with F_0 being the incoming flux, normal to the cloud top. Cloud base ($z = H$) is purely absorbing. We use the homogeneous cloud case as a reference for the total transmittance/reflectance computations, e.g. R_{1D} results from the *fixed* mean extinction

$$\overline{\sigma} = \frac{1}{L_x L_y H} \iiint_{M_0} \sigma(\boldsymbol{x})\,\mathrm{d}\boldsymbol{x} = \frac{\overline{\tau}}{H}.$$

We then compare to R_{1D} the corresponding outcome R_{3D} for any realization $\sigma(\boldsymbol{x})$ of the optical variability with the *same* mean. Note that holding the mean $\sigma(\boldsymbol{x})$ constant is equivalent to conserving mass, cf (9) for the relation between $\sigma(\boldsymbol{x})$ and scattering particle density.

The flow obeys $\nabla \cdot [\sigma_t(\boldsymbol{x})^{-1}\nabla J] = 0$ with Robin-type BCs $[1 - \chi\sigma_t(\boldsymbol{x})\partial_z]J|_{z=0} = 4$, $[1 + \chi\sigma_t(\boldsymbol{x})\partial_z]J|_{z=H} = 0$. Domain-average reflectance is then given by

$$R_{3D} = \overline{R(x, y)} = \frac{1}{2L_x L_y} \int_0^{L_x} \int_0^{L_y} J(x, y, 0)\,\mathrm{d}x\,\mathrm{d}y - 1.$$

A straightforward but tedious non-perturbative computation yields [121]

$$\frac{\delta R}{R_{1D}} = 3\chi\frac{\overline{\delta\sigma(\boldsymbol{x})\delta F_z(\boldsymbol{x})}}{\overline{\sigma}F_0}, \qquad (123)$$

where $\delta R = R_{3D} - R_{1D}$, $\delta F_z(\boldsymbol{x}) = F_z^{(3D)}(\boldsymbol{x}) - F_z^{(1D)}(z)$ and $\delta\sigma(\boldsymbol{x}) = \sigma(\boldsymbol{x}) - \overline{\sigma}$. So the relative change in R caused by 3D effects is proportional to the spatial correlation between

- fluctuations of extinction—hence of density—relative to and normalized by its mean value and
- deviations of net *vertical* flux from the 1D RT prediction (based on the mean extinction) and normalized by the incoming flux.

Figure 17 shows schematically how these quantities vary in opposite directions. This systematic anti-correlation will clearly dominate the spatial averaging. We thus predict that $\delta R < 0$: reflectance of a 3D cloud is always less than reflectance for the homogeneous medium with the same total amount of scattering material.

This prediction applies to the large-scale flow of radiation in (or around) clouds. The same forecast was made in section 5.1.2 based on the ICA as applied to domain averages. However, the present computation makes no such approximation. One can imagine 3D optical media decomposed into vertical columns of finite width where each column has the same total optical depth (large enough for diffusive transport to prevail), but the distribution of extinction
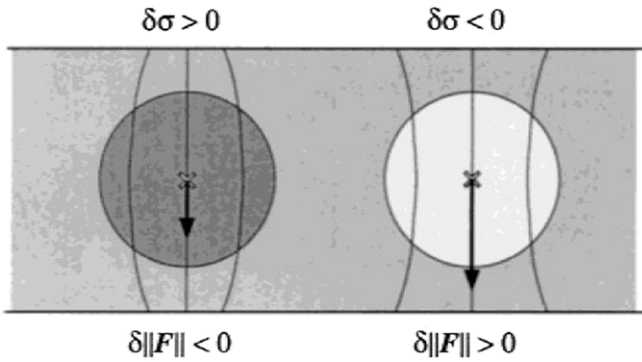
Figure 17. *Schematic of radiation channeling at a non-absorbing wavelength.* Regions with positive and negative fluctuations of extinction are illustrated for a geometrically plane-parallel cloud under uniform normal or diffuse illumination. They have opposite effects on the local values of the vertical component of the vector flux. Reproduced from [121].
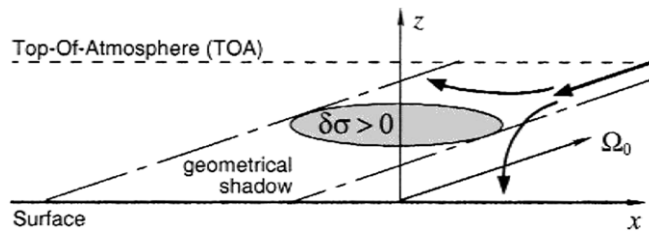

Figure 18. *Radiation channeling by a finite cloud under oblique illumination.* Both the reflected-to-space and transmitted-to-ground radiance fields are affected, positively by the flux deflected on the illuminated side, negatively by the shadowing. Reproduced from [121].

in each one is random. In this case of constrained randomness, $R_{ICA} = R_{1D}$ yet we still have $R_{3D} < R_{1D}$ because of how the radiant energy is 'channeled,' to adopt the expression of Cannon [187]. As seen in figure 17, the solar radiation is essentially reflected off the opaque regions of the cloud and concentrated into the tenuous ones.

The inherently 3D phenomenology of radiative channeling emerging from the above analysis is based, for simplicity, on an isotropic illumination scenario. The symmetry of the illumination can be thought of as a spatial average over the hemisphere illuminated at any one time by the Sun. However, the idea of a uniform cloud layer covering the planet as a reference is not very helpful. So it is of interest to ask about channeling in the case of a collimated and, in general, oblique illumination. Figure 18 illustrates this situation, and we see that the 3D cloud-driven perturbation of the flow contributes to the reflected light returning space *and* to the transmitted light that reaches the surface. We thus expect that 3D effects not captured by the ICA will largely, but not completely, cancel in quantities averaged over extended domains.

6.2. Large-scale fluxes for GCMs, small-scale fluxes for LES/CRMs

The essentially constant irradiation of the Earth with solar radiation, from the UV to the shortwave IR, is the primary

source of energy for the climate system. So the climate-driven task for RT is to compute across the whole solar spectrum how much energy is deposited at the surface, how much in the various parts of the atmosphere, and how much goes back to space. Other physical models take care of the rest of the story: what happens to the influx of solar heat as it is pooled with other types of heat flux (e.g. phase changes).

The fundamental quantity of interest here is $-\nabla \cdot \boldsymbol{F}_\lambda$ in $W\,m^{-3}\,nm^{-1}$. Once spectrally integrated, it is eventually converted into the solar contribution to the heating rate expressed in $^\circ\,day^{-1}$. By conservation of radiant energy (16) for steady sources, this rate can be computed from $\sigma_{a\lambda}(\boldsymbol{x})J_\lambda(\boldsymbol{x})$ as long as both direct and diffuse radiation are included, that is when the $Q_\lambda(\boldsymbol{x}) \equiv 0$ convention is used in (8) and the solar irradiation is captured in the BCs (37) for the RTE. So the kinetic recipe is simple: (i) determine what is the local density of radiant energy $J_\lambda(\boldsymbol{x})/c$ in $J\,m^{-3}\,nm^{-1}$ from (13), then (ii) multiply by the local collision rate $c\sigma_{a\lambda}(\boldsymbol{x})$ for radiative absorption processes in s^{-1}, then (iii) integrate over the solar spectrum. This is of course easier said than done with RT models. The spatial scale at which we wish to know $\int_0^\infty (-\nabla \cdot \boldsymbol{F}_\lambda)\,d\lambda$ will determine the approach. In the quest for improved methods for treating the spatial RT problem it is equally important to keep in mind that the spectral integration also has inherent error, which has been studied in great detail under the 1D RT assumption [188, 189]. From the end-user's perspective, only the total (spatial+spectral) error that matters, as well as the computational effort (in CPU cycles) it takes to get the answer.

Figure 19 illustrates schematically the two main situations encountered in atmospheric RT targeting the energy budget. The rather large domains spanned by a single cell in a typical GCM or a generic column in a CRM.

In the former case (upper left-hand panel), net horizontal fluxes are arguably of minor importance. Indeed, from our investigation of the spatial Green function in transmission or reflection, we suspect that horizontal fluxes will unfold at most over scales comparable to the thickness of the medium. In this case, the medium is much wider than it is thick. So there is at least a chance that horizontal fluxes will cancel. On the other hand, it matters greatly to get the vertical fluxes right. So it seems that we will have to address vertical correlations in clouds [190] sooner than their horizontal counterparts [191]. This is the ideal situation for the ICA and that approximation has indeed proven very effective in improving the problem of RT in GCM grid-cells; see section 7.1.

In the latter case (right-hand panel of figure 19), what is happening in neighboring columns clearly matters a lot. In this model for small-scale cloud processes, it is patently absurd to force the radiation to flow up and down ... yet that is what is done routinely. This is the effect of legacy: radiation parametrizations in CRMs are inherited from GCMs, the obvious place a dynamical modeler would go to find a radiation scheme. This radical modeling short-cut is certainly efficient, but is it justified?
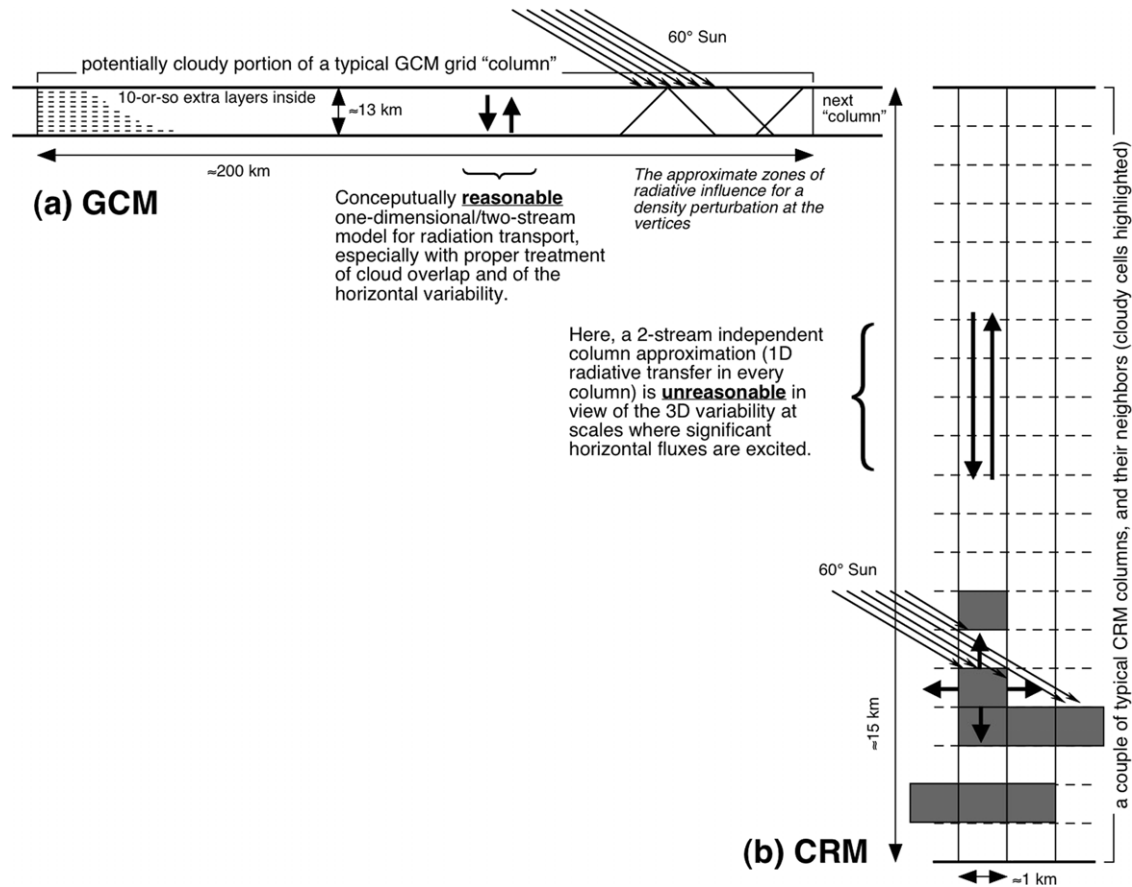
Figure 19. *Schematic of the GCM solar RT problem and the same for a cloud-process (CRM or LES) model.* The aspect ratio of the GCM grid-cell on the right-hand since it is very large; this is very helpful in simplifying the RT problem, largely by bringing the ICA to bear on the estimation of the domain-average heating rate profile. The aspect ratio of a typical column in a CRM or LES is roughly the inverse of that of the GCM grid-cell; this is a scenario for all kinds of 3D RT effects, starting with shadowing cells downstream from the Sun, and re-illuminating ones upstream. From [145].

Mechem *et al* [192] recently showed that it is justified to rely on the ICA based on an extensive study of coupled 3D RT (using SHDOM) and cloud dynamics (using the University of Oklahoma bin-microphysics LES) ... for *nocturnal* boundary cloud simulations. Of course, the only radiation in these studies was in the TIR spectrum, which is emission/absorption-dominated. Solar radiation by contrast is scattering-dominated. Although absorption by the surface or (gases and particles in) the air is a necessary ingredient for dynamical impact, scattering redistributes the radiant energy $J(x)$ in all three spatial dimensions in highly non-trivial ways. We are not aware of any systematic investigation of the impact of *solar* 3D RT effects (shadowing, channeling, etc) on cloud dynamics using computational multi-physics models. We suspect the effect can be significant. A preliminary study of 3D–1D solar RT differences in cloud dynamics using the community Weather Research and Forecasting model [193] led to a $\approx 10\%$ difference in precipitation during the life-cycle of a convective storm system (O'Hirok, personal communication).

In summary, it remains an open challenge to devise a way of computing 3D solar heating rates in 3D cloud models efficiently enough to be coupled to the fluid dynamics in the physics-based simulation.

6.3. Scale breaks: the spatial Green function revealed

6.3.1. The Landsat scale break. Without the benefit of angular and spatial integrations that promote cancellations, remote sensing signals (i.e. small-scale radiances) can be affected by 3D RT effects much more than domain-average fluxes. Consider high-resolution imagers such as the Thematic Mapper (TM) on Landsat with 30 m pixels, the Advanced Spaceborne Thermal Emission and Reflection Radiometer (ASTER), even the MODerate resolution Imaging Spectro-radiometer (MODIS) and the Multi-angle Imaging Spectro-Radiometer (MISR) with 15 m, 250 m and 275 m pixels, respectively on NASA's Terra platform. Every element of radiant energy in those small pixels that originated from somewhere else in the scene contributes to 3D RT effects that, by definition, are not captured by the IPA. These imaging systems indeed have pixel scales that are small compared with outer cloud scales, in particular, geometrical thickness H. Recalling that the spatial reach of the transmitted and reflected Green functions are, to a first approximation, $\sim H$. That is precisely how far we expect horizontal/non-IPA transport will routinely will reach.

Figure 20 shows the Fourier spectrum of a Landsat (≈ 30 m resolution) image of a small (≈ 60 km) portion of an
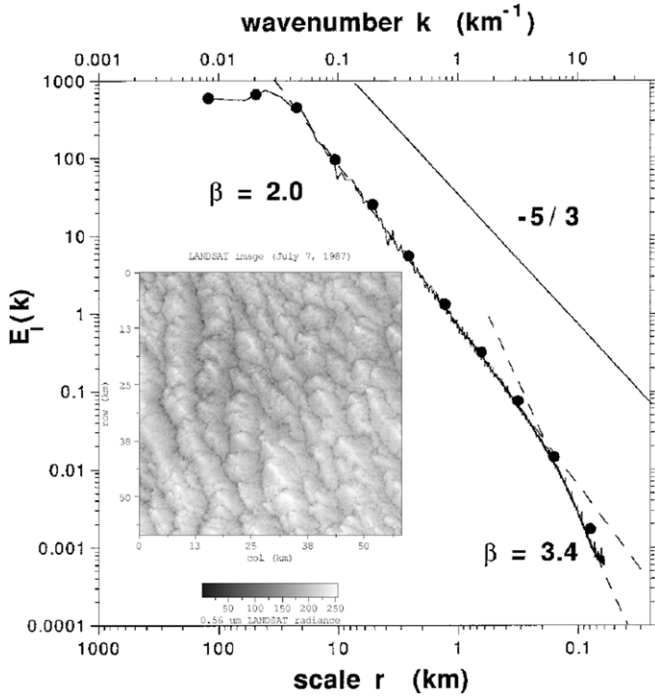
Figure 20. *The Landsat scale-break, as observed in Fourier space.* This wavenumber spectrum $E_I(k)$ for the nadir radiance field is the azimuthal average of the 2D Fourier mode energies for a large portion of a Landsat-5 TM image, itself of a small portion of marine Sc deck off the coast of Southern California. We observe three distinct regimes where $E_I(k)$ goes as $k^{-\beta}$: $\beta \approx 0$ (no spatial correlations), from $r = 1/k \approx 100$ to 30 km; $\beta \approx 5/3$ (turbulence), from 30 to 0.2 km; $\beta \gtrsim 3$ (radiative smoothing), from 200 m to the Nyquist scale 60 m. Full details in Davis *et al*'s paper [178]. The inset, from [151], shows a 61×61 km^2 portion of another Landsat image (0.52–0.69 μm channel) of the same cloud type captured during the same field campaign: the 1987 First ISCCP Regional Experiment (FIRE'87) [194].

extensive and persistent marine strato-cumulus cloud deck. Such clouds are major contributors to the Earth's global albedo, hence climate balance, hence are of considerable interest. It had been noticed [151, 195] that cloud radiance fields, as sampled by Landsat, exhibited a break in their $k^{-5/3}$ scaling around the equivalent in wavenumber space of about 1/3 to 1 km; at smaller scales (larger wavenumbers) there is a notable lack of variance relative to the extrapolated scaling law. Various explanations had been advanced for this scale break that involved a slew of processes ranging inherent cloud structure/dynamics ('it is real') [151] to a mismatch of the Thematic Mapper's sampling (instantaneous FOV) and true resolving power ('it is an artifact') [195]. Davis *et al* [178] explained the feature as a clear manifestation of 'radiative smoothing' [142, 196], which, in turn, is a direct consequence of horizontal transport of radiation over scales commensurate with $\langle \rho^2 \rangle_R^{1/2}$ from section 4 on Green functions. MC simulations of 3D RT in perfectly scaling multifractal cloud models were performed, which were considered at the time of heroic proportions (many multi-day runs). They showed that the scale associated with the critical wavenumber had the same behavior with respect to H, τ and even g, as the RMS horizontal transport distance, i.e. $\propto \sqrt{H\ell_t} = H/\sqrt{(1-g)\tau}$ from (94).

Radiative smoothing is always present but it is truly evident in wavenumber spectra only if $\theta_0 \lesssim 30°$. At more oblique illumination angles, brightening/shadowing effects (cf figure 18) produce a radiative *roughening* in the sense of enhanced amplitudes in Fourier space [197, 198]. This enhanced variability becomes manifest at scales determined by the amplitude of cloud-top height variations ($\lesssim H$) after projection along solar rays, hence $H \times \tan \theta_0$.

6.3.2. The Zenith-radiance scale break. If one can essentially visualize the spatial Green function for reflection in the Fourier spectrum of nadir radiance fields captured by space-based imagers with sufficient resolution, what about zenith radiance that reaches ground? Imaging is not an option but one can certainly point a narrow FOV (NFOV) radiometer upward at a ground station and collect a time series of zenith-radiance measurements $I_{zen}(\text{time})$. This is in fact quite easy to do, as long as radiometric calibration (and especially its maintenance) is not a requirement, as is the case here: only relative fluctuations are of interest, so the notorious 'arbitrary units' are good enough. Then, to interpret spatially what was measured temporally, Taylor's frozen turbulence hypothesis is invoked: $I_{zen}(\text{space}) = I_{zen}(\text{time})|_{\text{time=space/mean\_wind}}$.

The left panel in figure 21 shows $I_{zen}(x)$ from under an extensive St layer based on NFOV data for a non-absorbing (red) wavelength collected on 8 October 1998, at the Chilbolton Observatory (51.13°N, 1.43°W), UK, by Savigny *et al* [199, 200]; their sampling rate was 2 Hz, their longest record covered $\approx$4 h ($\approx$3 104 measurements), and they were able to collect on three other days during the same month. Rather than the frequency or wavenumber (Fourier) spectrum, the 2nd-order structure function was used: $\text{SF}(r) = \overline{[I_{zen}(x + r) - I_{zen}(x)]^2}$. It has the advantage that, if there are data drop-outs, they can simply be skipped. As for the k-dependence of the wavenumber spectrum, one naturally seeks power-law behaviors in r:

$$\sqrt{\text{SF}(r)} = \overline{[I_{zen}(x + r) - I_{zen}(x)]^2}^{1/2} \sim r^h, \qquad (124)$$

where h is the Hurst exponent, a.k.a. the (global) Hölder–Lipschitz exponent.

A variant of the Weiner–Khintchin theorem for non-stationary processes with stationary increments relates the wavenumber spectrum and the 2nd-order SF(r) [201]: they form a Fourier transform pair. In particular, if the spectrum scales as $k^{-\beta}$ with $1 < \beta < 3$ then $\beta = 2h + 1$ and, more generally speaking, $h = \min\{1, \max\{0, (\beta - 1)/2\}\}$. Recognizable scaling behaviors are $h = 0$ for all stationary processes (i.e. that are de-correlated over the associated range of r), $h = 1/3$ for turbulence-like variability (corresponds to a Fourier spectrum in $k^{-5/3}$, as for the simple fractal cloud model in figure 14) and $h = 1$ for all smooth (i.e. differentiable) fields. Interestingly, all three of these regimes are present in the right-hand panel of figure 21:

(i) at the smallest scales, up to the extent of the transmitted Green function, which is $\sim H$, $I_{zen}(x)$ is a smooth function ($h \lesssim 1$);
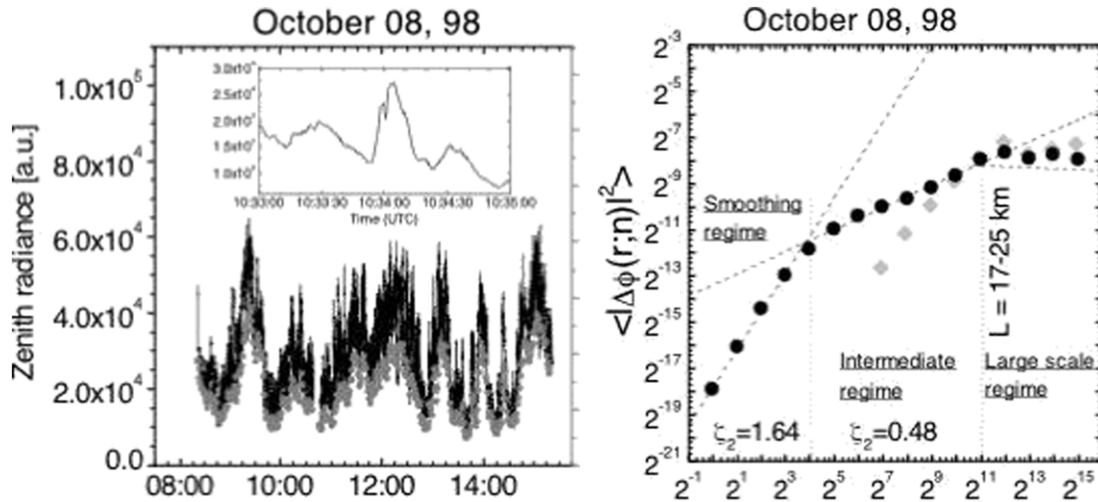
Figure 21. *The zenith-radiance scale break, as observed in the time domain using Taylor's frozen turbulence hypothesis.* Left: the solid black lines show the time series of I_{zen} in arbitrary units, resampled in order to show the whole record and leaving same visual impression as turbulence; the inset displays a small sample of the raw 2 Hz data showing the fully smoothed fluctuations. The bold gray points are for the *ground-based* time series of broadband flux; it behaves like a smoothed version of I_{zen}, but for a different reason: the angular integral of all the down-welling radiance corresponds to a large-scale spatial average determined by the cloud ceiling height. Right: SFs for I_{zen} and the broadband flux as functions of r expressed in samples. A nominal 5 m s^{-1} wind speed was used in the Taylor hypothesis and the exponent ζ_2 is denoted $2h$ in the main text. Reproduced from [199].

(ii) at the intermediate scales, the transmitted sunlight in $I_{zen}(x)$ follows the general turbulence-like structure of the cloud ($h \lesssim 1/3$);

(iii) at the largest scales, the fluctuations of transmitted sunlight are de-correlated ($h \approx 0$).

The small-scale behavior is as expected in a fully 3D RT regime where radiative smoothing occurs, noting that finite-size effects and noise prevent the empirical value of h from reaching the theoretical limit of unity. The two larger-scale behaviors are as expected in IPC/ICA regimes where the 1D RT model is a reasonable approximation, preferably adjusted for unresolved variability effects using one or another of the approaches described in section 5.1. Savigny *et al* [199] found the predicted transition from smooth behavior to turbulence-like behavior at time lags that translated (via Taylor's hypothesis) to spatial scales commensurate with the thickness of the cloud deck, which was known through a collocated millimeter-wave radar.

6.4. Retrievals of cloud properties

The above discussion of scale breaks is in the context of *forward* 1D RT modeling error. However, an immediate consequence is that the mapping of higher radiances to higher optical depths in 1D RT can be in error. At a minimum, the pixel adjacency effects manifested in radiative smoothing lead to PDFs of τ that are too narrow, but there can also be systematic biases due to unresolved variability. That is just a beginning. Numerous studies have focused on 3D-induced cloud remote sensing error (a few examples follow) and this issue continues to attract interest; see [202] for a recent statistical inquiry.

6.4.1. Cloud optical depth retrievals. The RT model used in standard satellite remote sensing retrievals of cloud properties is entirely 1D, being based on two main assumptions: clouds are horizontally homogeneous inside each satellite pixel (no unresolved variability effects), and the radiative effect of neighboring pixels is negligible (no resolved variability effects). Under these conditions, clouds can be represented as infinitely wide plane-parallel slabs with uniform, or possibly z-dependent, properties.

Horváth and Davies [203] quantified how frequently the above assumptions are met globally as a function of pixel scale using a high-resolution data set. Specifically, they used the above-mentioned MISR radiances reflected from water clouds over ice-free oceans. MISR views the Earth from the Terra platform at four VNIR wavelengths with nine cameras, ranging from a 70° zenith viewing forward through nadir to 70° viewing aft [204]. The time interval between the two most oblique observations is 7 min and the cross-track resolution is 275 m. Accurately co-registering the multi-angle observations, Horváth and Davies compared direct retrievals of cloud optical depth τ based on 1D RT [82] calculations for each camera. Their test used a passing rate based on 5% uncertainty as defined by the spread of the MISR pixel-scale retrievals across the nine cameras. Figure 22 shows the results of the comparison for clouds with $\tau > 3$. We see the passing rate increases with pixel size, i.e. clouds behave increasingly like plane-parallel slabs in direction space as the resolution is degraded. For a resolution of ≈ 1 km, only 20% of water clouds pass the test while at ≈ 10 km resolution this number increases to 35%. This does not prove that the retrieved τ is accurate (substantial effects are expected from unresolved variability at such large scales), but at least there is directional consistency with the 1D RT model.

For the above-mentioned MODIS instrument, which is onboard both Terra and Aqua platforms, Várnai and Marshak
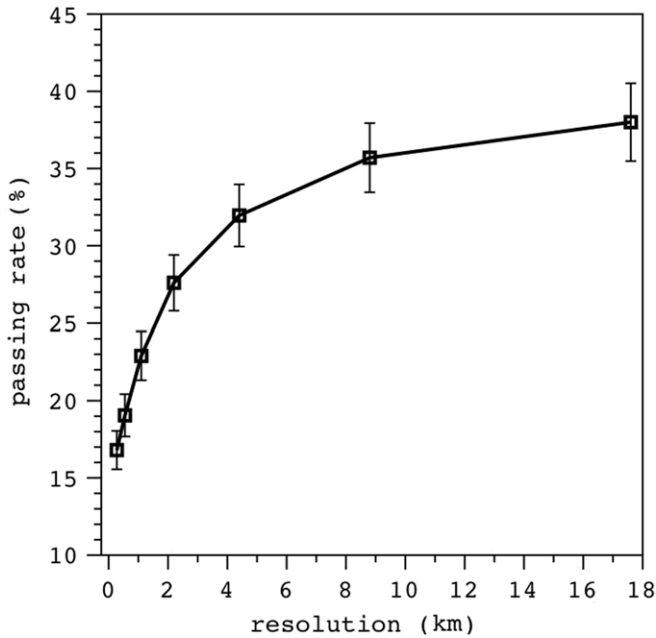
Figure 22. *Angular test for cloud '1Dness.'* Passing rate for Horváth and Davies' angular filter for 3D RT contamination is plotted as a function of pixel resolution. Clouds with (apparent) $\tau > 3$ were used. The tolerance for τ retrieval error, as defined by variance of the inferred τ across MISR's 9 cameras, was set to $\pm 5\%$. Reproduced from [203].

[205] used another criterion to study the effect of cloud inhomogeneity on optical depth retrievals. In contrast to MISR, MODIS takes measurements from a single viewing direction but at 36 wavelengths between 0.4 and 14 μm, with a spatial resolution of either 250 m, 500 m, or 1 km, depending on the wavelength[8]. MODIS operationally retrieves cloud optical depth τ and effective particle size r_e using the two-wavelength 1D Nakajima–King algorithm [206]. To quantify 3D RT effects, one can see that illuminated cloud pixels will appear systematically thicker than the shadowed ones, Várnai and Marshak combined MODIS' VIS and TIR images at 1 km resolution. Capitalizing on the strong thermal stratification of the atmosphere, TIR radiance variations can be used to retrieve cloud-top height, from there, normals are computed, followed by the pixel-scale solar incidence angle. The observed asymmetry between the sunny-side and shadow-side pixels was then used as a measure of the deviation of cloud structure from the assumption of plane-parallel geometry. Figure 23 illustrates the asymmetry for two SZAs: 30° and 65°. Each point here represents a separate 50×50 km^2 area. These panels show that 3D effects are much stronger for oblique illumination and thicker clouds. Based on 3D RT calculations for simple stochastic cloud models, Várnai and Marshak [207] suggested that the mean retrieval uncertainty caused by 3D effects can be parametrized in a simple linear form as

$$\delta\tau \approx \tau \times (\theta_0/300°), \qquad (125)$$

where θ_0 is the SZA expressed in degrees. For example, for

---

[8] Resolution degrades as λ increases, largely to keep the SNR at an acceptable level across the spectrum.

oblique illumination of $\theta_0 = 60°$, the relative error is in the order of $\pm 20\%$.

The first example includes only the (lower) liquid water clouds, while the second study accounts for all clouds: low and high, ice and liquid, overcast and broken. However, if the analysis is limited to Sc only, the retrieval errors caused by the 1D assumptions will be much lower. Indeed, 200–400 m thick marine Sc can cover areas of 1000 km in size and are, perhaps, the 'most plane-parallel' clouds [123]. As an example, Zinner and Mayer [208] first simulated 3D fields of marine stratocumulus at high horizontal resolution, and then used a sophisticated MC model [209] to calculate the radiation reflected from clouds, as it would have been measured by satellite instruments with different resolutions. Then they compared the results of 1D retrievals with the known cloud optical depths. They found that for MODIS' 1 km resolution, the 1D assumptions of neglecting resolved and unresolved variability result in errors within 5–20%, depending on SZA. Recently, Kato and Marshak [210] studied the dependence of cloud optical depth retrieval errors on solar and viewing geometries. Their marine Sc fields were generated using an LES-based cloud-process model [211] and satellite measurements were simulated with Evans' SHDOM model [170]. Based on their simulations and MODIS viewing and solar geometry, they concur with Zinner and Mayer, concluding that the error of cloud optical depth retrieval for marine Sc, at least over northeastern Pacific, was on average less than 10%.

6.4.2. Cloud droplet-size retrievals. When discussing the retrieval of cloud optical depth τ in the previous section, we implicitly assumed it to be independent of cloud droplet size, as defined conventionally by r_e in (3). This assumption is not generally valid and MODIS in fact retrieves the pair $\{\tau, r_e\}$ from two-band combinations [206]: one liquid water absorption band (1.6, 2.1 or 3.7 μm) and one non-absorbing band (0.65, 0.86 or 1.2 μm) [212], recalling from section 2.2 that $\sigma_a \sim r_e$ to a first approximation. The choice of non-absorbing band depends on the underlying surface. Since water absorbs differently in the three MODIS absorbing bands, the less absorbing (1.6 μm) band and the more absorbing (3.7 μμm) band complement the 2.1 μm band. Recall from diffusion theory in the presence of weak absorption (section 3.1.5) that reflected radiance originates primarily from a layer of thickness $L_d \sim (\sigma_a\sigma_t)^{-1/2}$ in (73), which is $\lesssim H$ if absorption matters. Thus, the trio of absorbing channels with different values of $\sigma_a(r_e)$ coarsely probes the vertical variation of droplet size in the upper portions of the cloud [213, 214].

The operational MODIS algorithm provides retrieval uncertainties for both τ and r_e for each cloudy pixel. This uncertainty is derived from the sensitivity of τ and r_e to plane-parallel homogeneous cloud top reflectance, quantified using partial derivatives of τ and r_e with respect to reflectance in both water-absorbing and non-absorbing bands [216]. The usual sources of uncertainty to be considered are calibration, atmospheric corrections and surface albedo. In this subsection, we discuss the further uncertainty in retrievals of r_e caused by
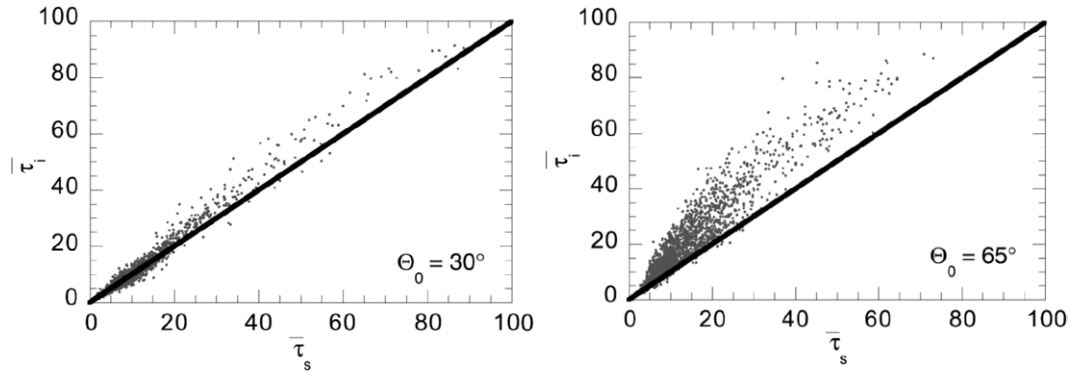
Figure 23. *Asymmetry of cloud optical depth retrievals between sunny-side pixels (vertical axis) and shadow-side pixels (horizontal axis).* Each point represents average optical depth in a $50 \times 50 \, km^2$ area. Only areas with cloud fractions larger than 10% were examined. Left: $\theta_0 = 30°$. Right: $\theta_0 = 65°$. Reproduced from Horvath A and Davies R 2004 Simultaneous retrieval of cloud motion and height from polar-orbiter multiangle measurements *Geophys. Res. Lett.* **31** L01102. Copyright [2004] American Geophysical Union. Reproduced by permission of American Geophysical Union.

unaccounted 3D cloud structure, both *resolved* (at scales larger than a pixel) and *unresolved* (at a sub-pixel scaled).

The effect of unresolved variability follows directly from the highly nonlinear relationship between reflectance and effective radius r_e, through the single-scattering co-albedo, $1 - \varpi_0 = \sigma_a/\sigma$. That relationship is monotonic (a good thing for remote sensing); specifically, it is a decreasing and convex function; to see this, we can think of $R(\infty) = 1 - A(\infty)$ in (75) as a rough approximation of how reflectivity depends on $1 - \varpi_0 \propto r_e$ at large but finite τ. Because of the strong convexity of $R(\infty)$ (in $-\sqrt{r_e}$), the ICA-type average of sub-pixel reflectances will be smaller than the pixel average of the effective radii [215]. In other words, ignoring sub-pixel variability of r_e always results in a retrieval that underestimates the true pixel-averaged value. The stronger the nonlinearity in the relationship, the larger the underestimation.

As compared with the effect of unresolved variability on the retrieval of r_e, the radiative effect of resolved pixel-to-pixel variability is not so straightforward. However, under some general assumptions (reasonable for large enough τ and r_e, say, $\tau > 10$ and $r_e > 5 \, \mu m$), Marshak *et al* [215] found that pixel adjacency effects will always increase the domain-averaged retrieved r_e with respect to the value that would be retrieved in a uniform plane-parallel surrounding. In other words, ignoring the resolved variability leads to an overestimation of the domain-average droplet size. Note that this is opposite to the negative bias from sub-pixel variability.

We illustrate here the retrieval of r_e using a cumulus cloud field generated with an LES model [211]. The cloud field consists of $100 \times 100 \times 36$ cells with grid sizes $66.7 \times 66.7 \times 40 \, m^3$, respectively. Figure 24(*a*) shows optical thickness and figure 24(*b*) cloud-top height. For simplicity, cloud droplet scattering has been described by a Mie phase function for constant $r_e = 10 \, \mu m$. For SZA at 60°, with illumination from the north (top of images) and a surface albedo α of 0.2, nadir radiance fields at the non-absorbing (0.67 μm) and water-absorbing (2.13 μm) wavelengths calculated with a MC code are shown in figures 24(*c*) and (*d*), respectively.

We now assume that τ and r_e are unknown. They are then inferred for each cloudy pixel from the pair of reflectances

$\{R_{0.67}, R_{2.13}\}$ using the Nakajima–King retrieval algorithm [206]. We will focus on the retrieval of r_e, comparing inferred values with the predetermined $r_e = 10 \, \mu m$.

We see in figure 24(*e*) that about 30% of all cloudy pixels have a saturated value of r_e at 30 μm. This is the area where $R_{2.13}$ is low. Low reflectance at 2.13 μm can result from either (i) small optical thickness, (ii) large effective radius, (iii) dark surface, (iv) 3D radiative effects, shadowing in particular or (v) any combination of the above. The average optical thickness, τ, of pixels with a retrieved value of $r_e = 30 \, \mu m$ is 24, which is quite large; the true r_e of those pixels is 10 μm, and the surface is relatively bright ($\alpha = 0.2$ at both wavelengths). Thus the most likely reason for small $R_{2.13}$ is shadowing.

The smallest scale in figures 24(*a*)–(*e*) is 67 m. Spatial averaging of the measurements improves somewhat the retrievals. Figure 24(*f*) shows the retrieved values of r_e when both $R_{0.67}$ and $R_{2.13}$ are averaged over 5×5 pixels (335 m) before the retrieval is performed. Indeed, the number of saturated pixels with respect to r_e decreased from 30% to 18%, i.e. averaging dilutes the shadowing effect, and thus lowers the retrieved value of r_e.

It is interesting to relate the retrievals of r_e to the retrievals of optical thickness τ. Following Cornet *et al* [217], we subdivide all cloudy pixels into two categories based on their retrieved values of cloud optical thickness. Pixels where the true optical thickness, τ_{3D}, is larger than the retrieved optical thickness, τ_{1D}, will be called 'shadowed' while pixels with $\tau_{1D} > \tau_{3D}$ will be called 'illuminated;' see figure 25. As was pointed out by Cornet *et al*, the retrieved r_e in the shadowed regions ($\tau_{1D} < \tau_{3D}$) are much larger than the ones in the illuminated ones ($\tau_{1D} > \tau_{3D}$), as if there was more absorption [118, 218, 219]. To conclude, overestimation of r_e corresponds to underestimation of τ.

6.5. Aerosol optical depth retrievals, near broken clouds

Aerosols are very poorly understood agents in the climate system, particularly their impact on cloud optics [16] and physics [15]. Aerosol optical thickness (AOT) is therefore a high-value retrieval from satellites because global coverage
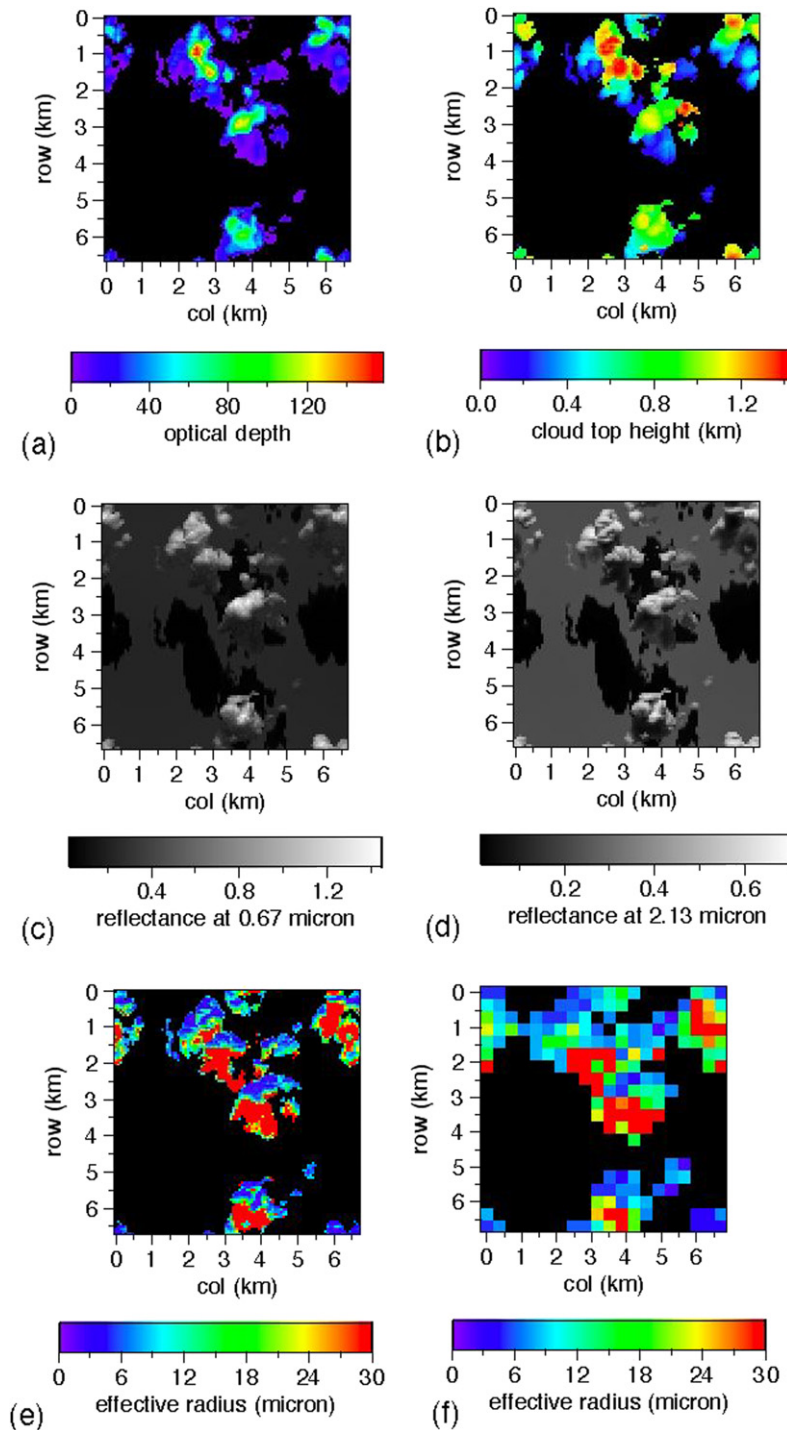
Figure 24. *3D RT effects in cloud droplet-size retrievals.* (*a*) Cloud optical thickness field. (*b*) Cloud-top height above the surface. The cloud is illuminated from the north with a 60° SZA. Droplet scattering is described by a Mie phase function computed with $r_e = 10\,\mu$m. The surface is assumed to be Lambertian with uniform spectrally invariant surface albedo 0.2. (*c*) Nadir reflectance fields at 0.67 μm calculated by MC with 5×10^8 histories. The average simulation error is less than 2%. (*d*) Same as in panel (*c*) but for nadir reflectance at 2.13 μm. (*e*) r_e retrieved from reflectances on panels (*c*) and (*d*). (*f*) Same as in (*e*) but for reflectances averaged over 25 pixels. Reproduced from [215].

is necessary to track the long-range transport and property evolution of the airborne particulates, starting at their sources. Some are anthropogenic, coming from industrial activity, deliberate biomass burning and all manner of land-use change.

Numerous studies based on satellite observations have reported a positive correlation between cloud amount and AOT [222–226]. This positive correlation can be explained

as a result of physical phenomena such as the humidification of aerosols in the relatively moist cloud environment, or it can result from remote sensing artifacts such as cloud contamination of the cloud-free fields of view used in the aerosol retrievals.

There are two ways that clouds affect the retrievals of aerosols [137]: (i) the existence of small amounts of sub-pixel
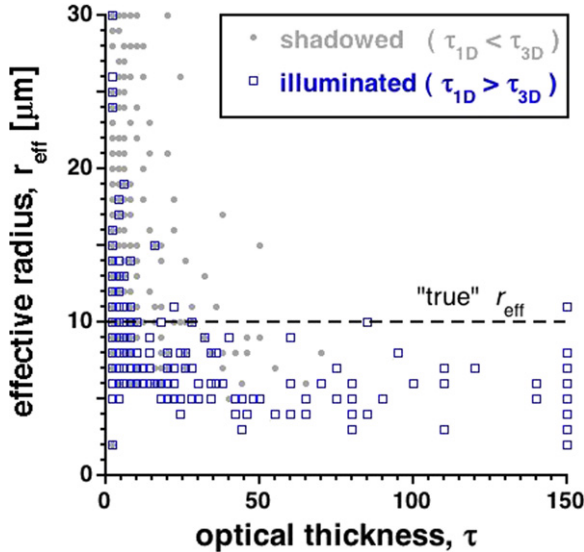
Figure 25. *Correlation between retrieved r_e and τ for 'illuminated' and 'shadowed' areas in the Cu cloud field in figure 24.* Radiance was averaged over 2×2 pixels (134 m grid). The horizontal dashed line indicates the true $r_e = 10\,\mu$m, prescribed uniformly across the simulated cloud scene. Note that the maximal allowable retrieval value was set to 150 for optical thickness τ and to $30\,\mu$m for effective radius r_e. Reproduced from [215].

size clouds in pixels identified as being cloud-free and (ii) an enhancement in the illumination of the cloud-free column through the reflection of sunlight by nearby clouds. When the pixels are relatively large, only the first type (unresolved variability), cloud contamination is considered. The second type (resolved variability), also called the 'cloud adjacency effect,' is more pronounced when satellite pixels are relatively small (e.g. ∼0.5 km for MODIS and MISR). Kobayashi *et al* [227], Cahalan *et al* [228], Nikolaeva *et al* [174] and Wen *et al* [220] studied the cloud adjacency effect when cloud-free pixels are brightened by reflected light from surrounding clouds using 3D RT calculations. Both cloud contamination and the cloud adjacency effect may substantially increase reflected radiation and thus lead to significant overestimates of the AOT. However, these two types of cloud effect have different impacts on the retrieved AOT:

- sub-pixel clouds increase AOT by increasing the apparent contribution due to large particles (aerosol 'coarse' mode composed of sea salt, dust, etc);
- cloud adjacency mostly increases the apparent contribution due to small particles (aerosol 'fine' mode composed of smoke, ash, pollution, gas-to-particle conversion products, etc).

We illustrate here the effect of cloud adjacency for broken cumulus clouds as observed by MODIS and ASTER. ASTER views the Earth from nadir direction at high (15 m) spatial resolution [229]. Figure 26(*a*) shows a $68 \times 68\,km^2$ ASTER image of a region in Brazil taken on 25 January 2003, when biomass burning occurred. The $15 \times 15\,km^2$ box in the left lower corner is also zoomed in figure 26(*b*). The original 15 m resolution imagery was aggregated to the 90 m resolution and cloud optical depth τ was retrieved. Wen *et al* [220] then used

3D and 1D RT calculations to determine the cloud-induced 'enhancement' as the average difference between the 3D and 1D reflectances for all cloud-free pixels

$$\delta R = \overline{R_{3D}(x, y) - R_{1D}}. \qquad (126)$$

Figure 26(*c*) shows the cloud-induced enhancement field $R_{3D}(x, y) - R_{1D}$ in clear-sky regions at $0.47\,\mu$m, assuming the same amount of aerosols (AOT $= 0.1$) for the whole scene. We see that clouds enhance the reflectance almost everywhere; the average enhancement δR is 0.019, which corresponds to roughly 0.1–0.2 increase in AOT. From the climate modeling perspective, this enhancement is much too large to be ignored [230]. As shown by Wen *et al* [231], 80% of this enhancement is due to cloud-to-molecule scattering interaction even though the Rayleigh optical thickness at $0.47\,\mu$m, 0.186, is not much larger than the AOT. However, aerosols are forward-peaked scatters, although less than cloud droplets (with $g \approx 0.7$, down from 0.85). So the broader vertical distribution of molecules and the lateral illumination geometry from clouds to intra-cloud regions with substantial fractions of their local direction space covered by bright illuminated cloud boundaries favor the near-isotropic scattering of molecules toward space. In more quantitative terms, scattering angles encountered in the retrievals of aerosol properties are typically between 90° and 130° and, in this range, phase functions for aerosols are much smaller than the Rayleigh phase function; see figure 3 where the H–G model, as a representative of typical aerosol scattering, is about an order of magnitude lower than Rayleigh.

Figure 27 demonstrates a striking example of a good correlation between clear-sky reflectances observed by MODIS (on the same Terra satellite as ASTER) and simulated reflectances for the same pixels that were generated assuming constant aerosol optical thickness throughout the whole scene plotted in figure 26(*a*). The simulated clear-sky reflectance values were obtained through 3D RT calculations that account for the distribution of cloud optical properties retrieved from MODIS and ASTER radiances. The correlation between observed and simulated values indicates that, in reality, higher clear-sky reflectance is not necessarily caused by larger AOT. It could rather be a 3D RT effect of Cu clouds in neighboring areas. How to unravel real and apparent variations of aerosol quantity and quality in the vicinity of clouds remains an open research question in remote sensing science.

7. Mitigation of 3D damage to 1D RT modeling

For the past couple of decades, we have seen increasing effort by atmospheric 3D RT specialists to bring to the broader community of RT end-users practical ways of making their modeling more realistic than with the familiar 1D RT they use, often without questioning its applicability. This is true for applications to radiation energy budget estimation as well as to cloud, aerosol and surface remote sensing.

7.1. Large-scale fluxes for GCMs, small-scale fluxes for LES/CRMs

At first glance, the problem of 3D RT through an atmospheric column populated with broken and/or multiple cloud layers
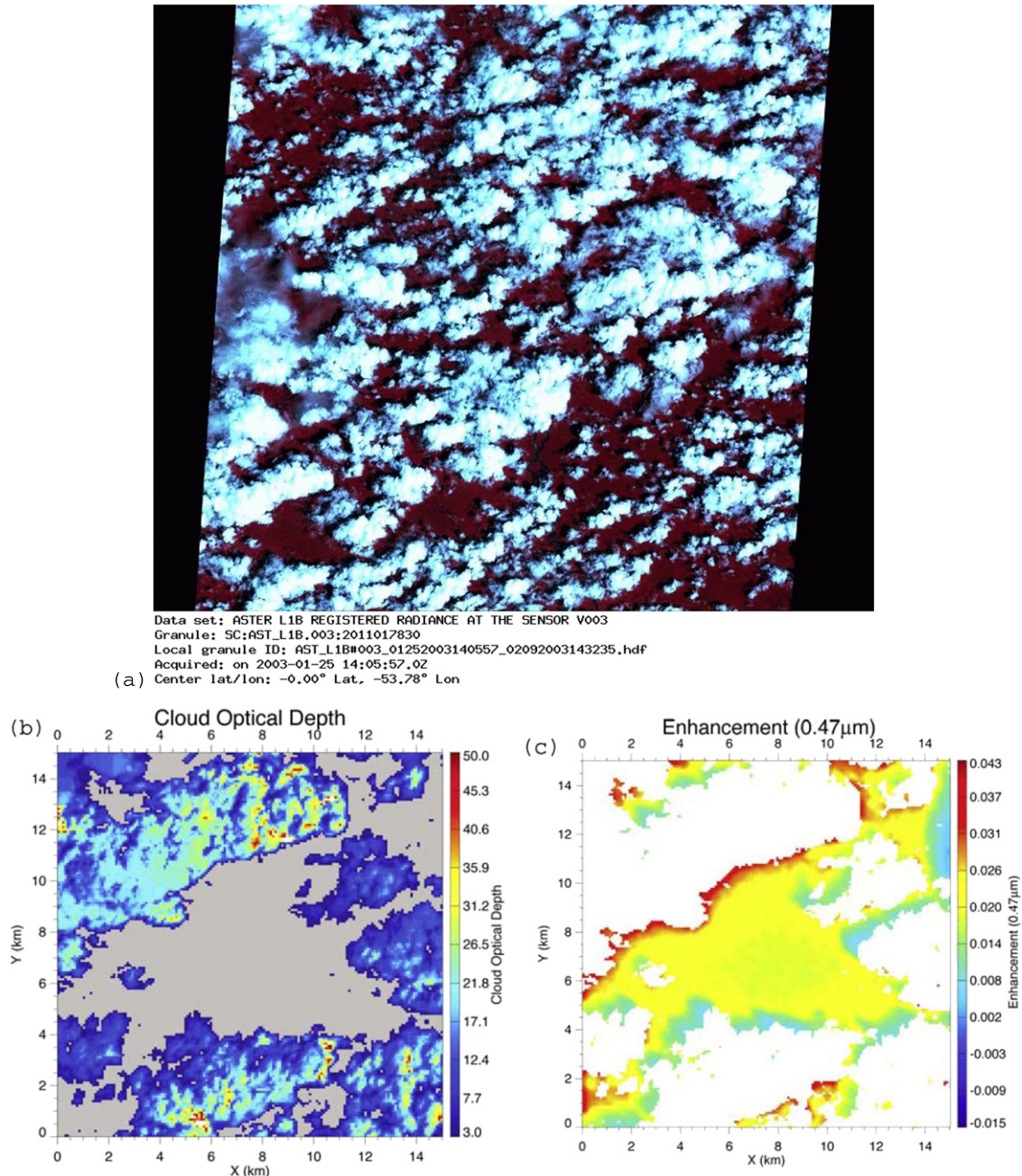
Data set: ASTER L1B REGISTERED RADIANCE AT THE SENSOR V003
Granule: SC:AST_L1B.003:2011017830
Local granule ID: AST_L1B#003_01252003140557_02092003143235.hdf
Acquired: on 2003-01-25 14:05:57.0Z
Center lat/lon: -0.00° Lat, -53.78° Lon

Figure 26. *Impact of cloud-induced 3D RT on clear-sky nadir radiances and associated aerosol retrievals.* (*a*) ASTER image centered at (0°N, 53.78°W) acquired on 25 January 2003. Panels (*b*)–(*c*) are zoomed into the lower left-hand corner. (*b*) Cloud optical depth retrieved from ASTER at 90 m resolution. The cloud cover is 59%; average cloud optical depth is 14. *(c)* Enhancement of reflected radiation due to 3D RT effects for clear regions at 0.47 μm. Cloudy pixels are masked as white. The mean enhancement δR in (126) is 0.019. Reproduced from [220].

seems intractable, except maybe with heavy-duty numerical methods. Depending on what radiative properties are targeted, that first impression may be quite inaccurate.

7.1.1. The GCM solar RT problem. Consider the problem described in section 6.2 on computing solar heating rates (i.e. broadband radiative flux divergence) in large domains such as GCM grid-cells, ~100 km on a side. Surely we can start by neglecting radiative interactions with neighboring regions since the vertical extent of the cloudy layer (10–15 km) is small by comparison with the horizontal size. Moreover,

in mainstream GCMs only a few pieces of information are provided about the clouds, layer-by-layer: cloud fraction, mean cloud optical depth (and maybe its variance), as well as cloud optical properties resulting from microphysics (especially ϖ_0 and g for the 2-stream computation) as functions of wavelength.

This is clearly fertile ground for all three classes of 3D RT techniques overviewed in section 5.1 that address unresolved variability: homogenization/effective medium, ICA and mean-field approaches. They have all been used with varied degrees of success. However, we must note that, until quite
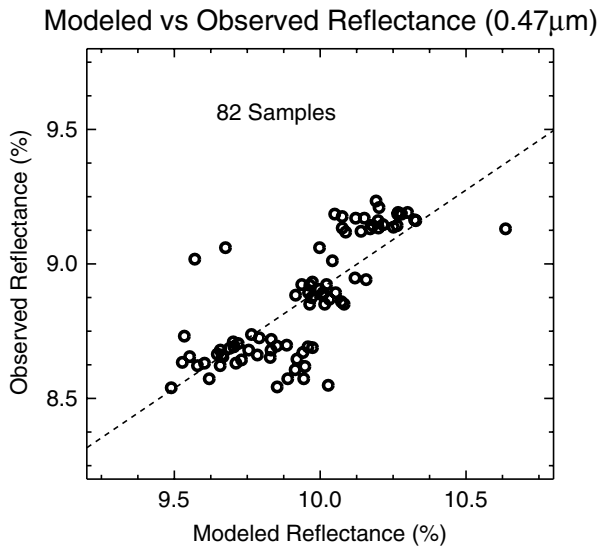
Modeled vs Observed Reflectance (0.47μm)

Figure 27. *Reflectance measured by MODIS versus 3D RT simulations assuming constant AOT.* The plot includes those 0.5 km pixels that were used in calculating operational MODIS aerosol product at 10 km resolution [221]. This figure was graciously contributed by Dr Guoyong Wen (NASA-GSFC/UMBC-GEST).

recently, it was not clear what 'success' means. This is indeed a situation where we know that doing nothing leads to systematic bias, by Jensen's inequality. But the extra burden in CPU cycles is a serious concern, any improvement must be computationally cost-effective. So this led to a burst of creativity in the 3D RT community during the 1990s described briefly in section 5.1 and in more depth by Barker and Davis [114] in a relatively recent survey. In the mid-2000s, the steady progress in computer hardware performance enabled the emergence of CRMs, leading to MMFs. At the same time, it made MC the standard approach in 3D RT. So, even though the RT embedded in CRMs is still 1D (cf section 7.1.2), they deliver 3D cloud structures of immediate relevance to GCMs. CRMs were developed largely for that purpose. Computing vertical profiles of the *domain-average* radiative heating rate with MC is now very feasible, and approximating that outcome is the goal of any new parametrization of RT in GCMs.

There has not been a systematic comparison of the numerous *candidate* 3D RT models for unresolved cloud variability based on the above-mentioned testbed provided by CRMs and MC, not even of one representative from each of the three categories. However, a major comparison study of all *existing* 1D RT models has been performed [12]. A key player was the gamma-weighted two-stream approximation (GWTSA) of Barker co-authors [127–129] described in section 5.1.2 and used to illustrate the *statistical* version of the ICA. A clear winner emerged from the comparison study that generalized the GWTSA: the MC independent column approximation (McICA) model developed, specifically with GCMs in mind [232]. McICA is an efficient numerical method of estimating large-scale broadband boundary fluxes and flux-divergence profiles, hence radiative heating/cooling rates, that is unbiased with respect to the *local* ICA standard used in

CRMs. It creatively merges the concepts

- of MC, viewed simply as a robust random quadrature method (rather than a numerical solution of the 3D RTE) and
- of IPA, appropriately renamed ICA (for independent *column* approximation) in this context of radiation energy budget computation, where there are no pixels *per se*.

Recall that we target here the domain-average broadband fluxes, hence spatial–spectral-angular integrals of the radiance field that matter for the energy budget in a single grid-cell of a GCM. Since such domains extend for 50–200 km in both horizontal directions, one can capitalize on the quasi-cancellation of all localized 3D RT features affecting both reflection and transmission. Ideally, we would like to bring the residual 3D–1D (spatial domain) RT modeling error down to the level already accepted by the GCM community for the spectral-domain computations. McICA basically pools these inevitable modeling errors and uses a random quadrature rule for the *combined* spatial and spectral integrations. This has the curious effect that, for one sample in a McICA sub-gridscale computation, a cloudy sub-column is randomly generated (with specified rules) and assigned a random wavelength.

In spite of the MC part of the acronym, there is actually no 3D RT going on here beyond the above-mentioned test cases for model performance assessment/comparison. The statistical version of the ICA is accepted as good enough for the climate modeling application at hand. However, current GCMs predict at best a fractional cloud coverage of the horizontal domain *for each of many atmospheric layers*: $A_c(n)$ for the nth layer. The most basic optical properties for the cloudy and clear portions are also predicted, only those required by the two-stream/diffusion 1D RT model: optical depth τ, single-scattering albedo ϖ_0 and asymmetry factor g. See section 3.1.3 ($\varpi_0 = 1$) and section 3.1.5 ($\varpi_0 < 1$) and also refinements in the literature accounting for the collimated solar beam directly transmitted to layer n [70]. Since, by definition, the ICA makes no attempt at the RT impact of spatial correlations of cloud structure in the horizontal plane, the only remaining issue is how to distribute the cloudy portions of the GCM grid-cell vertically. How to place it in layer n, in view of clouds in neighboring layers $n \pm 1$?

The generally accepted rule is known as the 'maximum/random overlap' rule: if two adjacent layers have non-vanishing $A_c(n)$, then the cloudy portions are required to overlap as much as possible; if there is a cloud-free layer between two cloudy ones, overlap is random. It is not easy to work out the combinatorics underlying this rule explicitly [12]. So, at the spatial core of the McICA model is a stochastic sub-column cloud generator that circumvents this awkward maximum/random overlap rule and uses instead a simple exponential decorrelation law [233]. The price to pay for the elimination of any intra-ICA modeling bias by adopting McICA sampling is of course the numerical noise inherent to the MC quadrature method. So we have to ask, in the context of GCMs: is accuracy more important than precision? In an application where the proper partition of the energy budget matters a lot,

we of course require an accurate (unbiased) answer and, moreover, experimentation has shown that GCM models can assimilate dynamically a considerable amount of MC integration noise [234].

In summary, McICA has proven to be a very good stop-gap solution in GCM-driven RT modeling that balances adaptively the error in spectral and spatial integrations. Over the past few years, the McICA has been adopted by most GCMs [235], including the majority of those mature enough to be used in the comprehensive assessments and forecasts of the anthropogenic effects on the climate system published on a regular basis by the Intergovernmental Panel on Climate Change (IPCC) [11, for the most recent release].

7.1.2. The LES/CRM solar RT problem.

What about LES-based cloud-process models and CRMs? And, by extension, what about those 'research' GCMs that incorporate CRMs in each ∼100 km cell? Based on our discussion in section 6.2, the associated ranges of scales (tens of meters to a few kilometers for LES, and 1 km to 100 km in CRMs) are highly vulnerable to inherently 3D effects, especially in the LES range. If the dynamical cloud model is used in lieu of the stochastic sub-column cloud generator in the McICA, little difference is noted in the domain-average fluxes [236]. That is to say that, as far as the radiative part of the large-scale energy budget is concerned, added realism in cloud representation has a small impact within the framework of 1D RT. The remaining question is the quantitative impact of 3D RT effects *not captured by the ICA* on the detailed cloud dynamics, as captured by CRMs. If it has little impact, then why? The issue cannot be put to rest confidently unless there is sufficient understanding. If it does, then what can be done about it in a practical way? How does one design representative case-studies and, since 3D MC will be the almost unavoidable benchmark, how can we guarantee uniformly accurate heating rates across a large CRM grid?

At the time of writing, these remain open questions. For a survey of the highly desirable class of 3D RT approximation (efficient-yet-accurate-enough) models that target the detailed spatial distribution of solar heating rates, we refer the interested reader to Davis and Polonsky's relatively recent review [145, and citations therein].

7.2. Cloud remote sensing, corrected for 3D RT effects

In the previous subsection, we have gone from the GCM issue of unresolved cloud variability, and its state-of-the-art McICA solution, to the current challenge of 3D 'adjacency' effects of individual cloudy cells in LES models or CRMs. Moving on to radiances instead of fluxes, and narrow-band spectral sampling rather than broadband integration, we now address remote sensing concerns.

Here, the pixel scale can be too small for 1D RT to be anywhere near realistic, even if the clouds are stratiform (near-plane-parallel outer geometry). More precisely, the pixel footprint is so small that, even if it were internally homogeneous, net horizontal fluxes coming from denser or more tenuous neighboring pixels will affect observed radiances at cloud top or cloud base. Can we mitigate local biases caused

by radiative interactions between adjacent small-scale pixels, and thus estimate what a 1D RT treatment of a real 3D cloud would yield?

Alternatively, can't we just retroactively make the pixel big enough that we can ignore these net horizontal fluxes and focus only on the pixel-average vertical transport? Maybe, but this tactic of avoidance (as opposed to mitigation) leads right back to the issue of unresolved variability that will then have to be accounted for.

7.2.1. Nonlocal independent pixel approximation (NIPA).

We describe here a specific method proposed as a step toward improved accuracy of cloud property retrievals based on the business-as-usual procedure involving 1D RT models. We first consider satellite imagery, and then ground-based time series measurements of zenith radiance where the notion of a pixel is replaced by a short radiometric exposure to down-welling diffuse radiation within a narrow FOV instrument.

With their ∼30 m pixels, NASA's series of Landsat missions, carrying Thematic Mapper instruments, are by far the most popular assets delivering high-resolution cloud imagery, high enough that it is affected significantly by adjacency effects, cf section 6.3.1. To the best of our knowledge, the first deliberate attempt to go beyond quantification and attempt to mitigate this inescapable 3D RT effect in clouds was by Marshak *et al* [237] who proposed the 'nonlocal IPA' (NIPA).

NIPA is based on the intuitive idea that multiple-scattering processes cause an *apparent* smoothing of the cloud structure, as observed in the remotely sensed radiance field [142, 196, 178]. Rather than run a full 3D RT simulation with an expensive MC code, or even a more efficient grid-based solver such as SHDOM [170], one can simply apply a low-pass filter (smoothing kernel) to the IPA prediction, the computational cost of which has already been accepted. This approximate 3D RT method works well, at least for stratiform clouds under near-normal illumination.

We note that what is required here is the Fourier transform $\tilde{P}(\vec{k})$ of the smoothing kernel $P(\vec{\rho})$ since we wish to perform the convolution product of P and the IPA-derived radiance field $I_{\mathrm{IPA}}(\vec{\rho})$ in the horizontal plane:

$$I_{\mathrm{NIPA}}(\vec{\rho}) = \iint P(\vec{\rho}')I_{\mathrm{IPA}}(\vec{\rho} - \vec{\rho}')\,\mathrm{d}\vec{\rho}', \qquad (127)$$

which becomes a simple product in Fourier space, $\tilde{I}_{\mathrm{NIPA}}(\vec{k}) = \tilde{P}(\vec{k})\tilde{I}_{\mathrm{IPA}}(\vec{k})$. The Fourier-space reflected Green functions for point-wise illumination can be put to use here. They will depend parametrically on H, τ, g and ϖ_0. Depending on whether local albedo or nadir radiance is targeted, we could choose a spatial Green function for isotropic (section 4.1) or normal [108] illumination.

Marshak *et al* [237] had an even more pragmatic approach. Eschewing normalized solutions in Fourier space of boundary-value PDE problems, they used a convenient two-parameter expression like (110) but for ρ instead of τ and averages based on cloud radiative Green functions. The authors did their proof-of-concept computations with cloud models having optical depth variability in a single horizontal direction, say, x.

The required 1D Fourier transform of (110), with $\tau \mapsto |x|$ and division by 2 (to cover the support extended to all of $\mathbb{R}$), yields

$$\tilde{P}(k) = \frac{\cos\left[a\tan^{-1}\left(\frac{\langle|x|\rangle k}{a}\right)\right]}{\left[1 + \left(\frac{\langle|x|\rangle k}{a}\right)^2\right]^{a/2}}. \qquad (128)$$

This smoothing kernel acts in Fourier space as a particular kind of low-pass filter; features rather gentle power-law cut-offs in k^{-a} at wavenumber $k^\star \approx 1/\langle|x|\rangle_R$. z

Power-law tails in $\tilde{P}(k)$ are a natural choice to reconcile the spatial correlations observed in satellite images of extensive stratocumulus [178] with those observed with airborne *in situ* probes [148] for the same type of cloud system. The latter have scale-invariant (power-law) internal structure, obviously driven by turbulence; specifically, one finds extinction (actually, LWC) fluctuations in $k^{-5/3}$, typically over scales from approximately tens of kilometers down to tens of meters. Satellite (nadir-looking) radiances also have this trend, which follows from the IPA (a nonlinear but monotonic mapping of local τ to local radiance), but only down to a scale found by numerical simulation to be $\approx\sqrt{\langle\rho^2\rangle_R}$ [196, 178]. Above the associated cut-off wavenumber, a trend approaching k^{-3} is found.

Figure 28 illustrates the NIPA procedure for the fractal model for variable stratiform clouds described in figure 14. The differences between MC, IPA and NIPA are easy to see. The upper panel shows, on the one hand, $\tau(x)$ for a 2 km portion of the synthetic fractal cloud that extends to 12.8 km (and is periodically replicated beyond that). On the other hand, both MC and IPA predictions are plotted for the local albedo: we see how the IPA responds immediately to the fractal variability while the MC results are much like a running mean over several pixels. The lower panel shows MC, IPA and NIPA predictions for the local value of nadir radiance over the same portion of cloud. By comparing the two registered panels, we see that the MC radiance field is not as smooth as its counterpart for albedo, patently because there is no angular integration. The NIPA computation used the smoothing kernel in (128) with $\langle|x|\rangle = 0.1$ km (8 pixels) and $a = 0.5$. Finally, the bottom curve shows how much the prediction error with respect to MC 'truth' is reduced by going from the IPA to the NIPA.

That completes the description of NIPA as a means to improve the realism of the *forward* IPA model by introducing scale-specific smoothness. The *inverse* NIPA consists in taking actual or synthetic cloud radiances and applying the corresponding roughening filter to restore the IPA and, from there, perform straightforward retrievals of (say) the cloud optical depth field. Formally, that amounts to solving (127), viewed as an integral equation, for $I_{\text{IPA}}(\vec{\rho})$ knowing $I_{\text{NIPA}}(\vec{\rho})$ from 3D RT computations, as in the present demonstration or from observations [238].

In an ideal (infinite-accuracy, noiseless) world, one only needs to perform the inverse FFT of $\tilde{I}_{\text{IPA}}(\vec{k}) = \tilde{I}_{\text{NIPA}}(\vec{k})/\tilde{P}(\vec{k})$. However, $1/\tilde{P}(\vec{k})$ is a high-pass filter that will amplify any
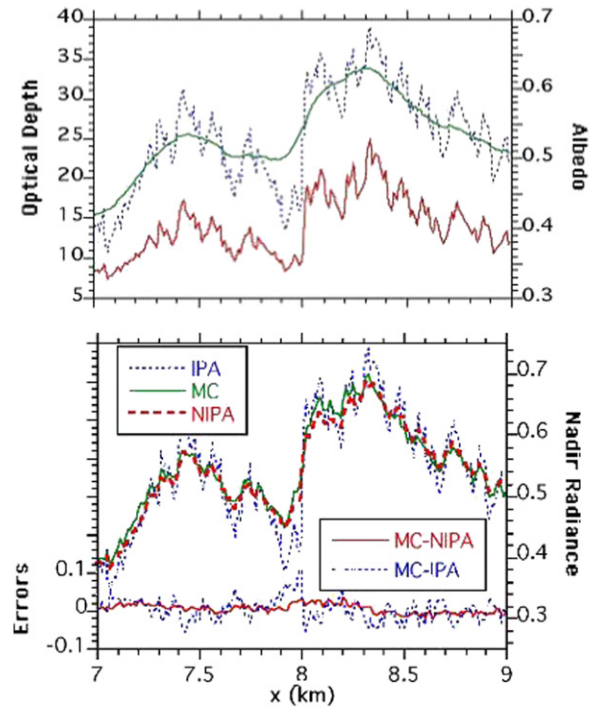

Figure 28. *Comparison of simulated reflectivity fields for a portion of a fractal stratocumulus cloud.* Top: on the left-hand axis, we read the 1D horizontal variation in x of local optical depth $\tau(x)$ (lower curve); the vertically uniform cloud is generated with a 10-step bounded cascade process described in figure 14 with $\bar{\tau} = 13$ and $H = 0.3$ km (pixel/grid-scale = 12.5 m). The upper curves (right-hand axis) in the same panel show the associated fluctuations of albedo $R(x)$, the normalized up-welling flux in (49) for steady and uniform illumination, using both IPA and MC schemes; SZA is $22.5°$ and scattering is according to a Deirmendjian C1 phase function at a red wavelength for simplicity (both water- and land-surface albedoes are negligibly small). Bottom: the right-hand axis is the same as in the top panel but for normalized nadir radiance in (41) rather than hemispherical flux, under the same conditions of spatially uniform and steady illumination, and the computational NIPA scheme is added. The lower curves (left-hand axis) highlight the reduced error with respect to MC when NIPA is used instead of IPA. Reproduced from [150].

noise or small-scale numerical error. This is a classic ill-posed (i.e. numerically unstable) inverse problem. Marshak *et al* [237] demonstrate on 'observations' obtained with a MC code (where the 'truth' is known) that careful Tikhonov-type regularization [239] can be used to estimate $I_{\text{IPA}}(\vec{\rho})$ even in the presence of considerable noise from the MC scheme itself and, from there, obtain reasonable estimates of the local value of τ from a pre-computed inverse map of τ to nadir radiance based on 1D RT.

7.2.2. Other 3D–1D RT compensation methodologies. NIPA's use of spatial Green functions is not unique in the field of efficient 3D–1D RT compensation techniques. A notable effort involves an adjoint perturbation formalism for forward 3D effects as defined by $\delta E = E_{3D} - E_{1D} = (f, I_{3D} - I_{1D})$ from (122), where f is used to define a specific feature of interest, such as an instrument response. The perturbation $I_{3D} - I_{1D}$ is evaluated from spatial Green functions operating on the perturbed transport and scattering operators in (116). Formal

expansions were derived to arbitrary order [240] and the first-order theory was worked out on specific examples [241].

Neural networks were also brought to bear by Cornet and co-authors on the problem of forward 3D RT [242, 243] and inverse 3D RT based on simulated observations [244–246]. Another statistical approach based on multivariate regression has been explored [247]. All these algorithms show a substantial improvement in retrieval accuracy. However, all of them are still in 'research' mode and much work would have to be done to implement them in an operational pipeline for retrieving cloud optical depth from satellite measurements on the fly.

It is commonly believed that the more observations of solar radiation reflected from clouds into different directions are used, the more accurate the retrieved cloud properties will be. Evans *et al* [248] recently asked themselves if we can do better with multiple viewing angles, as compared with nadir-only reflectance. They simulated MISR multi-angular measurements with SHDOM for a large number of cloud fields generated with an LES model. They then retrieved the mean and standard deviation of $\tau(x, y)$ using a neutral network algorithm trained on some of the LES + SHDOM fields and evaluated on the others. They found that for large Sc clouds, multi-angular measurements decrease the mean optical depth retrieval error by 20–40% (respectively, for $45°$ and $25°$ SZA) while for small Cu clouds the retrieval error decreases only by 13%. These small improvements for Cu clouds suggest that multiple directions do not necessarily contribute substantially to more accurate retrievals. However, the statistical retrievals based on 3D RT, even with only one direction, were shown to be much more accurate than standard retrievals based on 1D RT.

7.3. Broken cloud impacts on aerosol property retrievals

As previously mentioned in (section 6.5), cloud–molecular interaction is the dominant mechanism for cloud-induced enhancement of the reflectance in the cloud-free column, at least for shorter wavelengths and boundary-layer cumulus over dark surfaces [231]. Here we assume that the enhancement is *entirely* due to Rayleigh scattering, i.e. the enhancement comes from the re-illumination of the molecular layer through the reflection of sunlight by the surrounding clouds. Consider a simple two-layer model with broken clouds below and a uniform molecular layer above (figure 29, top panel). Marshak *et al* [137] recently suggested that the cloud enhancement of reflected radiation, δR, be defined as the difference between the following two radiances: R_1 reflected from a broken cloud field with a scattering Rayleigh layer above it and R_2 reflected from the same broken cloud field but with the molecules in the upper layer causing extinction, but no scattering. In other words,

$$\delta R = R_1 - R_2, \tag{129}$$

where, as in (55),

$$R_1(\theta_0, \theta) = R_{\mathrm{m}}(\theta_0, \theta) + T_{\mathrm{m}}(\theta_0) \frac{\alpha_{\mathrm{c}}(\tau, \theta_0)}{1 - \alpha_{\mathrm{c}}(\tau, \theta_0) R_{\mathrm{m}}^{(\mathrm{dif})}} T_{\mathrm{m}}^{(\mathrm{dif})}(\theta), \tag{130}$$

$$R_2(\theta_0, \theta) = R_{\mathrm{m}}(\theta_0, \theta) + T_{\mathrm{m}}(\theta_0)\alpha_{\mathrm{c}}(\tau, \theta_0) T_{\mathrm{m}}^{(\mathrm{dif})}(\theta), \tag{131}$$
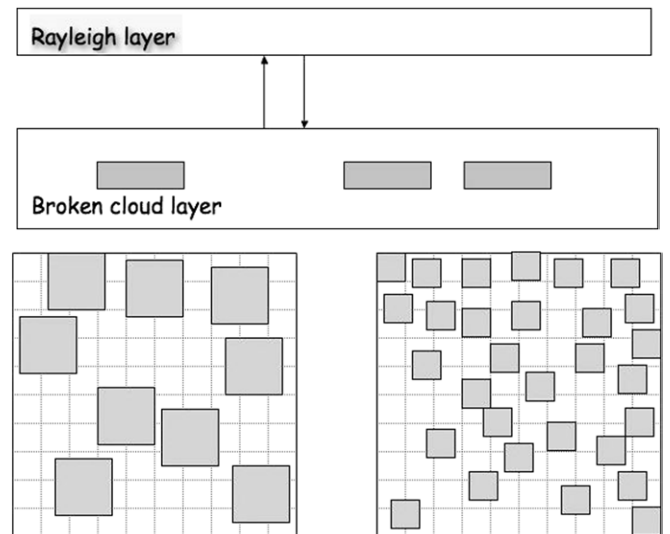

Figure 29. *Schematic of the two-layer 3D stochastic model for cloud enhancement estimation.* Top: optically thick but broken clouds are below, with an optically thin Rayleigh scattering layer above. Bottom: two examples of the Poisson distribution of broken clouds. These fields both have cloud fraction $A_{\mathrm{c}} = 0.30$ in a $10 \times 10 \, \mathrm{km}^2$ area. For a cloud vertical thickness of 1 km, the left panel has cloud aspect ratio $\gamma = 2$ and the right panel has $\gamma = 1$. The uniform plane-parallel limit of the model corresponds to $A_{\mathrm{c}} = 1$ for any γ. The two-state (cloudy/clear) ICA limit is obtained for any $0 < A_{\mathrm{c}} < 1$ and $\gamma \to \infty$, meaning a single very flat (i.e. plane-parallel) cloud radiance with weight A_{c} in the domain-average and clear-sky radiance with weight $1 - A_{\mathrm{c}}$.

sub-index 'm' standing for molecular and 'c' for cloud. $R_{\mathrm{m}}(\theta_0, \theta)$ is the reflectance for the molecular layer with no clouds below (known technically as 'planar albedo'). Cloud-layer reflectance, viewed here as a lower surface, is denoted accordingly $\alpha_{\mathrm{c}}(\tau, \theta_0)$; it is the critical parameter in this simple model because, in addition to cloud optical depth τ and SZA θ_0, it depends on the broken cloud layer's geometry. $T_{\mathrm{m}}(\theta_0)$ is the transmittance through the molecular layer with direct sunlight incident from above while $T_{\mathrm{m}}^{(\mathrm{dif})}(\theta)$ is the transmission through the molecular layer for diffuse illumination from below, into direction θ. Finally, $R_{\mathrm{m}}^{(\mathrm{dif})}$ is the reflectance of the molecular layer illuminated by diffuse radiation from below (known technically as 'spherical albedo'). With the sole exception of α_{c}, all the quantities in (129)–(131) are 1D and are calculated using a standard plane-parallel RT code.

To calculate the cloud reflectance for broken cloudy regions, α_{c}, we can use a one-layer Poissonian model for broken clouds originally proposed by Titov in 1990 [131]. The main parameters in the model are (i) cloud fraction A_{c}; (ii) average cloud optical depth τ, which is normally quite large and (iii) cloud aspect ratio, γ, defined as the ratio of the cloud's horizontal to vertical dimensions. One can also think of aerosols filling the space between the clouds with AOT $\tau_{\mathrm{a}}(\lambda)$, which is normally quite small. The lower panel of figure 29 shows examples of two broken cloud fields with the same value of $A_{\mathrm{c}} = 30\%$ and $\gamma = 2$ and 1. Output of the stochastic RT model is the azimuthally and domain-averaged upward and downward fluxes, with downward fluxes subdivided into diffuse and direct components.

Note that, out of the three principal input parameters, two (averaged cloud optical depth, τ, and cloud fraction, A_c) can be determined from the MODIS Cloud Product suite. The third parameter (cloud aspect ratio γ) is not readily available. Fortunately, the cloud enhancement is not very sensitive to the aspect ratio, at least for small SZA. The results of detailed numerical simulations of the enhancement by Wen *et al* [220] were shown to be in relatively good agreement with this simple modeling exercise by Marshak *et al* [137].

It is also interesting to note that the ratio of cloud-induced enhancements at two wavelengths λ_1 and λ_2 in (129)–(131) is only weakly sensitive to cloud properties (τ is almost independent of λ), and is therefore determined by the Rayleigh scattering molecular layer. Indeed,

$$\Re(\lambda_1, \lambda_2) = \frac{\delta R(\lambda_1)}{\delta R(\lambda_2)} = C(\lambda_1, \lambda_2; \theta, \theta_0) \frac{1 - \alpha_c(\tau, \theta_0) R_{m\lambda_2}^{(\mathrm{dif})}}{1 - \alpha_c(\tau, \theta_0) R_{m\lambda_1}^{(\mathrm{dif})}},$$
(132)

where the $R_{m\lambda}^{(\mathrm{dif})}$ terms are relatively small, and we have defined

$$C(\lambda_1, \lambda_2; \theta, \theta_0) = \frac{T_{m\lambda_1}(\theta_0) T_{m\lambda_1}^{(\mathrm{dif})}(\theta) R_{m\lambda_1}^{(\mathrm{dif})}}{T_{m\lambda_2}(\theta_0) T_{m\lambda_2}^{(\mathrm{dif})}(\theta) R_{m\lambda_2}^{(\mathrm{dif})}}.$$
(133)

This means that the ratio of cloud-induced enhancements at two different wavelengths is essentially independent of cloud properties, and depends *only* on θ_0 and θ; hence can be pre-calculated.

To mitigate the retrieval errors from the cloud-induced enhancement, Kassianov and Ovtchinnikov [249] recently proposed to use reflectance ratios to retrieve aerosol optical depth. Based on (132)–(133), the underlying idea of their method is that ratios are less sensitive to 3D cloud effects than reflectances themselves. In other words, they assumed that

$$\Re_{3D}(\lambda_1, \lambda_2) = \frac{R_{3D}(\lambda_1)}{R_{3D}(\lambda_2)} = \frac{R_{1D}(\lambda_1) + \delta R(\lambda_1)}{R_{1D}(\lambda_2) + \delta R(\lambda_2)}$$

$$\approx \frac{R_{1D}(\lambda_1)}{R_{1D}(\lambda_2)} = \Re_{1D}(\lambda_1, \lambda_2),$$
(134)

thus

$$\Re_{3D}(\lambda_1, \lambda_2) \approx \Re_{1D}(\lambda_1, \lambda_2) \equiv \Re(\lambda_1, \lambda_2).$$
(135)

Their method was tested in a simulated case using two ratios at three wavelengths λ_1, λ_2 and λ_3. At given solar and viewing angles, this approximately constant ratio is a function of AOT, aerosol model and the underlying surface albedo. AOT, as a function of wavelength λ, is then described by a power law, $\tau_a(\lambda) = \beta \lambda^{-\alpha}$, as in (4); this closes the retrieval problem with two unknowns (α and β) and two observations, namely, $\Re_{3D}(\lambda_1, \lambda_2)$ and $\Re_{3D}(\lambda_1, \lambda_3)$. The sensitivity of the proposed retrieval method to errors from measurements and RT modeling was recently evaluated [250].

8. Exploitation of 3D RT phenomenology in remote sensing

To summarize the two previous sections, the '3D RT is too complicated and expensive' argument for keeping operational cloud remote sensing grounded in 1D RT is getting old, and hopefully will soon be obsolete, as the community gains research-based experience and institutional computing facilities harness more power. Earth, Clouds, Aerosols and Radiation Experiment (EarthCARE) is a future joint EU-Japan mission focused on clouds and aerosols, the next major Earth observation satellite to be launched by the European Space Agency (ESA) and instrumented jointly with the Japan Aerospace Exploration Agency (JAXA). With a planned launch in 2013, EarthCARE is in the planning stages for its suite of retrieval algorithms, both conventional and experimental. The latter effort, spearheaded by Barker (Meteorological Service of Canada) and Donovan (Koninklijk Nederlands Meteorologisch Instituut), will be synergistic across multiple instruments and fully 3D as far as RT is concerned. If successful, the 1D/plane-parallel paradigm will be on its way out, and the new one will embrace the 3D structure of the real world. We are confident that NASA's planning will be as forward-looking for its future Aerosol, Clouds and ocean Ecosystem (ACE) mission with, at the time of writing, launch planned for the 2020 timeframe.

In this final technical section, we take the final step away from 1D RT and examine some emerging cloud observation techniques that are inherently 3D—they are not even conceivable in a modeling framework limited to 1D RT. Some are astonishingly simple, given the right kind of data.

8.1. Variable cloudiness observed from below, with zenith radiance

8.1.1. Spectral signatures.
Figure 30 shows a 22 minute fragment of zenith radiance measured by a ground-based 'Cimel,' a multi-channel sun-photometer pointing straight up. The Cimel has a narrow FOV of $1.2°$ and four filters at 0.44, 0.67, 0.87 and $1.02\,\mu\mathrm{m}$ designed for retrieving aerosol properties under clear-sky conditions. In our example, the Cimel measured zenith radiance at $20\,\mathrm{s}$ temporal resolution while in 'cloud' mode, i.e. constant zenith viewing (as opposed to a special sky scan optimized for aerosol property retrievals).

There are three distinct regions in figure 30, from left to right: a single unbroken cloud, broken clouds, and clear sky. For clear-sky conditions, due to Rayleigh scattering and optically thicker aerosol at shorter wavelengths, zenith radiance increases as wavelength decreases from 1.02 to $0.44\,\mu\mathrm{m}$. By contrast, under cloudy skies, radiances in channel 0.44 and $0.67\,\mu\mathrm{m}$ are almost indistinguishable; this is also true for channels 0.87 and $1.02\,\mu\mathrm{m}$. This is a clear indication that, in the presence of clouds, the spectral contrast in surface albedo (back-reflected from clouds) dominates over Rayleigh and aerosol effects. In contrast to the small fluctuations typical for clear and overcast skies, broken clouds show sharp changes in radiances around cloud edges.

More formally, we can distinguish three main cases based on cloud–vegetation radiative interactions:

(1) *Atmosphere dominates.* In this case,

$$I_{0.44} \gg I_{0.67} > I_{0.87} > I_{1.02}$$
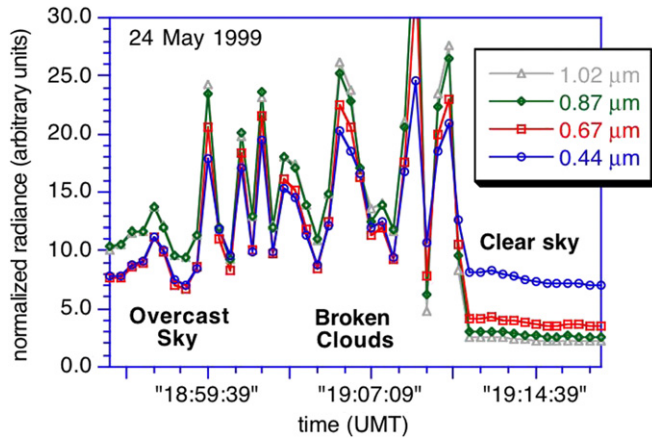(136)

and aerosol optical properties can be retrieved.

Figure 30. *Zenith radiance measured by a Cimel sun-photometer at Greenbelt, MD, on 24 May 1999.* Four channels 0.44, 0.67, 0.87 and 1.02 μm are used. The measured radiance has relative (channel-to-channel) calibration and is normalized by the solar flux at the TOA in the corresponding spectral interval. The ordinate's 'arbitrary units' are therefore linear for T (abcissa, $\hat{z}$) from (42).

(2) *Vegetated surface and cloud dominates.* In this case,

$$I_{0.44} \approx I_{0.67} < I_{0.87} \approx I_{1.02} \qquad (137)$$

and cloud optical properties can be retrieved, given the surface albedo.

(3) *Transition between the first two cases.* This scenario is characterized by rapid changes between the ordering of I_λ from cloudy to clear and back. In this case, neither aerosol nor cloud properties can be reliably retrieved using only one wavelength.

By analogy with the well-known Normalized Difference Vegetation Index (NDVI) [251], Marshak *et al* [252] proposed the Normalized Difference Cloud Index (NDCI) defined as the ratio between the difference and sum of two normalized zenith radiances measured for two narrow spectral bands in the NIR (0.87 μm) and RED (0.67 μm) spectral regions:

$$\text{NDCI} = \frac{I_{\text{NIR}} - I_{\text{RED}}}{I_{\text{NIR}} + I_{\text{RED}}}. \qquad (138)$$

Compared with a two-valued optical depth versus zenith-radiance relationship that makes its retrieval impossible without ancillary information [91], the transmitted NDCI is a monotonic function with respect to optical depth [252]. Conventional methods of estimating cloud optical depth from surface fluxes use either broadband [253] or multi-wavelength [254] radiometry, and are expected to work well only for overcast skies [255]. In sharp contrast, the NDCI-based retrieval technique is much less sensitive to cloud structure. The sensitivity is weak because the NDCI-based method eliminates the part of downward radiation that did not have interactions with surface; this radiation is the most sensitive to both illumination conditions and cloud inhomogeneity [252, 256]. As follows from the relations in (136)–(137), the NDCI will be negative for a clear sky and positive for an overcast sky. In the case of broken clouds, NDCI can take on either positive or negative

values, depending on whether there is a cloud in the zenith direction or not.

The first shortcoming of the NDCI-based retrieval technique comes from the underestimation in 1D RT of zenith radiance for large optical depth in NIR. Indeed, in the NIR, the 1D RT prediction for radiance systematically underestimates the actual 3D radiances for large optical depths. This has a simple explanation: for 3D clouds, more radiation is transmitted (by Jensen's inequality and/or by oblique channeling); thus more surface-leaving radiation is reflected back from thick clouds to the ground-based sensor.

Another shortcoming innate to all concepts based on spectral-indices is that the spectral information is reduced to one number by algebraic transformation; see, e.g. Tian *et al* [257]. In other words, instead of *two* spectral values of zenith radiances in RED and NIR, only *one*, NDCI, is used. Each measurement can indeed be assigned to a specific point on the $(I_{\text{RED}}, I_{\text{NIR}})$ plane, equivalently:

$$\eta = \sqrt{I_{\text{RED}}^2 + I_{\text{NIR}}^2}, \qquad (139)$$

$$\alpha = \tan^{-1}(I_{\text{RED}}/I_{\text{NIR}}). \qquad (140)$$

Both coordinates can depend on the cloud optical depth. However, NDCI is a function of α only,

$$\text{NDCI} = \frac{1 - \tan \alpha}{1 + \tan \alpha}, \qquad (141)$$

and thus cloud optical depth can vary considerably yet leave NDCI unchanged.

Instead of using a single index such as NDCI, Marshak *et al* [90] directly utilized radiance observations on the RED versus NIR plane (see figure 31). Since most vegetated surfaces are dark at red wavelengths and bright at NIR wavelengths, points above the diagonal correspond to cloudy situations due to surface–cloud interactions, while points below the diagonal correspond to clear sky. Since the surface is dark in the RED region, having the same RED radiances at points A and B indicates that they have the same values of cloud optical depth, τ. However, they have different radiances in the NIR region. Clearly, more surface–cloud interactions occur and more photons reach the ground for point B. This indicates that point B corresponds to a smaller cloud fraction than point A. This can all be made more quantitative in the method referred to hereinafter as 'REDvsNIR,' which retrieves both optical depth and 'effective' cloud fraction from a point in the RED versus NIR plane. Note that points A and C in figure 31 have the same NDCI but correspond to different values of τ and effective cloud fraction.

Next we briefly discuss the REDvsNIR retrieval method proposed in Marshak *et al* [90] and validated by Chiu *et al* [91]. The method retrieves overhead cloud optical properties in any cloud situation using measurements of zenith radiance at 0.673 and 0.870 μm wavelengths, and only requires the presence of green vegetation in the surrounding area.

We first note that for plane-parallel clouds over a Lambertian surface, any ground-based measurement of
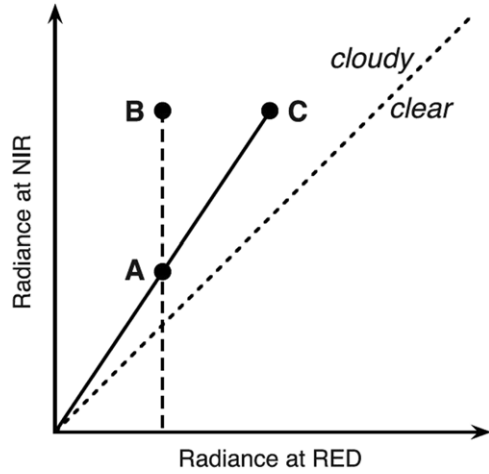
Figure 31. *Schematic of the REDvsNIR algorithm.* See main text for description of the method for retrieving cloud optical depth τ and cloud fraction A_c.

radiance I can be expressed as [258]

$$I = I_0 + T_0 \frac{\alpha}{1 - \alpha R} I_s. \tag{142}$$

The first term on the right-hand side, I_0, is downward radiation calculated for a black (non-reflecting) surface, while the second term is radiation introduced by interactions between clouds and the underlying surface. The cloud–surface interactions are fully determined by α, T_0, R and I_s, where α is the albedo of the underlying surface; T_0 is the transmittance of monochromatic flux over a black surface; R is the spherical albedo of clouds for uniform and isotropic illumination from below; and finally, I_s is the radiance generated at the upper boundary by an isotropic source at the surface.

Consider the following approximation:

$$T_0 \approx (1 - A_c) \times 1 + A_c \times T_0^{(pp)}, \tag{143}$$

where A_c is cloud fraction and $T_0^{(pp)}$ is total transmittance over a black surface in the uniform plane-parallel assumption. We can then rewrite (142) as an explicit function of cloud optical depth τ and A_c. For the RED and NIR wavelengths, we obtain

$$I_{RED}(\tau, A_c) = I_{0,RED}(\tau)$$
$$+ \frac{[1 - (1 - T_{0,RED}^{(pp)})A_c]\alpha_{RED}}{1 - \alpha_{RED} R_{RED}(\tau)} I_{s,RED}(\tau),$$

$$I_{NIR}(\tau, A_c) = I_{0,NIR}(\tau)$$
$$+ \frac{[1 - (1 - T_{0,NIR}^{(pp)})A_c]\alpha_{NIR}}{1 - \alpha_{NIR} R_{NIR}(\tau)} I_{s,NIR}(\tau), \tag{144}$$

where it is assumed that the dependence on A_c comes only from (143).

Note that A_c accounts here not only for the fraction of cloudy 'pixels' in the zenith-radiance time series but also for the horizontal photon transport [259, for instance] that is ignored by 1D RT. Therefore, A_c is *not* the real cloud fraction but rather a 'radiatively effective' one that forces 1D
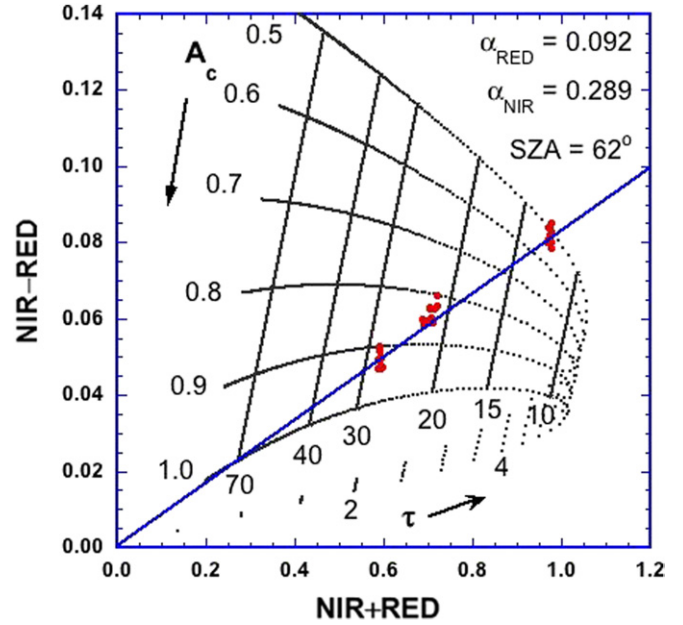

Figure 32. *Illustration of the $\{A_c, \tau\}$ retrieval algorithm based on* (144) *with real measurements.* DISORT-calculated values of $I_{NIR} + I_{RED}$ and $I_{NIR} - I_{RED}$ are plotted for a wide range of τ and A_c for SZA = 62° and surface albedos $\alpha_{RED} = 0.092$ and $\alpha_{NIR} = 0.289$. When A_c is constant and τ varies, the set of calculated values define the cloud-fraction isolines. When τ is constant and cloud fraction varies, the set of values define the τ-isolines. Values $I_{NIR} + I_{RED}$ and $I_{NIR} - I_{RED}$ (30 dots, with 10 for each cluster) are from the Cimel measurements at the ARM site in Oklahoma on 28 July 2002. Measurements were taken around 13 : 45Z, 13 : 58Z and 14 : 11Z respectively, corresponding to decreasing abscissa NIR + RED. The straight line through (0,0) corresponds to NDCI ≈ 0.08, hence $\tau \approx 80$ along the $A_c = 1$ line.

RT calculations to give the same values of I_{NIR} and I_{RED} as the measured (3D) ones. In this case, one may allow A_c to be negative! Then it immediately follows from (143) that T_0 can exceed 1 and will thus be able to mimic reflectance off cloud edges that reaches the surface. This commonly observed phenomenon [134, 260, for typical examples] often leads to surface fluxes in excess of the values predicted by 1D RT. Detailed explanations, examples and discussions can be found in Marshak *et al* 's 2004 paper [90].

As an example of retrievals, figure 32 shows a NIR-RED versus NIR + RED plane with Cimel measurements at the DOE Atmospheric Radiation Measurement (ARM) site in Oklahoma (97.48°W, 36.61°N) on 28 July 2002. The plot illustrates I_{NIR} and I_{RED} as functions of τ and A_c calculated by using the DISORT 1D RT model to compute the various quantities in (144) for SZA = 62° and surface albedoes $\alpha_{RED} = 0.092$ and $\alpha_{NIR} = 0.289$. Three groups of data points (10 points per group) measured by the ARM Cimel are also plotted. The data points, while having different values of I_{NIR} and I_{RED} thus being located at different positions on the plane, have almost the same NDCI—a straight line through the (0,0) point. Therefore, if retrieved from it, the same optical depth would have arisen ($\tau \approx 80$ for $A_c = 1$). However, as follows from the plot, these groups correspond to three different $\{A_c, \tau\}$ pairs of cloud properties: {0.9, 28}, {0.8, 22} and {0.4, 12} with clearly different values of τ.

8.1.2. Spatial signatures. Stratiform clouds (St and Sc) may have cloud-top and cloud-base altitudes that are relatively well-defined, at least over horizontal scales up to a few times their thickness H. A plane-parallel slab assumption may therefore be reasonable for their *outer* geometry. However, these clouds are generally quite turbulent environments; so their *inner* structure is highly variable. Microphysical probes on aircraft have sampled the spatial variability of LWC, and its wavenumber spectrum indeed follows the ubiquitous $k^{-5/3}$ law [105, 261, among others], even though the turbulence is far from Kologorov's [262] statistically isotropic and homogeneous model and condensed water is far from being a passive scalar. LWP, vertically integrated LWC, can be measured from ground-based microwave radiometers (MWRs) [151, among others]. Time-series of LWP, viewed as frozen turbulence advected past the instrument (much like in wind-tunnel experiments), leads to the same conclusion. In contrast, solar radiation observed from space or ground follows the turbulence-driven $k^{-5/3}$ law too, but only down to a characteristic wavenumber $k^\star$. At smaller scales (larger k), the spectrum dips to lower levels of variability. In section 6.3, we have shown observations and 3D RT simulations of this scale break. We were able to explain the scale break by introducing the inherently 3D RT phenomenon of 'radiative smoothing' [196], in essence, an observable manifestation of the spatial Green function for multiple scattering [178].

So we have, on the one hand, at least an indirect observation of the Green function and, on the other hand, a reasonable diffusion-based theory of RT Green functions, at least for optically thick clouds. We used this conjunction in the NIPA (section 7.2.1) to mitigate the 3D RT effect of radiative smoothing for the purposes of cloud remote sensing in the conventional sense where an operational 1D RT model is used as a predictor for cloud radiances. However, there is also here a clear opportunity for a remote sensing retrieval of H using simple passive instrumentation.

Indeed, suppose we have a ground-based NFOV radiometer recording zenith radiance, as did Savigny *et al* [200]. Then either Fourier or structure-function analysis of the time series yields an empirically determined characteristic scale $r^\star(=1/k^\star)$ where the break occurs in the scaling. This determination does not call for any radiometric calibration, only a reliably constant gain factor that converts the incoming radiance into photo-electrons or current. We know from the detailed 3D RT computations shown in section 6.3.2 that

$$r^\star \sim \langle \rho^2 \rangle_T^{1/2}, \tag{145}$$

where sub-index T stands for transmitted light. Finally, we know from diffusion theory (section 4.1) that

$$\langle \rho^2 \rangle_T^{1/2} \approx \sqrt{2/3}\, H,$$

if necessary with small correction terms dependent on cloud optical thickness τ and asymmetry factor g (cf section 4.1), and possibly also the cosine of the SZA μ_0. Now, μ_0 is known, $g \approx 0.85$ for low-level liquid water clouds, and τ can be inferred independently from passive but *calibrated* radiometry (as described, e.g. in section 3.2). The latter determination is, in essence, based on the inversion for τ of transmitted flux

$\mu_0 F_0 \times T(\tau, g; \mu_0)$, or of zenith radiance (with the added but tractable issue of ambiguity). The only remaining question is therefore about the precise relation to use in (145). Is a simple proportionality enough and, if so, does the constant depend on anything we should know about? Computational 3D RT can answer this question using realistic cloud models.

One might start worrying about a fundamental inconsistency that is building up here. We detect and quantify a scale break, which presumes *turbulent cloud* structure ... and we then invoke results from analytic diffusion theory that are based on a *uniform cloud* assumption. What that means of course is that the retrieved H and τ are 'effective' cloud properties: those of the uniform slab that give the observed values of $T(\tau, g; \mu_0)$ and $\langle \rho^2 \rangle_T(H, \tau, g; \mu_0)$. Is that good enough? That question will depend on the application, but we can be sure that in some cases the biased answers are not acceptable. That is why we now have *refined* theory for RT Green function observations, even with the framework of diffusion. We have models for estimating the impact of unresolved small-scale variability that the measurements have basically averaged over. In fact three different types of model were discussed in section 5.1. Although they were generally designed with the radiation budget of $\sim$100 km GCM grid-cells in mind, there is no fundamental reason why they cannot be applied, with proper thought, to unresolved spatial variability in remote sensing observations. Again, particularly attractive here are homogenization techniques such as Cairns' renormalization (cf section 5.1.1).

So, looking up from the ground at stratiform clouds, we can tell their thickness using 3D RT phenomenology and relatively simple instrumentation. What about looking down from aircraft or space? The opportunity for remote passive determination of H remains just as good, with one caveat. Since we have

$$\langle \rho^2 \rangle_R^{1/2} \propto H/\sqrt{(1-g)\tau}, \tag{146}$$

from section 4.1, where sub-index R stands for transmitted light, we will definitely need to know τ—and not just for correction terms. So we will have to use an instrument with absolute radiometric calibration (or a collocated one, possibly with coarser resolution). Moreover, the prefactor in (146) will likely depend on μ_0, as is the case for temporal Green function moments [108], and there will be a notable (x, y) anisotropy if μ_0 is significantly < 1. The role for computational 3D RT is still there to refine the connection between $r^\star$ and some combination of $\langle x^2 \rangle_R$ and $\langle y^2 \rangle_R$.

Another fundamental concern arises at this point. Solar 1D RT in clouds is not sensitive to vertical variations in extinction $\sigma(z)$ as long as other optical properties are not dependent on altitude. Indeed, the natural independent variable in the 1D RTE is $\tau(z) = \int_0^z \sigma(z') \, dz'$. So, beyond the key position of the source, R and T (spatially integrated Green functions) do not depend on what side is up or down if ϖ_0 and g are constant. This cannot be true of $\langle \rho^2 \rangle_R$, a measure of horizontal transport from the source position to the observation point, if the cloud is actually denser at its top than at its base. And that is indeed what we learn from elementary cloud physics, a.k.a. 'parcel theory' [263]: moist air and CCN,

rising in an adiabatic environment. For the natural assumption of a fixed number of CCN, hence cloud droplets, adiabatic growth predicts a linear trend in LWC(z) where it is 0 at z_{base} and maximal at z_{top}. This leads to a power law for $\sigma(z)$ in $|z - z_{base}|^{2/3}$.

Diffusion theory, based on (29), for a (pulsed) point-wise boundary source remains tractable for $D(z) = 1/(1 - g)\sigma(z)$ with a power-law trend $D(z) \propto |z - z_{base}|^{-\zeta}$, with $0 \leqslant \zeta \leqslant 1$. However, the solution has already sufficiently complicated expressions for a constant-gradient model

$$\sigma(z) = \overline{\sigma} \times \left[1 + \frac{\Delta}{H} \left(z - \frac{z_{base} + z_{top}}{2} \right) \right], \qquad (147)$$

with $0 \leqslant |\Delta| \leqslant 2$. The case of $\Delta < 0$ corresponds to observation *and source* points above the cloud, which applies to passive solar measurements, while the $\Delta > 0$ scenario corresponds to observation *and source* below (cf section 8.3.3 for an application). Moreover, a straightforward least-squares minimization [108] maps ζ to

$$\Delta(\zeta) = \pm 6 \times \left[2 \left(\frac{\zeta + 1}{\zeta + 2} \right) - 1 \right], \qquad (148)$$

hence $\zeta = 2/3$ to $\Delta(2/3) = -3/2$ in the solar case. MC simulations by Davis *et al* [108] show that, for all Green function moments of interest here, the difference between using the power-law model or the linear model using $\Delta(\zeta)$ is negligible.

The two panels in figure 33 show three key Green function moments (two in time, one in space), all normalized to H, as functions of Δ for reflected and transmitted light; $(1-g)\tau$ is set at 8.1. Continuously varying diffusion-theoretical predictions are compared with sparse but representative MC validation data. Focusing on the spatial statistic (RMS ρ) in transmission geometry (bottom panel), the diffusion model has singular behavior when $|\Delta| \to 2^-$ (σ vanishes at cloud base). Maybe worse is that the correction for stratification has the wrong sign for this particular value of τ; this is not the case at larger τ and a parametrization based on that regime can be used [108]. The effect is 2nd-order in $|\Delta|$ anyway. In reflection (top panel), the effect of Δ is 1st-order and there is no singularity in this observation geometry ($\Delta < 0$) applicable to both solar and laser sources. Here again, Davis *et al* propose in [108] an accurate parametrization (based on logarithmic derivatives in Δ at $\Delta = 0$), at least for the RMS ρ and mean ct (used further on).

We have now taken care of all the most important structural and optical properties of a Sc cloud in the forward diffusion-based RT model for RMS ρ, hence the direct observable $r^\star$. Yet there remains one main obstacle for implementation of the above algorithm for a passive determination of H from above, given τ. It is the need for Landsat- or ASTER-like pixel sizes in the tens of meters since radiatively smoothed scales need to be resolved. Earth observation satellites that target global coverage do not have this level of spatial resolution since they require wider swaths. Nonetheless, there may some day be high-altitude unmanned airborne vehicles (UAVs), or even stratospheric balloons [264], that will deliver the required resolution.
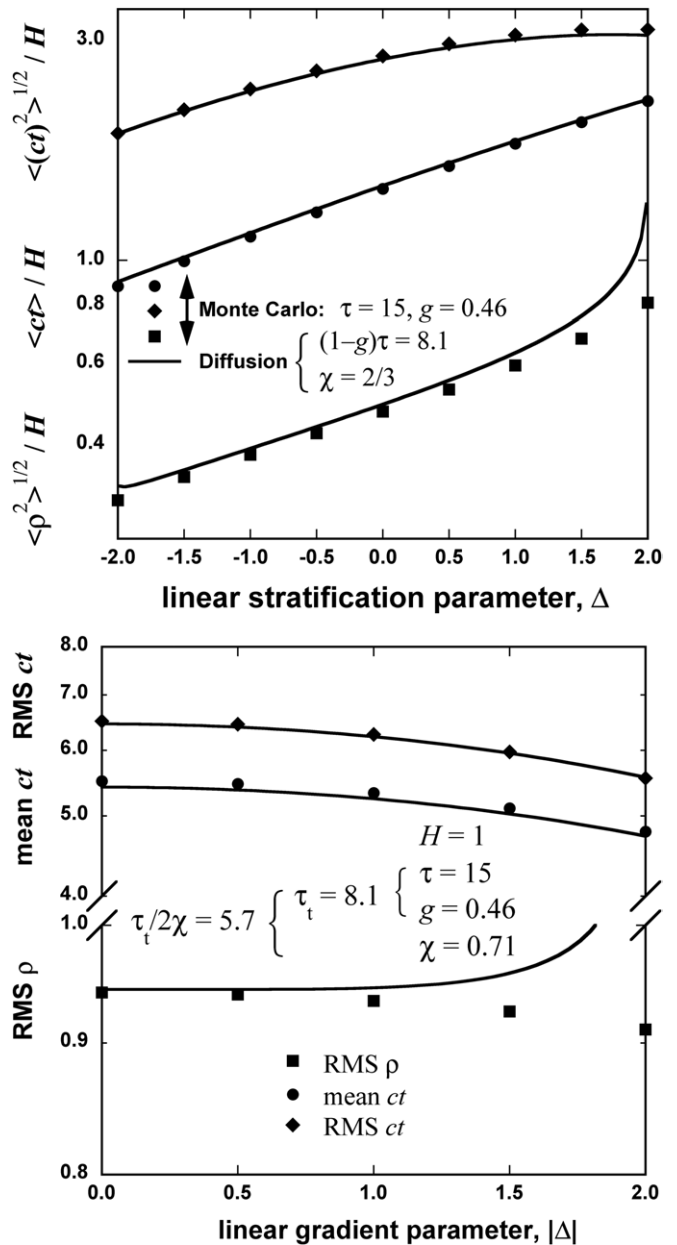

Figure 33. *Effects of cloud stratification on moments of Green functions.* Top: reflected light, in semi-log axes, where diffusion predictions for the prescribed cloud ($\tau_t = 8.1$) are in solid lines while the MC validation data are plotted with bold symbols; we note the presence of a logarithmic singularity in $\langle \rho^2 \rangle_R$ at $\Delta = +2$. Bottom: same as above but for transmitted light for the same clouds; we note the nearly flat behavior of $\langle \rho^2 \rangle_T$ away from $|\Delta| = 0$ and up to the onset of the logarithmic singularity at $|\Delta| = 2$. Reproduced from [108].

In the meantime, it is important to promote multi-pixel approaches, like the above procedure, in the physics-based remote sensing community at large (beyond just clouds). The industry has indeed been dominated since its inception by single-pixel methods predicated on the assumptions that (1) *all* the desirable information is somehow encoded in the multi- or hyperspectral dimension of the data and (2) that there are too many pixels coming down the pipeline to start processing more than one at a time. The previous subsection is one more proof that there are indeed vast amounts of cloud, aerosol and
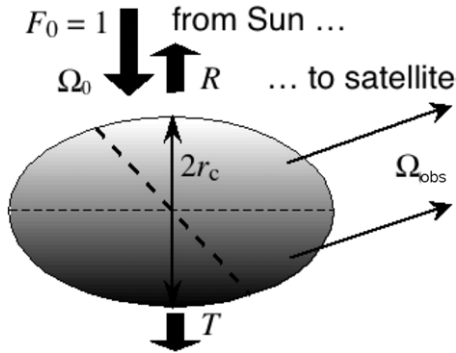
Figure 34. *Remote observation geometry for a finite isolated spheroidal cloud.*

surface information still to mine for in spectral data. However, it is time to challenge that preconception, just because it limits our horizon unnecessarily.

We return to the determination of the important properties of dense stratiform clouds $\{\tau, H\}$ using *passive* observations in section 8.3.2; we will be taking, curiously, a time-domain Green function perspective. The same endeavor, but with *active* remote sensing technology, will be pursued in section 8.3.3.

8.2. Cloud-sensing sideways

8.2.1. Horizontally finite clouds, in isolation. In section 3.3, we provided a closed-form expression for the total reflectivity R and transmittivity T of a homogeneous non-absorbing spherical cloud defined, respectively, as the boundary fluxes through the illuminated and shaded hemispheres, normalized to the incoming solar flux. In that case, $R + T = 1$, by conservation, and the non-trivial result obtained from diffusion theory by Davis [98] is that R/T is given by $(1-g)\tau/2\chi$, where $\tau_t = (1-g)\tau = (1-g)2\sigma r_c$ is the diameter of the sphere in scaled optical units, i.e. in transport MFPs. In fact, noting that the same can be said of the all too familiar plane-parallel slab clouds if one takes $\tau = \sigma H$, it is speculated that the result is true for any oblate spheroidal cloud illuminated along its shortest axis. From there, it is probable that many other shapes of uniform diffusive clouds have the same optical property,

$$R/T \propto (1-g)\tau, \tag{149}$$

if we continue (i) to partition R and T according to illumination and (ii) to define τ based on a linear measure of the outer size of the cloud.

This opens an opportunity for truly 3D cloud remote sensing with, to boot, no need for absolute radiometric calibration. Indeed, it is topologically impossible to have in the same image both reflected and transmitted light if the cloud is a horizontally infinite plane-parallel slab. In sharp contrast, most vantage points give a view of both the illuminated and shaded sides of an arbitrary ellipsoid illuminated along its shortest axis, as illustrated in the schematic in figure 34. This does not give us R/T as defined above in terms of boundary fluxes, but we can get an estimate based on radiances measured at some stand-off distance. As previously mentioned, to go from
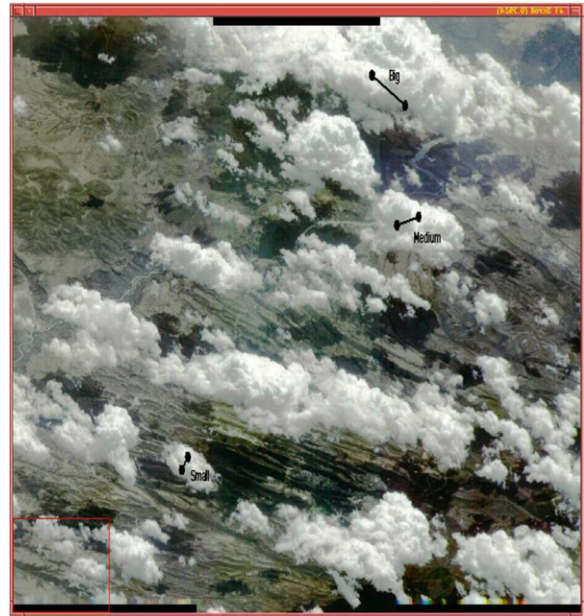

Figure 35. *'True-color' channel combination of an MTI scene of Los Alamos (NM) in the presence of broken clouds.* This is a look from $57.4°$degree off-nadir in the aft direction, i.e. from a position to the north of the target. Local SZA was $54°$ and $\approx 175°$ away from the viewing direction in azimuth. The positions of three pairs of cloudy regions that were used to compile radiance statistics are highlighted. Cloud-to-cloud and cloud-to-ground radiative interactions are neglected in the retrievals.

a radiance I to a flux F, we need an angular model. Opaque, highly reflective clouds are not far from being Lambertian (isotropic) reflectors, so we can surmise that $F = \pi I$. As for the unit sphere that defines direction space, the physical space that defines the spherical cloud's boundary can only be sampled sparsely.

Hence we need to estimate spatial integrals over entire hemispheres of hemispherical boundary fluxes, but we can only measure remotely a few radiances. Clearly, the more directions the better, but spatial (as well as angular/Lambertian) uniformity assumptions are still in order. It is relatively easy to find (by hand) distinct pixels that are representative of R and T, and preferably many of each, if there is sufficient spatial resolution. Assume now that these pixels have radiances $I_R = I(x_R, \Omega_{obs})$ and $I_T = I(x_T, \Omega_{obs})$, respectively, and that the response of the imaging detector is flat across the whole field of pixels—a statement about *relative* calibration. Then we have built a case for using I_R/I_T to estimate R/T that in turn can be used to estimate τ based on (i) our confidence in g's quasi-invariance in warm clouds and (ii) knowledge of the proportionality factor in (149). The said proportionality constant, and possibly higher-order correction terms, can be derived from theory or computation. Note that we do not need to target the outer cloud size, diameter $2r_c$, because here, unlike H for slab clouds, it is obtainable by direct mensuration of the image. Knowing the geometrical diameter $2r_c$ and effective optical diameter τ, we can estimate the volume-averaged cloud extinction with $\sigma = \tau/2r_c$.

Figure 35 shows how the above algorithm was applied to hand-picked clouds in a very broken Cu cloud field above

Los Alamos, NM, USA ($35.875°$N, $106.3245°$W), collected on 22 September 2000, at 19:05 UTC. The data were captured by the Multispectral Thermal Imager (MTI) satellite [265] from a viewing direction of $\approx 60°$ off-nadir. MTI was a satellite mission funded by the US Department of Energy (DOE) as a technology demonstration in dual-purpose Earth observation, partly for nuclear proliferation detection, partly for environmental science. The only important facts about MTI that need to be known here are (i) that its 14 spectral channels included VNIR wavelengths where there is virtually no absorption by droplets or tropospheric gases and (ii) that its spatial resolution was 5 m at VIS and one NIR wavelengths, otherwise 20 m.

Three clouds were picked to cover the range of outer sizes, then small patches of pixels in the easily identified sunny and shady portions of each cloud were hand-selected and the mean radiances, as well as their standard deviations, were computed and used as the inputs I_R and I_T. The proportionality constant for the sphere, $1/2\chi \approx 3/4$, was used for simplicity in (149) to derive estimates of τ, assuming of course $g = 0.85$. The 'big,' 'medium' and 'small' clouds yielded effective τ-values of 45 ± 11, 43 ± 10 and 26 ± 7, respectively. These numbers are realistic for such clouds.

As in the prototype algorithm presented in section 8.1.2 to obtain H for stratiform clouds, the above algorithm to obtain τ for cumuliform clouds is mono-spectral but multi-pixel. So it serves as a second counterpoint to the mono-pixel but multi-spectral theme used in mainstream remote sensing of clouds, aerosols, surfaces, etc. As it stands, it has the same obstacle for implementation: the need for unusually high-resolution imaging that is generally precluded by the need for global coverage. Again, there may be some day a constellation of suborbital platforms with inexpensive non-calibrated sensors that can nonetheless be used to support physics-based remote sensing of the environment using the kind of technique presented here. Alternatively, the lower spatial resolution readily available from space assets (approximately few hundreds of meters) can be used if one can unravel mixtures of R, T, and clear sky. This should be possible given enough multi-angle data, such as provided by MISR (275 m pixels).

8.2.2. Horizontally finite clouds, with microphysical stratification. What if one could measure the vertical profiles of the cloud microphysical properties by retrieving them from the solar radiation reflected directly off cloud sides? As we mentioned earlier, all existing operational retrieval algorithms are based on the plane-parallel approximation that does not take into account the cloud horizontal's structure. In terms of cloud aspect ratio, $\gamma = L/H$, where L and H are horizontal and vertical dimensions of the clouds, respectively, the main plane-parallel assumption used for any remote sensing retrieval is that γ is very large (cf figure 29). In that case, the satellite always sees either the cloud top or the clear sky. From there, in the case of cloud, using the 1D Nakajima–King algorithm [206], a pair of reflectances at non-absorbing and droplet-absorbing bands indicates both how optically thick the clouds are (by
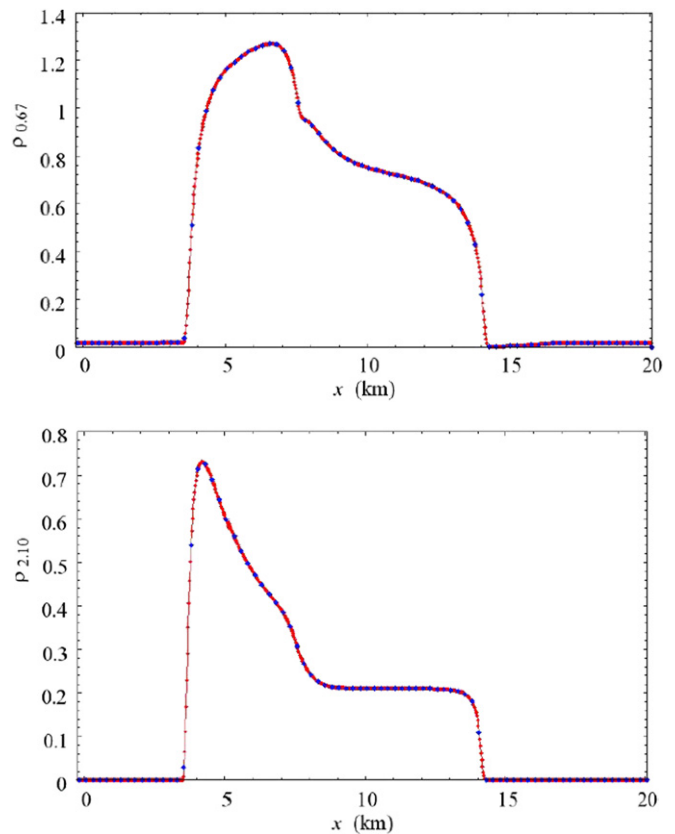

Figure 36. *Reflectance from a single cuboidal cloud with a variable droplet effective radius.* Cloud height $H = 4$ km, cloud width $L = 6.5$ km (aspect ratio $\gamma = 1.6$), flat cloud top, $\tau = 80$, SZA $= 60°$, VZA $= 45°$ with the Sun in the back of the sensor. Droplet effective radius r_e increases linearly with height from 5 to 25 μm. Reflectance from cloud top is at the right side of the cloud edge while reflectance from cloud side is at the left. Dots indicate 'measurements' sampled at $\delta x = 0.25$ km resolution. Horizontal axis starts at $x = 0$, which is 3.5 km away from the first cloud-side measurement. Altogether, there are $H \times \tan(\text{VZA})/\delta x = 16$ cloud-side measurements that go from $x = 3.5$ km to $x = 7.5$ km on horizontal axis. Cloud top starts at $x = 7.5$ km and ends at $x = 14$ km. Top: $\lambda = 0.67 \mu$m. Bottom: $\lambda = 2.1 \mu$m.

estimating τ) and how much condensed water they contain from (68): CWP $\approx (2/3)\rho_w r_e \tau$ (by estimating r_e).

For cloud-side remote sensing in the solar spectrum, Marshak *et al* [266] and Martins *et al* [267] suggested using the same two wavelengths: one non-absorbing (0.67μm) and one with strong absorption by liquid water (2.1μm). In contrast to the 1D plane-parallel approximation, 3D RT is used for interpreting the observed reflectances. As a proof-of-concept that the signature of the 'true' effective particle size is detectable in the observable reflectances at $\lambda = 0.67$ and 2.1μm in a statistical sense, these authors experimented on a few examples of simulated radiance fields reflected from cloud fields generated by a simple stochastic cloud model with prescribed vertically variable microphysics.

Figure 36 shows an example of reflectances from cloud side and cloud top for two wavelengths: 0.67 and 2.1μm calculated with SHDOM [170]. The droplet effective radius r_e increases linearly with height from 5 μm (at the cloud base) to 25 μm (at the cloud top). Cloud geometrical thickness
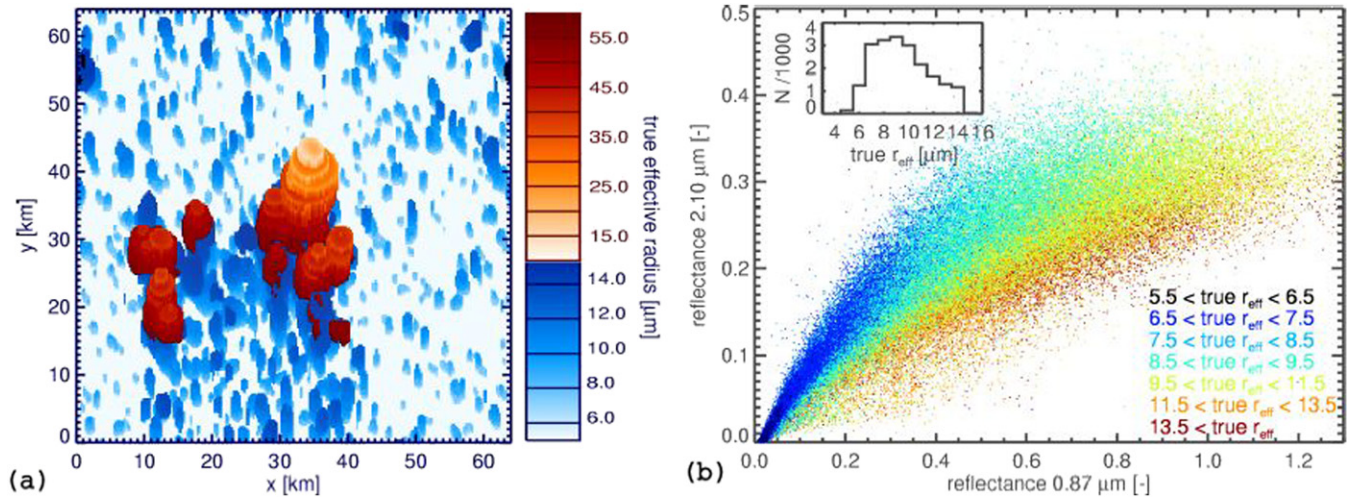
Figure 37. *Feasibility of remote determination of effective droplet radius along the sides of convective clouds.* (*a*) True (i.e. prescribed) effective radius for droplets (blue) and ice particles (red). Smallest droplet radii are at the bottom of the cloud cells, largest droplets around 15 μm are at the top of the liquid water volume just below the largest ice effective radius values ($r_e = 60 \mu$m). The color-scale for r_e is 'painted' onto a 3D isosurface of constant CWC that defines cloud boundaries. (*b*) Observed reflectance values for $\lambda = 0.87$ and 2.1 μm for certain true r_e ranges (droplets only). SZA = 45°, VZA = 60° with the Sun in the back of the sensor. The inserted histogram illustrates the underlying true r_e distribution.

$H = 4$ km and cloud optical thickness is $\tau = 80$ (thus extinction coefficient is 20 km^{-1}). With horizontal resolution $\delta x = 0.25$ km and viewing zenith angle (VZA) $\theta = 45°$, there are $H \times \tan\theta / \delta x = 16$ cloud-side 'measurements.' We see that, under relatively low solar illumination (60° SZA), $I_{0.67}$ reaches its maximum near the cloud top (which is at $x = 7.5$ km) where most of the photons are already reflected back from the cloud side without either transmission through the cloud and escape from cloud base, nor reflection from the cloud top. The horizontal size L of this cloud is only 6.5 km and, with the extinction coefficient 20 km^{-1}, $\gamma \approx 1.6$ is not sufficiently large to reach a stable 1D plane-parallel regime at cloud top. As a result, $I_{0.67}$ decreases steadily from the illuminated cloud edge to the shadowed one. In contrast, $I_{2.10}$ has a flat plateau, 5 km across, where the 3D reflectance perfectly matches the 1D one. Because droplet size increases with height, the maximum is reached much lower than in the case of conservative scattering. It is around 1 km from cloud base where $r_e = 9$–11 μm. With a further increase in r_e, reflectance $I_{2.10}$ drops fast and reaches a flat 1D level on the cloud top ($r_e = 25 \mu$m) at only $\approx$1 km from the edge.

To account for the complex 3D nature of cloud geometry and ensuing RT, Zinner *et al* [268] recently tested the approach in realistic cloud-observing situations. They used a CRM [269] to provide complex 3D structures of ice, water and mixed-phase clouds, from the early stage of convective development to mature deep convection. A 3D MC-based RT model [209] was used to simulate realistically the proposed observations. A large number of cloud data sets and corresponding simulated observations provided a large database for an experimental Bayesian retrieval.

As an example, figure 37 shows a simulated cloud field and calculated reflectances. Left panel shows the 'truth,' i.e. the value of r_e that is visible for the given observational perspective into the cloud structure. Due to the complexity

of 3D cloud structure and 3D RT a wide range of possible reflectance values at 0.87 and 2.1 μm occurs for each value of r_e (right panel, with droplets only). This differs clearly from the classical picture of 1D RT through plane-parallel clouds where a clear deterministic one-to-one map exists between a pair of reflectances $\{I_{0.87}, I_{2.10}\}$ and one pair of cloud optical thickness and droplet effective radius values $\{\tau, r_e\}$, for given surface, viewing and illumination conditions [206, 212]. In spite of blurring the separation by r_e, the core information of droplet size is still visible in the reflectance picture. For example, there is clear evidence that smaller 2.1 μm reflectance is related to larger cloud particle size. To demonstrate the performance of the experimental Bayesian retrievals, Zinner *et al* used an independent simulation of an additional cloud field as a synthetic testbed; see [268] for full details.

8.3. Direct observation of Green functions in time and/or space

The spatial Green function of clouds for multiple scattering, generally without droplet absorption, has already been used extensively. It was used to assess 3D RT effects (e.g. in the Landsat scale break), to mitigate them (e.g. using NIPA) and was even exploited, albeit indirectly, to estimate cloud thickness from passive solar observations using 3D RT phenomenology (see section 8.1.2). This is quite remarkable for a purely mathematical construct based in fact on linear transport in a uniform plane-parallel medium, or its approximation by the diffusion limit. The 3D RT information content of the Green function comes entirely from the concentration of the source to a single point in space.

We now ask what if we could observe the cloud's Green function directly? Moreover, we broaden our scope from the steady-state problem and the spatial Green function to its temporal and space–time counterparts.

8.3.1. Pathlength statistics 1, space-based wide-FOV/multiple-scattering lidar. We start with purely temporal Green functions excited by a uniformly distributed pulse of light. We would gladly observe this Green function using time-sampled radiometry, if such a physical source exists. Approximations do. Imagine a normally diverging laser pulse (say, 1.2 mrad) impinging on a cloud from a transmitter at a very large stand-off distance. Also imagine that the receiever FOV is somewhat larger, as for standard ground-based lidar systems, but maybe more (say, 3.5 mrad). That was precisely one of the possible configurations used by the first lidar system launched into low-Earth orbit (LEO), and returned, in the cargo-bay of Space Shuttle Discovery. The STS-64 mission thus carried the Lidar-In-space Technology Experiment (LITE) to ≈260 km altitude on 9–20 September 1994 [270]. More precisely, that wider FOV was used on the nighttime side (no solar background noise) of orbit #135, which overflew an extensive marine Sc deck off the coast of Southern California. The transmitter produced 0.5 J pulses at 532 nm (using a frequency-doubled Nd : YAC solid-state laser) with a 10 Hz rep-rate, and the receiver had a 1-m diameter telescope. It was a rather hefty instrument, but it was the first to go to space and operate according to specs.

The diameter of LITE's laser beam was ≈0.3 km at cloud top, and the footprint for its FOV ≈0.9 km. So the detected light could have been transported horizontally anywhere between 0 and 1.2 km (from one side of the laser beam to the opposite side of the FOV); within its FOV, it collected *all* the available light transported less than 0.6 km. The targeted marine boundary-layer clouds have H in the range 0.2–0.5 km. Optical depth τ is in the range 4–40, hence $0.6 \lesssim (1-g)\tau \lesssim 6$ (typically with a skewed, log-normal-type distribution). Also, it tends to correlate loosely with H, specifically, $H \sim \tau^{2/3}$ [271]. Using typical values, $H = 0.3$ km, $\tau = 13$, (94) then gives the RMS spread of the spatial Green function as ≈0.3 km, and this number is expected to go up or down only by a factor of $3^{\pm1/6}$ (0.8–1.2) on average. So we can confidently say that LITE has captured most of the multiply scattered laser light coming its way.

Among the ≈2000 pulses returned from this 13 min segment, four were particularly interesting because they were in close proximity and not saturated at their peak values. They are shown in figure 38. The point at which the optical 'echo' appears to come below sea-level is indicated, and this makes the pulse stretching by multiple scattering particularly evident. From these signals the background (in this case, shot and electronic) noise level can be determined visually and the above-noise signal can be used to estimate temporal moments, $\langle ct \rangle_R$ and $\langle (ct)^2 \rangle_R$. From there, one can use (95)–(96), but as recently refined [107] for collimated beam effects, to infer both H and τ. The outcome is $\tau \approx 17$ and $H \approx 0.28$ km, which is not unreasonable in view of the marine Sc climatology briefly described above. An independent refinement for stratification effects by Davis *et al* [272], possibly over-compensating, leads to $\tau \approx 11$ and $H \approx 0.4$ km, which is still well within the climatology.

Other methods of analysis based on explicit expressions for the time-domain signal concur with these numbers [59], and
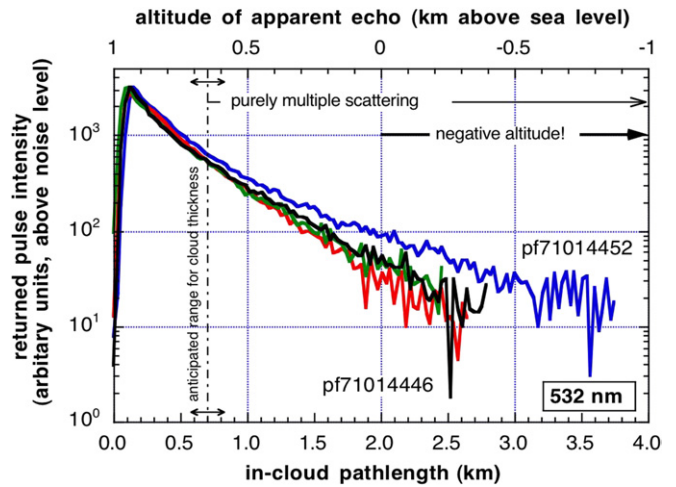

Figure 38. *Four non-saturated LITE pulses returned from an optically thick marine Sc deck.* Time-dependent reflected radiance $R(t)$ is plotted in arbitrary (engineering) units as a function of altitude of the apparent echo (upper axis) and path inside the cloud (lower axis), respectively, the interpretations applicable to the conventional single-backscattering model for the lidar signal and to the new multiple-scattering model that is favored here.

could be used in the presence of saturated portions because the range of time-bins used in the retrieval can be varied by the user. To illustrate with a consistency check, we can use the effective $\{H, \tau\}$ pair obtained for the uniform cloud assumption in (87). Assuming $\chi = 2/3$ for simplicity, this predicts the $ct^\star$ to be ≈0.50 km. The observed value in figure 38 is ≈0.54 km, and the 7% difference is well within experimental error.

8.3.2. Pathlength statistics 2, high-resolution O$_2$ A-Band spectroscopy. To study and exploit temporal statistics, one does not need to obtain explicit time-domain data as long as Laplace-domain data are available. In the case of multiple scattering in the cloudy atmosphere, there happens to be an emerging observational technology that gives us access to Laplace-space data. It is high-resolution differential optical absorption spectroscopy (DOAS) in the 'A-band' of oxygen at 759–771 nm, which was mentioned briefly in section 2.1. The lower panel of figure 2 for O$_2$ optical depth $\kappa_\nu \times H$ across a typical low-level stratus cloud layer. For the instrumentalist's convenience, it sits roughly at the maximum of the solar spectrum when expressed in photons s^{-1} m^{-2}.

The important property of O$_2$ used here is that, being a dominant component of air, its density n is known everywhere with high accuracy. We also know its optical absorption cross-section $\xi_a(\nu)$ very well as a function of wavenumber ν, given pressure and temperature (i.e. altitude). So, we know its absorption coefficient $\kappa_\nu = n \times \xi_a(\nu)$ as a function of ν, and it varies over several orders of magnitude (cf figure 2). Therefore, for a known path L and a known source of broadband radiance $I(0)$, we are able to predict *directly* transmitted radiance from Beer's law:

$$I_\nu(L) = I(0) \exp(-\kappa_\nu L). \qquad (150)$$

This is the simple forward model for DOAS of a gas, O$_2$ or other, at least for high-enough resolution that we do not need

to convolve the spectral variations with a 'slit' function. In practice, that is never quite true. The point here is that we will need this high-enough resolution to justify the use of Beer's law of exponential transmission as a reasonable approximation for the RT-based signal model. In DOAS, we focus on the direct transmittance factor $T_{\text{dir}}(\nu, L) = I_\nu(L)/I(0)$, where $I(0)$ can be determined empirically by seeking a wavelength with negligible absorption, yet not too far from the absorption band of immediate interest, to avoid questions about the spectral invariance assumed for the scattering and reflection.

In operational DOAS, one does not know everything in (150). Unforeseen spectral features can be used to detect and identify unknown molecules in the path. Alternatively, the strength of the spectral lines can be used to estimate the density of a molecular species with a known cross-section. In the present case of multiple-scattering in clouds, we know everything about the molecules but not the path $L(\equiv ct)$ *per se*, because it is in fact a random variable. Consequently, if we know $G(ct, \boldsymbol{x}, \boldsymbol{\Omega})$, the temporal Green function for the uniform boundary source of interest in solar radiation from $(3 + 1)$D RT at the A-band wavelength but only for scattering/reflection processes, then the forward model in (150) becomes

$$I_\nu(\boldsymbol{x}, \boldsymbol{\Omega}) = \int_0^\infty G(ct, \boldsymbol{x}, \boldsymbol{\Omega}) e^{-\kappa_\nu ct} \, dct, \qquad (151)$$

which is sometimes called the 'equivalence' theorem [273, 274]. Note that, apart from again forgetting the slit-function convolution, we have not yet decided what kinds of spatial ($\boldsymbol{x}$) and angular ($\boldsymbol{\Omega}$) integrations we will use, if any. If we do not know the Green function, it is not too serious if nature gives the left-hand side of (151) from measurements and we are only interested in temporal moments, as defined in (89)–(90). Indeed, we can recognize in the equivalence theorem the temporal part of the Fourier–Laplace transform in (81) but where $\kappa_\nu c$ plays the role of s. This enables us to use the recipe in (92) to obtain successive moments of t, hence of ct.

So we end up in this paradoxical situation where two radically different kinds of instrument—one active and monochromatic, and the other passive and hyperspectral (many contiguous spectral bands)—can be brought to bear on studies of path length. Each of these has a host of technological idiosyncrasies, enough that each instrument class is owned by a different community of observation experts. Yet they can deliver the same primary products, namely, $\langle (ct)^q \rangle_R$ ($q = 1, 2$ and possibly more). Having obtained from an O_2 A-band spectrum at least the first two moments of path length, we can perform the same cloud property retrievals as demonstrated above with LITE data. Thus, $\{H, \tau\}$ would be the final ('level 2') product.

If, for any reason, we prefer not to estimate the moments explicitly, we still have a compelling moment-based argument that there is enough cloud information content in $I_\nu(\boldsymbol{x}, \boldsymbol{\Omega})$ to perform the same remote sensing task. One way to do that is to fit the spectroscopic data, re-ordered by value of $\kappa_\nu c$, which yields a monotonically decreasing function. The nonlinear model could be one or another of the analytic expressions for $\tilde{R}(s)$ from sections 3–4 or from the literature since the effects of oblique collimated illumination have recently been

incorporated [107]. The optimal choice of cloud parameters is then found by fixing χ (or μ_0) and g, and varying the pair in $\{H, \tau\}$ to fit the data.

All of this is for reflected light of course, which means that the A-band instrument must be *above* the clouds, either on an aircraft or a satellite. There is a long and venerable line of theoretical and observational studies, many done in the former Soviet Union, on A-band spectroscopy from above ground that, incidentally, has other applications than cloud remote sensing. This literature is surveyed in great detail in a recent review paper by Davis *et al* [108]. Spectrometers that happen to cover the A-band or are custom-built for it have thus been flown for a long time, both on aircraft and in space. However, only now are we achieving the spectral resolving power we need to fully benefit from this opportunity in cloud remote sensing. In particular, we were looking forward to the cloudy pixel data from the imaging A-band spectrometer on the Orbiting Carbon Observatory (OCO) mission; figure 2 was in fact computed at the exquisite spectral resolution OCO's instrument. Unfortunately, the launch vehicle failed ... but we are looking forward to the replacement mission (not yet appropriated by NASA at the time of writing).

It is interesting to note that OCO's mission had nothing to do with clouds and everything to do with mapping CO_2 globally. The only programmatic reason OCO had an O_2 A-band instrument was to deliver the CO_2 column density as a mixing ratio expressed in ppms, which is the way the greenhouse gas (GHG) monitoring community likes to see it (as opposed to $g \, m^{-2}$). This is a recurring scenario in instrument and algorithm development, particularly for space, at the cutting-edge of remote sensing science: we start by using something that exists for some other reason, because a new concept will take a long time to prevail all the way to funding decisions and implementation.

At least two academic institutions have invested time and effort to deploy high-resolution O_2 A-band spectrometers at ground-based stations in recent years. This of course forces us to work with the light transmitted by clouds. Interestingly, both the University of Heidelberg (K Pfeilstiker, PI) [275–277] and the State University of New York at Albany (Q Min, PI) [278–281] teams have focused their A-band research on assessing the spatial complexity of clouds rather than the remote sensing tasks described above. This is a good thing because we recall from section 4 that the 2nd-order temporal moment of the transmitted Green function, $\langle (ct)^2 \rangle_T$, adds nothing new to the information conveyed by the 1st-order moment, $\langle ct \rangle_T$, their ratio being essentially constant across variations of τ; see (99)–(100) and figure 10. These teams both started with studies of $\langle ct \rangle_T$ and moved on to $\langle (ct)^2 \rangle_T$ with upgraded resolving power. Overall, the better the spectral resolution and, just as importantly, the out-of-band rejection of the slit function, the more pieces of path length information that can be inferred [278].

For their basic O_2 A-band DOAS data analysis, both the Heidelberg and the SUNY-Albany groups used a compromise between the two approaches sketched above. They used a nonlinear fit in Laplace/κ_ν-space. Specifically, they used the

Laplace transform of the gamma distribution in (110), but for random variable ct instead of τ, i.e.

$$\tilde{P}(s/c) = \frac{1}{\left(1 + \langle ct \rangle_T \frac{s/c}{a}\right)^a}, \qquad (152)$$

where s/c is identified with κ_ν. This is like its Fourier-space use in the NIPA (section 7.2.1), but with the two first moments of path ct rather than horizontal transport ρ. In this case, the parameters to determine numerically by fit are $\langle ct \rangle_T$ and a, where the latter value immediately yields the interesting ratio $\upsilon = \langle (ct)^2 \rangle_T / \langle ct \rangle_T^2$ through $a = (\upsilon^2 - 1)^{-1}$.

To the above two teams at universities, we add a National Oceanic and Atmospheric Administration (NOAA) team that made a successful foray into this research area. Interestingly, Portmann $et\ al$ [282] used the weaker O_2 B-band ($\sim$687 nm) and relatively low-resolution, but good enough to extract the mean path length. Also, their focus was primarily on completely overcast skies and they therefore reached very good agreement between their observed values of τ and $\langle ct \rangle_T$ with straightforward 1D RT predictions.

Because $\sqrt{\langle (ct)^2 \rangle_T} \propto \langle ct \rangle_T \propto (1 - g)\tau \times H$, there are more unknowns (τ, H) than independent observations by ground-based A-band instruments in cloud remote sensing role, even when limited to single/unbroken layers. They must therefore be used in synergy with one or more ancillary cloud-probing sensors, e.g. the new exploitation of the solar background in MPLs to determine τ from I_{zen} (as explained in section 3.2). Another instrument pairing could include the simple NFOV radiometers that can be used to derive τ if calibrated, and H if not. The latter scenario uses (98), as explained in section 8.1.2. Moreover, the raw data may even be sampled from the A-band instrument at the non-absorbing wavelengths, otherwise used only to normalize the radiances within the absorption band. At any rate, given H (e.g. from a NFOV) or τ (e.g. from an MPL's solar background), A-band will give the other cloud parameter through the observed value of $\langle ct \rangle_T$ and the prediction for it in (99), or a refinement that accounts for oblique collimated illumination and/or stratification.

With access to $\langle ct \rangle_T$ and $\langle (ct)^2 \rangle_T$, the Heidelberg and SUNY-Albany groups noticed that the empirical relationship between $\langle ct \rangle_T$ and τ undergoes a qualitative change when the cloudy skies go from a single unbroken layer to a complex scene with multiple and/or broken layers. For a given τ (obtained by some other means), $\langle ct \rangle_T$ is radically reduced by 3D RT effects for given H. This is as predicted in sections 5.1.2 and 5.1.3 and other theoretical studies, most notably by Stephens $et\ al$ [283, and references therein]; these last authors made extensive use of time-dependent MC methods applied to specific realizations of fractal or data-driven stochastic cloud-field models.

The Heidelberg group adopted the anomalous diffusion (mean-field 3D RT) model from section 5.1.3. They find that the vast majority of cloudy skies had effective Lévy indices α between 1 and 2 [276, 277], where the upper bound corresponds to the standard 1+1D RT model. They also found that the ratio $\sqrt{\langle (ct)^2 \rangle_T} / \langle ct \rangle_T$ was essentially independent of both τ (as predicted for uniform slab clouds using PDEs) and α (the more-or-less chaotic cloudiness). Figure 39 illustrates this interesting finding by Scholl $et\ al$ [277] that challenges current models. Davis' [63] recent mean-field model based on anomalous transport generalizes the anomalous diffusion theory and explains the constant ratio. However, it is really just a MC-based computational technique that uses an ad hoc substitution of exponentially distributed steps with a tunable power-law. Analytical solutions leading to predictions for prefactors and pre-asymptotic corrections, as were obtained for the normal diffusion model, are of course desirable; they may be obtainable following the formalism of Buldyrev $et\ al$ [284] based on pseudo-differential operators (i.e. fractional derivatives).

In summary, there are basically two cloud-probing functions for hi-res O_2 A-band spectroscopy depending on sky conditions. If the cloud structure is simple, a single near plane-parallel layer, then A-band spectrometry is a cloud remote sensing technique bringing more or less information to the table depending on the vantage point: are we looking at reflected or transmitted sunlight? If the cloud structure is complex, with either multiple or broken layers, then (i) A-band responses can detect it and (ii) A-band signals can help to assess—and maybe parametrize—the 3D RT effects.

What good is the later functionality of O_2 A-band DOAS? We must recall that the most challenging case for radiation budget estimation in a GCM grid-cell is for the shortwave heating rates when the cloud structure is complex. A-band is after all about how multiple scattering in and between clouds affects the process of gaseous absorption, which is key to climate when the gas is energetically relevant in the solar spectrum (primarily, GHGs H_2O and CO_2). So it is clear that, if there is a claim that a given GCM shortwave parametrization for cloudy columns makes accurate broadband predictions using all the important species, then it should be able to do so for O_2 since it is very well mixed.

Therefore, by slightly tweaking GCM shortwave parametrizations to become A-band signal predictors (rather than broadband integrators), the O_2 A-band's strong response to 3D cloud structure can be exploited. By making it a sensitive diagnostic of 3D RT effects, it can be used to evaluate the performance of GCM shortwave parametrizations, for given clouds. This activity would normally lead to improved solar RT parametrizations, up to the point where the weakest link in the GCM physics is somewhere else, probably in the forecast of cloud amount and optical properties based on microphysics. Even then, A-band may be able to help by providing a radiative criterion for what is a good-enough representation of the clouds from the important standpoint of shortwave gaseous absorption.

8.3.3. Wide-FOV/multiple-scattering cloud lidar, at suborbital ranges. Our last technical topic is a small conceptual extension of cloud remote sensing with space-based/wide-FOV lidar pioneered with LITE (cf section 8.3.1). If the stand-off distance is not so great, surely there is a way of *directly* recording the spatial part of the Green function excited by the pulsed laser beam. We already know from section 4.2, that this
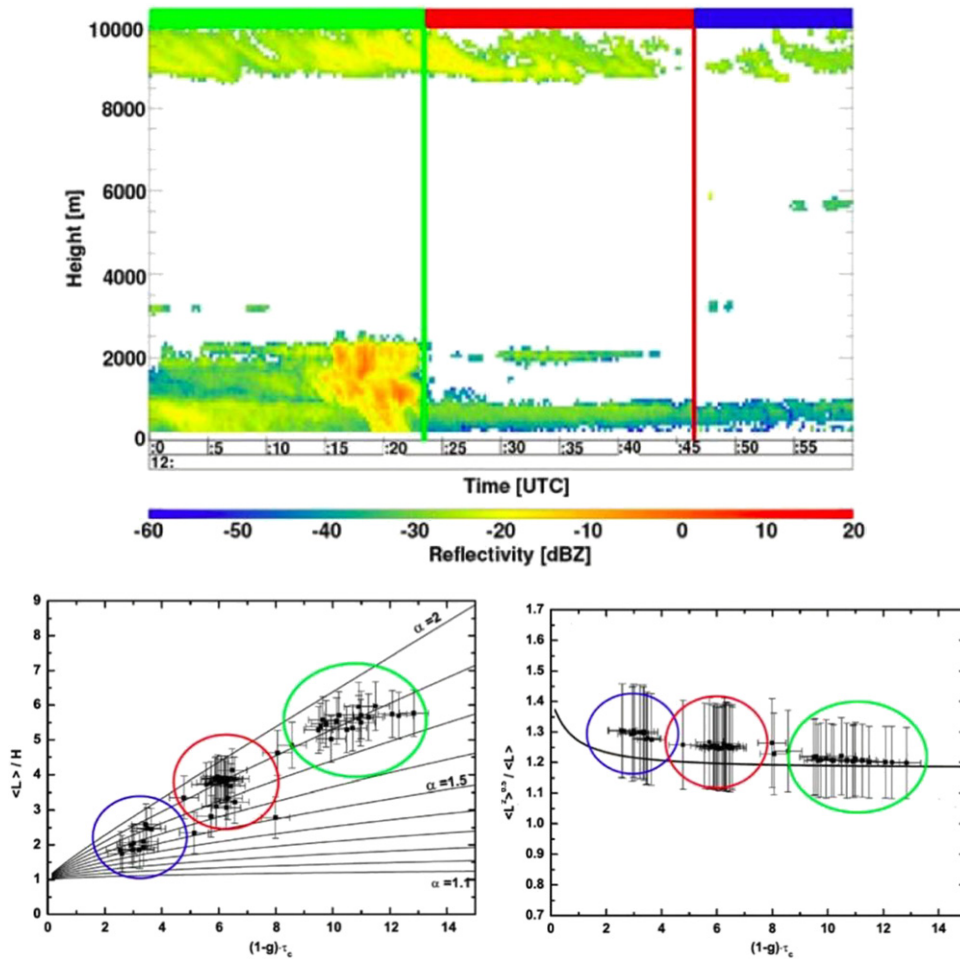
Figure 39. *Millimeter-Wave Cloud Radar (MMCR) transects and path length moments from O_2 A-band for the cloudy sky over Cabauw, NL, on 11 May 2003.* The upper panel shows the structure of clouds according to the collocated MMCR as a function of time, roughly for 1 h. The scene is color-coded for three successive periods where the clouds go from two solid layers to a more and more broken structure. The lower left-hand panel shows $\langle ct \rangle_T/H$, H being the thickness of the whole cloud system (from the MMCR), and $\langle ct \rangle_T$ from the 2nd-generation University of Heidelberg O_2 A-band spectrometer. This ratio is plotted as a function of scaled optical depth $\tau_t = (1-g)\tau$ (obtained from other collocated instruments). Overlaid on the data is an ad hoc hybrid model that used the prefactor and pre-asymptotic corrections in (95) but the scaling exponent for τ_t taken from section 5.1.3. The lower right-hand panel shows $\sqrt{\langle (ct)^2 \rangle_T}/\langle ct \rangle_T$ as a function of τ_t for the same observations. We note the essentially constant RMS/mean ratio. Reproduced from [277].

added information will help determine the cloud properties of immediate interest $\{H, \tau\}$.

As far as we know, two groups have worked on this task assuming different stand-off distances. The NASA–GSFC team (led by R F Cahalan) developed an airborne device that operates from $\sim$10 km above cloud top; it was baptized as the [cloud] THickness from Off-Beam Returns (THOR) system. The Los Alamos National Laboratory team (led by a present author, AD, and S P Love) developed a ground-based device that operates from $\sim$1 km below cloud base; it was baptized as the Wide-Angle Imaging Lidar (WAIL) system. Both projects succeeded at the proof-of-concept level for nighttime operation in the relevant environment [110, 111]. The receeiver hardware implementations were very different at the focal plane as well as the fore-optics. In spite of the identical signal physics, the adopted data analysis procedures were also very different in philosophy and in execution.

THOR was designed to produce an azimuthally integrated profile of the spatial part of the Green function; it is based on

eight different concentric bundles of fiber-optics that channel the spatially partitioned light from the focal plane to as many fast detectors (designed for otherwise standard lidar work).

WAIL went through two receivers, both being imagers. The first was a special detector custom-built at Los Alamos National Laboratory (LANL) for the Remote Ultra-Low Light Imaging (RULLI) program [285]. It worked well for laboratory mock-ups [286] and in the far field for real clouds [287]. However, it could not cope with the huge dynamic range without a cumbersome system of density filters used in the deployments. The second receiver was an off-the-shelf gated/intensified CCD camera that has far more capability than has been harnessed so far; of prime interest here is the possibility of adaptive exposure times for different time gates, given the hugely variable signal levels.

Both WAIL and THOR were fielded at a coordinated validation campaign in March 2002, respectively , at and above the previously mentioned DOE ARM program's climate monitoring facility in Oklahoma. An extended stratus layer
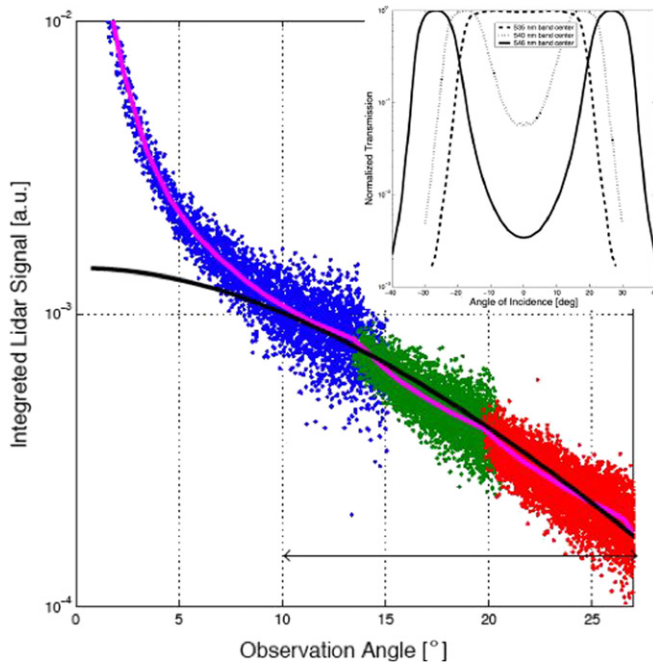
Figure 40. *Observed and predicted spatial Green function.* The color-coded data points are from LANL's WAIL instrument, collected on 25 March 2002, at the ARM Southern Great Plains site under overcast skies. The three colors correspond to the three background-suppression interference filters used to rebuild the spatial Green function from three successive acquisitions; their angular responses at the laser wavelength (532 nm) are displayed in the inset on a log scale. Also plotted is a smoothed version of the observations from a moving-mean filter (magenta curve), and the signal prediction from the diffusion-based forward RT model (black curve), as optimally fit to the data by varying $\{H, \tau\}$. Only the $\theta(\rho)$ region highlighted with the arrows was used to compute the fitting cost-function, as it is where the diffusion model can be used with some confidence. Reproduced from [111].

developed and was thus probed, from both sides, by wide-FOV/multiple-scattering lidar systems. The objective was to compare THOR and WAIL cloud property retrievals with those obtained from operational ARM instruments. The outcome for both systems and data analysis procedures compared well with standard ARM products or a cloud-cover reanalysis based on radiosonde profiles, and are thus deemed 'validated.'

Figure 40 shows one example of how WAIL data were processed. Since WAIL's (and, for that matter, THOR's) time-domain signals are not fundamentally different from those of LITE, we choose to display some spatial data. Every point corresponds to the time-integrated signal at each pixel from the gated/intensified CCD plotted as a function of its distance to the pixel estimated to be where the laser beam hit the cloud base. The three primary colors are for three separate background-suppression filters used to reduce the (lunar) noise level; see inset. Each of the 10 nm band-width interference filters also had a characteristic angular response at the fixed laser wavelength (532 nm) and the trio were necessary to build up the full 53° FOV image—in fact 'movie' (before the illustrated time-integration was performed).

One interesting aspect of the spatial signal displayed in figure 40 is that it is severely truncated. For instance, multiplication by $\rho^2 \times 2\pi\rho$, which is preliminary to estimating

$\langle \rho^2 \rangle_R$, leads to an increasing curve that levels but does not decay to zero. So moment estimation is useless. The cloud was too low or the 53° FOV was too small. That is one of the reasons why it proved important to obtain more approximate but explicit expressions for the Green functions in space and time [59, 103]. Their free cloud parameters can be fit to the space–time data *only where data are available* and *only where the model is known to be valid.* As previously mentioned, the trick to obtain Fourier–Laplace invertible solutions is to rewrite the BCs approximately as Dirichlet-type rather than Robin-type. The resulting analytical prediction for $R(\rho)$ is shown in the figure, as fitted to the data (black curve).

8.3.4. Wide-FOV/multiple-scattering cloud lidar and O_2 A-band: a general discussion. In view of the many technological and logistical differences between the LANL and GSFC systems and in the way their signals were analyzed, we see their joint successes as an overarching validation of the whole idea of using direct space–time Green function observation to probe clouds and retrieve important cloud properties. This successful innovation of lidar technology adds tremendous capability to active cloud remote sensing. Indeed, standard (on-beam/single-scattering) lidar cannot penetrate clouds with $\tau \gtrsim 3$, even after corrections for multiple forward scatterings that reduce the *apparent* extinction, and that is precisely where these off-beam/multiple-scattering lidar systems start performing.

The successful analysis of LITE cloud data surveyed in section 8.3.1 reinforces to this validation statement and, at the same time, defines LITE a forerunner of the emerging concept we refer generically to as Multiple-Scattering Cloud Lidar (MuSCL). Another novel active technique for probing the bulk properties of clouds was mentioned in the introductory section, *in situ* cloud lidar [21, 22], which was developed at the University of Colorado and by Stratton Park Engineering Company (SPEC), Inc. (Boulder, Co) ⟨http://www.specinc.com/⟩. Its signal physics are the same as in THOR and WAIL (and, like LITE's, purely temporal). It should therefore be considered as part of the same class of MuSCL techniques. Who cares if the source and sensor are *inside* the cloud? It is still a *remote* detection of the presence of cloud boundaries above and below the aircraft, hence its estimate of H. The other cloud property it delivers is *volume-averaged* extinction for the cloudy air all around the aircraft, in other words, τ/H.

It is interesting to ask about the spatial resolution of Green function observation techniques, both passive and active. It is inherently adaptive. Imagine, for instance, a ground-based MuSCL system such as WAIL. Basically, it is the width of the spatial Green function, which itself depends on $\{H, \tau\}$, because the retrieval is in effect for volume-averaged cloud properties. The volume is $\sim H \times \langle \rho^2 \rangle_F(H, \tau)$, with $F = R$ for WAIL and $F = T$ for ground-based A-band. In any application (such as climate prediction) where solar RT matters, this is the optimal resolution; the unresolved variability is then, by definition, incorporated into the Green function measurement.

We cannot close this discussion without mentioning that active Green function observation with wide-FOV/multiple-scattering lidar has other applications than clouds in

environmental science, and it has analogs in other branches of science altogether. All that is required really is a highly scattering optical medium, the instrumentation can be adapted to a wide variety of scales and levels of access to the medium, starting in the lab and ending (why not?) with planetary missions. As an example, the THOR team has proposed to use its technology to probe sea ice and snow cover [288]. Applications to turbid coastal water also come to mind.

Since the 1990s, the new medical imaging field of 'diffuse optical tomography' [289] has gone from the concept to the lab to clinical applications. It is predicated on the fact that soft tissue is highly scattering in the NIR, but anomalies (small tumors, aneurysms and so on) are either highly absorbing or they behave like optical voids. With enough sampling of the space–time Green functions from any number of source-and-sensor positions, one can reconstruct the medium at a coarse scale that may be sufficient for screening and diagnostics. This novel and inherently non-invasive tomography was enabled by progress in computational physics and numerical analysis: there are now extremely fast solvers for the (3+1)D diffusion equation in arbitrary outer and inner geometry. In this context, WAIL and THOR are a poor-man's version of optical tomography suitable for clouds. Only one sample of the space–time Green function allowed, but it can be assumed that the only 'anomaly' to be located is the absorbing boundary of the cloud opposite the illuminated one, hence H. Also, we wish to estimate the volume-averaged scattering coefficient of the cloudy medium, hence $\overline{\sigma} = \tau/H$, which is a known quantity in the biomedical application. The strong response of O_2 A-band products (i.e. $\langle (ct)^q \rangle_F$ for $q = 1, 2, 3, \ldots$) to 3D complexity in cloud structure is another manifestation of the crude but valuable tomographic capability of radiative Green function observation.

It is too early to know how the atmospheric science community at large will assimilate and use this new kind of information. What we do know, since section 4, is that reflected A-band spectra will contain more cloud information than their transmitted counterparts. Conceivably, one could retrieve $\{H, \tau, \Delta, \epsilon, \cdots\}$ or $\{H, \tau, \alpha, \cdots\}$, referring to internal structure parameters used in previous subsections. Moreover, when we get such data from space, we will have global coverage of the daytime hemisphere. And for the nighttime side of the orbit, a co-manifested MuSCL system (with a FOV similar to LITE's) will hopefully be there to pick up the relay.

In view of the technicalities of Green function observation and the ensuing physics-based data processing, it is very likely that—as in the medical profession for tomography—there will be a natural separation of labor into subject-matter experts (remote sensing scientists) and end-users engaged in Earth-science endeavors that are much bigger than the remote sensing. Each type of individual will be easily identifiable and each individual will have distinctive passions. These sub-communities will have to understand intimately each other's needs and interests if Earth science is to benefit fully from the new technology.

9. Summary and outlook

Driven by climate and remote sensing applications, we reviewed the physics underlying the transport of solar (and some laser) radiation through the Earth's cloudy atmosphere. We encountered along the way many challenging problems stemming from (i) the spatial complexity of real clouds and (ii) the physical complexity of multiple-scattering processes. For each problem that presented itself, we discussed state-of-the-art solutions, emphasizing those that bring physical insights that can be used again and again. We discovered in particular that Green functions play a key role in almost every aspect of the phenomenology of 3D radiative transfer in and between the clouds, the aerosols, the gases and the surface. We also discovered that, even though the problem at hand is steady-state, time-dependent radiation transport has proved very helpful. After all, transport of radiant energy unfolds in space, and time for that to happen is implicit.

One century ago, Peter Debye published a seminal paper [3] on scattering of EM waves by spheres, one at a time, and his paper appeared only a year after the better-known one by Gustav Mie [2]. Radiative transfer in 1D in the presence of multiple scattering is older, although maybe not by much, since it can be traced back at least to Arthur Schuster's 1905 paper [4] on visibility through fog. At the time of writing, we cross the significant milestone of a half-century of research in 3D radiative transfer in spatially variable media such as clouds, which started (as far as we know) with Giovanelli's landmark 1959 paper [8] applying a perturbative diffusion theory of 3D radiation transport to plane-parallel media with a regular sine-wave structure.

Taking a historical perspective on this development, we have identified three phases and the associated thrusts continue to this day.

- First, there was a long period of *damage assessment* since 1D radiative transfer had become the *de facto* standard model in all the application areas, spanning from solar heating rate estimation for the energy cycle in climate models to the translation of pixel-scale reflected or transmitted solar radiances into inherent optical or microphysical cloud properties.

- Then came attempts to *mitigate this damage* since, realistically, we expect that 1D radiative transfer is not going away any time soon. At any rate, its status will slowly evolve from being *the* point of reference, simply because it is so popular, to being just one possible approximation to 3D reality that happens to simplify radically the computations. Enhancements of its range of validity via 3D–1D bias mitigation will help in practical situations.

- Finally, as our understanding of 3D radiative transfer phenomena matures, we enter a new era where we embrace the spatial complexity and find ways to *exploit inherently 3D radiative transfer processes* and thus re-invigorate the science and technology of cloud remote sensing. We have every reason to believe that both passive and active modalities will emerge, and we can already detect a trend toward techniques that avoid the costly and cumbersome need for absolute radiometric calibration.

At all three levels, the preliminary question about any specific 3D radiative transfer problem at hand is whether the spatial variability is resolved or unresolved, given the scale of interest. That scale can be either the computational grid constant or the remote sensing pixel size. Approaches for treating unresolved variability invariably have a stochastic flavor (and often analytical methods work well), while those we apply to cases of resolved variability are necessarily deterministic (and typically lead to a computational scheme).

As part of a second generation of 3D radiative transfer experts, following in the steps of pioneers, the present authors are confident that the field has a bright future. There are clear signs that the old paradigm grounded in stalwart 1D radiative transfer is waning and that a new paradigm grounded in theoretical, computational and observational 3D radiative transfer is gaining considerable momentum.

Acknowledgments

References

[1] Hamblyn R 2001 *The Invention of Clouds: How an Amateur Meteorologist Forged the Language of the Skies* (New York: Farrar, Straus, and Giroux)

[2] Mie G 1908 Beiträge zur Optik trüber Medien, speziell kolloidaler Metallösungen *Annal. Phys., Lpz.* **330** 377–445

[3] Debye P 1909 Der lichtdruck auf kugeln von beliebigem material *Annal. Phys., Lpz.* **335** 57–136

[4] Schuster A 1905 Radiation through a foggy atmosphere *Astrophys. J.* **21** 1–22

[5] Lommel E 1887 Die photometrie der diffusen zurüchwerfung *Sitzber. Acad. Wiss. München* **17** 95–124

[6] Chowlson O 1889 Grunzüge einer mathematischen theorie der inneren diffusion des lichtes *Bull. Acad. Imp. Sci. St. Petersburg* **33** 221–56

[7] Chandrasekhar S 1950 *Radiative Transfer* (Oxford: Oxford University Press) (reprinted by (New York: Dover))

[8] Giovanelli R G 1959 Radiative transfer in non-uniform media *Aust. J. Phys.* **12** 164–70

[9] Richards P I 1956 Scattering from a point-source in plane clouds *J. Opt. Soc. Am.* **46** 927–34

[10] Chandrasekhar S 1958 On the diffuse reflection of a pencil of radiation by a plane-parallel atmosphere *Proc. Natl Acad. Sci. USA* **44** 933–40

[11] Solomon S, Qin D and Manning M (ed) 2007 *Climate Change 2007 The Physical Science Basis* (Geneva: Intergovernmental Panel on Climate Change)

[12] Barker H W and 31 co-authors 2003 Assessing 1D atmospheric solar radiative transfer models: interpretation and handling of unresolved clouds *J. Clim.* **16** 2676–99

[13] Randall D A, Khairoutdinov M, Arakawa A and Grabowski W 2003 Breaking the cloud-parameterization deadlock *Bull. Am. Meteorol. Soc.* **84** 1547–64

[14] Tao W-K *et al* 2009 A multiscale modeling system: developments, applications, and critical issues *Bull. Am. Meteorol. Soc.* **90** 515–34

[15] Albrecht B A 1989 Aerosols, cloud microphysics, and fractional cloudiness *Science* **245** 1227–30

[16] Twomey S A 1991 Aerosols, clouds and radiation *Atmos. Environ.* A **25** 2435–42

[17] Ramanathan V 2001 Aerosols, climate, and the hydrological cycle. *Science* **294** 2119

[18] Mishchenko M I, Cairns B, Kopp G, Schueler C F, Fafaul B A, Hansen J E, Hooker R J, Itchkawich T, Maring H B and Travis L D 2007 Accurate monitoring of terrestrial aerosols and total solar irradiance: introducing the glory mission *Bull. Am. Meteorol. Soc.* **88** 677–91

[19] Diner D J, Davis A, Hancock B, Gutt G, Chipman R A and Cairns B 2007 Dual photoelastic modulator-based polarimetric imaging concept for aerosol remote sensing *Appl. Opt.* **46** 8428–45

[20] Stephens G L *et al* and the CloudSat Science Team 2002 The CloudSat mission and the A-train *Bull. Am. Meteorol. Soc.* **83** 1771–90

[21] Evans K F, Lawson R P, Zmarzly P and O'Connor D 2003 *In situ* cloud sensing with multiple scattering cloud lidar: simulations and demonstration. *J. Atmos. Ocean. Technol.* **20** 1505–22

[22] Evans K F, O'Connor D, Zmarzly P and Lawson R P 2006 *In situ* cloud sensing with multiple scattering cloud lidar: design and validation of an airborne sensor *J. Atmos. Ocean. Technol.* **23** 1068–81

[23] Barkstrom B, Harrison E, Smith G, Green R, Kibler J, Cess R and the ERBE Science Team 1989 Earth Radiation Budget Experiment (ERBE) archival and April 1985 results *Bull. Am. Meteorol. Soc.* **70** 1254–62

[24] Wielicki B A, Barkstrom B R, Harrison E F, Lee R B, Louis Smith G and Cooper J E 1996 Clouds and the Earth's Radiant Energy System (CERES): an Earth Observing System experiment *Bull. Am. Meteorol. Soc.* **77** 853–68

[25] Kurucz R L, Furenlid I, Brault J and Testerman L (ed) 1984 *Solar Flux Atlas from 296 to 1300 nm* 2nd edn (Sunspot, NM: National Solar Observatory)

[26] Anderson D E and Cahalan R F 2005 The SOlar radiation and Climate Experiment (SORCE) mission for the NASA Earth Observing System (EOS) *Solar Phys.* **203** 3–6

[27] Loeb N G, Kato S and Wielicki B A 2002 Defining top-of-the-atmosphere flux reference level for Earth radiation budget studies *J. Clim.* **15** 3301–9

[28] Collins W D, Valero F P J, Flatau P J, Lubin D, Grassl H and Pilewskie P 1996 Radiative effects of convection in the tropical Pacific *J. Geophys. Res.* D **101** 14999–5012

[29] Fu Q and Liou K N 1993 Parameterization of the radiative properties of cirrus clouds *J. Atmos. Sci.* **50** 2008–25

[30] Li J and Barker H W 2005 A radiation algorithm with correlated-k distribution: I. Local thermal equilibrium *J. Atmos. Sci.* **62** 286–309

[31] Bartle R G 1995 *The Elements of Integration and Lebesgue Measure* (New York: Wiley)

[32] Goody R M and Yung Y L 1989 *Atmospheric Radiation Theoretical Basis* (New York: Oxford University Press)

[33] Cox C and Munk W 1954 Measurement of the roughness of the sea surface from photographs of the sun's glitter *J. Opt. Soc. Am.* **44** 838–50

[34] Coakley J A Jr, Bernstein R L and Durkee P A 1987 Effect of ship-stack effluents on cloud reflectivity *Science* **237** 1020–2

[35] Nussenzveig H M 1992 *Diffraction Effects in Semiclassical Scattering* (Cambridge: Cambridge University Press)

[36] Bohren C F and Huffman D R 1983 *Absorption and Scattering of Light by Small Particles* (New York: Wiley)

[37] Mishchenko M I, Travis L D and Lacis A A (ed) 2002 *Scattering, Absorption, and Emission of Light by Small Particles* (Cambridge: Cambridge University Press)

[38] Deirmendjian D 1969 *Electromagnetic Scattering on Spherical Polydispersions* (New York: Elsevier)

[39] Warren S G 1984 Optical constants of ice from the ultraviolet to the microwave *Appl. Opt.* **23** 1206–25

[40] Grenfell T C and Warren S G 1999 Representation of a non-spherical ice particle by an assembly of spheres *J. Geophys. Res.* D **104** 31697–709

[41] Takano Y and Jayaweera K 1985 Scattering phase matrix for hexagonal ice crystals computed from ray optics *Appl. Opt.* **24** 3254–63

[42] Macke A 1993 Scattering of light by polyhedral ice crystals *Appl. Opt.* **32** 2780–8

[43] Mishchenko M I and Travis L D 1994 T-matrix computations of light scattering by large spheroidal particles *Opt. Commun.* **109** 16–21

[44] Mishchenko M I, Travis L D and Mackowski D W 1996 T-matrix computations of light scattering by non-spherical particles *J. Quant. Spectrosc. Radiat. Transfer* **55** 535–76

[45] Yang P and Liou K N 1996 Finite-difference time domain method for light scattering by small ice crystals in three-dimensional space *J. Opt. Soc. Am.* A **13** 2072–85

[46] Mishchenko M I, Hovenier J W and Travis L D (ed) 2000 *Light Scattering by Nonspherical Particles: Theory, Measurements, and Applications* (San Diego, CA: Academic)

[47] Born M and Wolf E 1999 *Principles of Optics: Electromagnetic Theory of Propagation, Interference and Diffraction of Light* 7th expanded edn (New York: Cambridge University Press)

[48] Hansen J E and Travis L D 1974 Light-scattering in planetary atmospheres *Space Sci. Rev.* **16** 527–610

[49] Mishchenko M I 2002 Vector radiative transfer equation for arbitrarily shaped and arbitrarily oriented particles: a microphysical derivation from statistical electromagnetics *Appl. Opt.* **41** 7114–35

[50] Mishchenko M I 2006 Radiative transfer in clouds with small-scale inhomogeneities: the microphysical approach *Geophys. Res. Lett.* **33** L14820

[51] Mishchenko M I 2008 Multiple scattering, radiative transfer, and weak localization in discrete random media: unified microphysical approach *Rev. Geophys.* **46** RG2003

[52] Mihalas D 1979 *Stellar Atmospheres* 2nd edn (San Francisco, CA: Freeman)

[53] Kostinski A B 2001 On the extinction of radiation by a homogeneous but spatially correlated random medium *J. Opt. Soc. Am.* A **18** 1929–33

[54] Davis A B and Marshak A 2004 Photon propagation in heterogeneous optical media with spatial correlations: enhanced mean-free-paths and wider-than-exponential free-path distributions *J. Quant. Spectrosc. Radiat. Transfer* **84** 3–34

[55] Eddington A S 1916 On the radiative equilibrium of stars *Mon. Not. R. Astron. Soc.* **77** 16–35

[56] Gerber H, Takano Y, Garrett T J and Hobbs P V 2000 Nephelometer measurements of the asymmetry parameter, volume extinction coefficient, and backscatter ratio in arctic clouds *J. Atmos. Sci.* **57** 3021–34

[57] Baran A J, Francis P N, Labonnote L C and Doutriaux-Boucher M 2001 A scattering phase function for ice cloud: Tests of applicability using aircraft and satellite multi-angle multi-wavelength radiance measurements of cirrus *Q. J. R. Meteorol. Soc.* **127** 2395–416

[58] Baran A J 2009 A review of the light scattering properties of cirrus *J. Quant. Spectrosc. Radiat. Transfer* **110** 1239–60

[59] Polonsky I N and Davis A B 2005 Off-beam cloud lidar: a new diffusion model and an analysis of lite returns *Technical Report* LA-UR-05-0794 Los Alamos National Laboratory, Los Alamos (NM)

[60] Larsen E W 1980 Diffusion theory as an asymptotic limit of dtransport theory for nearly critical systems with small mean free paths *Annal Nucl. Energy* **7** 249–55

[61] Pomraning G C 1989 Diffusion theory via asymptotics *Transp. Theory and Stat. Phys.* **18** 383–428

[62] Davis A and Marshak A 1997 Lévy kinetics in slab geometry: scaling of transmission probability *Fractal Frontiers* ed M M Novak and T G Dewey (Singapore: World Scientific) pp 63–72

[63] Davis A B 2006 Effective propagation kernels in structured media with broad spatial correlations, illustration with large-scale transport of solar photons through cloudy atmospheres *Computational Methods in Transport—Granlibakken 2004* (*Lecture Notes in Computational Science and Engineering* vol 48) ed F Graziani (New York: Springer) pp 84–140

[64] Joseph J H, Wiscombe W J and Weinman J A 1976 The delta-Eddington approximation for radiative flux transfer *J. Atmos. Sci.* **33** 2452–9

[65] Henyey L C and Greenstein J L 1941 Diffuse radiation in the galaxy *Astrophys. J.* **93** 70–83

[66] Nicodemus F E, Richmond J C, Hsia J J, Ginsberg I W and Limperis T 1977 Geometrical considerations and nomenclature for reflectance *Technical Report NBS Monograph* No 160 (Washington, DC: National Bureau of Standards)

[67] Martonchik J V, Bruegge C J and Strahler A 2000 A review of reflectance nomenclature used in remote sensing *Remote Sens. Rev.* **19** 9–20

[68] Lenoble J (ed) 1985 *Radiative Transfer in Scattering and Absorbing Atmospheres: Standard Computational Procedures* (Hampton, VA: Deepak)

[69] Stephens G L 1978 Radiation profile in extended water clouds: I. Theory *J. Atmos. Sci.* **35** 2111–22

[70] Meador W E and Weaver W R 1980 Two-stream approximations to radiative transfer in planetary atmospheres: a unified description of existing methods and a new improvement *J. Atmos. Sci.* **37** 630–43

[71] Takano Y and Liou K N 1989 Solar radiative transfer in cirrus clouds: I. Single-scattering and optical properties of hexagonal ice crystals *J. Atmos. Sci.* **46** 3–18

[72] Li J and Ramaswamy V 1996 Four-stream spherical harmonic expansion approximation for solar radiative transfer *J. Atmos. Sci.* **53** 1174–86

[73] Lu P, Zhang H and Li J 2009 A comparison of two-stream DISORT and Eddington radiative transfer schemes in a real atmospheric profile *J. Quant. Spectrosc. Radiat. Transfer* **110** 129–38

[74] Coakley J A Jr and Chylek P 1975 The two-stream approximation in radiative transfer: including the angle of the incident radiation *J. Atmos. Sci.* **32** 409–18

[75] Dickinson R E, Zhou L, Tian Y, Liu Q, Lavergne T, Pinty B, Schaaf C B and Knyazikhin Y 2008 A three-dimensional analytic model for the scattering of a spherical bush *J. Geophys. Res.* **113** D20113

[76] Bohren C F, Linskens J R and Churma M E 1995 At what optical thickness does a cloud completely obscure the sun? *J. Atmos. Sci.* **52** 1257–9

[77] Tape W 1994 *Atmospheric Halos* (*Antarctic Research Series* Number 64) (Washington, DC: American Geophysical Union)

[78] Stephens G L 1978 Radiation profile in extended water clouds: II. Parameterization schemes *J. Atmos. Sci.* **35** 2123–32

[79] Welch R M and Zdunkowski W G 1982 Backscattering approximations and their influence on Eddington-type solar flux calculations *Contrib. Atmos. Phys.* **55** 28–42

[80] King M D and Harshvardhan 1986 Comparative accuracy of selected multiple scattering approximations *J. Atmos. Sci.* **43** 784–801

[81] Kokhanovsky A A 2006 Asymptotic radiative transfer *Light Scattering Reviews* vol 1, ed A A Kokhanovsky (Berlin: Springer) pp 253–89

[82] Stamnes K, Tsay S-C, Wiscombe W J and Jayaweera K 1988 Numerically stable algorithm for discrete-ordinate-method radiative transfer in multiple scattering and emitting layered media *Appl. Opt.* **27** 2502–09

[83] Garcia R and Siewert C 1985 Benchmark results in radiative transfer *Transp. Theory Stat. Phys.* **14** 437–84

[84] Chiu J C, Marshak A, Wiscombe W J, Valencia S C and Welton E J 2007 Cloud optical depth retrievals from solar background signals of micropulse lidars *IEEE Geosc. Remote Sens. Lett.* **4** 456–60

[85] Yang Y, Marshak A, Chiu J C, Wiscombe W J, Palm S P, Davis A B, Spangenberg D A, Nguyen L, Spinhirne J and Minnis P 2008 Calibration of solar background signal for retrievals of cloud optical depth from the Geoscience Laser Altimeter System (GLAS) *J. Atmos. Sci.* **65** 3531–27 (doi:10.1175/2008JAS2744.1)

[86] Spinhirne J D, Rall J A R and Scott V S 1995 Compact eye-safe lidar systems *Rev. Laser Eng.* **23** 112–8

[87] Welton E J, Voss K J, Quinn P K, Flatau P J, Markowicz K, Campbell J R, Spinhirne J D, Gordon H R and Johnson J E 2002 Measurements of aerosol vertical profiles and optical properties during INDOEX 1999 using micropulse lidars *J. Geophys. Res.* D **107** D8019

[88] Campbell J R, Hlavka D L, Welton E J, Flynn C J, Turner D D, J.D. Spinhirne, Scott V S and Hwang I H 2002 Full-time, eye-safe cloud and aerosol lidar observation at Atmospheric Radiation Measurement program sites: instruments and data processing *J. Atmos. Ocean. Technol.* **19** 431–42

[89] Welton E J and Campbell J R 2002 Micropulse lidar signals: uncertainty analysis *J. Atmos. Ocean. Technol.* **19** 2089–94

[90] Marshak A, Knyazikhin Y, Evans K D and Wiscombe W J 2004 The 'red versus nir' plane to retrieve broken-cloud optical depth from ground-based measurements *J. Atmos. Sci.* **61** 1911–25

[91] Chiu J C, Marshak A, Knyazikhin Y, Wiscombe W J, Barker H W, Barnard J C and Luo Y 2006 Remote sensing of cloud properties using ground-based measurements of zenith radiance *J. Geophys. Res.* D **111** D16201

[92] Holben B N *et al* 1998 AERONET—a federated instrument network and data archive for aerosol characterization *Remote Sens. Environ.* **66** 1–16

[93] Chiu J C, Huang C-H, Marshak A, Slutsker I, Giles D M, Holben B N, Knyazikhin Y and Wiscombe W J 2009 Cloud optical depth retrievals from the Aerosol Robotic Network (AERONET) cloud mode observations *J. Geophys. Res.* at press

[94] Davies R 1978 The effect of finite geometry on the three-dimensional transfer of solar irradiance in clouds *J. Atmos. Sci.* **35** 1712–25

[95] Preisendorfer R W and Stephens G L 1984 Multimode radiative transfer in finite optical media: I. Fundamentals *J. Atmos. Sci.* **41** 709–24

[96] Stephens G L and Preisendorfer R W 1984 Multimode radiative transfer in finite optical media: II. Solutions *J. Atmos. Sci.* **41** 725–35

[97] Barkstrom B R and Arduini R F 1977 The effect of finite size of clouds upon the visual albedo of the Earth *Radiation in the Atmosphere* ed H-J Bolle (Princeton, NJ: Science Press) pp 188–90

[98] Davis A B 2002 Cloud remote sensing with sideways-looks: theory and first results using Multispectral Thermal Imager (MTI) data *SPIE Proc.* **4725** 397–405

[99] Ganapol B D, Kornreich D E, Dahl J A, Nigg D W, Jahshan S N and Temple C A 1994 The searchlight problem for neutrons in a semi-infinite medium *Nucl. Sci. Eng.* **118** 38–53

[100] Kornreich D E and Ganapol B D 1997 Numerical evaluation of the three-dimensional searchlight problem in a half-space *Nucl. Sci. Eng.* **127** 317–37

[101] Machida M, Panasyuk G Y, Schotland J C and Markel V A 2009 Green's function for the radiative transport equation in slab geometry *J. Phys. A: Math. Gen.* at press

[102] Zege E P, Ivanov A P and Katsev I L 1991 *Image Transfer Through a Scattering Medium* (Heidelberg: Springer)

[103] Polonsky I N and Davis A B 2004 Lateral photon transport in dense scattering and weakly absorbing media of finite thickness: asymtotic analysis of the space–time Green function *J. Opt. Soc. Am.* A **21** 1018–25

[104] Feller W 1971 *An Introduction to Probability Theory and its Applications* vol 1 and 2 (New York: Wiley)

[105] Davis A B, Cahalan R F, Spinehirne J D, McGill M J and Love S P 1999 Off-beam lidar: an emerging technique in cloud remote sensing based on radiative Green-function theory in the diffusion domain *Phys. Chem. Earth* B **24** 177–85
    Davies A B, Cahalan R F, Spinehirne J D, McGill M J and Love S P 1999 Off-beam lidar: an emerging technique in cloud remote sensing based on radiative Green-function theory in the diffusion domain *Phys. Chem. Earth* B **24** 757–65 (erratum)

[106] Davis A B and Marshak A 2002 Space-time characteristics of light transmitted through dense clouds: a Green's function analysis *J. Atmos. Sci.* **59** 2713–27

[107] Davis A B 2008 Multiple-scattering lidar from both sides of the clouds: Addressing internal structure *J. Geophys. Res.* D **113** 14S10

[108] Davis A B, Polonsky I N and Marshak A 2009 Space-time Green functions for diffusive radiation transport, in application to active and passive cloud probing *Light Scattering Rev.* vol 4, ed A A Kokhanovsky (Heidelberg: Springer) pp 169–292

[109] Clothiaux E E, Miller M A, Albrecht B A, Ackerman T P, Verlinde J, Babb D M, Peters R M and Syrett W J 1995 An evaluation of a 94 GHz radar for remote sensing of cloud properties *J. Atmos. Ocean. Technol.* **12** 201–29

[110] Cahalan R F, McGill M J, Kolasinski J, Várnai T and Yetzer K 2005 THOR, cloud THickness from Offbeam lidar Returns *J. Atmos. Ocean. Techol.* **22** 605–27

[111] Polonsky I N, Love S P and Davis A B 2005 Wide-angle imaging lidar deployment at the ARM Southern Great Plains site: intercomparison of cloud property retrievals *J. Atmos. Ocean. Technol.* **22** 628–48

65

[112] Redner S 2001 *A Guide to First-Passage Processes* (Cambridge: Cambridge University Press)

[113] Chandrasekhar S 1943 Stochastic problems in physics and astronomy *Rev. Mod. Phys.* **15** 1–89

[114] Barker H W and Davis A B 2005 Approximation methods in atmospheric 3D radiative transfer: II. Unresolved variability and climate applications *3D Radiative Transfer in Cloudy Atmospheres* (Heidelberg: Springer) ed A Marshak and A B Davis pp 343–83 chapter 6

[115] Cahalan R F 1994 Bounded cascade clouds: Albedo and effective thickness *Nonlinear Proc. Geophys.* **1** 156–67

[116] Jensen J L W V 1906 Sur les fonctions convexes et les inégalitiés entre les valeurs moyennes *Acta Math.* **30** 175–93

[117] Tiedtke M 1996 An extension of cloud-radiation parameterization in the ECMWF model: the representation of subgridscale variations in optical depth *Mon. Weather Rev.* **124** 745–50

[118] Cairns B, Lacis A A and Carlson B E 2000 Absorption within inhomogeneous clouds and its parameterization in general circulation models *J. Atmos. Sci.* **57** 700–14

[119] Rossow W B, Delo C and Cairns B 2002 Implications of the observed mesoscale variations of clouds for the Earth's radiation budget *J. Clim.* **15** 557–85

[120] Rossow W B and Schiffer R A 1999 Advances in understanding clouds from ISCCP *Bull. Am. Meteorol. Soc.* **80** 2261–87

[121] Davis A B and Marshak A 2001 Multiple scattering in clouds: Insights from three-dimensional diffusion/P_1 theory *Nucl. Sci. Eng.* **137** 251–80

[122] Di Girolamo L and Davies R 1997 Cloud fraction errors caused by finite resolution measurements *J. Geophys. Res.* D **102** 1739–56

[123] Cahalan R F, Ridgway W, Wiscombe W J, Bell T L and Snider J B 1994 The albedo of fractal stratocumulus clouds *J. Atmos. Sci.* **51** 2434–55

[124] Cahalan R F, Ridgway W, Wiscombe W J, Gollmer S and Harshvardhan 1994 Independent pixel and Monte Carlo estimates of stratocumulus albedo *J. Atmos. Sci.* **51** 3776–90

[125] Harshvardhan and Randall D 1985 Comments on 'The parameterization of radiation for numerical weather prediction and climate models' *Mon. Weather Rev.* **113** 1832–3

[126] Stephens G L 1985 *Mon. Weather Rev.* **113** 1834–5 (Reply to Harshvardhan and Randall)

[127] Barker H W 1996 A parameterization for computing grid-averaged solar fluxes for inhomogeneous marine boundary layer clouds: I. Methodology and homogeneous biases *J. Atmos. Sci.* **53** 2289–303

[128] Barker H W, Wielicki B A and Parker L 1996 A parameterization for computing grid-averaged solar fluxes for inhomogeneous marine boundary layer clouds: II. Validation using satellite data *J. Atmos. Sci.* **53** 2304–16

[129] Oreopoulos L and Barker H W 1999 Accounting for subgrid-scale cloud variability in a multi-layer, 1D solar radiative transfer algorithm *Q. J. R. Meteorol. Soc.* **125** 301–30

[130] Avaste O A and Vainikko G M 1974 Solar radiative transfer in broken clouds *Izv. Acad. Sci. USSR Atmos. Ocean. Phys.* **10** 1054–61

[131] Titov G A 1990 Statistical description of radiation transfer in clouds *J. Atmos. Sci.* **47** 24–38

[132] Kassianov E 2002 Stochastic radiative transfer in multilayer broken clouds: I. Markovian approach *J. Quant. Spectrosc. Radiat. Transfer* **75** 373–93

[133] Kassianov E, Ackerman T P, Marchand R and Ovtchinnikov M 2002 Stochastic radiative transfer in multilayer broken clouds: II. Validation tests *J. Quant. Spectrosc. Radiat. Transfer* **75** 375–416

[134] Lane D E, Goris K and Somerville R C 2002 Radiative transfer through broken clouds: observations and model validation *J. Clim.* **15** 2921–33

[135] Zhuravleva T and Marshak A 2005 On the validation of the Poisson model of broken clouds *Izv. Atmos. Ocean. Phys.* **41** 713–25

[136] Byrne R N, Somerville R C J and Subasilar B 1996 Broken-cloud enhancement of solar radiation absorption *J. Atmos. Sci.* **53** 878–86

[137] Marshak A, Wen G, Coakley J A Jr, Remer L A, Loeb N G and Cahalan R F 2008 A simple model of the cloud adjacency effect and the apparent bluing of aerosols near clouds *J. Geophys. Res.* D **113** D14S17

[138] Pomraning G C 1986 Transport and diffusion in a statistical medium. *Transp. Theory Stat. Phys.* **5** 773–802

[139] Levermore C D, Pomraning G C, Sanzo D L and Wong J 1986 Linear transport theory in a random medium *J. Math. Phys.* **27** 2526–36

[140] Malvagi F, Byrne R N, Pomraning G C and Somerville R C J 1993 Stochastic radiative transfer in a partially cloudy atmosphere *J. Atmos. Sci.* **50** 2146–58

[141] Stephens G L 1988 Radiative transfer through arbitrary shaped optical media: II. Group theory *J. Atmos. Sci.* **45** 1837–49

[142] Stephens G L 1988 Radiative transfer through arbitrary shaped optical media: I. A general method of solution *J. Atmos. Sci.* **45** 1818–36

[143] Samorodnitsky G and Taqqu M S 1994 *Stable Non-Gaussian Random Processes* (New York: Chapman and Hall)

[144] Lévy P 1937 *Théorie de l'Addition des Variables Aléatoires* (Paris: Gauthier Villars)

[145] Davis A B and Polonsky I N 2005 Approximation methods in atmospheric 3D radiative transfer: II. Resolved variability and phenomenology *3D Radiative Transfer in Cloudy Atmospheres* ed A Marshak and A B Davis (Heidelberg: Springer) pp 283–340 chapter 5

[146] Huang D, Liu Y and Wiscombe W J 2008 Determination of cloud liquid water distribution using 3D cloud tomography *J. Geophys. Res.* D **113** D13201

[147] Marshak A, Davis A, Cahalan R F and Wiscombe W J 1994 Bounded cascade models as non-stationary multifractals *Phys. Rev.* E **49** 55–69

[148] Davis A B, Marshak A, Gerber H and Wiscombe W J 1999 Horizontal structure of marine boundary-layer clouds from cm- to km-scales *J. Geophys. Res.* D **104** 6123–44

[149] Schertzer D and Lovejoy S 1987 Physical modeling and analysis of rain and clouds by anisotropic scaling multiplicative processes *J. Geophys. Res.* **92** 9693–714

[150] Marshak A and Davis A B 2005 Scale-by-scale analysis and fractal cloud models *3D Radiative Transfer in Cloudy Atmospheres* ed A Marshak and A B Davis (Heidelberg: Springer) pp 653–63

[151] Cahalan R F and Snider J B 1989 Marine stratocumulus structure during FIRE *Remote Sens. Environ.* **28** 95–107

[152] Cahalan R F, Silberstein D and Snider J 1995 Liquid water path and plane-parallel albedo bias during ASTEX *J. Atmos. Sci.* **52** 3002–12

[153] Marshak A, Davis A, Wiscombe W J and Titov G 1995 The verisimilitude of the independent pixel approximation used in cloud remote sensing *Remote Sens. Environ.* **52** 72–8

[154] Evans K F and Wiscombe W J 2004 An algorithm for generating stochastic cloud fields from radar profile statistics *Atmos. Res.* **72** 263–89

[155] Hogan R J and Kew S F 2005 A 3D stochastic cloud model for investigating the radiative properties of inhomogeneous cirrus clouds *Q. J. R. Meteorol. Soc.* **131** 2585–608

[156] Schmidt K S, Venema V, Di Giuseppe F, Scheirer R, Wendisch M and Pilewski P 2007 Reproducing cloud microphysics and irradiance measurements using three 3D cloud generators *Q. J. R. Meteorol. Soc.* **133** 765–80

[157] Venema V, Meyer S, Garcia S G, Kniffka A, Simmer C, Crewell S, Lohnert U, Trautmann T and Macke A 2006 Surrogate cloud fields generated with the iterative amplitude adapted Fourier transform algorithm *Tellus. Ser. A, Dyn. Meteorol. Oceangr.* **58** 104–20

[158] Prigarin S and Marshak A 2009 A simple stochastic model for generating broken cloud optical depth and cloud-top height fields *J. Atmos. Sci.* **66** 92–104

[159] Siebesma A P and Jonker H J J 2000 Anomalous scaling of cumulus cloud boundaries *Phys. Rev. Lett.* **85** 214–7

[160] Evans K F and Marshak A 2005 Numerical methods *3D Radiative Transfer in Cloudy Atmospheres* ed A Marshak and A B Davis (Heidelberg: Springer) pp 243–81 chapter 4

[161] Cahalan R F and 26 co-authors 2005 The international Intercomparison of 3D Radiation Codes (I3RC): bringing together the most advanced radiative transfer tools for cloudy atmospheres *Bull. Am. Meteorol. Soc.* **86** 1275–93

[162] Kalos M H 1963 Importance sampling in Monte Carlo shielding calculations. I. Neutron penetration through thick hydrogen slabs *Nucl. Sci. Eng.* **16** 227–34

[163] Ueki T and Larsen E W 1996 Deterministic theory of Monte Carlo variance *Trans. Am. Nucl. Soc.* **75** 133–5

[164] Case K M and Zweifel P F 1967 *Linear Transport Theory* (Reading, MA: Addison-Wesley)

[165] Vladimirov V 1963 *Mathematical Problems in the One-Velocity Theory of Particle Transport* AECL-1661, At. Energy of Can. Ltd

[166] Bal G 2009 Inverse transport theory and applications *Inverse Problems* **25** 055006

[167] Larsen E W 1982 Unconditionally stable diffusion synthetic acceleration methods for the slab geometry discrete ordinates equations: I. Theory *Nucl. Sci. Eng.* **82** 47

[168] Ramone G L, Adams M L and Nowak P F 1997 A transport synthetic acceleration method for transport iterations *Nucl. Sci. Eng.* **125** 257

[169] Balsara D 2001 Fast and accurate discrete ordinate methods for multidimensional radiative transfer: I. Basic methods *J. Quant. Spectrosc. Radiat. Transfer* **69** 671–707

[170] Evans K F 1998 The spherical harmonics discrete ordinate method for three-dimensional atmospheric radiative transfer *J. Atmos. Sci.* **55** 429–46

[171] Evans K F 1993 Two-dimensional radiative transfer in cloudy atmospheres: the spherical harmonic spatial grid method *J. Atmos. Sci.* **50** 3111–24

[172] Trasi N S, de Oliveira C R E and Haigh J D 2004 A finite element spherical harmonics model for radiative transfer in inhomogeneous clouds: I. The EVENT model *Atmos. Res.* **72** 197–221

[173] Cook P A, de Oliveira C R E, Haigh J D and Goddard A J 2004 A finite element spherical harmonics model for radiative transfer in inhomogeneous clouds: II. Some applications *Atmos. Res.* **72** 223–37

[174] Nikolaeva O V, Bass L P, Germogenova T A, Kokhanovisky A A, Kuznetsov V S and Mayer B 2005 The influence of neighboring clouds on the clear sky reflectance with the 3-D transport code RADUGA *J. Quant. Spectrosc. Radiat. Transfer* **94** 405–24

[175] Ferlay N and Isaka H 2006 Multiresolution analysis of radiative transfer through inhomogeneous media: I. Theoretical development *J. Atmos. Sci.* **63** 1200–12

[176] Ferlay N, Isaka H, Gabriel P and Benassi A 2006 Multiresolution analysis of radiative transfer through inhomogeneous media: II. Validation and new insights *J. Atmos. Sci.* **63** 1213–30

[177] Stephens G L 1986 Radiative transfer in spatially heterogeneous, two-dimensional anisotropically scattering media *J. Quant. Spectrosc. Radiat. Transfer* **36** 51–67

[178] Davis A, Marshak A, Cahalan R F and Wiscombe W J 1997 The Landsat scale break in stratocumulus as a three-dimensional radiative transfer effect: Implications for cloud remote sensing *J. Atmos. Sci.* **54** 241–60

[179] Marchuk G I 1995 *Adjoint Equations and Analysis of Complex Systems* (Norwell, MA: Kluwer Academic)

[180] Pincus R and Evans K F 2009 Computational cost and accuracy in calculating three-dimensional radiative transfer: results for new implementations of Monte Carlo and SHDOM *J. Atmos. Sci.* **66** 3131–46

[181] Sobol I M 1974 *The Monte Carlo Method* (Chicago, IL: University of Chicago Press)

[182] Spanier J 1995 *Quasi-Monte Carlo Methods for Particle Transport Problems* (*Lecture Notes in Statistics* Number 106) (New York: Springer)

[183] Marchuk G I, Mikhailov G, Nazaraliev M, Darbinjan R, Kargin B and Elepov B 1980 *The Monte Carlo Methods in Atmospheric Optics* (New York: Springer)

[184] Iwabuchi H 2006 Efficient Monte Carlo methods for radiative transfer modeling *J. Atmos. Sci.* **63** 2324–39

[185] Várnai T and Marshak A 2009 MODIS observations of enhanced clear sky reflectance near clouds *Geophys. Res. Lett.* **36** L06807

[186] King M D, Radke L F and Hobbs P V 1990 Determination of the spectral absorption of solar radiation by marine stratocumulus clouds from airborne measurements within clouds *J. Atmos. Sci.* **47** 894–907

[187] Cannon C J 1970 Line transfer in two dimensions *Astrophys. J.* **161** 255–64

[188] Stephens G L, Gabriel P M and Partain P T 2001 Parameterization of atmospheric radiative transfer: I. Validity of simple models *J. Atmos. Sci.* **58** 3391–409

[189] Gabriel P M, Partain P T and Stephens G L 2001 Parameterization of atmospheric radiative transfer: II. Selection rules *J. Atmos. Sci.* **58** 3311–423

[190] Stephens G L, Wood N B and Gabriel P M 2004 An assessment of the parameterization of subgrid-scale cloud effects on radiative transfer: I: Vertical overlap *J. Atmos. Sci.* **61** 715–32

[191] Wood N B, Gabriel P M and Stephens G L 2005 An assessment of the parameterization of subgrid-scale cloud effects on radiative transfer: II. Horizontal inhomogeneity *J. Atmos. Sci.* **62** 2895–909

[192] Mechem D B, Kogan Y L, Ovtchinnikov M, Davis A B, Evans K F, and Ellingson R G 2008 Multidimensional longwave forcing of boundary layer cloud systems *J. Atmos. Sci.* **65** 3963–77

[193] Skamarock W C, Klemp J B, Dudhia J, Gill D O, Barker D M, Duda M G, Huang X-Y, Wang W and Powers J G 2008 A description of the Advanced Research WRF, Version 3 *Technical Report* NCAR/TN475 + STR, National Center for Atmospheric Research TECHNICAL NOTE, Boulder (CO)

[194] Cox S K, McDougal D S, Randall D A and Schiffer R A 1987 FIRE – The First ISCCP Regional Experiment *Bull. Am. Meteorol. Soc.* **68** 114–18

[195] Lovejoy S, Schertzer D, Silas P, Tessier Y and Lavallée D 1993 The unified scaling model of atmospheric dynamics and systematic analysis of scale invariance in cloud radiances *Ann. Geophys.* **11** 119–27

[196] Marshak A, Davis A, Wiscomb W J and Cahalan R F 1995 Radiative smoothing in fractal clouds *J. Geophys. Res.* D **100** 26247–61

[197] Zuidema P and Evans K F 1998 On the validity of the independent pixel approximation for the boundary layer clouds observed during ASTEX *J. Geophys. Res.* D **103** 6059–74

[198] Oreopoulos L, Marshak A, Cahalan R F and Wen G 2000 Cloud three-dimensional effects evidenced in Landsat spatial power spectra and autocorrelation function *J. Geophys. Res.* D **105** 14777–88

[199] von Savigny C, Funk O, Platt U and Pfeilsticker K 1999 Radiative smoothing in zenith-scattered sky light transmitted through clouds to the ground *Geophys. Res. Lett.* **26** 2949–52

[200] von Savigny C, Davis A B, Funk O and Pfeilsticker K 2002 Large-scale stationarity in time-series of zenith radiance under cloudy skies *Geophys. Res. Lett.* **29** 1825

[201] Papoulis A and Pillai S U 2001 *Probability, Random Variables and Stochastic Processes* (New York: McGraw-Hill Science/Engineering/Mathematics)

[202] Gabriel P, Barker H W, O'Brien D, Ferlay N and Stephens G L 2009 Statistical approaches to error identification for plane-parallel retievals of optical and microphysical properties of three-dimensional clouds: Baysian inference *J. Geophys. Res.* D **114** 06207

[203] Horváth Á and Davies R 2004 Simultaneous retrieval of cloud motion and height from polar-orbiter multiangle measurements *Geophys. Res. Lett.* **31** L01102

[204] Diner D J *et al* 1998 Multi-angle Imaging SpectroRadiometer (MISR) instrument description and experiment overview *IEEE Trans. Geosci. Remote Sens.* **36** 1072–87

[205] Várnai T and Marshak A 2002 Observations of three-dimensional radiative effects that influence MODIS cloud optical thickness retrievals *J. Atmos. Sci.* **59** 1607–18

[206] Nakajima T and King M D 1990 Determination of optical thickness and effective radius of clouds from reflected solar radiation measurements: I. Theory *J. Atmos. Sci.* **47** 1878–93

[207] Várnai T and Marshak A 2001 Statistical analysis of the uncertainties in cloud optical depth retrievals caused by three-dimensional radiative effects *J. Atmos. Sci.* **58** 1540–8

[208] Zinner T and Mayer B 2006 Remote sensing of stratocumulus clouds: uncertainty and biases due to inhomogeneity *J. Geophys. Res.* D **111** D14209

[209] Mayer B 2009 Radiative transfer in the cloudy atmosphere *Eur. Phys. J. Conf.* **1** 75–99

[210] Kato S and Marshak A 2008 Solar zenith and viewing geometry dependent errors in satellite retrieved cloud optical thickness: marine stratocumulus case *J. Geophys. Res.* D **114** 01202

[211] Stevens B and Lenschow D H 2001 Observations, experiments, and large eddy simulations *Bull. Am. Meteorol. Soc.* **82** 283–94

[212] Platnick S, King M D, Ackerman S A, Menzel W P, Baum B A, Riedi J C and Frey R A 2003 The MODIS cloud products: algorithms and examples from Terra *IEEE Trans. Geosci. Remote Sens.* **41** 459–73

[213] Platnick S 2000 Vertical photon transport in cloud remote sensing problems *J. Geophys. Res.* D **105** 22919–35

[214] Chang F-L and Li Z 2002 Estimating the vertical variation of cloud droplet effective radius using multispectral near-infrared satellite measurements *J. Geophys. Res.* D **107** 4257

[215] Marshak A, Platnick S, Várnai T, Wen G and Cahalan R F 2006 Impact of 3D radiative effects on satellite retrievals of cloud droplet sizes *J. Geophys. Res.* D **111** DO9207

[216] Platnick S, Pincus R, Wind B, King M D, Gray M and Hubanks P 2005 An initial analysis of the pixel-level uncertainties in global MODIS cloud optical thickness and effective particle size retrievals *SPIE Proc.* **5652** 1–12

[217] Cornet C, Buriez J-C, Riedi J, Isaka H and Guillemet B 2005 Case study of inhomogeneous cloud parameter retrieval from MODIS data *Geophys. Res. Lett.* **32** L13807

[218] Szczap F, Isaka H, Saute M, Guillemet B and Ioltukhovski A 2000 Effective radiative properties of bounded cascade absorbing clouds: definition of effective single scattering albedo *J. Geophys. Res.* D **105** 20635–48

[219] Petty G 2002 Area-average solar radiative transfer in three-dimensionally inhomogeneous clouds: the independently scattering cloudlet model *J. Atmos. Sci.* **59** 2910–29

[220] Wen G, Marshak A, Cahalan R F, Remer L A and Kleidman R G 2007 3D aerosol–cloud radiative interaction observed in collocated MODIS and ASTER images of cumulus cloud fields *J. Geophys. Res.* D **112** D13204

[221] Remer L A *et al* 2005 The MODIS aerosol algorithm, products, and validation *J. Atmos. Sci.* **62** 947–73

[222] Loeb N G and Manalo-Smith N 2005 Top-of-atmosphere direct radiative effect of aerosols over global oceans from merged CERES and MODIS observations *J. Clim.* **18** 3506–26

[223] Ignatov A, Minnis P, Loeb N, Wielicki B, Miller W, Sun-Mack S, Tanré D, Remer L, Laslo I and Geier E 2005 Two MODIS aerosol products over ocean on the Terra and Aqua CERES SSF *J. Atmos. Sci.* **62** 1008–31

[224] Zhang J, Reid J S and Holben B N 2005 An analysis of potential cloud artifacts in MODIS over ocean aerosol optical thickness product *Geophys. Res. Lett.* **32** L15803

[225] Kaufman Y J *et al* 2005 A critical examination of the residual cloud contamination and diurnal sampling effects on MODIS estimates of aerosol over ocean *IEEE Trans. Geosci. Remote Sens.* **43** 2886–97

[226] Matheson M A, Coakley J A Jr and Tahnk W R 2005 Aerosol and cloud property relationships for summertime stratiform clouds in the northeastern Atlantic from AVHRR observations *J. Geophys. Res.* D **110** D24204

[227] Kobayashi T, Masuda K, Sasaki M and Mueller J 2000 Monte Carlo simulations of enhanced visible radiance in clear-air satellite fields of view near clouds *J. Geophys. Res.* D **105** 26569–76

[228] Cahalan R F, Oreopoulos L, Wen G, Marshak A, Tsay S-C and DeFelice T 2001 Cloud characterization and clear sky correction from Landsat 7 *Remote Sens. Environ.* **78** 83–98

[229] Yamaguchi Y, Kahle A B, Tsu H, Kawakami T and Pniel M 1998 Overview of Advanced Spaceborne Thermal Emission and Reflection radiometer (ASTER) *IEEE Trans. Geosci. Remote Sens.* **36** 1062–71

[230] Mishchenko M I, Cairns B, ,Hansen J E, Travis L D, Burg R, Kaufman Y J, Martins J V and Shettle E P 2004 Monitoring of aerosol forcing of climate from space: analysis of measurement requirements *J. Quant. Spectrosc. Radiat. Transfer* **88** 149–61

[231] Wen G, Marshak A and Cahalan R F 2008 The role of molecular Rayleigh scattering in the enhancement of clear sky radiance in the vicinity of cumulus clouds *J. Geophys. Res.* D **113** D24207

[232] Pincus R, Barker H W and Morcrette J J 2003 A fast, flexible, approximate technique for computing radiative transfer in inhomogeneous cloud fields *J. Geophys. Res.* D **108** 4376–9

[233] Räisänen P, Barker H W, Khairoutdinov M F, Li J and Randall D A 2004 Stochastic generation of subgrid-scale cloudy columns for large-scale models *Q. J. R. Meteorol. Soc.* **130** 2047–67

[234] Räisänen P, Barker H W and Cole J 2005 The Monte Carlo Independent Column Approximation's conditional random noise: impact on simulated climate *J. Clim.* **18** 4715–30

[235] Barker H W, Cole J N, Morcrette J, Pincus R, Räisänen P, von Salzen K and Vaillancourt P A 2008 The Monte Carlo

Independent Column Approximation: an assessment using several global atmospheric models *Q. J. R. Meteorol. Soc.* **134** 1463–78

[236] Cole J N S, Barker H W, O'Hirok W, Clothiaux E E, Khairoutdinov M F and Randall D A 2005 Atmospheric radiative transfer through global arrays of 2D clouds *Geophys. Res. Lett.* **32** L19817

[237] Marshak A, Davis A, Cahalan R F and Wiscombe W J 1998 Nonlocal independent pixel approximation: direct and inverse problems *IEEE Trans. Geosc. Remote Sens.* **36** 192–205

[238] Iwabuchi H and Hayasaka T 2003 A multi-spectral non-local method for retrieval of boundary layer cloud properties from optical remote sensing data *Remote Sens. Environ.* **88** 294–308

[239] Tikhonov A N and Arsenin V Y 1977 *Solutions of Ill-Posed Problems* (*Scripta Series in Mathematics*) (Washington, DC: Winston)

[240] Box M A, Polonsky I N and Davis A B 2003 Higher-order perturbation theory applied to radiative transfer in non-plane-parallel media *J. Quant. Spectrosc. Radiat. Transfer* **78** 105–18

[241] Polonsky I N, Box M A and Davis A B 2003 Radiative transfer through inhomogeneous turbid media: implementation of the adjoint perturbation approach at the first-order *J. Quant. Spectrosc. Radiat. Transfer* **78** 85–98

[242] Faure T, Isaka H and Guillemet B 2001 Neural network analysis of the radiative interaction between neighboring pixels in inhomogeneous clouds *J. Geophys. Res.* D **106** 14465–84

[243] Faure T, Isaka H and Guillemet B 2001 Mapping neural network computation of high-resolution radiant fluxes of inhomogeneous clouds *J. Geophys. Res.* D **106** 14961–74

[244] Faure T, Isaka H and Guillemet B 2002 Neural network retrieval of cloud parameters of inhomogeneous and fractional clouds: Feasibility study *Remote Sens. Environ.* **77** 123–38

[245] Faure T, Isaka H and Guillemet B 2002 Neural network retrieval of clouds parameters from high-resolution multi-spectral radiometric data *Remote Sens. Environ.* **80** 285–96

[246] Cornet C, Isaka H, Guillemet B and Szczap F 2004 Neural network retrieval of cloud parameters of inhomogeneous cloud from multispectral and multiscale radiance data: feasibility study *J. Geophys. Res.* D **109** D12203

[247] Zinner T, Mayer B and Schröder M 2006 Determination of three-dimensional cloud structures from high-resolution radiance data *J. Geophys. Res.* D **111** D08204

[248] Evans K F, Marshak A and Várnai T 2008 The potential for improved cloud optical depth retrievals from the multiple directions of MISR *J. Atmos. Sci.* **65** 3179–96

[249] Kassianov E and Ovtchinnikov M 2008 On reflectance ratios and aerosol optical depth retrieval in the presence of cumulus clouds *Geophys. Res. Lett.* **35** L06807

[250] Kassianov E, Ovtchinnikov M, Berg L, McFarlane S A and Flynn C 2009 Retrieval of aerosol optical depth in vicinity of broken clouds from reflectance ratios: sensitivity study *J. Quant. Spectrosc. Radiat. Transfer* **110** 1677–89

[251] Tucker C J 1979 Red and photographic infrared linear combination for monitoring vegetation *Remote Sens. Environ.* **8** 127–50

[252] Marshak A, Knyazikhin Y, Davis A, Wiscombe W J and Pilewskie P 2000 Cloud–vegetation interaction: use of normalized difference cloud index for estimation of cloud optical thickness *Geophys. Res. Lett.* **27** 1695–8

[253] Leontieva E and Stamnes K 1994 Estimations of cloud optical thickness from ground-based measurements of incoming solar radiation in the Arctic *J. Clim.* **7** 566–78

[254] Min Q-L and Harrison L C 1996 Cloud properties derived from surface MFRSR measurements and comparison with GOES results at the ARM SGP site *Geophys. Res. Lett.* **23** 1641–4

[255] Boers R, van Lammeren A and Feijt A 2000 Accuracy of optical depth retrieval from ground-based pyranometers *J. Atmos. Ocean. Technol.* **17** 916–27

[256] Barker H W and Marshak A 2001 Inferring optical depth of broken clouds above green vegetation using surface solar radiometric measurements *J. Atmos. Sci.* **58** 2989–3006

[257] Tian Y, Zhang Y, Knyazikhin Y, Myneni R B, Glassy J, Dedieu G and Running S W 2000 Prototyping of MODIS LAI and FPAR algorithm with LASUR and LANDSAT data *IEEE Trans. Geosci. Remote Sens.* **38** 2387–401

[258] Box M A, Gerstl S A W and Simmer C 1988 Computation of atmospheric radiative effects via perturbation theory *Beitr. Phys. Atmos.* **62** 193–9

[259] Titov G A 1998 Radiative horizontal transport and absorption in stratocumulus clouds *J. Atmos. Sci.* **55** 2549–60

[260] Chylek P, Borel C, Davis A B, Augustine J and Hodges G 2004 Effect of broken clouds on satellite-based columnar water vapor retrieval *IEEE Geosc. Remote Sens. Lett.* **1** 175–8

[261] Gerber H, Boers R, Jensen J, Davis A, Marshak A and Wiscombe W J 2001 Spectral density of cloud liquid water content at high frequencies *J. Atmos. Sci.* **58** 497–503

[262] Kolmogorov A N 1941 Local structure of turbulence in an incompressible liquid for very large Reynolds numbers *Dokl. Akad. Nauk SSSR* **30** 299–303

[263] Rodgers R R and Yau M K 1989 *A Short Course in Cloud Physics* 3rd edn (Burlington, MA: Butterworth and Heinmann)

[264] Pankine A, Li Z, Parsons D, Purucker M, Weinstock E, Wiscombe W and Nock K 2009 Stratospheric satellites for earth observation *Bull. Am. Meteorol. Soc.* **90** 1109–19

[265] Weber P G, Brock B C, Garrett A J, Smith B W, Borel C C, Clodius W B, Bender S C, Rex Kay R and Decker M L 1999 Multispectral Thermal Imager mission overview *SPIE Proc.* **3753** 340–6

[266] Marshak A, Martins J V, Zubko V and Kaufman Y J 2006 What does reflection from cloud sides tell us about vertical distribution of cloud droplet sizes? *Atmos. Chem. Phys.* **6** 5295–305

[267] Martins J V, Marshak A, Remer L, Rosenfeld D, Kaufman Y J, Fernandez-Borda R, Koren I, Zubko V and Artaxo P 2007 Remote sensing the vertical profile of cloud droplet effective radius, thermodynamic phase, and temperature *Atmos. Chem. Phys. Discss.* **7** 4481–519

[268] Zinner T, Marshak A, Lang S, Martins J V and Mayer B 2008 Remote sensing of cloud sides of deep convection: toward a three-dimensional retrieval of cloud particle size profiles *Atmos. Chem. Phys.* **8** 4741–57

[269] Tao W-K and Simpson J 1993 The Goddard cumulus ensemble model: I. Model description *Terr. Atmos. Ocean Sci.* **4** 35–72

[270] Winker D M, Couch R H and McCormick M P 1996 An overview of LITE: NASA's Lidar In-space Technology Experiment *Proc. IEEE* **84** 164–80

[271] Minnis P, Heck P W, Young D F, Fairall C W and Snider J B 1992 Stratocumulus cloud properties derived from simultaneous satellite- and island-based measurements during FIRE *J. Appl. Meteorol.* **31** 317–39

[272] Davis A B, Winker D M and Vaughan M A 2001 First retrievals of dense cloud properties from off-beam/multiple-scattering lidar data collected in space *Laser Remote Sensing of the Atmosphere: Selected Papers from the 20th Int. Conf. on Laser Radar (ILRC 20),*

9–14 July 2000 (Vichy, France) ed A Dabas and J Pelon (Palaiseau: École Polytechnique) pp 35–8

[273] Irvine W M 1964 The formation of absorption bands and the distribution of photon optical paths in a scattering atmosphere *Bull. Astron. Inst. Neth.* **17** 226–79

[274] Ivanov V V and Sabashvili Sh A 1972 Transfer of resonance radiation and photon random walks *Astrophys. Space Sci.* **17** 13–22

[275] Pfeilsticker K, Erle F, Funk O, Veitel H and Platt U 1998 First geometrical path lengths probability density function derivation of the skylight from spectroscopically highly resolving oxygen A-band observations: I. Measurement technique, atmospheric observations, and model calculations *J. Geophys. Res.* D **103** 11483–504

[276] Pfeilsticker K 1999 First geometrical path lengths probability density function derivation of the skylight from spectroscopically highly resolving oxygen A-band observations: II. Derivation of the Lévy-index for the skylight transmitted by mid-latitude clouds *J. Geophys. Res.* D **104** 4101–16

[277] Scholl T, Pfeilsticker K, Davis A B, Baltink H K, Crewell S, Löhnert U, Simmer C, Meywerk J and Quante M 2006 Path length distributions for solar photons under cloudy skies: Comparison of measured first and second moments with predictions from classical and anomalous diffusion theories *J. Geophys. Res.* D **111** 12211–26

[278] Min Q-L and Harrison L C 1999 Joint statistics of photon path length and cloud optical depth *Geophys. Res. Lett.* **26** 1425–8

[279] Min Q-L, Harrison L C and Clothiaux E E 2001 Joint statistics of photon path length and cloud optical depth: case studies *J. Geophys. Res.* D **106** 7375–85

[280] Min Q-L and Clothiaux E E 2003 Photon path length distributions inferred from rotating shadowband spectroradiometer measurements at the Atmospheric Radiation Measurment Program Southern Great Plains site *J. Geophys. Res.* D **108** 4456–64

[281] Min Q-L, Harrison L C, Kiedron P, Berndt J and Joseph E 2004 A high-resolution oxygen A-band and water vapor band spectrometer *J. Geophys. Res.* D **109** 2202–10

[282] Portmann R W, Solomon S, Sanders R W and Daniel J S 2001 Cloud modulation of zenith sky oxygen path lengths over Boulder, Colorado: measurement versus model *J. Geophys. Res.* D **106** 1139–55

[283] Stephens G L, Heidinger A K and Gabriel P M 2005 Photon paths and cloud inhomogeneity: an observational strategy to assess effects of 3D geometry on radiative transfer *3D Radiative Transfer in Cloudy Atmospheres* ed A Marshak and A B Davis (Heidelberg: Springer) pp 587–616 chapter 13

[284] Buldyrev S V, Gitterman M, Havlin S, Kazakov A Ya, da Luz M G E, Raposo E P, Stanley H E and Viswanathan G M 2001 Properties of Lévy flights on an interval with absorbing boundaries *Physica* A **302** 148–61

[285] Priedhorsky W C, Smith R C and Ho C 1996 Laser ranging and mapping with a photon-counting detector *Appl. Opt.* **35** 441–52

[286] Davis A B, Ho C and Love S P 1998 Off-beam (multiply-scattered) lidar returns from stratus: II. Space-time measurements in a laboratory simulation *19th Int. Laser Radar Conf. (ILRC 19) Proceedings (Annapolis, MD, 6–10 July 1998)* ed U Singh *et al* (Washington, DC: NASA Center for Aero-Space Information (CASI)) pp 55–8

[287] Love S P, Davis A B, Ho C and Rohde C A 2001 Remote sensing of cloud thickness and liquid water content with Wide-Angle Imaging Lidar *Atmos. Res.* **59–60** 295–312

[288] Várnai T and Cahalan R F 2007 Potential for airborne offbeam lidar measurements of snow and sea ice thickness *J. Geophys. Res.* C **112** 12S90 (doi:10.1029/2007JC004091)

[289] Yodh A and Chance B 1995 Spectroscopy/imaging with diffusing light *Phys. Today* **48** 34–40